Sheffield Hallam University

A Sheffield Hallam University thesis

REFERENCE

**Return to Learning Centre of issue
Fines are charged at 50p per hour**

Molecular Dynamics Simulations of the Bombardment of Iron by Chromium Ions

Fatima Chami

A thesis submitted in partial fulfillment of the requirements of

Sheffield Hallam University

for the degree of Doctor of Philosophy

September 2006

Abstract

This thesis presents the results of an investigation of Cr keV bombardment of a crystalline Fe surface by molecular dynamics simulations. Different parameters of the bombardment were considered in particular those that pertain to surface pretreatment prior to PVD hard coatings.

Molecular dynamics simulations of 200 eV to 5 keV Cr bombardment of α-Fe at normal incidence have been performed at crystal temperatures of 0 K, 300 K and 700 K using many body potentials which were modified to properly represent the energetic interaction range. The sputtering yield increases with energy showing an enhancement at crystal temperature 700 K, the same as for adatom formation. Defect production, such as vacancies and interstitials, increase in general with energy, and their distribution profiles change with the crystal temperature.

The directional effect on the bombardment of Fe(100) surface at temperature 700 K, with 2.4 keV Cr shows a factor of two enhancement in the sputtering yield at low oblique angles with the initiation of reflection of Cr ions at high oblique incidence. Bombardment with noble gas ions has shown to be efficient and to produce a positive mass effect on sputtering compared to using a metal ion. Non linear enhancement of the total and cluster sputtering yield has been observed under diatomic Cr_2 projectile bombardment of Fe at 2.4 keV and 4.8 keV per dimer. The depth of origin of the sputtered particles seems to be insensitive to the bombardment parameters, but the sputtering rate of the surface does depend on the incidence parameters. The increase of sputtering yield at different bombardment conditions is the result of high yield events.

Acknowledgments

...To my parents

"*The process of scientific discovery is, in effect,
a continual flight from wonder* "

"*If we knew what it was we were doing, it
would not be called research, would it* "

Albert Einstein

Advanced studies

As a part of the course of PhD study, a number of conferences and workshops were attended in chronological order:

- Sixth Sheffield Arc Bond Sputtering (ABS) days, July 2000, Sheffield, UK

- Seventh Sheffield Arc Bond Sputtering (ABS) days, July 2001, Sheffield, UK

- Presentation at the *CCP5*, July 2001, UMIST, Manchester, UK

- Workshop on *Multiscale Simulation Radiation Damage in FeCr Alloy*, October 2002, SCK.CEN, Mol, Belgium

- Presentation at the *6th International Conference on Computer Simulation of Radiation Effect in Solids (COSIRES)*, June 2002, Dresden, Germany

- *Postgraduate Research in Electronics and Photonics*, April 2003, Exeter University, UK

- *UK Network on Defects in Si and SiGe Meeting*, June 2004, Sheffield Hallam University, UK

- Presentation at the *14th International Conference on Ion Beam Modification of Materials* September 2004, Asilomar, Pacific Grove , California USA

An extremely valuable experience was the close collaboration with the modelling group at SCK.CEN, Belgium, thanks to Dr. L.Malerba.

Contents

iv

Chapter 1

Introduction

Bombardment processes [1–3] find many applications in materials science and technology, in particularly techniques based on plasma or directed beam interaction are widely used in nano and micro technology to coatings technology. The deposition of protective coatings has shown a great importance in increasing the life of bearing systems which are challenged by harsh operating conditions, aggressive media and hostile environments [4].

There are a wide variety of hard coatings dependant on the application [5–7]. For example diamond like carbon (DLC) coatings [8] have been used for surgical implants such as orthopaedic alloys, to reduce friction, improve bio compatibility and corrosion resistance and to act as a diffusion barrier.

Today's most challenging market for hard coatings is in high quality cutting tools, in particular for dry high speed cutting operations where the benefits are both economic and environmental [9, 10]. This type of application demands hard coatings, e.g. TiAlN, with high oxidation resistance, high hardness and low friction [11,12]. To achieve a durable effect of such coating, strong adhesion and high density are essential. These requirements are not exclusive to the coating or to the substrate materials but must apply to the coating-substrate interface. Adhesion of coatings is one of the most important and difficult tasks of surface engineering because the different physical and chemical properties of the coating and substrate materials at the interface region. Especially for those

coatings with predominantly covalent bonding structure on metallic substrates, where adhesion is usually very poor. Surface treatment by bombardment prior to coating, is a key step to promote adhesion and life time of the subsequent hard coating. This is evidenced by the morphology of the generated interface and the modification of surface layers by implantation of elements like Cr, Nb, or N which have demonstrated a significant influence on the adhesion, hardness and wear resistance of the coating [13–16].

1.1   Overview of PVD Hard Coating

Physical vapour deposition (PVD) method (*namely conventional and unbalanced magnetron sputtering, arc and electron beam evaporation*) for the formation of hard coating, is carried out in a system which etches and coats subsequently. This system is known as Arc Bond Sputtering (ABS)[1], since it combines the high energy and ionisation flux of Cathodic Arc (CA) mode for bombardment and surface etching, and the low energy of Un-Balanced Magnetron (UBM) sputtering mode for coating or deposition [17,18].

The choice of arc cathode material which will constitutes an ion source for metal ion etching of steel substrates owes to the characteristics of high melting point and high vapour pressure in order to minimise number and size of macro particles or droplets emitted from the cathode. Cr was found to be well suited in this respect [14,15]. Droplets emitted from an arc source can cause growth of defects affecting the subsequent coating roughness and can reduce etching efficiency as shown in Fig.1.1, where 100 nm of steel was removed with respect to the area overshadowed by the deposited droplet during Cr bombardment. The morphology of the interface changes with the conditions of bombardment of the substrate as illustrated in Fig.1.2 and Fig.1.3, by the formation of a fine layer at the interface between the steel substrate and coating (TiAlN) when the

---

[1]A schematic cross section of the ABS coating chamber is shown in Appendix B
[2]transmission electron microscope (TEM)

2
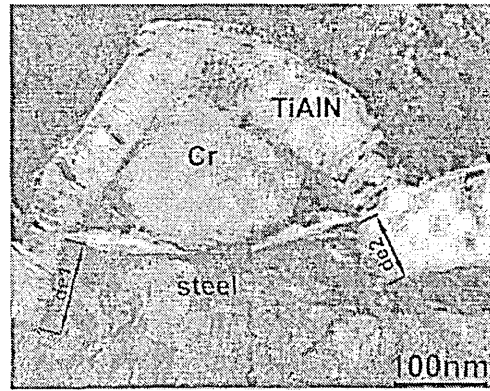
Figure 1.1: Evidence for removal of $\approx$ 100nm of steel by Cr- bombardment and for Cr droplet effect on the coating TiAlN Ref. [19]

(a)   (b)
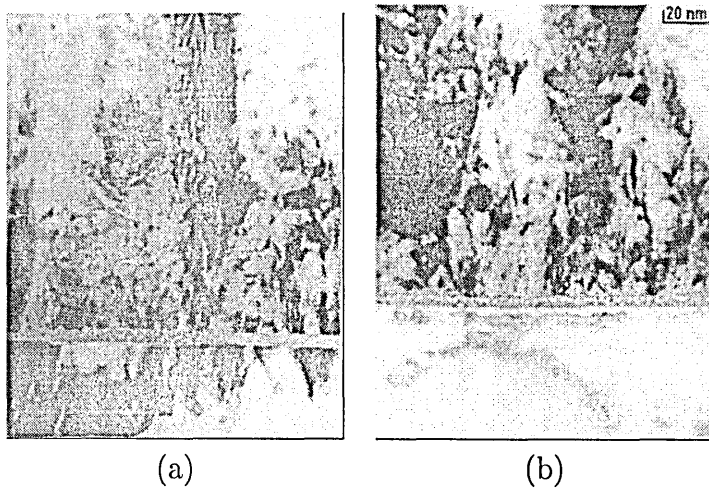
Figure 1.2: Cross-sectional TEM[3] images of TiAlN/steel taken for Cr ion bombarded steel biased at voltage U_b : a) -1200 V, b) -1000 V (after ref. [19])

(a)   (b)
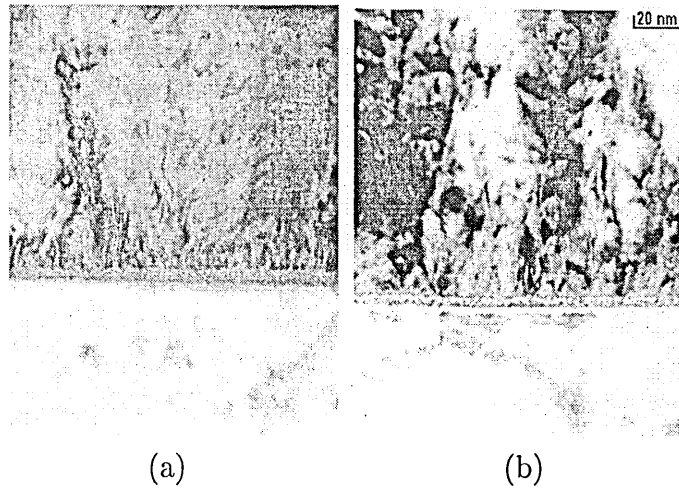
Figure 1.3: Same as Fig.1.2 at U_b : a) -800 V, b) -600 V (after ref. [19])
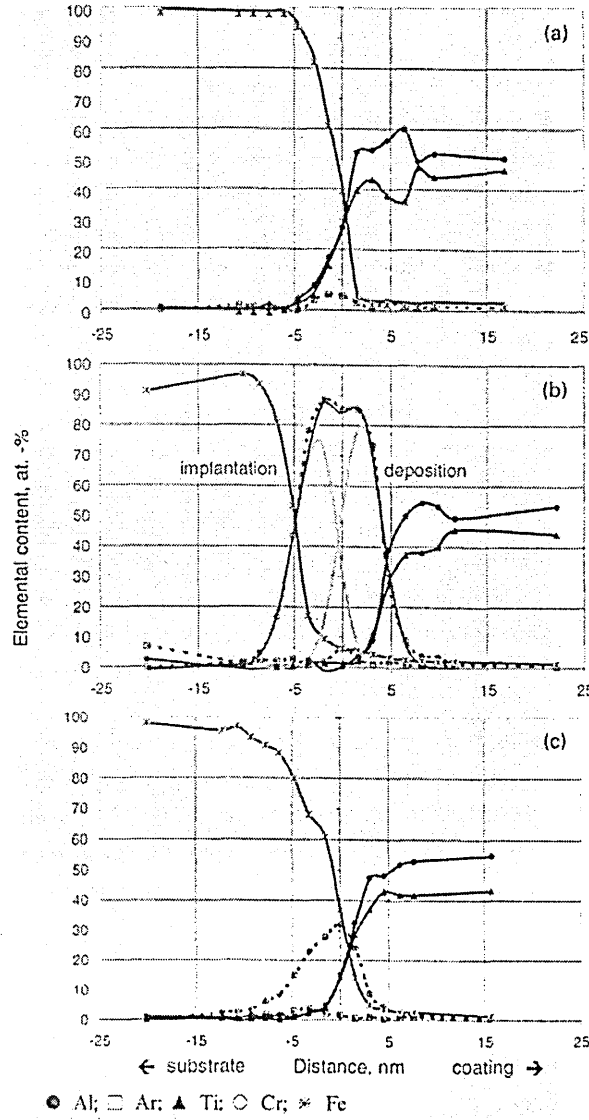
Figure 1.4: STEM-EDX[4] profiles across coating/substrate interface (TiAlN/steel) at various ion bombardment and bias voltage U_b : a) Ar -1200 V, b) Cr -600 V, c) Cr -1200 V (after ref. [5])

Cr ion energy increases by applying a higher bias voltage (Ub)[3] [5,8,15,20]. The compositional profiles across the coating substrate interface in Fig.1.4, show a distinctive influence of ion bombardment on the microchemistry of the interface. In Fig.1.4(a) a simple interface structure is generated by noble gas Ar bombardment (Ub= -1200 V), where the steep decrease of Fe concentration

---

[3](Ub is the bias voltage applied at the substrate to accelerate the metal ions generated by cathodic arc)
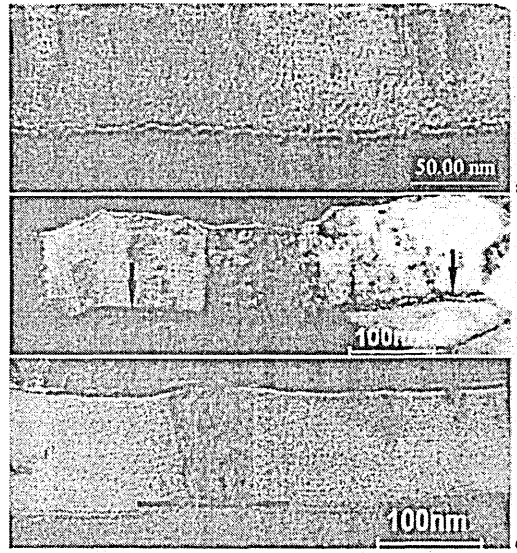
Figure 1.5: Bright field TEM images of TiAlN/steel interface of given surface bombardment : a) Ar -1200 V (underfocused), b) Cr -600 V (underfocused), c) Cr -1200 V (overfocused)(after ref. [5])

(substrate) corresponds to a steep increase of Ti and Al signal (coating) with a 5 at.% Ar accumulation. At low energy (Ub= -600 V) and for the metal ion Cr bombardment, a completely different profile is observed in Fig.1.4(b), where the substrate material (Fe) and the coating material (Ti,Al) are now separated by a broad Cr peak which may be resolved in two components. The component adjacent to the substrate is attributed to Cr implantation while the component adjacent to the coating is due to Cr deposition. When the accelerating voltage is increased as the same level as Ar bombardment, the Cr peak intensity in Fig.1.4(c), drops dramatically at the interface compared to Fig.1.4(b), and a pronounced penetration of Cr into the steel substrate occurs. This significant effect of Ar and Cr bombardment on the michrochemistry of the interface is accompanied by a change in the microstructure of the near interface region as it appears by TEM images in Fig.1.5. The sharply defined interface by Ar ion bombardment in Fig.1.5(a) correlates with the STEM-EDX profile, and the initiation of competitive growth of the coating is typical of ceramic growth on

5
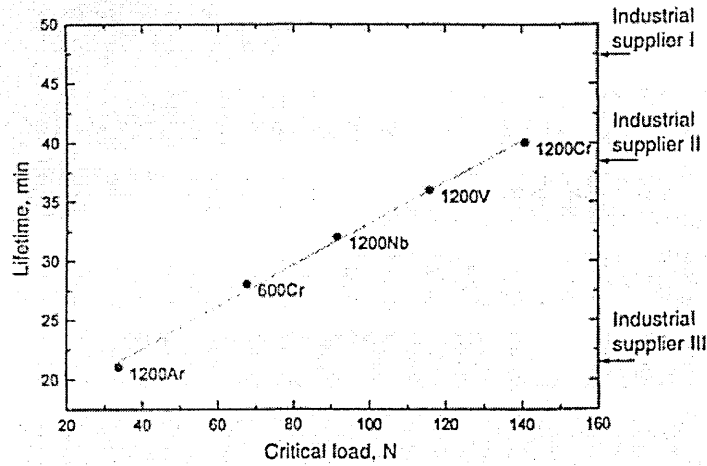
Figure 1.6: Correlation between tool life time and critical load values from same coating deposited after various sputter etching procedures, with comparison to three commercially available hard coating (after ref. [5])

steel substrate [21]. In Fig.1.5(b) a much broader interface with the dark ribbon stem from the Cr deposit under low energy Cr ion bombardment, as advanced earlier (Fig.1.4(b)).

In Fig.1.5(c) a large homogeneous area of uniform diffraction extends over several nanometres, is observed. This is indicative of regions of identical crystallographics orientation where local epitaxial growth developed, and can be related to the high content of implanted Cr revealed by STEM-EDX profile (Fig.1.4(c)). Implanted Cr is responsible for an increase of the lattice parameter of the substrate which should reduce the lattice mismatch between steel and coating therefore leading to a local epitaxial growth.

Increasing the Cr ion energy changes substantially the microstructure of the interface and the growing film. Further evidence of ion bombardment effect is on adhesion of the coating during tool performance tested by the critical load measurement (scratch test[5]) shown in Fig.1.6. The critical load increases from 33 N for Ar, to 68 N for Cr at Ub =-600 V, and to 141 N for Cr ion bombardment at Ub=-1200V.

---

[4]Scanning transmission electron microscope - energy dispersive X-ray (STEM-EDX)

[5]In scratch test a diamond tip is drawn over the sample surface under stepwise or continously increasing normal force

The strong correlation between interface microchemistry, microtructure and adhesion test implies that ion bombardment conditions prior to coating can produce low interfacial energy which enables local epitaxial growth and hence an optimised adhesion.

1.2 Aims

Hard coating needs to be carried out on a clean surface, i.e. contamination free surface like native oxide, to promote adhesion and durability. In this respect, pretreatment of the surface by bombardment has become one of the key processes to surface engineering. However, bombardment encompasses many parameters such as nature of the bombarding species, energy, current, and environment whether in vacuum or plasma atmosphere. It is practically difficult to assess the effect of each parameter separately and all experiments abide to a predefined process for a given application of the coated system. Interest has therefore developed in the use of computer simulation techniques to better understand the mechanisms of bombardment and give an insight of the individual effect of each bombardment parameter.

There are two basic types of simulators for ion bombardment of solid. The first, called Molecular Dynamics (MD) [22], deterministically tracks the motion of all particles in the ion-solid system and it can thus be precise. The second type of simulator, called Monte Carlo (MC) based on the Binary Collision Approximation (BCA) [23–25], tracks the motion of ions deterministically, but the motion of atoms which make up the solid is treated stochastically. A common problem with MC method is the random model selection of the next colliding atom, which does not always have a physical meaning. Hence, further improvement to this method has lead to the widely used BCA code known as the Marlowe code [25]. BCA codes are being successfully used for predicting ion implantation ranges. However, they fail to give an accurate picture of the structure of the damage left after implantation. This is due to the breakdown

7

of the idea of individual binary collision at low energy when many body effects become important and the exact trajectories deviate significantly from their asymptotes on which the BCA is based [23]. Therefore, MD sounds more promising for fully presenting the energetic interaction range, relying on an appropriate interatomic potential model.

In this thesis we aim to study the effect of Cr bombardment parameters on Fe crystallite as matrix element of steels, using MD approach. In order to carry out this study, it is necessary to develop a model potential for the Cr-Fe and Fe-Fe interaction which is capable to represent scattering event due to collision. The simulation attempts to predict the implantation depth of projectiles atoms, the number of atoms sputtered from the surface, and the degree of damage created in the target and its location. These are the main outcomes to be correlated against bombardment parameters and with reference to experiment on metal etching. The most interesting aspect of simulation is to provide a detailed microscopic understanding of the primary damage state of the system after bombardment which is not easily accessible by experiment.

A thorough literature review revealed that bombardment simulation is scarce for bcc metals in particular iron (Fe) compared to fcc metals i.e. copper (Cu). The library of computational data available deals mostly with bulk displacement cascade in Fe relevant to radiation damage [26–30], and the first study invoking Fe surface was reported on the effect of cascades initiation site relative to the free surface [31]..

1.3   Thesis Summary

Aside from this introduction the thesis is organised as follows.

Chapter 2 overviews the fundamental concepts of ion-solid interaction that is atomic collisions. A thorough review of theories to predict the experimental observables upon surface bombardment such as sputtering and defects are presented.

In Chapter 3 a survey of interatomic potentials for modelling metallic system is reviewed together with those potentials relevant to model scattering in bombardment.

Chapter 4. illustrates the details of the implementation and procedure of molecular dynamics method. The simulation model for bombardment with inherent approximation and potential adjustment are presented. The last part of this chapter is devoted to the Cr-Fe potential validation from the computational calculation of equilibrium properties.

Chapters 5-7 are the results of the simulations of keV bombardment of Fe that pertains to surface pretreatment. Chapters 5 and 6 are devoted to Cr bombardment in which the energy, target temperature and direction are investigated, while Chapter 7 examines the projectile parameters such as its nature, mass, and size.

Finally, the mains results of this thesis are summarized together with conclusions and suggestion for future work and are made in Chapter 8. Some initial results for fluence dependence which is considered to be null in this study, are included in Appendix A.

Chapter 2

Principles Of Atomic Collisions

Introduction

Owing to the extensive use of ion bombardment at the energy range relevant
to materials characterisation and surface engineering[1] it is perhaps justified
to have a brief look at the processes involved in ion bombardment in order
to identify those processes most amenable to MD simulations. Starting with
the fundamental process, the mechanism of an individual atomic collision is
described and the development of this process into a cascade is shown. Next,
the energy loss process of an ion is examined. The way this energy is dissipated
is in the form of material removal, damage and heat transfer. The former is
called sputtering and its prediction is of great experimental interest, therefore
the physics of sputtering with analytical treatment is reviewed. Besides
sputtering, models for damage generation are also presented.

Most theories of ion transport in matter are based on linear approximation
of the Boltzman transport equation in an amorphous medium [32], and it
is important to understand the theory in order to perceive the advantage of
numerical computer simulation. The reader can find more detailed description
of the theoretical formulations reviewed here in Ref. [23, 32]

---

[1]Introduction Chapter

(a)   (b)
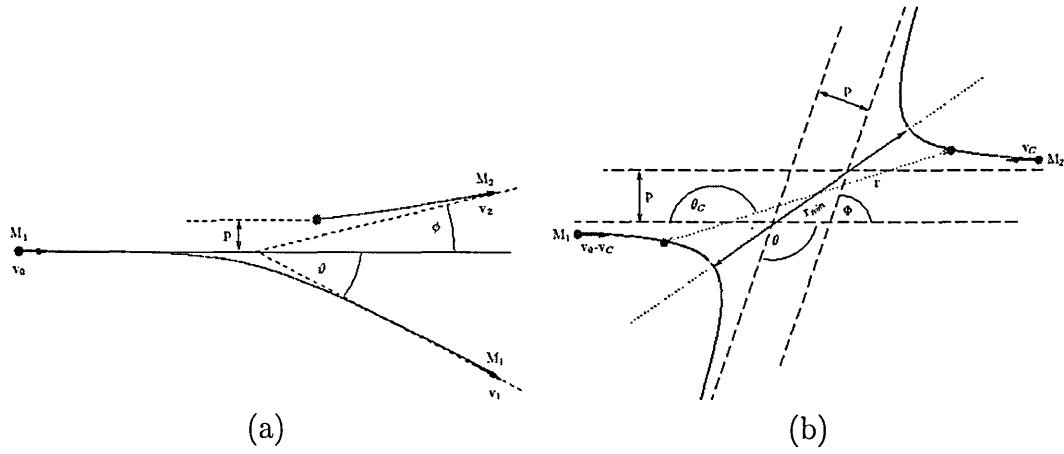
Figure 2.1: Two-body scattering process represented in: a)the laboratory (L.) system, b)the centre of mass coordinate (CM) system, M_1,M_2 are the masses of respectively the incident particle with velocity v_0 and the initially resting particle. v_1 and v_2 are the velocities after the scattering process for respectively incident and resting particle. ϑ and ϕ are the deflection angles in L system while θ is the scattering angle in CM system with velocity v_c (adapted from Ref. [23]).

2.1 Atomic Collision

An energetic ion moving in a solid undergoes interaction with the nuclei and the electrons of the target material. Based on Bohr's assumption, such interaction can be separated into an ion-nuclei interaction treated as an elastic collision process, and the ion-electron interaction treated as inelastic collision process without any scattering effect. For the elastic collision, each of the colliding particles are scattered as shown in Fig.2.1 and the non-relativistic conservation laws of energy Eq.(2.1) and momentum (longitudinal Eq.(2.2) and transverse Eq.(2.3)) can be used since the particle velocities are of the order of 0.1 % of the speed of light.

$$E = \frac{M_1 \cdot v_0^2}{2} = \frac{M_1 \cdot v_1^2}{2} + \frac{M_2 \cdot v_2^2}{2} \qquad (2.1)$$

$$M_1 \cdot v_0 = M_1 \cdot v_1 \cdot \cos(\vartheta) + M_2 \cdot v_2 \cdot \cos(\phi) \qquad (2.2)$$

$$0 = M_1 \cdot v_1 \cdot \sin(\vartheta) + M_2 \cdot v_2 \cdot \sin(\phi) \qquad (2.3)$$

11

Besides the initial energy and momentum, the scattering in Fig.2.1 is characterised by the impact parameter, p, which is the minimum distance between the two particles if they would pass without interaction . However, the particles are not solid spheres but ions or atoms [23, 32], so a repulsive potential $V(r)$ must be introduced in order to substitute for a finite radius so that scattering event can be determined. From a rigorous solution of the motion of two body scattering process in centre of mass coordinate (Fig.2.1.b), the scattering angle Θ is deduced [23, 32]:

$$\Theta = \pi - 2p \int_{r_{min}}^{\infty} \frac{dr}{r^2 \left[1 - \frac{V(r)}{E_c} - \left(\frac{p}{r}\right)\right]^{1/2}} \tag{2.4}$$

where E_c is the kinetic energy of the centre of mass, p is the collision impact parameter and r is the distance between the two particles. This is the general orbit equation for two-body central force scattering [23].

The energy, T, transferred by the incoming particle with energy E to the target particle is given by:

$$T = \gamma E sin^2 \frac{\Theta}{2} \tag{2.5}$$

where Θ is the scattering angle in the centre-of-mass frame and γ is the energy transfer coefficient with M_1 and M_2 the atomic masses of respectively, the incident particle and the target particle.

$$\gamma = \frac{4M_1 M_2}{(M_1 + M_2)^2} \tag{2.6}$$

The maximum energy transfer occurs during a head-on collision so that

$$T_m = \gamma E \tag{2.7}$$

Based on equations Eq.(2.4) and Eq.(2.5), the atoms set into motion by the ion can be calculated and these moving atoms constitute the 'cascade'. The simple kind of cascade is called *linear* and it is characterised by a low density of
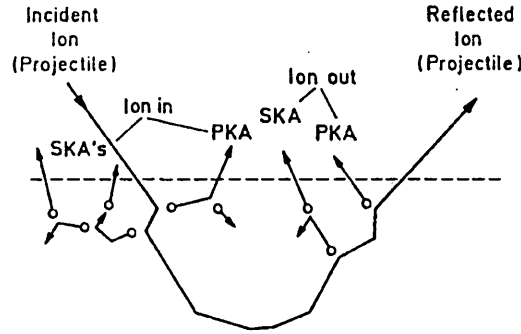
Figure 2.2: Schematic representation of recoils generated by projectile ion as it strikes and backscatters the solid surface (After Fig.12.1 of Ref. [23])

collisions and deposited energy and binary treatment of collisions. An example of the linear cascade is shown in Fig.2.2 where the incident ion generates primary knock-on atoms (PKA) which in their turn generate secondary knock-on atoms (SKA) and a cascade of higher order recoils propagates.

The concept of linearity cascade originates from linear approximation of the Boltzman equation (BE) transport theory, which implies that the interaction between the incoming particles and their own perturbation in the target are explicitly excluded. The linear approximation is valid only in the early stage of the ion-solid interaction and it can not describe non-binary collisions or the latter stages of the cascade. The linear BE can predict a number of important experimental observables and is more amenable to analytical treatment than its full non-linear counterpart [32–34].

2.2   Cross-Sections

The probability that a number of incident particle I will experience a certain interaction with a target atom is function the cross section σ

$$\frac{I}{I_0} = Nx\sigma \qquad (2.8)$$

13

where I_0 is the total number of incident particles, N is the atomic number density of the target (atoms/volume), and x is the thickness of the target. The important interaction here is a collision which results in the energy loss of the incident particle with energy E to target atoms. This energy loss is described by the stopping cross section $S(E)$. Since the particle can interact with atomic nuclei and electrons, $S(E)$ can be expressed as a sum of nuclear $S_n(E)$ and electronic $S_e(E)$ stopping cross sections. Hence, the total energy loss, also called the total stopping power (eV Å^{-1}) per unit distance dx travelled by an ion in a solid target of density N is given by:

$$\frac{dE}{dx} = \left(\frac{dE}{dx}\right)_n + \left(\frac{dE}{dx}\right)_e = -N[S_n(E) + S_e(E)] \qquad (2.9)$$

The degree of contribution of each of them is determined by the ion velocity. Ions having velocities v much greater than $v_F = \nu_B Z_1^{2/3}$, known as Fermi velocity, where Z_1 is the atomic number of the ion and v_B is the Bohr velocity (0.2227 (MeV/amu)$^{0.5}$), are expected to lose energy by electronic excitation and ionisation of the stopping medium. At lower velocities, $v << v_0$, nuclear stopping becomes dominant.

2.2.1 Nuclear Stopping

Analytically, the nuclear stopping cross section $S_n(E)$ of an ion can be integrated if one knows the statistics of energy transfer T in elastic collisions over all impact parameters or scattering angles

$$S_n(E) = \int_0^{T=T_m} T d\sigma(E, T) \qquad (2.10)$$

where $d\sigma(E, T)$ is the scattering cross section and it depends on the atomic potential model used to describe the interaction.

Based on the power approximation of the Thomas-Fermi [35, 36] interatomic model, i.e., with a potential of the form $V(r) \propto r^{1/m}$ where m is a parameter related to the steepness of the potential, Lindhard [37] approximated

14

the scattering cross-section at low energy ($\epsilon \leq 1$) in reduced energy unit ϵ (Eq.2.15), by the expression:

$$d\sigma(E,T) \approx C_m E^{-m} T^{-1-m} dT \qquad (2.11)$$

with

$$C_m = \frac{\pi}{2} \lambda_m a_L^2 \left(\frac{M_1}{M_2}\right)^m \left(\frac{2Z_1 Z_2 e^2}{a_L}\right)^{2m} \qquad (2.12)$$

Z_1 and Z_2 are the nuclear charges, and M_1 and M_2 the masses of the projectile and the target, respectively. e is the electron charge ($e^2 = 14.4eV \ \mathring{A}$). a_L is the Lindhard screening length and is given by

$$a_L = \left(\frac{9\pi^2}{128}\right)^{1/3} a_B(Z_1^{2/3} + Z_2^{2/3})^{-1/2} = 0.4685 \ (Z_1^{2/3} + Z_2^{2/3})^{-1/2} \mathring{A} \qquad (2.13)$$

where a_B is the Bohr radius $a_B = 0.529\mathring{A}$. λ_m is function of the parameter m and its values span from 0.5 for $m = 1$ to 24 for $m=0$, λ_m, λ_m is tabulated in Ref. [38]. $S_n(E)$ takes then the following form used in Sigmund's sputtering model

$$S_n(E) = \frac{1}{1-m} C_m \gamma^{1-m} E^{1-2m} \qquad (2.14)$$

Lindhard's reduced energy unit is expressed by

$$\epsilon = \frac{M_2}{M_1 + M_2} \ \frac{a_L}{Z_1 Z_2 e^2} \ E \qquad (2.15)$$

ϵ can also be written as a function of the so called Thomas-Fermi energy E_{TF} (Eq.2.17):

$$\epsilon = \frac{E}{E_{TF}}, \quad E_{TF} = \frac{Z_1 Z_2 e^2}{a_L} \ \frac{M_1 + M_2}{M_2} \qquad (2.16)$$

$$E_{TF}(eV) = 30.74 \ \frac{M_1 + M_2}{M_2} Z_1 Z_2 (Z_1^{2/3} + Z_2^{2/3})^{-1/2} \qquad (2.17)$$

To give an impression of the order of the reduced energy, ϵ is plotted in Fig.2.3 for various ion bombardment of Fe and the corresponding values of E_{TF} given in Table 2.1.
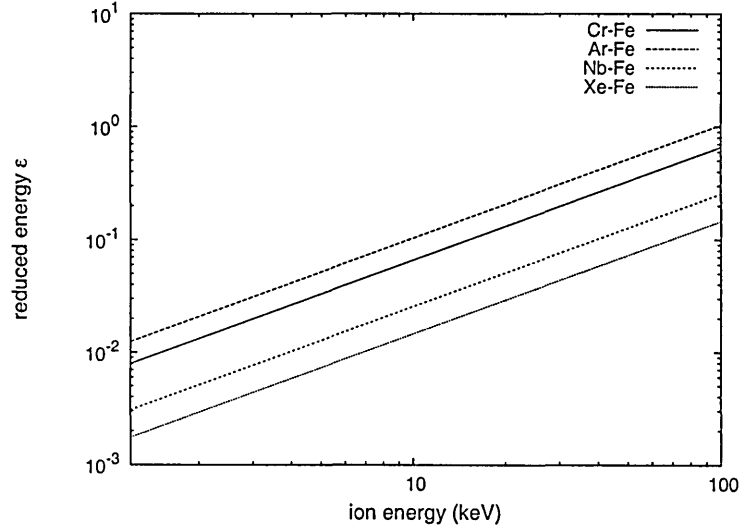
Figure 2.3: Reduced energy ϵ as a function of the ion energy (keV)

Projectile (M_1)	Ar (40)	Cr (52)	Nb (93)	Xe (131)
E_{TF}	96.7	152.2	391.2	685.9
E_{Max}	29	45.7	117.4	205.7

Table 2.1: Thomas-Fermi energy E_{TF} in keV and the maximum nuclear stopping energy E_{Max} for different ion bombardment of Fe target (M_2=56)

S_n can be defined in a universal way by the use of the reduced energy ϵ and a reduced nuclear stopping cross-section $s_n(\epsilon)$ as:

$$S_n(E) = 4\pi a_L Z_1 Z_2 e^2 \frac{M_1}{M_1 + M_2} s_n(\epsilon) \tag{2.18}$$

where the dimensionless $s_n(\epsilon)$ can be written from Eq.(2.14) and Eq.(2.15) as:

$$s_n(\epsilon) = \frac{\lambda_m}{2(1-m)} \epsilon^{1-2m} \tag{2.19}$$

Since the nuclear stopping depends on the interatomic potential used for atomic collision, other analytical forms of $s_n(\epsilon)$ were devised such as those given by Eq.(2.20) to Eq.(2.22) and plotted in Fig.2.4. Eq.(2.20) was derived by Mastsunami et al's [39] from an analytic fit to theoretical stopping power

16
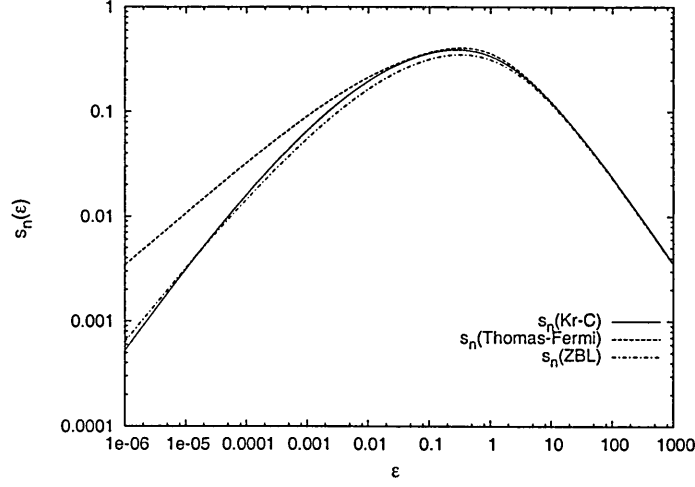
Figure 2.4: Nuclear stopping cross-section s_n^{KrC}, s_n^{TF} and s_n^{ZBL} function of the reduced energy unit ϵ

data given by Lindhard et al. [40] based on the Thomas-Fermi potential model [35,36], while Eq.(2.21) is based on the Kr-C potential [41]. In addition to the analytic approximation Eq.(2.22) derived from the universal ZBL potential by Ziegler et al's [42]

$$s_n^{TF} = \frac{3.441\sqrt{\epsilon}\ln(\epsilon + 2.718)}{1 + 6.355\sqrt{\epsilon} + \epsilon(6.882\sqrt{\epsilon} - 1.708)} \tag{2.20}$$

$$s_n^{KrC} = \frac{0.5\ln(1 + 1.288\epsilon)}{\epsilon + 0.1728\sqrt{\epsilon} + 0.008\epsilon^{0.1504}} \tag{2.21}$$

$$s_n^{ZBL}(\epsilon) = \begin{cases} \frac{\ln(1+1.1383\epsilon)}{2\cdot(\epsilon+0.01321\cdot\epsilon^{0.21226}+0.19593\cdot\epsilon^{0.5})} & \text{for } \epsilon \leq 30 \\ \frac{\ln(\epsilon)}{2\cdot\epsilon} & \text{for } \epsilon > 30 \end{cases} \tag{2.22}$$

It is worth mentioning in Fig.2.4 that $s_n^{TF}(\epsilon)$ cross section is too large at low energies ($\epsilon < 0.1$) compared $s_n^{KrC}(\epsilon)$. Also note that $s_n(\epsilon)$ has a maximum which occurs at about $\epsilon = 0.3$. Thus the maximum nuclear stopping is reached at an energy $E = E_{Max}$ deduced from Eq.(2.16). Examples of E_{Max} are given in Table 2.1 for different ion bombardemnt of Fe.

In modern computer simulations, the nuclear energy loss comes automatically into the picture due to the force interaction between the ion and the atoms, and an explicit analytical form is not needed at all.

17

2.2.2 Electronic Stopping

However, with the electronic stopping power, electrons cannot be localised and treated as point masses because of their significant wave characteristics. Therefore, the parameterisation of the electronic energy loss was developped according to the ions velocity, as outlined in Fig.2.5. Such velocity dependence results from two competing phenomena increase of the ion charge state and decrease of the interaction time with larger velocity.

Low-Energy Ions

For slow ions satisfying $(v < v_B Z_1^{2/3}$, region 1 in Fig.2.5), the electronic stopping cross section is derived from a parameterization which is either local (i.e. impact parameter dependent on the position in the lattice) or non-local (i.e. friction type which is same everywhere in the lattice).

Local energy loss Firsov [43] derived the expression

$$S_e^F(E) = 0.325(Z_1 + Z_2)\left(\frac{E}{M_1}\right)^{\frac{1}{2}} \tag{2.23}$$

Firsov's model estimates the electronic energy loss per ion-atom collision as due to the passage of electrons from one particle to the other. When the ion moves away from the atom, the electrons return so that electronic shells remain undistorted.

A better approach to Firsov's model was proposed by Oen and Robinson [44], since Fisov's model was derived for atoms with many electrons and may not be a good approximation for light ions.

Non-Local energy loss Lindhard and Scharf (LS) [45] derived the expression

$$S_e^{LS}(E) = 8\pi e^2 a_B \frac{Z_1^{7/6} Z_2}{(Z_1^{2/3} + Z_2^{2/3})^{3/2}} \left(\frac{E}{M_1}\right)^{\frac{1}{2}} \tag{2.24}$$

18
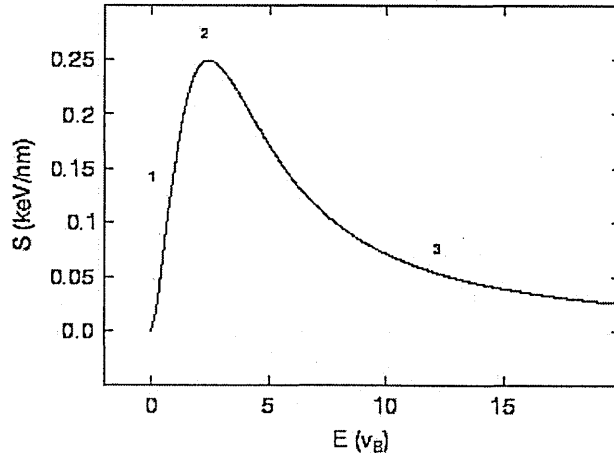
Figure 2.5: Electronic stopping power of He in C function of the energy in unit of Bohr velocity (from Ref. [32])

Lindhard and Scharf used a model of slow heavy ion moving in a uniform electron gas. Electron impinging on the ion transfer net energy which is proportional to their drift velocity (relative to the ion).

The non-local parameterisation cannot cope with crystalline material because the structure has lattice directions, called channels where electron densities are considerably lower than elsewhere in the crystal and so the stopping power is not constant. In this respect, Kitagawa and Ohtsuki [46] formulated the electronic stopping for high and low density electron gas using local density approximation. However, most metals are somewhere between these two extremes.

$$S_e(E) = kE^{1/2} \tag{2.25}$$

Note that the models presented above have all one common property in the energy dependance given by Eq.(2.25), where k is a model dependant constant.

High-Energy Ions

At high energy ($v \gg \nu_B Z_1^{2/3}$, region 3 in Fig.2.5) above ~ 0.5 MeV/amu, the electronic stopping cross section can be predicted within the Bethe-Bloch (BB) quantum mechanical model (Refs. within [23,32]). Bethe's formula for the electronic stopping is given by:

$$S_e^{BB}(E) = 4\pi \frac{Z_1^2 e^4}{mv^2} Z_2 \ln \left(\frac{2mv^2}{I} \right) \qquad (2.26)$$

where I is the mean excitation energy of the atom in its ground state. Bloch's correction to Eq.(2.26) lead to the Bethe-Bloch formulation [23,32], which was further modified by the so-called Barkas effect term [47,48].

$$S_e^{-1} = (S_e^{LS})^{-1} + (S_e^{BB})^{-1} \qquad (2.27)$$

In the intermediate energy range ($v \approx \nu_B Z_1^{2/3}$, region 2 in Fig.2.5), the electronic stopping can be described by Eq.(2.27) [23] since it is a much more complicated issue to handle theoretically.

ZBL General Approach

Ziegler, Biersack and Littmark (ZBL) have proposed a general method of determining electronic stopping for all atomic projectiles in all elements in a wide energy range [23,42]. The so-called ZBL electronic stopping is based on the Brandt-Kitagawa (BK) theory [49] which factorizes the electronic stopping of a heavy ion ($Z_1 > 2$) into an effective charge of the electronic stopping of proton (ZBL uses Hydrogen stopping S_e^H) given by:

$$S_e^{ZBL} = S_e^H (\gamma Z_1)^2 \qquad (2.28)$$

where γ is functional expression of the Fermi velocity v_F, Bohr velocity v_B and particle velocity v. The ZBL electronic stopping is proportional to E at

20

low energy and proportional to lnE at high energy as in the Beth-Bloch (BB) formulation. Despite being one of the most popular electronic stopping, the ZBL approach has shown to overestimate the stopping forces due to electrons and gives rise to ultra-shallow profiles range [50]. This is a consequence of the stopping being uniform throughout the crystal due to the non local model of the BK theory. As a possible alternative local model such as the phase-shift based electronic stopping model for Fermi-surface electron [51], and Land and Brennan (LB) [52] approach based on the modified Firsov's model using Hartree-Fock electronic densities are capable of predicting elemental profile in any implant direction against experiments [50,53]

2.3 Physics of Sputtering

The ejection of atoms from a solid whose surface is bombarded by energetic particles is termed sputtering. This process is encountered in materials technology and to a large extent in material characterisation, .e.g. depth profiling. However, sputtering can be undesirable in a fusion reactor where wall erosion causes a loss of material leading to thinning of the wall and to plasma contamination [54,55].

Sputtering occurs when the kinetic energy received by target atoms located close to the surface, is greater than U_b the surface binding energy, e.g equals the energy of sublimation for most metals. Sputtering is quantified by the yield, Y, the average number of atoms removed from a solid target per incident particle:

$$Y = \frac{number\ of\ atoms\ removed}{number\ of\ incident\ particles} \qquad (2.29)$$

Three distinct regimes for sputtering have been discerned so far from simulation studies: single knock-on, where the sputtered atoms are essentially primary recoil atoms (PKA), up to few hundred eV; linear cascade, where secondary recoil atoms (SKA) and higher generation recoil atoms are produced, at keV energies; and spike where the spatial density of moving atoms is large, at

tens of keV or higher. The nonlinear sputtering or spike regime corresponds to the microexplosion effect which has been indirectly observed in numerous experimental sputtering studies. Furthermore, it is expected to produce a crater on the sample surface which have indeed been observed [56,57]

2.3.1 The Sigmund Theory

The first theoretical study of sputtering was done in 1969 by Sigmund [58]. In this study, an integro-differential equation was developed for the sputtering yield, from an approximation to the solution of the Boltzman transport equation. Sigmund based his theory on the fundamental assumptions that the target medium is isotropic and homogeneous, so the transport of particles can be described by Boltzman's equation, and that the distribution of the particles velocities is isotropic. The medium is assumed to be semi-infinite, with a planar surface. Also, the collisions are binary thus a simple scattering interaction potential can be used to obtain an expression for the cross-section. Finally, Sigmund uses the last key assumption that the energy E is well above the effective surface barrier energy (100-200 eV). His main conclusion is that sputtering is proportional to the energy deposited near the surface by the incoming ion

$$Y = \Lambda \ F_D(E) \tag{2.30}$$

where Λ [Å/eV] contains material properties of the target such as surface binding energy U_b

$$\Lambda = \frac{\Gamma_m}{8(1-2m)} \ \frac{1}{NC_m U_b^{1-2m}} \tag{2.31}$$

$$\Gamma_m = \frac{m}{\psi(1) - \psi(1-m)} \tag{2.32}$$

ψ is the digamma function defined as $\psi(x) = dln\Gamma(x)/dx$

$$\Lambda \approx \frac{0.042}{NU_b} \tag{2.33}$$

22

$F_D(E)$ is the density of energy deposited at the surface in units of [eV/Å], given by

$$F_D(E) = \alpha \, N \, S_n(E) \qquad (2.34)$$

α is dimensionless function of the target to ion mass ratio. $S_n(E)$ is the nuclear stopping cross-section in units of eV.Å^2 was defined earlier in Eq.(2.14). Sigmund used a constant screening radius ($a_{BM} = 0.219$Å) related to the Born-Mayer potential [3]. In the case of energies smaller than 1 keV (m=0), Sigmund's formula reduces to

$$Y(E) \approx \frac{3}{4\pi^2} \alpha \frac{\gamma E}{U_b} \qquad (2.35)$$

2.3.2 Semi-Empirical Formulas

Most of the analytical formulas of sputtering derive from Sigmund formula to which empirical parameters or dependences are added to better fit the published experimental data. They are all based on the following factorisation:

$$Y(E, E_{th}, E_{TF}) = Q \, \varphi(E/E_{th}) \, s_n(\epsilon) \qquad (2.36)$$

$$Y\left(\frac{\epsilon}{\delta}, \epsilon\right) = Q \, \varphi\left(\frac{\epsilon}{\delta}\right) \, s_n(\epsilon) \qquad (2.37)$$

$$\delta = \frac{E_{th}}{E_{TF}} \qquad (2.38)$$

where E is the projectile energy, E_{th} is the threshold energy and E_{TF} is the Thomas-Fermi energy given by Eq.(2.17). The function $s_n(\epsilon)$ is the reduced nuclear stopping cross section given by (Eq.2.20-22) and it is function of the reduced energy ϵ (Eq.2.15). The function $\varphi(E/E_{th})$ is determined empirically to provide the best description of data in the threshold region. Q is treated as a fitting parameter. The electronic stopping contribution to the sputtering yield, Y, is usually included in Q in an implicit way or explicitly.

From this factorisation, Bohdansky and Matsunami developed the two widely used analytical expressions of sputtering yield for normal ion incidence on solids.

---

[3]the Born-Mayer potential is described in Chapter 3

Bohdansky

The original Bohdansky formula was introduced in 1984 [59]. It is based on the reduced nuclear Thomas-Fermi stopping cross-section $s_n^{TF}(\epsilon)$ (Eq.2.20) and the function $\varphi(E/E_{th})$ takes the form:

$$\varphi(x) = \left(1 - \frac{1}{x^{2/3}}\right)\left(1 - \frac{1}{x}\right)^2, x = \frac{E}{E_{th}} \qquad (2.39)$$

It is known (Fig.2.36) that $s_n^{TF}(\epsilon)$ cross section is too large at low energies ($\epsilon < 0.1$) compared to the one based on the Kr-C potential. Furthermore, the calculated data using the Kr-C potential are in good agreement with experimental data in many cases. Therefore, Bohdansky formula was revised in 1994 by including the Kr-C stopping cross-section [60] :

$$Y(E) = 0.042 \left(\frac{R_p}{R_a}\right) \frac{\alpha S_n(E)}{U_b} \left(1 - \left(\frac{E_{th}}{E}\right)^{2/3}\right)\left(1 - \frac{E_{th}}{E}\right)^2 \qquad (2.40)$$

Newer calculated sputtering yields give values below the threshold obtained from the fit with the revised Bohdansky formula. For this reason a new fit formula was recently developed in which the treshold term or function $\varphi(x)$ appears as [61]

$$\varphi(x) = \frac{(x-1)^\mu}{\lambda + (x-1)^\mu} \qquad (2.41)$$

This formula is a good description especially near the threshold, where older fit formula failed.

Matsunami

Matsunami [62] used the function $\varphi(E/E_{th})$ of the from of Eq.(2.42) and several revisions have been made to the original formula. The latest revision was published in 1996 and called the third Matsunami formula (Eq.2.43) which was proposed by Yamamura [63].

$$\varphi(x) = (1 - x^{-1/2})^s \qquad (2.42)$$

$$Y(E) = \frac{0.042 Q \alpha^\star}{Ub} \frac{S_n(E)}{1 + As_e(\epsilon)} \left(1 - \left(\frac{E_{th}}{E} \right)^{1/2} \right)^s \qquad (2.43)$$

where $s_e(\epsilon)$ is the inelastic electronic stopping cross-section (reduced unit) given here as:

$$s_e(\epsilon) = k\epsilon^{1/2} \qquad (2.44)$$

where

$$k = 0.0793 \frac{(M_1 + M_2)^{3/2}}{M_1^{3/2} M_2^{1/2}} \frac{Z_1^{2/3} Z_2^{1/2}}{(Z_1^{2/3} + Z_2^{2/3})^{3/4}} \qquad (2.45)$$

More recently, a new semi-empirical equation based on the approach of Matsunami et al. has been developed [64]. This equation includes a new atomic density term and avoids the arbitrary term Q. Moreover a unified analytic representation of the sputtering yield for normal incidence was proposed by Janev et al. [65]. This representation introduces a generalized energy parameter $\eta = \eta(\epsilon, \delta)$ (Eq.2.46), and a normalized sputtering yield $\tilde{Y}(\eta)$ (Eqs.(2.47),(2.48)). ϵ and δ were introduced earlier in the general factorization of the sputtering yield.

$$\eta = a\left(\frac{\epsilon}{\delta} - 1 \right) + b\left[\left(\frac{\epsilon}{\delta} \right)^\gamma - 1 \right] + 1 \qquad (2.46)$$

$$\tilde{Y} = \frac{Y(E, E_{th}, E_{TF})}{QG(\delta)} = \frac{Y(\epsilon, \delta)}{QG(\delta)} \qquad (2.47)$$

$$\tilde{Y} = \left(1 - \frac{1}{\eta} \right)^\alpha \left[\frac{A \log \eta}{\eta} + \frac{B}{\eta^2} \right] \qquad (2.48)$$

Shulga

Very recently, Shulga [66] developed a formula based on Sigmund's result for low energy (¡1 keV) sputtering in which he decoupled the density dependence from the target element dependence, and obtained an equation of the form

$$Y(E) = A_s \frac{N^{ps}}{U_b^{qs}} Y_s(E) U_b \qquad (2.49)$$

25

where $Y_s(E)$ denotes sigmund's low energy sputtering yield (Eq.2.35) given previously. The quantities A_s, qs, ps are fit parameters.

Yamamura

Yamamura [67] described the angular dependence of the sputtering yield by a factor to the yield at normal incidence, his formulation is

$$Y(E, \theta) = Y(E, 0)[cos(\theta)]^{-f} \exp\left[\left(1 - \frac{1}{cos\theta}\right) sin(\eta)\right] \qquad (2.50)$$

with

$$\eta = \pi/2 - \theta_{opt} \qquad (2.51)$$

where the incidence angle θ and θ_{opt} are counted from the surface normal and θ_{opt} is high sputter yield angle. f and η are used as fit parameters. This formula was revised [61] to better describe the case of low incident energies and self-bombardment as well as heavy projectile. The new formulation

$$Y(E, \theta) = Y(E, 0)\left[cos\left(\frac{\theta}{\theta_0}\frac{\pi}{2}\right)^c\right]^{-f} \exp\left[b\left(1 - 1/cos\left(\frac{\theta}{\theta_0}\frac{\pi}{2}\right)^c\right)\right] \qquad (2.52)$$

$$\theta_0 = \pi - arcos\left(\frac{1}{1 + E/E_{sp}}\right)^{1/2} \qquad (2.53)$$

f, b, c are fit parameters and the value θ_0 is given by Eq. 2.53, where the binding energy of the projectile E_{sp} has to be provided. Foe selfbombardment E_{sp} is equal to surface binding enrgy U_b [61].

2.3.3 Other Sputtering Theories

Thompson [68] also proposed in 1986 a model for sputtering based on the analysis of the energy spectrum of atoms sputtered by high energy heavy ion. His formulation at normal incidence does not contain the kinetic energy of the incident ion:

$$Y = \frac{\pi^2 a_0^2 N^{2/3}}{8e} \frac{E_R}{U_b} \frac{M_1(Z_1 Z_2)^{5/6}}{M_1 + M_2} \qquad (2.54)$$

where E_R =13.6 eV is the Rydberg energy. Thompson model is valid in the regime where sputtering is considered to be energy-independent, in tens of keV range.

Based on a quantum statistical analysis of a three-body collision mecanism, Wilhem [69] derived in 1985 a model for sputtering specific to energies near threshold. His model does not rely on BCA and its approximate form is:

$$Y(E) \approx \frac{1}{24} h_{1/2} \sigma(E_{th}) N^{2/3} \left(\frac{(M_1/M_2)^2}{1 + 2M_2/M_1} \right)^{3/2} \frac{(E - E_{th})^2}{E_{th}^2} \mathcal{H}(E - E_{th})$$

(2.55)

where $h_{1/2}$ is a dimensionless coefficient resulting from the quantum statistical treatment of the interaction and the quantity σ is the elastic ion-atom cross section. $\mathcal{H}$ is the heaviside step function. Athough this relation may seem extremely promising, the theoretical evaluation of $h_{1/2}$, and σ are very difficult.

Beyond the theoretical treatments reviewed so far, two theoretical approaches specific to the high energy (non-linear) spike sputtering regime were described in Refs. [70,71]. Briefly, the first approach is a hydrodynamical analysis based on shock wave model, while the second approach known as the heated zone model, is based on a solution of the heat conduction in a cylindrical spike.

2.3.4   Sputtering Threshold

The sputtering threshold is defined to be the lower limit of ion energy below which no sputtering occurs. It is of great importance when sputtering is not desirable. Analytical expressions for the threshold energy have been proposed as a function of the mass ration M_1/M_2, surface binding energy U_b and the energy transfer coefficient γ (Eq.2.6). The most commonly used are the one proposed by Bohdansky [72]

$$E_{th} = \begin{cases} U_b/(\gamma(1 - \gamma)) & M_1/M_2 < 0.2 \\ 8U_b((M_1/M_2)^{2/5} & M_1/M_2 \, 0.2 \end{cases}$$

(2.56)

27

and the revised Bohdansky formula [60] introduces the threshold energy in the different form with $b_1=7$, $b_2=-0.45$, $b_3=0.15$, $b_4=1.12$

$$\frac{E_{th}}{U_b} = b_1 \left(\frac{M_2}{M_1}\right)^{b_2} + b_3 \left(\frac{M_2}{M_1}\right)^{b_4} \tag{2.57}$$

and the expression proposed by Matsunami et al. [62]

$$\frac{E_{th}}{U_b} = 1.9 + 3.8 \left(\frac{M_1}{M_2}\right) + 0.134 \left(\frac{M_2}{M_1}\right)^{1.24} \tag{2.58}$$

Finally Yamamura and Tawara [63] proposed on the base of the most recent experimental data, the following expression

$$E_{th} = \begin{cases} (1 + 5.7(M_1/M_2))(U_b/\gamma) & M_1 < M_2 \\ 6.7(U_b/\gamma) & M_1 > M_2 \end{cases} \tag{2.59}$$

However, the sputtering threshold remains controversial to date, its strong correlation with surface binding energy and the projectile to target mass ratio is now well established but has not been linked to any other particular material properties.

2.4 Material Damage

Damage starts when the energy received by the target atom exceeds *the lattice displacement energy* E_d which is about 15-40 eV for most metals [23]. E_d is the minimum energy to knock an atom far enough into the lattice so that it will not immediatly hop back into its original site, such a knock-on-atom is called recoil. When the recoil is generated an empty lattice site -*vacancy*- remains behind and when the recoil comes to rest in between regular lattice positions, it is termed -*interstitial*. In some cases, the recoil is generated with no vacancy left behind such collisions are called *replacement*.

Examples of processes which come into play in material damage are sputtering, ion mixing and ion implantation.

2.4.1 Modified Kinchin-Pease Model

In the Kinchin and Pease [73] model, the number of Frenkel pairs defects N_F(vacancy-interstitial) generated by an implanted ion is proportional to the energy transferred from the ion to the primary recoil, assuming only elastic collisions and hard spheres particles[3]. By dropping these two assumptions Norgett et al. [74] modified the Kinchin-Pease formula to the following :

$$N_F = \begin{cases} 0 & \text{for } E_\nu < E_d \\ 1 \ (replacement) & \text{for } E_d \leq E_\nu < \frac{2 \cdot E_d}{0.8} \\ 0.8 \cdot E_\nu/(2 \cdot E_d) & \text{for } E_\nu \geq \frac{2 \cdot E_d}{0.8} \end{cases} \qquad (2.60)$$

where E_ν is the energy which goes into nuclear collisions $E_\nu = E(1+k_d \cdot g(\epsilon_d))^{-1}$

$$g(\epsilon_d) = 3.4008 \cdot \epsilon_d^{\frac{1}{6}} + 0.40244 \cdot \epsilon_d^{\frac{3}{4}} + \epsilon_d \qquad (2.61)$$

$$k_d = 0.1337 \cdot \frac{Z^{\frac{2}{3}}}{M^{\frac{1}{2}}} \qquad \epsilon_d = 0.0115 \cdot Z^{-\frac{7}{3}} \cdot E \qquad (2.62)$$

with the charge Z and the mass M of the particles involved in the collision. Note that using E_ν justifies that the electronic energy loss of the recoils are accounted. The modified Kinchin-Pease model is valid for energies of the primary recoil below (25 keV $Z^{\frac{4}{3}}$ M). This energy limit is about 106 Mev for Fe which is significantly higher than the energy used for bombardment. Furthermore this model does not give any information about the location of the vacancies and interstitials. Therefore it is assumed for bulk damage case that all point defects are located in the vicinity of the position of the primary knock-on.

2.4.2 Channelling and De-Channelling

Channelling is a significant phenomenon for ion energies ranging from keV up to several tens of MeV and its importance increases as the ion energy increases.

---

[3]Hard sphere model is described in Chapter 3

High energy channelling is dominated by planar channelling (ions traverse between sheets of atoms), whereas low-energy channelling is dominated by axial channelling (ions traverse between rows of atoms).

In the case of polycrystalline materials the effect of channelling is reduced but is not insignificant while it is important in a crystalline structure and can be spotted from the tail of range profiles. Because the ranges for ions entering the crystal in a channel are longer than the non-channelling direction ranges. It can be concluded immediately that the stopping power in the channelling direction is smaller than those in the random direction.

Ion channelling is the result of not only a lower stopping power in the centre of the channel but also a focusing effect by the atoms at the edges of the channels. However, the probability that a particle is removed from a channel (de-channeling) is increased by the presence of points defects. Therefore it is important to consider damage accumulation during the calculation of a particle trajectory.

Conclusion

This chapter has introduced the principles of atomic collision and physical sputtering phenomena. Other phenomena associated with ion bombardment of surface, were also introduced.

Sputtering is an experimental observable which has been the subject of numerous theoretical studies. However, the number of analytical tools reviewed for the estimation of sputtering yield are each valid for a certain conditions determined mainly by the energy range. Essentially, at very low energy where the two body scattering approach is not valid. Even though the formula proposed by Wilhem has the best justification for low energy but it remains difficult to use. Moreover, analytical study of the non linear sputtering is yet a difficult issue to handle analytically from full non-linear Boltzman

transport equation. The properties of the medium are not specifically linked to the surface binding energy which is one of main inputs to predict sputtering in addition to the controversial threshold energy.

To sum up, atomic collisions are complex process to be modelled in its entirety using an analytical approach, leaving numerical simulation as the method of choice.

Chapter 3

The Nature of Interatomic Potentials

Introduction

The computational simulation of materials properties in condensed matter is challenged by the availability of a model potential able to supply the total energy and the interatomic forces of real materials. The state of art approach is to use quantum mechanics for the electrons and nuclei of which the material consists. That is, solving the following Schrödinger equation, known as first principle calculation i.e. ab initio

$$\hat{H}\psi = E\psi \tag{3.1}$$

where E and ψ are the total energy and wave function of the system and $\hat{H}$ is the total Hamiltonian. Theoretically well founded approximations have been introduced to solve Eq.3.1 without affecting the accuracy of the solution [75]. That is, the adiabatic approximation [76] which permits the electronic and nuclear coordinate of the total wave function ψ to be separated based on their disparate masses. The self consistent field approximation [75] under which the many electron interactions are mapped into that of a single electron moving in

an effective nonlocal potential which can be obtained within the scheme of the Hartree-Fock theory [75] or the density functional theory (DFT) [77]. The latter scheme is the central focus of most ab initio calculation for metals. The direct use of the ab initio method to perform a full quantum simulation is at great computational cost and is limited to small systems of a hundred or so atoms.

The Born-Oppenheimer approximation [75] uncouples the nuclear and electronic degrees of freedom, introducing the concept of potential energy surfaces which can be described using model potential energy functions. In the best of circumstances, an empirical approach [135] is adopted to define such potential functions. Such approaches use a fitting strategy [118,135] to represent the real behaviour of a physical system, and can handle large systems similar to those addressed here for modelling bombardment [78–81].

The underlying physics of empirical potentials originates from the inclusion of the energetic consequence of the band theory without explicitly calculating the details of the band. Almost all potential models which exist are empirical and a variety of pair-wise additive and many body interatomic potentials have been developed for modelling different classes of materials, such as metals [82–86], non-metals [87,88], semi-conductors [89–91], etc.

In the previous chapter, interatomic potentials were introduced analytically to derive the scattering cross-section in atomic collision. However, the scattering has a short life and range interaction and the system will soon after reach its equilibrium state inherent to long range interaction. It is essential to define a potential dependent on the nature of interactions in the physical system under study and the level of accuracy required. In this respect we shall review model potentials that are directly relevant to equilibrium properties in metals and in particular iron as a material of interest as well as those called high energy interaction potentials applied to non-equilibrium system.

3.1 Potential Energy Function

In general, the total potential energy of an N body system (relative to atoms or ions at infinity), may be expanded in terms of interactions involving up to N particles [92,93]. This approach is roughly analogous to Taylor expansions of the energy about its minimum:

$$V = \sum_{i}^{N} V_i^{(1)} + \sum_{i}^{N-1} \sum_{j>i}^{N} V_{ij}^{(2)} + \sum_{i}^{N-2} \sum_{j>i}^{N-1} \sum_{k>j}^{N} V_{ijk}^{(3)} + \ldots + V_{123\ldots N}^{(N)} \qquad (3.2)$$

$V_i^{(1)}$ often called the one-body term, is induced by an external force field. The two-body term $V^{(2)}$ describes the direct interaction between particles i and j. The three-body and higher order terms cast light on the local environment such as the angles between the bonds. Truncating this series to the third order term on the grounds that the four -body and higher order terms are negligible, avoids complexity and reduces the computational burden. A model potential is a mathematical description of terms such as $V_{ij}^{(2)}, V_{ijk}^{(3)}$. Constructing such a model potential involves two steps:

- choosing a functional form which is dependant on geometrical quantities such as distances or angles, or on intermediate variables such as atom coordinations, and setting a certain number of free parameters.

- finding a parametrization method in other words: how the free parameters are chosen and which properties are to be fitted.

The second step is very important as it defines the applicability range of the model potential. Almost all forms of empirical potentials [94] which exist at present are valid for systems at equilibrium, since experimental data far away from equilibrium are rare or not available. Therefore it is advisable to bear in mind that any atomistic simulation can only answer questions that are within the validity of the model potential. selected examples will be given in section (3.4).

3.2 Pair potentials

In a pair potential only two-body terms are retained in the expansion of the potential function Eq.(3.2). In the absence of an external field, configurational energy of N atoms assembly becomes :

$$V = \sum_{i=1}^{N-1} \sum_{j>i}^{N} V_{ij}(r_{ij}) \tag{3.3}$$

where V_{ij} denotes the functional form of the potential, ultimately dependant on the interatomic separation r_{ij} between atoms i and j. Pair potentials are consistent with close-packed structures, being the minimum configurational energy, in particular for solids noble gas. For other solids, some qualitative calculations were carried out for defect properties in metals like Fe and Cu [95–99], since no better potential were available. However, the elastic properties are inaccurately represented and consequently lattice dynamical properties i.e. defects, are often wrongly predicted by pair potentials [110, 116]. However, some qualitative calculation were carried out for defect properties in metals like Fe and Cu [95–99], since no better potential were available. We review some of the most elementary pair potentials largely applied in simulation.

3.2.1 Hard Sphere Potential

The simplest pair potential is the hard sphere potential its form is given by

$$V_{ij}(r_{ij}) = \begin{cases} 0 & r_{ij} > r_c \\ \infty & r_{ij} \leq r_c \end{cases} \tag{3.4}$$

where r_c is the diameter of the atom. This potential provides no information on the system energy but it has been used to study packing in colloidal systems [100] and in solid systems [101] ie. stability of face centred cubic packing (fcc) over hexagonal close packing (hcp). It was used to describe collision dynamics in cascade [102].
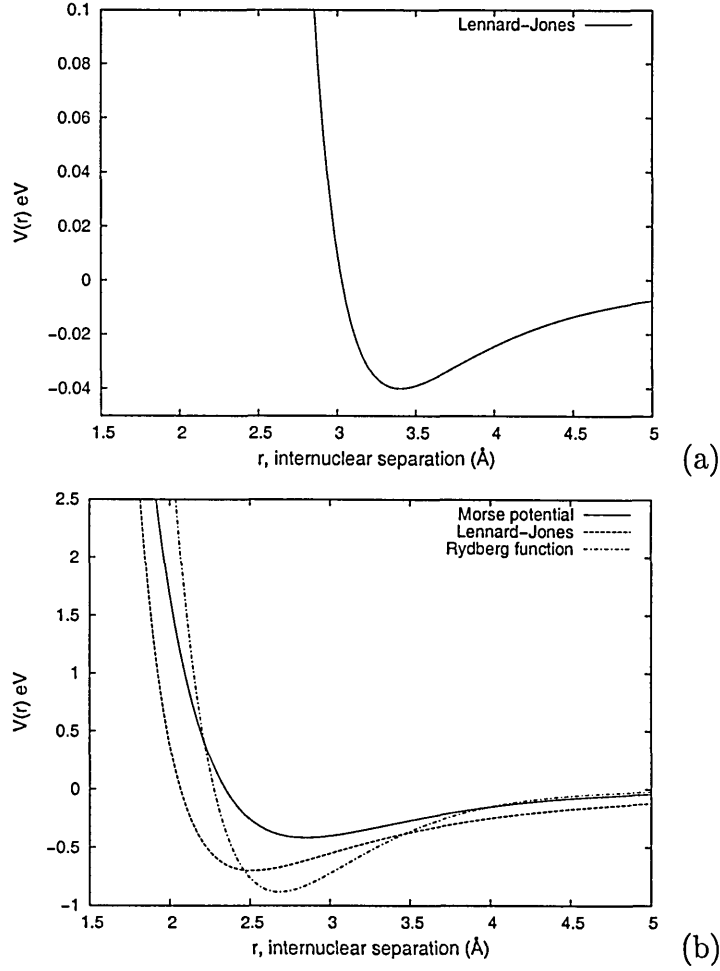
Figure 3.1: a) LJ potential for Ar-Ar (fcc) and b) LJ potential for Fe-Fe (fcc) including the Morse potential and Rydberg Function for Fe-Fe (bcc)

3.2.2 The Lennard-Jones (LJ) Potential

The general form of the potential proposed by Lennard and Jones (LJ) [87] is expressed by a power dependance:

$$V_{ij}(r_{ij}) = \lambda_n r_{ij}^{-n} - \lambda_m r_{ij}^{-m} \tag{3.5}$$

and the so called 6-12 LJ is the most used, with $m=6$ and $n=12$:

$$V_{ij}(r_{ij}) = 4\epsilon \left[\left(\frac{\sigma}{r_{ij}} \right)^{12} - \left(\frac{\sigma}{r_{ij}} \right)^{6} \right] \tag{3.6}$$

where ϵ is the well depth of the pair interaction and σ the hard sphere radius ($V(\sigma) = 0$), i.e. for Argon $\epsilon = 0.01eV$, $\sigma = 3.4$ Å. The terms in m and n model respectively the attractive and repulsive part. This potential was originally developed for solid noble gases which it represents reasonably well. The only bonding in these system is mediated by the weak Van der Waals dispersion forces, and the closed-shell configuration of an atom in the free state is not significantly perturbed by the coordination environment of that atom.

$$V_{ij}(r_{ij}) = \epsilon \left[\left(\frac{r_{min}}{r_{ij}} \right)^m - \frac{m}{n} \left(\frac{r_{min}}{r_{ij}} \right)^n \right] \tag{3.7}$$

When applied to metals, LJ potential is given by (Eq.3.7), where $r_{min} = 2^{1/6}\sigma$ is the distance at the minimum of the potential and *values for m=7 and n=3.5 have been employed for metal Fe*. LJ potential is consistant with phase stability of close-packed structure like fcc Fe ($\epsilon = 0.7eV$, $\sigma = 2.517$ Å) [103,104] but serves only to gain some qualitative insight into defects in metals [105]. The LJ potentials for the fcc metal Fe and the fcc solid noble gas Argon are given in Fig. 3.1 for illustration.

3.2.3   The Morse Potential

The Morse potential [82] has a functional form which dispenses completely with power law:

$$V_{ij}(r_{ij}) = D \left[\exp\left(-2\alpha \left(r_{ij} - r_0 \right) \right) - 2\exp\left(-\alpha \left(r_{ij} - r_0 \right) \right) \right] \tag{3.8}$$

where D is the depth of the attractive well, r_0 is the equilibrium distance at which the potential has its minimum, and the third parameter α denotes the slope or the range at which the potential reaches zero (i.e. respectively are 0.4174 eV, 1.3885 Å^{-1}, 2.845 Å for Fe [23]). The first term constitutes the repulsive part and the second term dominates at large separation. The Morse potential initially intended to model covalently bonded diatomic molecules, has

also been used for cubic metals [106–108,116]. With similar functional form, the Rydberg potential [88] has shown better results than the Morse potential for a good number of diatomic molecules [109], but for metals the results by the two potentials are not very different in particularly the elastic constants. The early repulsive character of the Morse potential compared to the LJ potential, illustrated in Fig. 3.1.b, ascribed to Morse potential to be used at very low energy interactions where yet the attractive forces are significant.

3.2.4 Evidence of Many Body Effects

Pair potentials can be directly applied to a completely arbitrary configuration of atoms. However, for systems of more pratical interest such as metals and semiconductors, the pair potentials fail badly. This is due to the many-body contribution of these solids which is significant. Since pair potentials discount any local environment dependancy, they are inadequate to model situations with open electronic shells, where strong localized bonds may form, or where there is a delocalized "electron sea". There are five important properties which are key indicator of many body effect over the simpler pair potential description. In the case of noble metals focusing particular on gold, these properties are [110]:

- the first property known as the 'Cauchy relation' $C_{12} = C_{44}$. Cubic solids have three distinguishable elastic constants which are by convention labeled C_{11}, C_{12} and C_{44}. In these solids, interaction with central pairwise force derived from pair potential leads consequently to the equality $C_{12} = C_{44}$ [112] for the crystal to be stable . As shown in Table 3.1, the Cauchy equality holds for rare gas solids and some simple metals (alkali metal:Li,Na), but for most cubic metals the ratio C_{12}/C_{44} is far from unity. For noble metals the ratio C_{12}/C_{44} is around 2, reaching a spectaculary high value of 3.89 for gold Au. The existance of the so-called Cauchy pressure $P_C = \frac{1}{2}(C_{12} - C_{44})$ [113] (whether positive or negative) is a good indication of many-body forces.

Element	Structure	C_{12}/C_{44}	E_{vac}/E_{coh}
LJ	fcc	1.0	1.0
Ar	fcc	1.12	0.95
Kr	fcc	1.08	0.66
Li	bcc	1.12	0.21
Na	bcc	1.19	0.38
Al	fcc	2.29	0.19
Pb	fcc	2.47	0.25
Fe	bcc	1.15	0.47
Ni	fcc	1.26	0.36
Pt	fcc	3.28	0.26
Cu	fcc	1.61	0.33
Ag	fcc	2.03	0.36
Au	fcc	3.89	0.25
Yb	fcc	0.59	0.42

Table 3.1: Indications of Many-Body Effects in Cubic Solids [111]

- pair potentials predict the energy of formation of an unrelaxed vacancy (E_{vac}) to be identical to the cohesive energy (E_{coh}) [110]. However, the ratio E_{vac}/E_{coh} as shown in Table 3.1, is much less than unity leading to an E_{vac} of typically one third of E_{coh} . This result applies for all metals even alkali metals for which the Cauchy equality holds which does not mean that the many body forces are negligeble for these simple metals.

- surface properties in a system modelled by pair potentials are very different from those of real metals. The best evidence is that the spacing at a metal surface between the first and second layer is expanded relative to the bulk in a pair potential model, while the experimental fact deduced from diffraction studies, shows that the spacing of the most open surface generally contracts [114,115].

- Finally, the use of pair potentials to simulate the melting process leads to a melting temperature T_m in excess of that usually observed by a factor of $1.5 - 2.0$ [110,116]. This means that metals exhibit some "extra cohesion" with respect to pairwise systems.

Since the mid '80's researchers started to determine how to improve predicted proprieties of materials to experimental ones by incorporating many body contribution in potential functions.

3.3 Many Body Potentials

Moving beyond pair potentials, there are two main approaches for including many body character in the interatomic potential scheme. The first approach is to adopt an explicit description of high order terms in the potentials energy series in Eq.(3.2). The second approach is implicit through a functional volume-dependency with the very early work done for Fe metal in [117]. In the following, an overview of the various model potentials most widely used in computer simulations of metals and semiconductors are given.

3.3.1 The Murrell-Morttram potential

The Murrell-Morttram potential (MM) truncates the many-body expansion in equation Eq.(3.2) at the three body level [83]. The two body term is a Rydberg energy function [88, 109]

$$V_{ij}(r_{ij}) = -D\left(1 + a_2\rho_{ij}\right)\exp\left(-a_2\rho_{ij}\right) \qquad (3.9)$$

where

$$\rho_{ij} = \frac{r_{ij} - r_e}{r_e} \qquad (3.10)$$

where D is the well depth, r_e is the equilibrium distance and a_2 determines the range of the interaction. The three-body term V_{ijk} is constrained to be symmetric to permutation of the three atoms ijk, and to annul as any of these atoms goes to infinity. To this end a combination of interatomic coordinates

Q_i are defined for a given triangle (i, j, k) by

$$\begin{pmatrix} Q_1 \\ Q_2 \\ Q_3 \end{pmatrix} = \begin{pmatrix} \sqrt{1/3} & \sqrt{1/3} & \sqrt{1/3} \\ 0 & \sqrt{1/2} & -\sqrt{1/2} \\ \sqrt{2/3} & -\sqrt{1/6} & -\sqrt{1/6} \end{pmatrix} \begin{pmatrix} \rho_{ij} \\ \rho_{jk} \\ \rho_{ki} \end{pmatrix} \qquad (3.11)$$

where $\rho_{\alpha\beta}$ is function of $r_{\alpha\beta}$ as in Eq.3.10. $r_{\alpha\beta}$ represents one of the three triangle edges $(r_{ij}, r_{jk}$ and $r_{ik})$. The three-body term then becomes:

$$V_{ijk} = DP(Q_1, Q_2, Q_3)F(a_3, Q_1) \qquad (3.12)$$

where D is the well depth and a_3 is the range of the three-body potential. P is a polynomial of cubic or quadratic level in the Q_i coordinates. P of cubic level is given by

$$\begin{aligned} P(Q_1, Q_2, Q_3) &= c_0 + c_1 Q_1 + c_2 Q_1^2 + c_3(Q_2^2 + Q_3^2) + c_4 Q_1^3 \\ &+ c_5 Q_1(Q_2^2 + Q_3^2) + c_6(Q_3^3 - 3Q_3 Q_2^2) \qquad (3.13) \end{aligned}$$

and the additional terms for the quadratic level is:

$$c_7 Q_1^4 + c_8 Q_1^2(Q_2^2 + Q_3^2) + c_9(Q_2^2 + Q_3^2)^2 + c_{10}Q_1(Q_3^3 - 3Q_3 Q_2^2) \qquad (3.14)$$

$F(a_3, Q_1)$ is a damping function which can be any of the following:

$$\begin{aligned} F(a_3, Q_1) &= \exp(-a_3 Q_1) \\ F(a_3, Q_1) &= \frac{1}{2}(1 - \tanh(a_3 Q_1/2)) \qquad (3.15) \\ F(a_3, Q_1) &= \operatorname{sech}(-a_3 Q_1) \end{aligned}$$

which all decay exponentially at long range though they have different short range behaviour. The MM potential has been applied to a wide range of systems including Group II and III metals, Group IV semiconductors and transition metals (Ref. are within the review reference [118]). Due to good

a_2	a_3	$D(eV)$	$R_e(\mathring{A})$	c_0	c_1	c_2	c_3	c_4
			c_5	c_6	c_7	c_8	c_9	c_{10}
6.55	9.6	0.8847	2.6832	0.1760	1.7958	5.0885	2.9047	2.2007
			6.1349	2.8605	13.2511	8.3421	4.5088	0.5670

Table 3.2: Dual optimized MM potential for Iron with cutoff of $3r_{nn}$ [118]

bulk and surface properties reproduced by this potential, it is well placed to study structure growth and dynamics of clusters. An important feature of the MM potential is its dual optimisation to fit simultaneously α-Fe and γ-Fe [118]. Such a global potential was also derived for calcium and strontium [119]. The parameters for iron using the dual MM potential are given in Table 3.3.1 [118].

3.3.2 The Tersoff potential

Motivated by quantum-mechanical bonding arguments that the most stable structure of a particular material results from a balance between the number of bonds formed, and the strength of the bond (the bond order), Tersoff [90,91] developed a unique functional form of a model potential which accomodates many-body effects in straightforward way. Tersoff suggested that

$$V = \sum_{i<j}^{N} V_{ij}$$
$$V_{ij} = f_C(r_{ij}) \left[f_R(r_{ij}) + b_{ij} f_A(r_{ij}) \right] \tag{3.16}$$

Here f_C is a smooth cuttoff function, to limit the range of the potential. The functions f_R and f_A represent respectively the repulsive and attractive term

of the potential and are taken to have the form

$$f_R(r_{ij}) = A \exp(-\lambda_1 r) \qquad (3.17)$$

$$f_A(r_{ij}) = -B \exp(-\lambda_2 r) \qquad (3.18)$$

The novel feature of the Tersoff potential is the environment dependence b_{ij}. It represents a measure of the bond order, as a function of the coordination of atoms i and j

$$b_{ij} = (1 + \beta^n \gamma_{ij}^n)^{-1/2n} \qquad (3.19)$$

where γ_{ij}, the effective coordination of atom i, is determined from

$$\gamma_{ij} = \sum_{k \neq i,j} f_C(r_{ik}) g(\theta_{ijk}) \exp\left[\lambda_3^3 (r_{ij} - r_{ik})^3\right] \qquad (3.20)$$

This feature was lacking in the earlier empirical potential for covalent solids of Stillinger and Weber [89], which has angle-dependent bond strengths with no density-dependent and the elastic properties were poorly described in particularly for Silicon. Although intended originally for covalently bonded solids like silicon and silicon carbide [120, 121], Tersoff-type model potentials have been applied to a wide range of metals such as Al, Fe, Cr and their oxides Al_2O_3 alumina, chomia Cr_2O_3 , Fe_2O_3 ferriate [122, 123]. In addition to other potentials of the Tersoff form developped for metals i.e. tungsten [124].

3.3.3 Embedded Atom Model (EAM)

This type of potential find its root from effective medium approximation to density functional theory [125, 126]. This appproach decribes the cohesion energy as the energy needed to embed an atom into the local electronic density resultant from a linear superposition of the electron densities of all other individual atoms in the system. Accordingly, Daw and Baskes [84] proposed the many body embedded atom model (EAM) potential which was initially parameterized to describe fcc metals such as Ni,Cu,Au,Pt, Pd and Ag with

nearly closed d shells, and were the first alternatives to the pair potential models. The general form is written as

$$V = \frac{1}{2} \sum_i \sum_{j \neq i} \phi_{ij}(r_{ij}) + \sum_i F(\rho_i) \qquad (3.21)$$

where ρ_i is the host electron density at the atom i site and $F(\rho_i)$ is the energy to embed the atom i into such a density ρ_i. $\phi_{ij}(r_{ij})$ represents the core-core repulsive interaction which usually represented by the Morse potential (see previous section) EAM potentials have been extensively applied among which we can list their use in the computation of hydrogen embrittlement in metals [127], to study surface composition of the Ni-Cu alloys [128], surface relaxation in Ni,Al and their ordered alloys [129] and surface self diffusion in fcc metals [130]. EAM potentials have been developed for bcc transition metals [131–134] and have been extended to study alloying for several fcc metals like Ni,Al,B and many others [135–137]. EAM has been applied to study impurity diffusion such as carbon interstitials in metals and inter metallics [138], to the growth of Cu-Ag(111) [139], to the cleavage fracture (far from equilibrium) in α Zr [140]. A new approach to the development of EAM potential is to fit experimental and first principles data for both the fcc and bcc phases [141]. With EAM potentials, excellent agreement has been obtained for phase stability and pressure-volume curve with the experimental data i.e. the universal equation of state of metals, and a reasonable agreement whas been obtained for the phonon frequency curves [142].

3.3.4 Finnis-Sinclair (FS) potential

Finnis and Sinclair (FS) [85] developed a short range empirical many body potential to study bcc transition metals (V, Nb, Ta, Cr, Mo, W, Fe). FS approach is based on the Second Moment Approximation of the Tight-Binding theory (SMA-TB) [143,144] in which the cohesive energy of a solid scales with the square root of its atomic coordination number. The functional form of the

FS potential is written as:

$$V = \sum_{i=1}^{N} \left[\frac{1}{2} \sum_{j \neq i} V_{ij}(r_{ij}) - A \sqrt{\sum_{j \neq i} \phi_{ij}(r_{ij})} \right] \qquad (3.22)$$

V_{ij} is a pair-wise repulsive interaction and it is represented by a quartic polynomial while a parabolic form is adopted for the many body contribution ϕ_{ij}

$$V_{ij} = (r_{ij} - c)^2 (c_0 + c_1 r_{ij} + c_2 r_{ij}^2) \qquad (3.23)$$

$$\phi_{ij} = (r_{ij} - d)^2 + \beta(r_{ij} - d)^3/d \qquad (3.24)$$

the cut off distances c and d lie between the second and third neighbours. Note that the cut off is an intrinsic part of the FS potential. The square root form of the many body term derives from the SMA-TB with the ϕ_{ij} interpreted as the sum of squares of hopping (overlap)integrals. Although, appropriate for transition and noble metals, the square root function was validated for all metals with any band filling [143] under the local charge neutrality approximation. The FS potentials are similar in form to the EAM potentials but their interpretations are quite different. The Finnis-Sinclair potential for iron and chromium will be used and so they are detailed here (see next Chapter). The parameters sets for Fe-Fe, and Cr-Cr interactions, were fitted by Finnis and Sinclair, to experimental data given in Table 3.3 for a perfect body-centered-cubic Fe and Cr crystals and the fit parameters are listed in Table 3.4. The many body potentials of Finnis and Sinclair were investigated to gauge their application to defect properties [146–148] FS model led to anomalies in the pressure-volume relationship for bcc transition metals vanadium and niobium. However, increasing the repulsive part of the FS potential overcomes such anomalies [149, 150]. Based on the approach of Finnis and Sinclair, many body potentials for several other fcc metals [151, 152] copper, silver, gold and nickel,aluminium [151, 152] have been constructed and extended to their alloys in particular noble metal alloys, with well reproduced phase diagram

45

Property	bcc Fe	bcc Cr
Cohesive Energy(eV)	4.28	4.10
Lattice constant(Å)	2.8665	2.8845
Elastic constants($10^{11}Pa$)		
C_{11}	2.431	3.871
C_{12}	1.381	1.035
C_{44}	1.219	1.008
Bulk Modulus B	1.731	1.980
Shear Modulus C'	0.525	1.418

Table 3.3: The ground state properties of Fe and Cr bcc lattice [85,145]

of the alloys and a reasonable concentration dependency of the alloy lattice parameter and elastic constant [152–154]. In addition to cubic metals, FS formalism was applied to hcp metals, i.e. titanium, by considering more structural parameters: two lattice constant and five elastic constant [155]. The FS potentials have been further generalised to model long range interaction such as the mechanical interactions between clusters of atoms, i.e. the interaction of an atomically sharp tip with a slab of material, by considering van der Waals type interaction [156]. The long-range FS potentials was applied to ten fcc metals (Ni,Cu,Rh,Pd,Ag,Ir,Pt,Au,Pb,Al) and their binary alloys [156,157]. In addition to FS potential, the SMA-TB scheme has been used by others to develop potential at long range up to the fifth-neighbour distance for fcc and hcp transition metals [158]. It has to be recalled, however , that treatment of bcc transition metals with potentials based on SMA or similar approximation schemes like FS or EAM are far from being completely successful, even if longer interaction ranges are adopted i.e. up to the fifth neighbour. The non closed structures require a more detailed description of the electron density DOS with inclusion of at least five moments of the distribution. It is worth noting that all the SMA-TB, FS of any kind and EAM schemes share the rectangular approximation for the electron density but bearing in mind that

Parameter	Fe-Fe	Cr-Cr
$c(\mathring{A})$	3.4	2.9
c_0	1.2371147	29.1429813
c_1	-0.3592185	-23.3975027
c_2	-0.0385607	4.7578297
$d(\mathring{A})$	3.569745	3.915720
$A(eV)$	1.828905	1.453418
β	1.8	1.8

Table 3.4: The parameters of the Finnis-Sinclair potentials (Eqs.3.23,3.24) for Fe and Cr bcc metals [85]

for d band metals the tight binding model is a useful picture and it can be applied at various levels of approximation.

3.3.5 Modified Embedded Atom Model (MEAM)

The EAM and FS formalisms do not account properly for magnetic effects or changes in shape of the local electronic density of states. Moreover, in transition metals the band structure is a mixture of fairly localized d- and nearly free sp-electrons. This introduces asymmetry into the electronic density distribution that give rise to directional effects. Evidence for this is given for instance by the negative values of the Cauchy pressure of Cr(bcc), and Be and Y (hcp), C_{12}-C_{44} and C_{13}-C_{44} respectively [113]. So an accurate description of bcc transition metals necessites the inclusion of angular terms as indicated from first principles calcutations [159]. Such terms make major contribution to structural energy differences. In this context, Baskes [86] developed the MEAM following the EAM concept but with a modified electron density background where the angular effects are captured by one variable, Γ, given by

$$\Gamma = \sum_{l=1}^{3} t^{(l)} (\rho^{(l)}/\rho^{(0)})^2 \qquad (3.25)$$

where $\rho^{(l)}$ is the partial electron density as defined in and $t^{(l)}$ are constants. The background electron density is determined by

$$\rho = \rho^{(0)} \frac{2}{1 + e^{-\Gamma}} \qquad (3.26)$$

The MEAM potentials have been developed for metals, semiconductors and diatomic gases, in total 26 elements: ten fcc, ten bcc, three diamond cubic and three gaseous materials [86] and revised for the case of nickel [160] and bcc transition metals [161,162]. Other approch to built up the potential is the bond angle dependant second moment approximation [163], tight binding total energy method [164] and higer order approximation of tight binding [165].

3.4 Rigid ion model potentials

This type of potential describe the interaction at close particle separations (i.e. $< 1\text{Å}$, far from equilibrium). In this case the two-body interaction is less questionable, mainly because the atomic electrons or the many body contribution represents a minor perturbation to the strong nuclear repulsion due to the overlap of closed electron shells. These potential models usually known as rigid ion models or repulsive wall are applied to modelling scattering in atomic collision.

3.4.1 Screened Coulomb Potentials

This model potential describes the Coulomb repulsion between the nuclei combined with a form of screening function for the interaction between the atomic electrons. The electronic screening is weak at significantly high energy ($\epsilon \gg 1$ irrelevant in keV region) because the nuclei can approch closer to each other than the screening radius, this is know as the Rutherford scattering. Screened Coulomb potentials were originally derived from first principles for an isolated atom and modified for the case of two atoms by Firsov [94]. Screened Coulomb

potentials are designed to model scattering at high energy interaction and their general analytical form is given by

$$V(r) = \frac{Z_1 Z_2 e^2}{4\pi\epsilon_0 r} \Phi(r) \qquad (3.27)$$

where Z_1 and Z_2 are the atomic numbers of the two interacting atoms, e is the electronic charge and ϵ_0 is the permittivity of free space. $\Phi(r)$ is the screening function expressed as

$$\Phi(r) = \sum_{i=1}^{n} c_i \exp\left(-d_i \frac{r}{a_s}\right) \qquad (3.28)$$

Different screening functions have been proposed in the literature. The popular ones are the Moliere, Kr-C and ZBL [32]. The ZBL potential with 4 non-zero term screening function was fitted by Ziegler, Biersack and Littmark to large quantities of ion implantation data from 216 ion target combination. The idea is to find a screening function independent of the atomic number but dependent on the screening length. The ZBL screening length is

$$a_s = 0.8853 a_B (Z_1^{0.23} + Z_2^{0.23})^{-1} \qquad (3.29)$$

where a_B is the Bohr radius and the numerical coefficient for the ZBL screening function are given in Table.3.5. The ZBL shows a good agreement with experiment [42] which made this potential the most widely used. Indeed, the ZBL potential will be used to model metal-metal close interaction and noble gas-metal interaction

3.4.2 The Born Mayer Potential

Another form of repulsive potential is given by Born and Mayer (BM) [166]

$$V_{ij}(r_{ij}) = A_{BM} \exp\frac{-r_{ij}}{a_{BM}} \qquad (3.30)$$

49

i	1	2	3	4
ZBL c_i	0.028171	0.28022	0.50986	018175
d_i	0.20162	0.40290	0.94229	3.1998
Moliere c_i	0.35	0.55	0.10	0
d_i	0.3	1.2	6.0	0

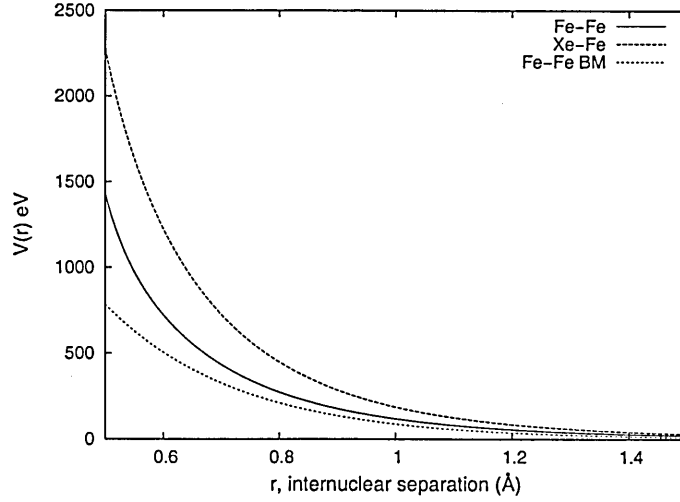Table 3.5: Coefficient of the ZBL and Moliere screening functions [23, 32]

Figure 3.2: Fe-Fe and Xe-Fe screened ZBL interaction, and Fe-Fe Born Mayer (BM) interaction

where A_{BM} is an energy parameter and a_{BM} a screening length. This potential was introduced to describe the near neighbour repulsion in ionic crystals [166]. However, it has shown to be capable to reproduce a good fit to the experimental data on the threshold energy of displacement for iron metal [167], for interactions up to about 100 eV[1]. Also used in Sigmund's theory [58]. The representation of the Born-Mayer and the ZBL potentials inside the nearest neighbour range for iron is given in Fig. 3.2 where the ZBL is strongly repulsive compared to Born-Mayer at close separation. Thus, this potential is less satisfactory to use in atomic collision because $V_{ij}(0) = A_{BM} \neq \infty$.

---

[1]Born Mayer is used in the Fe-Fe interaction in Chapter 4 page 64

50

Conclusion

The interatomic potentials considered so far in this chapter, are satisfactory applied to atomic collisions which involve the high energy potential, and to radiation damage or crystal defects studies which require the equilibrium and near equilibrium potential known as low energy interaction region. There remains a serious lack of information in the intermediate energy range, which is usually compensated by extrapolation technique. This point will be elaborated in the next chapter. In metals at equilibrium the many body potentials of either Finnis-Sinclair type or the embedded -atom type are the forms most often used in large scale MD simulations. While these potentials are attractive for their computational effeciency they are only physically well justified for simple sp -bonded metals and for transition metals with empty or nearlly filled d-electron bands. The square root functional form used by Finnis and Sinclair has been generalised to any band filling under the constraint of neutral atoms.

Chapter 4

Computational Approach and Preliminary Simulations

Introduction

With the widespread availability of the computer, science took a significant turn from analytical approach to computer based simulations which have become the most powerful tool to deal with complex problems in science that had been impossible to solve analytically. One such problem is the search for the phase space of an interacting many-body system encountered in many different sciences and in particular materials science. One of the standard computational methods for the study of the many body problem at the atomic scale is the Molecular Dynamics (MD) simulation method [22, 93, 168, 169]. Essentially, MD solves the classical Newtonian equations of motion for a system of N particles interacting with each other through a potential function. In addition to the many body problem inherent to MD, its attractive feature is the ability to handle large and complex systems for time scales inaccessible experimentally. Moreover, MD does not require a prior knowledge of the properties of the system under study, unlike other classical approaches such as molecular statics (MS) or Monte Carlo (MC) methods [93, 169]. MD offers means for studying both the equilibrium properties and

the non equilibrium phenomena in solids. These cited features are the main reasons that justify why MD is the most common and of first choice method for atomistic simulations in materials science in general and in condensed matter in particular.

This chapter is dedicated to introduce the methodology of MD simulation and the procedure to incorporate constraints so that MD can be realised in a range of thermodynamic ensembles including the micro canonical (NVE) and canonical (NVT) ensembles. The pertinent inter-atomic potentials that will be needed to model the metallics system Fe-Cr is discussed together with the computational approach to simulate the synergistic effects of ions bombardment at solid surfaces. Preliminarily, a set of simulations are carried out to assess the thermal equilibrium of the system before production runs and to monitor the correct incorporation of the damping protocol used in the simulation model. The chapter emphasis is put on the potential modification at high energetic interaction and validation through equilibrium properties calculation. To this end, the quenching scheme is implemented in the MD code. The developed MD code is made flexible since it can simulate very different physical scenarios with different initial conditions.

4.1   Molecular Dynamics Method

4.1.1   Equation of Motion

Molecular dynamics seeks to generate the phase space[1] trajectories of a system of particles over a finite time, by solving the classical Newton's laws of motion [22, 93, 169]. Consider a system of N atoms with positions r_i in cartesian coordinates, velocities v_i and accelerations a_i ($i = 1, 2, 3...N$). The equations of motions for these N atoms involve N coupled partial differential equations

$$m_i \frac{d^2 r_i}{dt^2} = F_i \qquad (4.1)$$

---

[1]The 3N coordinates and 3N momenta of a 3-dimensional N-particle system

where m_i is the mass of the atom i which is subject to a force F_i. If no external field is present and the system is conservative, F_i depends only on position and is derivable from an interatomic potential function V (taken to be of two and many body potential type in this thesis)

$$F_i = - \nabla_{r_i} V = m_i a_i \qquad (4.2)$$

Propagating these equations in a system with no external influence involves the following MD tasks:

- assign an initial position and velocity to each atom

- move all atoms to a new position a short time δt

- calculate the force on each atom and determine its acceleration

- determine the new velocity

- repeat from the second task

In this manner, the structural and energetics parameters of the system can be computed, in addition to dynamical information such as diffusion coefficients and mechanisms. All of these properties are usually functions of the position and velocities of the atoms in the system.

4.1.2   Integration Algorithm

For most model potentials the analytic form for solving Eq.(4.1) and Eq.(4.2) is unknown. Thus, the need for a numerical solution becomes imperative. A common numerical method to solve the differential equations relating to the time evolution of the coordinates is the Verlet's algorithm, in which the position of every particle i at time t is advanced by δt as follows:

$$r_i(t + \delta t) = 2r_i(t) + r_i(t - \delta t) + a_i(t)\delta t^2 \qquad (4.3)$$

where δt is the amount of time propagated, known as time step. This algorithm does not need the velocities to find the trajectories. However, for estimating the kinetic energy, the possible expression of the velocity is given by:

$$r_i(t) = (r_i(t + \delta t) + r_i(t - \delta t))/(2\delta t) \tag{4.4}$$

The Verlet algorithm is simplistic. A modification to Verlet algorithm based on the finite difference method lead to the velocity Verlet algorithm [170] in which the new position and velocity are computed in the following way:

$$r_i(t + \delta t) = r_i(t) + v_i(t)\delta t + \frac{1}{2}a_i(t)\delta t^2 \tag{4.5}$$

$$v_i(t + \delta t) = v_i(t) + \frac{1}{2}(a_i(t) + a(t + \delta t))\delta t \tag{4.6}$$

This algorithm does not store the positions at the time $t - \delta t$ compared to the original Verlet's algorithm. Both algorithms are know as low order methods. Higher order methods [171]that require only one evaluation of the forces per time step are to be preferred because of their order of accuracy. Such methods as the third order, two-step algorithm based on Adams-Bashforth method for updating the positions r_i and Adams-Moulton method for updating the velocities v [32,172]. Those are the two methods used in this thesis to update the position and the velocity in the following expressions:

$$r_i(t + \delta t) = r_i(t) + v_i(t)\delta t + (4a_i(t) - a_i(t - \delta t))\delta t^2/6 \tag{4.7}$$

$$v_i(t + \delta t) = v_i(t) + (5a_i(t + \delta t) + 8a_i(t) - a_i(t - \delta t))\delta t/12 \tag{4.8}$$

The acceleration a_i at the previous time step needs to be stored. The forces are evaluated after the calculation of $r_i(t + \delta t)$, before integrating the velocities. The method is not self-starting because $a_{-\delta t}$ is not defined. In this case the velocity Verlet algorithm is used over the first time step. The benefit of this method over the Verlet algorithm is that a long time step can be used
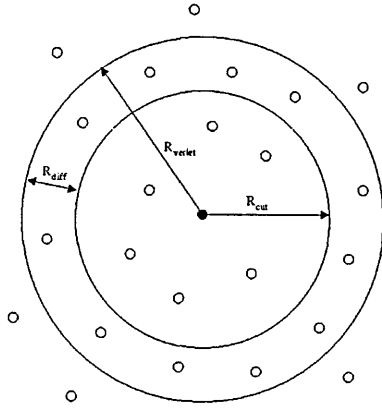
Figure 4.1: The potential cutoff sphere and the neighbour list sphere around a given atom (solid circle).

4.1.3 Neighbour List

When a potential function is parameterised with a spatial cutoff r_c, particles at a separation exceeding r_c do not interact. This assumption was used by Verlet [22,93,168] to identify and construct a neighbour list of particles that are within an expanded cutoff radius r_{verlet} equals to r_c plus a 'skin (5% of cutoff) as depicted in Figure 4.1. The list is refreshed when the sum of the largest displacements is larger than the skin depth. As the system gets larger and as the mobility of the particles becomes greater, e.g., impact simulation is one such system, either the frequency of list updates or the cutoff distance must increase. A more efficient way to speed up the computational time for these systems, is domain decomposition through linked cell algorithm [93,173]. The simulation cell is divided into grid or cells whose sides exceed r_{verlet}, and the atoms are assigned to the various cells, according to their positions. Each atom interacts with its nearest neighbours, located in both its own cell and the image cells that lie within a specified cutt-off radius as illustrated in Figure 4.2. This method dramatically reduces the number of unnecessary interatomic distance calculations within the $O(N)$ order, where N is the number of particles in the simulation. Thus, linked cell algorithm is used in this work.
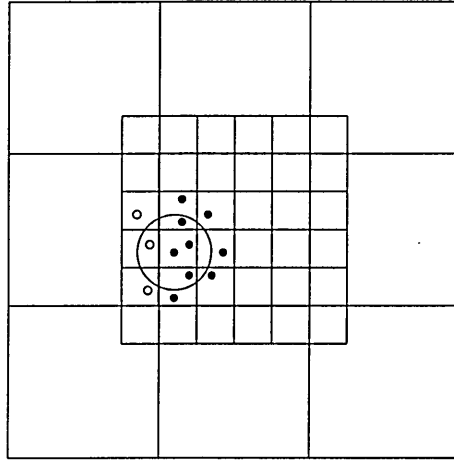
56

Figure 4.2: A two dimensional representation of a typical simulation cell partitioned into grids for cell-linked list method with its replica.

4.1.4 Periodic Boundary Conditions

The system on which the molecular dynamics simulation is carried out, contains a fixed number of atoms N, confined to a certain volume V and is called the simulation cell. The cell is replicated in all spatial dimensions generating its own periodic images of the original N atoms (fig. 4.2). This is the periodic boundary condition (PBC), and is introduced to remove the undesirable effects of the artificial surfaces due to finite size. PBC is used in conjunction with the minimum image convention where only nearest distance among all images is considered, making the system effectively infinite. To this end, the coordinates of the atoms in the cell are subjected to a condition of the form:

$$r_i \rightarrow r_i + L \tag{4.9}$$

where r is the position vectors of the atom i in a cartesian system in which three unit vectors i, j and k coincide with the three edges of the simulation cell(box). The periodic vector L is

$$L = L_x i + L_y j + L_z k \tag{4.10}$$

for a cubic cell of length L, L_x, L_y and L_z satisfy

$$L_{x,y,z} = \begin{cases} -(L) & \text{if x,y,z} \geq L \\ L & \text{if x,y,z} \leq L \\ 0 & \text{if } 0 < \text{x,y,z} < L \end{cases} \qquad (4.11)$$

x,y and z are the coordinates of the position vector r_i. For example, if an atom leaves the top face of the simulation cell,its image emerges from the bottom face. In this way atoms can move in all directions with the total number N in the simulation cell constant. PBC can be applied in two or three dimensions upon simulating a surface (slab geometry) or a bulk phase whilst explicitly treating only a small amount of material.

4.1.5 Constant Temperature Constraints

A constant-temperature MD (NVT ensemble) simulation can be realised in a variety of ways. The earliest methods are the simple velocity rescaling method proposed by Berendsen [174], and the stochastic Langevin-type method [93]. In addition to these methods, a new method that is quite rigorous in sampling canonical ensemble distribution of the phase space, was established by Nose [175] and Hoover [176] and is referred to as the extended system method, a good review is given in [177,178]. The temperature T is directly related to the kinetic energy by the well-known equipartition formula [22,93,168], assigning an average kinetic energy $k_B T/2$ per degree of freedom:

$$K = \frac{3}{2} N k_B T \qquad (4.12)$$

where k_B is the Boltzmann constant and N is the number of particles in the system. An estimate of the temperature is therefore directly obtained from the average kinetic energy K. For practical purposes, it is also common practice to define an "instantaneous temperature", $T(t)$, proportional to the instantaneous kinetic energy, $K(t)$, by a relation analogous to the one above.

Berendsen Thermostat

The particles velocities are rescaled at each simulation time step by a factor:

$$\left[1 + \frac{\delta t}{\tau}\left(\frac{T_0}{T} - 1\right)\right]^{1/2} \tag{4.13}$$

so as to bring T (instantaneous temperature) closer to T_0 (reference temperature) at a rate τ and to correct for the thermal drift [93, 174]. Here, δt is the integration time step and t_T is a timescale (about 250 fs for solids) for coupling to the thermal bath. With a gentle modification of the velocities, this method has a negligible effect on the dynamics of the system. It is used here to maintain the system at constant temperature during the equilibration stage.

Langevin Dynamics Method

In this method the particles velocities are modified during stochastic collision with some form of 'ghost 'particles. These collisions reset the particles velocities to new values and establish a balance between randomised thermal agitations and a frictional force [93, 177]. The equation of motion (4.1) is modified to

$$m_i\frac{d^2 r_i}{d^2 t} = F_i - \gamma m_i v_i + R(t) \tag{4.14}$$

where γ is the friction coefficient and $R(t)$ is a random force assigned from a Gaussian whose mean is zero and whose covariance is given by

$$< R(t)R(t') >= 2\gamma k_B T m_i \delta(t - t') \tag{4.15}$$

Using the velocity Verlet algorithm, the procedure of integrating the stochatic equation of motion [179] which is velocity dependant (Eq. 4.14) is to update first the positions (Eq.4.5) and 'half 'step velocities using Eq.4.16 where λ equals 1/2:

$$v(t + \delta t/2) = v(t) + \lambda a(t)\delta t \tag{4.16}$$

Following the force update, the velocity move is then completed according to the velocity verlet algorithm. The coefficients in Eq.4.15 ensure that the random force performs as much work on the particle as is dissipated. Langevin dynamics has been extensively and successfully used for simulating annealing [180]. We applied Langevin method in the impact simulation, to constraint the set of boundary atoms (bottom and four sides of the simulation cell) at the given reference temperature.

4.2   Potential Model

For the choice of potential model we considered two main factors, i.e. the accommodation of many-body effects as well as the compromise between the complexity of the functional form of the potential and the computational cost. A thorough review of the literature reveals that many model potentials have been developed for Fe [85, 118, 131–133, 141, 181–188] but few for Fe alloys, i.e. Fe-Cu [183],Fe-P [184] ,Fe-Cr [189], due to the lack of experimental data and the difficulty to fit these potentials. The first interatomic potential for the Fe-Cr alloy known to us is the Konish's potential [189]. This potential is constructed from the Finnis Sinclair (FS) [85] many body potential for each of Fe and Cr metals, therefore it is appropriate to consider the same nature of potential for the matrix element Fe from which the alloy is derived. Then the Fe-Fe and Cr-Cr interactions are modelled by FS potentials detailed in previous chapter. Note that computing efficiency is more readily achieved if the empirical potential functions are alike.

4.2.1   The Fe-Cr interaction

Konishi [189] designed a composite potential of the monoatomic Finnis-Sinclair potential for Fe and Cr, to reproduce the experimental heat of solution and size factor of the Fe-Cr alloy system. Recently, more effort have been focused on FeCr alloy as potential structural material for future fusion reactors. Hence,

FeCr alloy is becoming of a central interest for materials modelling and currently, potential development are on going for this alloy such as those by Wallenius [190] who fitted an EAM potential from ab initio calculation [191] driven by a concentration dependent approach and by others [192–194] (MEAM) and EAM [195]. Konishi designed Fe-Cr potential based on Johnson's approach for alloy model development [137]. The pair potential for Fe-Cr is expressed by

$$V^{Fe-Cr} = \frac{\beta}{2} \left\{ \frac{\phi^{Cr-Fe}}{\phi^{Fe-Fe}} V^{Fe-Fe} + \frac{\phi^{Fe-Cr}}{\phi^{Cr-Cr}} V^{Cr-Cr} \right\} \qquad (4.17)$$

the cross term ϕ^{Cr-Fe} and ϕ^{Fe-Cr} are assumed to be identical

$$\phi^{Fe-Cr} = \phi^{Cr-Fe} = \alpha \sqrt{\phi^{Fe-Fe} \phi^{Cr-Cr}} \qquad (4.18)$$

parameters α and β are 1.035 and 1.18, respectively. In the same frame work of Konishi et al., two Fe-Cr potentials were fitted with the parameters α and β set respectively to 1, 1.25 and 0.94, 0.9 [196].

The many body term in Eq.(3.22) for each element Fe , Cr can be extended to the Fe-Cr alloy system as follow

$$U_{many} = -\sum_{i=i_{Fe}} \sqrt{U^{Fe}} - \sum_{i=i_{Cr}} \sqrt{U^{Cr}} \qquad (4.19)$$

$$U^{Fe} = \sum_{j=j_{Fe}} A^{Fe^2} \phi^{FeFe}(r) + \sum_{j=j_{Cr}} A^{Fe} A^{Cr} \phi^{CrFe}(r) \qquad (4.20)$$

$$U^{Cr} = \sum_{j=j_{Cr}} A^{Cr^2} \phi^{CrCr}(r) + \sum_{j=j_{Fe}} A^{Fe} A^{Cr} \phi^{FeCr}(r) \qquad (4.21)$$

Figure 4.3 illustrates the pair potentials $V(r)$, Fig. 4.4 the atomic electron density ρ, and Fig. 4.5 the embedding functions F with a positive curvature corresponding to the weakening of successive bonds within the second moment tight binding approximation

Within the confines of isotropic treatment (no angular dependence) used for many body potentials, the current large scale simulations of metats are assumed to investigate a model metals rather than a real ones.
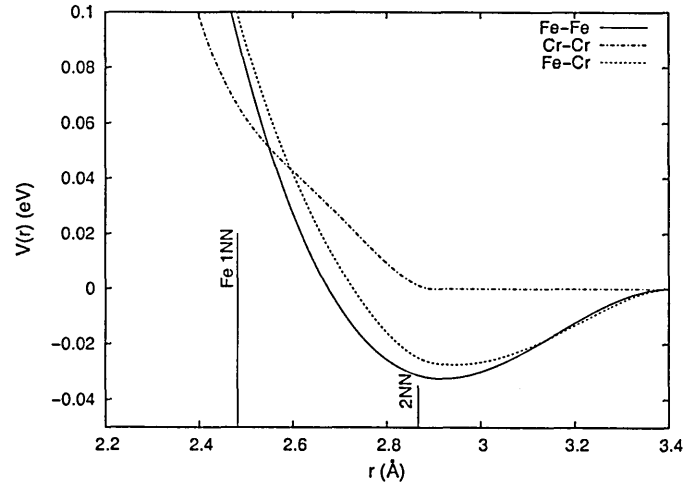
61

Figure 4.3: Two-body potential $V(r)$ for Fe-Fe, Fe-Cr, and Cr-Cr
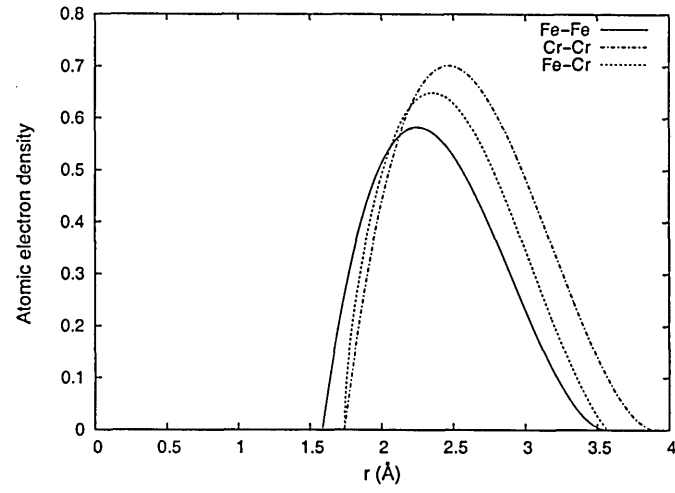

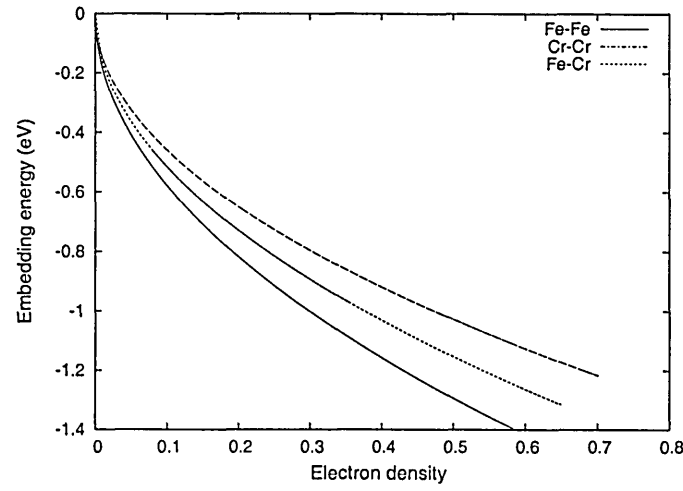Figure 4.4: Atomic electron density $\phi(r)$ for Fe-Fe, Fe-Cr, and Cr-Cr

Figure 4.5: Embedding function $F(\rho)$ for Fe-Fe, Fe-Cr, and Cr-Cr

62

4.2.2 Potential Modification for Energetics Interaction

An important point is that the empirical interatomic potential is only valid within the conditions it was fitted to. Since these conditions are experimental data mostly at equilibrium where attractive forces are significant, it is necessary to adjust the potential to non-equilibrium conditions such as scattering event, otherwise the system will collapse.

To simulate scattering event inherent to energetic interaction in bombardment, the FS potential requires additional adjustment for distances inside the normal nearest-neighbour spacing $0.8a_0$, particularly the repulsive pair term $V_{ij}(r)$ in Eq.(3.22) which has to be strong and dominant at small r. In this regime, the atom-atom interactions are well represented by a pairwise interactions between charged nuclei with the ZBL screened-Coulomb potential discussed earlier[2].

To bridge FS and ZBL potentials, an intermediate potential is needed for which the easiest choice is a cubic spline function given by (Eq.4.22).

The fitting distances (r_1, r_2) are carefully chosen to get a reasonable curvature in the region between r_1 and r_2. This approach has been used by Calder and Bacon [197], Ackland et al. [183] and others [79–81, 198, 199]. In this region ($r_1 \leq r \leq r_2$), we were able to make a smooth interpolation between the ZBL and Finnis-Sinclair (FS) potentials by use of a four-parameter exponential function for $V(r)$ of the form:

$$V(r) = exp(B_0 + B_1 r + B_2 r^2 + B_3 r^3) \qquad (4.22)$$

with the four-parameters $B_{i=0,3}$ chosen so that the function $V(r)$ and its first derivative $V'(r)$ are continuous at the knot points r_1 and r_2 (Eq.4.23), and its second derivative is as smooth as possible. The fitting distances of $V(r)$ at r_1, r_2 for FS and ZBL potential, respectively, are given in Eq.(4.23):

---

[2]Chapter 3, page 48

$$V(r_1) \quad = V_{ZBL}(r_1)$$

$$V'(r_1) \quad = V'_{ZBL}(r_1)$$

$$V(r_2) \quad = V_{FS}(r_2)$$

$$V'(r_2) \quad = V'_{FS}(r_2) \tag{4.23}$$

The four parameters for Fe-Fe, Cr-Cr and Fe-Cr are given in Table 4.1 . For Fe-Fe we have used the modified term developed by Calder and Bacon [197] in which $V(r)$ (Eq. 3.22) was transformed to a Born-Mayer (Eq. 3.30) in the region $(r_2 \leq r \leq r_3)$ with $(r_3 = 2.4507 \text{Å})$ and then adjusted in the same way as bove. As demonstrated by Mauryal [167], a Born-Mayer (BM) potential can reproduce a good fit to the experimental data on the threshold energy of displacement for iron [167], for interactions up to about 100 eV within the predefined range of r. This potential was discontinuous at the knot point r_2 of the exponential function so, it has been augumented by a linear term to better smooth the transition at r_2

$$V_{BM}(r) = 7069.7203 \exp(-4.3991821r) - 0.034161 \tag{4.24}$$

The resulting curve for $V(r)$ versus r is shown in Fig. 4.6 for Fe-Fe, Cr-Cr and Fe-Cr. The many body function $\phi(r)$ (Eq. 3.22) given by Finnis and Sinclair as well as the composite one (Eq.4.18) shown in Figure 4.4, go through a maximum and then fall below zero as r decreases further. To avoid numerical errors due to embedding function of negative density, we have taken $\phi(r)$ to be constant and equals to its maximum value ϕ_{max} for all r value smaller than $r_{\phi_{max}}$. As noted above, $V(r)$ must take the dominant contribution to Eq.(3.22) for small r, and so this approximation on $\phi(r)$ in this region is not significant. The corresponding maximum for each interaction are included in Table 4.1.

Coefficients	Fe-Fe	Cr-Cr	Fe-Cr
B_0	9.728018	9.667910	11.14981
$B_1(\mathring{A}^{-1})$	1.776518	-6.334543	-10.208190
$B_2(\mathring{A}^{-2})$	-26.668090	1.820231	3.986643
$B_3(\mathring{A}^{-3})$	23.319810	-0.529876	-0.828878
distance range $\mathring{A}$			
r_1 *(ZBL, $r < r_1$)*	0.31	0.80	0.30
r_2 *(Exponential, $r_1 < r < r_2$)*	0.62	2.30	2.35
r_3 *(BM, $r_2 < r < r_3$)*	2.4507	-	-
electronic density ϕ_{max}			
$r_{\phi_{max}}$	2.2476	2.465004	-
$\phi_{max}\ eV^2$	0.582674	0.701091	-

Table 4.1: Coefficients of the interpolation function (Eq.4.22) used over the range $r_1 \leq r \leq r_2$ and the total adjustment range of Finnis-Sinclair type potentials.
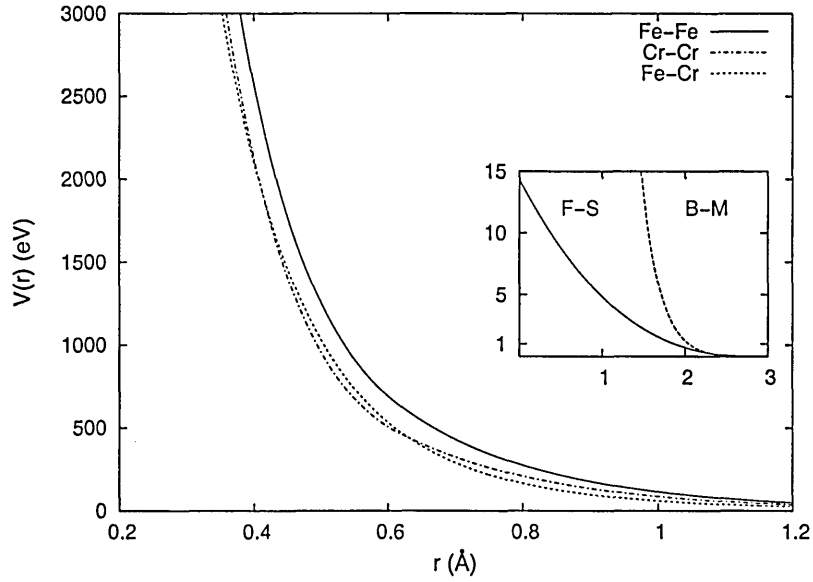
Figure 4.6: The repulsive potential functions $V(r)$ where the interpolation functions (Eq.4.22) join the ZBL and Finnis-Sinclair potentials. The inset figure shows the original repulsive term and the stiffened one zoomed in region 1-2 $\mathring{A}$

4.3 Ion-Surface Bombardment Model

The algorithms and procedures of MD discussed previously, are implemented to simulate the bombardment of energetic Cr ion on solid surface Fe(100). It should be noted that while energetic species are often referred as 'ions', it is actually assumed that these species are neutralised just before impact by fast Auger process or resonant charge transfer [200], and are therefore interacting with the surface as neutrals. Any charge contribution to the interatomic potential is thus ignored. Ion, impact, projectile and trajectory refer to the bombarding species and they are interchangeably used in this thesis.

4.3.1 The Fe(100)-Surface

In an Fe(100) surface, iron atoms are arranged in a body centered cubic (bcc) crystal with lattice parameter equals 2.8665 Å. The Fe-Fe interaction is modelled here by the Finnis-Sinclair potential, which was presented earlier[3]. The Fe-Cr interaction is modelled by the composite potential of Knodshi [189].

4.3.2 Electron Phonon Coupling (EPC)

It is well known that electron phonon coupling (EPC) has considerable effect on the macroscopic properties of metals, proven by experiment [201, 202] and theory [203, 204], e.g., a well-known effect of EPC is the temperature dependence on the electrical resistivity, and superconductivity[4].

In energetic displacement cascades, the electron-phonon coupling (EPC) regime manifests during the post collisional or thermal phase [205, 206] where true melting might occur substantially at high energy [207], and very hot atoms could lose some of their energy through electronic system by 'electron phonon coupling' (EPC) [205,206]. In the collisional phase the ion-electron interaction corresponds to the 'electronic stopping power' (ESP) regime [205].

---

[3]Chapter 3 page 44

[4]Empirical EPC constants for metallic elements can be extracted from experimental resistivity, specific heat and superconducting transition temperature [201]

The inelastic energy loss by electronic excitation due to ESP is negligeable in the keV energy range as discussed previously in Chapter 2.

Electron phonon coupling is not included in the simulation model for several reasons: no experiment has unambiguously demonstrated its importance in cascade dynamics and no procedure has been developed to correctly include EPC in an MD code. As a further argument, a review of investigation of the role of EPC on cascade dynamics by MD simulation is presented.

Treatment of EPC in cascade simulation has been carried out via simple model devised by Caro and Victoria and based on the local-density approximation of the stopping power [208]. Later, Finnis et al [209] extended the analysis of Flynn and Averback [205] for EPC based on the free electron approximation and incorporate the model in his simulation of low-energy cascade displacement in face centered cubic (fcc) metals. Finnis et al. [209] did not observe any obvious change of defect yield with increasing electron phonon coupling in Cu at cascade energy of 500 eV. They related this to unlikely formation of a quasi-liquid zone at the centre of the cascade at energies below 1 keV.

Gao et al. [210] adopted a similar model for EPC to that developed by Finnis et al [209], to study the effects of EPC strength on defects production by displacement cascade in α-Fe at energy of 2, 5 and 10 keV. Gao et al. [210] found that EPC enhances heat transfer from the cascade region and shortens the lifetime of the thermal or cooling phase. Also, the vacancy clustering fraction increases with increasing the strength of EPC. This mechanism inhibits the formation of dislocation vacancy loops. Note that cascade in Fe can collapse, for instance under heavy ion irradiation as evidenced from experiment [211, 212] and as revealed by thermal spike MD simulation when the initial concentration of vacancy is more than 20 at.% [213].

In the EPC model developed by Finnis et al [209], the flow of heat from ions to electrons during the thermal phase of the cascade can be expressed in the form of two coupled differential equations (Eq.4.26) [214]:

$$C_e \frac{\partial T_e}{\partial t} = k_e \nabla^2 T_e + g(T_i - T_e) \tag{4.25}$$

$$C_i \rho \frac{\partial T_i}{\partial t} = -g(T_i - T_e) \tag{4.26}$$

where T_i and T_e are the local temperature of the electron and ion system respectively. C_e and k_e are the heat capacity and thermal conductivity of the electron system, C_i is the specific heat capacity for the ion system, ρ is the density and g is the electron-phonon coupling constant. Finnis et al [209] calculated the parameter α_i $(= g/\rho C_i)$, the strength of the electron phonon coupling, as

$$\alpha_i = \frac{3\Theta_D \gamma_e \nu_F T_e}{\pi^2 r_0 C_i \rho T_0} \tag{4.27}$$

where Θ_D is the Debye temperature, γ_e the coefficient of the electron heat capacity, ν_F is the Fermi velocity, r_0 is the radius of the Wigner-Seitz cell and T_0 the temperature at which the electron mean free path λ, equals r_0, it is given by

$$T_0 = \lambda \frac{\langle T_i \rangle}{r_0}, \qquad \lambda = \frac{92,4}{\sigma} (r_0/a_B)^2 \tag{4.28}$$

where σ is the experimental electrical resistivity of the metal in the liquid state and $\langle T_i \rangle$ is chosen as the melting temperature. The values of parameters for the case of α-Fe are given in Table 4.2. EPC is estimated to be particularly strong in Fe and other metals like Ni, Pd, Pt [205, 209].

With the assumption that the electron temperature, T_e, remains close to ambient, the above EPC model has been implemented in the MD[5] code by adding a damping force to the equation of motion Eq.(4.1) with the damping coefficient β caluated by Finnis et al [209] as:

$$\beta = \alpha_i m_i \frac{T_i - T_e}{(T_i^2 + (T_e/20)^2)^{1/2}} \tag{4.29}$$

---

[5] Another approach to include EPC is by rescaling the velocities by a factor of the coupling constant [213]

Table 4.2: Parameters used in the calculation of EPC constant for α-Fe [210]

Θ_D(K)	464	ρ (kg m^{-3})	7870	r_0(nm)	0.141
T_0 (K)	$6.116 \; 10^3$	γ_e(J K^{-2}m^{-3})	704.57	λ (nm)	0.477
ν_F (m s^{-1})	$1.573 \; 10^6$	C_i (J K^{-1} kg^{-1})	444	σ ($\mu\Omega$ cm)	138

EPC is not incorporated in current simulations which may shorten the life time and reduce the density of the cooling phase. But the recent experiments of Stuchbery and Bezakova [215] give a lifetime of roughly 6 ps for the cooling or thermal phase in iron, which is in good agreement with simulation and would seem to rule out strong EPC effect in Fe as well as in other metals [207]. It was reported that the simulated mixing in surface bombardment in metallic systems without any EPC coupling is in agreement with experiment [207, 216] while its value is predicted to be lower than experiment when EPC was included [78]. Additionally, in cluster bombardment simulation where thermal phase is consistently well established, EPC has shown no influence on the sputtering yield and the only effect is the reduced rate of secondary emission [217].

From the above attempts to probe the effect of EPC from simulation and experiment and with consideration of the present energy bombardment range, we believe that neglecting electron phonon coupling in our simulation is feasible.

4.3.3   Simulation Model

Prior to the bombardment simulation, a finite α-Fe crystallite (also referred to as the 'cell', box or 'block' and it constitutes the target) with a bcc structure is generated exposing the 100 atomic planes along the y direction. The top side of the crystallite in this direction, represents a free surface towards vacuum to allow addition and removal of atoms, while the bottom side, atoms are fixed to prevent bulk motion and relaxation. Periodic boundary conditions (PBC) were imposed in the lateral directions (x, z). The crystallite was varied in size dependent on the ion energy, in order to contain the collision cascade initiated

Ion energy (keV)	Surface area ($\mathring{A}^2$)	Depth $\mathring{A}$	Depth (layers)	Block (atoms)
0.2	40x40	45	(32a)	6273
0.4	40x40	50	(35a)	6665
0.6	55x55	65	(45a)	16607
0.8	55x55	65	(45a)	16607
1.2	56x56	70	(50a)	19201
1.6	65x65	70	(50a)	26451
2.4	78x78	100	(70a)	51030
5.0	78x78	100	(70a)	51030

Table 4.3: The corresponding block sizes as function of the projectile energy. Layer thickness (a=1.4332 Å) is namely half a lattice parameter of bcc Fe.

by the incident projectile, and to be on line with the computing resources. Through a series of short test runs, we identified the critical size at which the cascade is channelled or may interfere with itself by periodic overlap. Then, we used sufficiently large crystallites for this not to be a common problem.

The crystallite sizes used here, are presented in Table 4.3 and are consistent with those found to be satisfactory for Fe by Calder et al. and Stoller [197,218]. Namely, the size of the crystallite in number of atoms has to be at least about 16 times the ion energy in electron volts.

At the start of the simulation the crystallite is thermally equilibrated at a given temperature T for typically 10 ps (picoseconds) to permit the equilibrium phonon modes to be established, as suggested for iron [197, 219]. Then, an energetic Cr ion is introduced at distance of $r_c = -4.73$ Å above the crystallite with assigned velocity such that the ion hits the surface in a specified impact zone and at a given incident angle.

The trajectories of the ion and all atoms are computed over a time scale of 6 to 12 ps. Note that, damping was applied to the atoms in the lateral boundaries in order to reduce the intensity of the energy wave reflected at the edges which is not realistic. This damping was included by means of Langevin dynamics.

4.3.4 Choosing A Timestep

There are two competing priorities in choosing the size of the time step: a long time step permits longer simulation times but a short time step increases the accuracy of the integration algorithm. In energetic impact simulations, where some atoms may move very fast relative to others, as a general rule the time step size is chosen such that the fastest atom does not move more than 5% of the interatomic distance d in one time step [23, 32]

$$\delta t = 0.05 d \sqrt{m/2E_{max}} \qquad (4.30)$$

where m is the mass of the particle which has the largest kinetic energy E_{max}. For an energetic Cr at 2.4 keV, the size of the time step (Eq.4.30) is estimated to 0.12 fs (femtoseconds). With decreasing energy the time step can be increased. So it is clearly appropriate to use a variable time step to minimise simulation time without affecting the quality of the simulation. As a check, different sets of variable time steps are used in running MD simulations of 2.4 keV Cr impact on 51000 atoms block of bcc Fe at temperature 300 K. The upper Figure 4.7 shows that the total energy of the system is conserved during the simulation when the time step was varied from 0.01 to 0.2 fs and from 0.05 to 0.5 fs. In contrast, the total energy drifts after a simulation time of 1500 fs when the time step was varied from 0.1 to 1 fs. Furthermore in the lower Figure 4.7, the system drifts drastically from the start of the simulation due to the initial time step value of 0.3 ps 9 (picoseconds) which is larger then the recommended value of 0.12 fs. Accordingly, the time step is chosen to be 0.05 fs in the early stage of the simulation and then becomes larger 0.2 fs towards the end of the simulation. This time step conserved energy to an acceptable degree and also allowed simulation to be performed in a reasonable amount of time. It is comparable to those used in cascade displacement and impact simulations [78, 197].
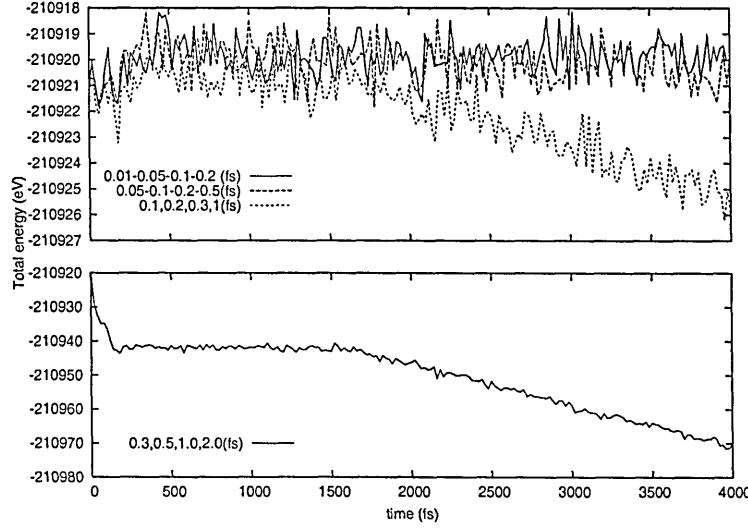
Figure 4.7: The total energy of the system during 2.4 keV impact simulation by MD at various time steps.

4.3.5 Impact Statistics

Due to the stochastic nature of bombardment, a minimum of 100 projectiles are considered at each bombardment condition to insure that the averaged results are statistically significant. Because a crystalline target surface has symmetry, the impact points were chosen to lie inside the irreducible symmetry zone(ISZ). Figure 4.8 shows the ISZ for the Fe(100) surface as a triangular shaped region for normal incidence, while as a square for oblique incidence. Sampling the ISZ can be either random by use one of the standard random number generator or quasi-random by use of the Halton sequence algorithm [220]. The latter gives a uniform spatial distribution as distinguished in the example given in Fig 4.9. Halton sampling is used in the case study of impacts accumulation, where the surface is allowed to change after each impact (each impact sees the history of its antecedent).

4.3.6 Analysis Criteria

Surface bombardment by energetic ions leads in addition to sputtered material, to the production of three types of defects : vacancies, adatoms and interstitials. These quantities reveal how the ions energy is dissipated and

72
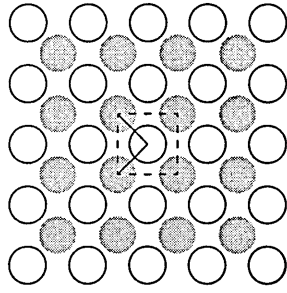
Figure 4.8: Schematic view of the bcc Fe(100) surface: first layer atoms (solid circle), second layer atoms (open circle); the Irreducible Symmetry Zone (ISZ) at normal incidence is triangle and at general incidence is square.
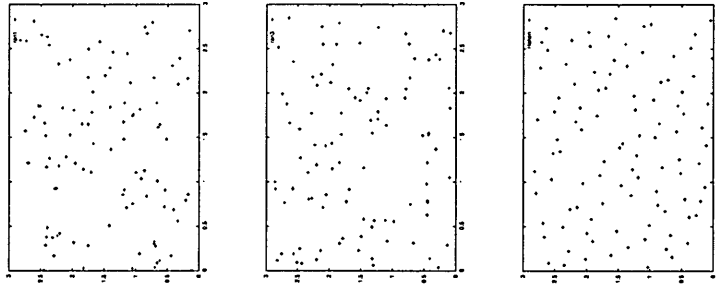
Figure 4.9: Spatial distribution of 100 impacts by random (Ran1, Ran3) and semi-random (Halton sequence) sampling of a square area of Fe (bcc) lattice parameter size.

subsequently how much damage is generated. To categorise each type of defect, we implemented in our simulation the following criteria:

(i) Any atom that does not lie within $0.3a_0$ (where $a_0 = 2.8665$ Å, is the lattice parameter for α-Fe) of an original lattice site is a displaced atom and conversely, any site that does not have an atom within $0.3a_0$ of it, is a 'vacant' site. This criterion is justified by the distance $0.725\ a_0$, at which two displaced atoms sit apart symmetrically about a lattice site in a stable <110> dumbbell configuration in α-Fe [197, 221].

(ii) A displaced atom is considered an interstitial whilst in the bulk or an adatom if it sits on top of the original surface. A replacement is defined when an original lattice site is occupied by a foreign (not the original but still Fe) atom.

73

(iii) A displaced atom is assumed to be sputtered if at the end of the cascade it is more than one lattice unit above the surface and has the y component of its velocity pointing outward from the surface. Note that this method can detect all ejected atoms and it does not account for the total energy of an atom to be positive which can be negative for atoms in an ejected cluster. Setting the detection plane in the proximity of the surface avoids long enough simulation times to detect low energy ejected atoms.

A number of criteria have been reported for the definition of interstitials and vacancies [79, 222]. These methods are similar to that of Karetta and Urbassek [223] who defined a candidate defect when no atom is found within a spherical region of radius, $r_l = 0.21$ a_0, around each lattice point. r_l is the Lindeman radius indicating the amplitude of lattice vibrations in a molten metal. For such a candidate defect a search is conducted in a larger sphere of radius 0.74 a_0. If no atom is found the defect is a vacancy. If two atoms are found the defect is an interstitial. If one atom is found, then the point is rejected. This definition sorts all interstitials as dumbbells and is useful at the end of the cascade but does not give a good description of the cascade in its early stage when the lattice is locally distorted.

Average Calculation Method

It is necessary to average over all projectile impacts (trajectories), due to the stochastic nature of bombardment. One of the important properties is the yield of sputtered species which is detailed here for the case of sputtered atoms in cluster form. The average yields are calculated as the raw number of all sputtered atoms for the total yield and the raw number of atoms linked in clusters for the cluster yield divided by the total number of trajectories. The cluster fraction is calculated as the ratio of the number of atoms comprising the sputtered clusters to the total number of sputtered atoms (here atoms are Fe). The same procedure is followed for any type of defect.

74

4.4 Preliminary Simulations

4.4.1 Potential Validation by MD Calculation

Cohesive Energy

As a first check of the interatomic potential model implemented in the MD code, we have examined the stability of the bcc phase versus volume (and thus strain) using total energy and force calculations by MD.

Fe and Cr bcc crystallites were used with three dimensions PBC to simulate bulk properties. A small isostatic compression was applied to the unit cell of each of Fe and Cr bcc crystallites. In practise, we distort the crystallite dimensions homogeneously along x, y and z directions by multiplying the lattice parameter by a factor, $exp(\gamma_1)$, where γ_1 is arbitrarily small (to remain in the elastic regime), and then we evaluate the energy E per atom.

Figure 4.10 clearly shows that the unit cell volumes and the corresponding lowest configurational energies for bcc Fe and Cr predicted by our calculation are in very good agreement with the equilibrium unit cell volumes and the cohesive energies given by experiment. Moreover, the bulk modulus B defined as the volumetric response of the solid to an external applied homogeneous pressure, can be obtained analytically from Fig. 4.10 as detailed for the case of Fe crystal. For Fe-Fe the dependence of E with a is well described by fitting a parabola of the form:

$$E = 7.02a^2 - 40.3891a + 53.8137 \qquad (4.31)$$

The bulk modulus B is then given by [224]

$$B = \frac{2}{9a}\frac{\partial^2 E}{\partial a^2} \qquad (4.32)$$

where lattice parameter a, equals $a_0 exp(\gamma_1)$. Here, $a_0 = 2.8665$ Å is the equilibrium lattice constant, and it is evaluated at the point of minimum energy
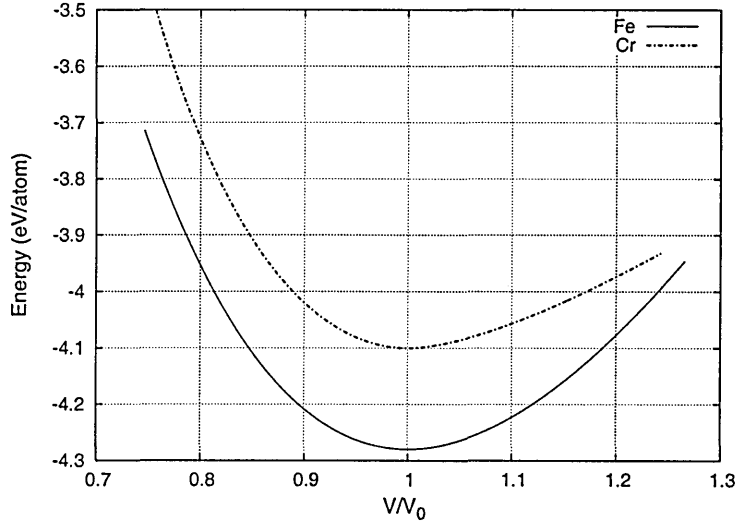
Figure 4.10: Configurational energy of bcc Fe and bcc Cr as function of unit cell volume based on Finnis-Sinclair potential. V_0 corresponds to the equilibrium unit cell volume given by the experiment.

(E=-4.28 eV) which is the cohesive energy for Fe. The bulk modulus, B, takes a value of 1.0884 eV $\mathring{A}^{-3}$ (1.7419 GPa), which is 99.37% of the experimental value [85, 145]. Elastic constants C' and C_{44} can be determined by applying tetragonal and trigonal strains [225] which is beyond the scope of this work. One important observation is that the FS potential is unable to reproduce the negative cauchy pressure $P_c = \frac{1}{2}(C_{12} - C_{44}) = \frac{1}{2}(B - C_{44} - \frac{2}{3}C')$ for some metals including Cr. Therefore, it can only be used for solute Cr at low concentration (up to a maximum of 20%).

Point Defects Properties

Further to the potential validation, point defect properties [68] such as formation and binding energies are two of the important quantities to expect the potential to reproduce reasonably with experiment whenever available. The kind of point defect studied here is the vacancy and the self interstitial atom(SIA) with the different configurations shown in Fig.4.11.

76
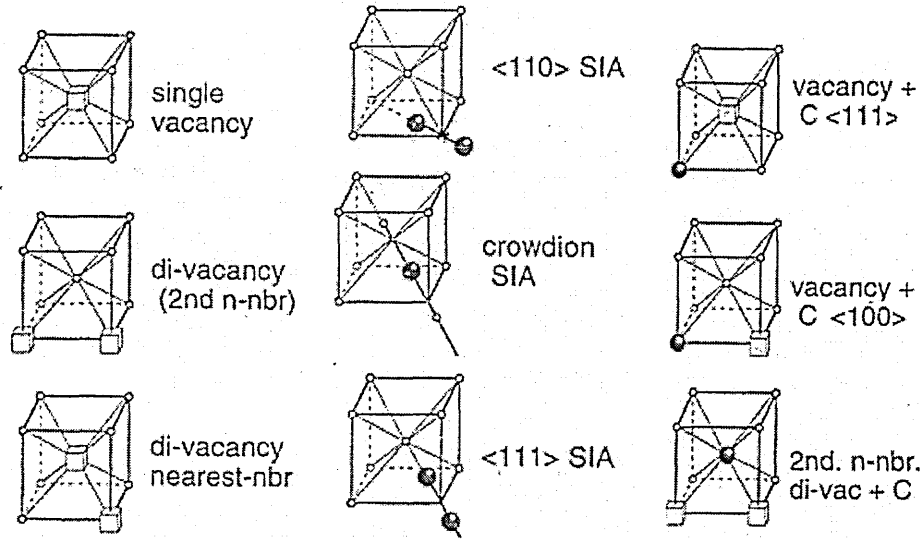
Figure 4.11: Schema illustrating the defects configuration in pure Fe: vacancy (left column); interstitial SIA (midle column) and vacancy in dilute Fe-Cr alloy with C refers to the solute atom (right column). adapted from Ref: [183]

Formation Energy: The defect formation energy E_f shows how difficult it is to create a defect in a perfect crystal structure and it is defined as the energy required to introduce one defect in a perfect lattice. For any kind of defective system X, E_f is given by:

$$E_f^{rlx} = E^{rlx}(X) - E^{rlx}(ref) \tag{4.33}$$

where rlx stands for the relaxed system, and E is the configuration energy of the systems X and ref, respectively with defect and without defect. The reference ref system here is the perfect bcc crystal of Fe with N lattice sites occupied by N atoms. The creation of a defect is modelled by alteration of the number of atoms, for example a single vacancy $X = N - 1$ and for a self interstitial atom $X = N + 1$. Note that if a lattice site is substituted by a solute atom (SA), then the substitution energy is expressed as:

$$E_s^{SA} = NE_{coh}^{rlx}(SA) - (N-1)E_{coh}^{rlx}(ref) - E_{coh}^{rlx}(SA) \tag{4.34}$$

77

Binding Energy: Once a defect is formed and if it is a composite defect XY, i.e. divacancy, the energy by which the parts of such a composite are bound is referred as the binding energy E_b^{XY} which can be defined in two ways. Either as the difference in the energy of the system with the parts being far separated (non-interacting), to the energy of the system with the composite defect (Eq.4.35.I). Or as the difference of the sum of the energy of formation of the parts, to the energy of formation of the composite defect (Eq.4.35.II).

$$E_b^{XY} = \begin{cases} E(X \ far \ Y) - E(XY) & I \\ E_f(X) + E_f(Y) - E_f(XY) & II \end{cases} \qquad (4.35)$$

Calculation Method A Fe crystallite with 3D PBC is generated as the reference system for defect energy calculation, and another crystallite with the same size (2662 lattice sites) is considered to be containing a defect.

A frequently used method to calculate the configurational energy for a system with defective structure at equilibrium, is by means of quenched molecular dynamics simulations [149]. The system is first equilibrated by MD at temperature 10 K to allow relaxation then it is quenched to temperature 0 K. The quenching sets to zero the *ith* component of the velocity of an atom each time the ith component of its acceleration changes sign : *i.e. when $v_i a_i < 0$.* In such case the atom is moving away from its local energy minimum and by forcing the velocity to vanish, this will quickly lead to its equilibrium position. The equilibration time is 100 fs and the quenching time is 200 fs.

We calculated the formation and binding energy of point defects namely a vacancy and an interstitial in pure Fe as well as in Fe-Cr solid solute with the presence of a Cr solute. For the formation of vacancies we chose a time step of one femtosecond while for interstitials or more complex structure it is safer to take a shorter time step because of the substantial distortion at the defect's neighbouring lattice sites.

78

Results

The results of the MD calculation are assembled in Table (4.4) and Table (4.5). In Table (4.4) the equilibrium lattice parameter a_0 and the cohesive energy E_{coh} for α-Fe deduced from the isostatic calculation are well reproduced with respect to the reported values from experiment [145,226] and simulation [131,133, 181,191]. The calculated vacancy formation energy E_f^V is found to fall in the experimental values [227] range with the ab initio [224] in the upper region and the empirical [131,133,181,191] in the lower region. The Cr atom substitution energy E_S^{Cr} calculated here is as an intermediate value between those with the concentration dependent potential fitted at different mixing enthalpy for Fe ferromagnetic (FM) and paramagnetic(PM) phase and at solute concentration given in the following order in Table (4.4) (FM at 5,10,20 %Cr, PM at 10%) [228]. The EAM potential of Farkas [195] predicts the highest substitution energy.

Table 4.4: Calculated properties of bcc Fe with reference to experiment and other calculations.

Property	Present Work	Reported Calculation	Experiment
a_0	2.8665	2.8660,[c] 2.8665,[d,e,g,l] 2.8669,[f] 2.8664,[h]	2.86 (100K),[a] 2.87 (300K) [b]
E_{coh}	4.28	4.28,[c,e,f,h,l] 4.29,[g] 4.31[d]	4.28 [b]
E_f^V	1.80	1.54,[c] 1.83,[d] 1.41,[e] 2.14,[f] 1.73,[g] 1.63,[h] 1.70[x], 1.86[l], 1.93-2.02 (ab initio)[p]	2.0±0.2[m] ≈1.6-1.75 [o] 1.5[n]
E_f^{VV}	$3.47^{(1nn)}$, $3.41^{(2nn)}$, $3.68^{(3nn)}$, $3.56^{(4nn)}$	[$3.26^{(1nn)}$, $3.22^{(2nn)}$][x]	-
E_S^{Cr}	0.158	$[0.05, 0.227, 0.418, 0.415]^R$, [-0,358, -0.384](ab initio)[R] 0.703 [w]	0.224

References: a [226], b [145], c [191], d [85], e [181], f [182], g [131,133]
　　　　　　h [185], l [188], m [227], n [229], o [230], p [224]
　　　　　　x [149], w [195], R [228]$_{FM(5,10,20),PM(10)}$

Table 4.5: Binding energy (eV) involving vacancies and Cr solute, and formation energy (eV) for interstitial.

Properties	Present Work	ab initio [224, 231]	Reported Calculation
Vacancy			
E_b^{V-V}(1nn)	0.15	0.14	0.14^x, 0.13^y, 0.41^f, 0.16^w, 0.19^R
E_b^{V-V}(2nn)	0.21	0.28	0.19^x, 0.20^y, $0.21^{w,R}$
E_b^{V-V}(3nn)	-0.07	-	
E_b^{V-V}(4nn)	0.05	-	0.05^y
Cr solute			
E_b^{V-Cr}(1nn)	0.024	0.029	0.10^w, $(0.035, 0.052)^R$
E_b^{V-Cr}(2nn)	-0.042	-0.01	0.042^w, $(0.051, 0.059)^R$
E_b^{Cr-Cr}(1nn)	0.026	-0.329	0.009^w, $(0.005, 0.034)^R$
E_b^{Cr-Cr}(2nn)	-0.030	-0.197	0.024^w, $(0.024, 0.043)^R$
E_b^{Cr-Cr}(3nn)	0.008	-	-0.003^R
$E_b^{Cr-Cr-Cr}$(1nn)	0.057	-0.79	0.016^w, $(0.016, 0.099)^R$
$E_b^{Cr-Cr-Cr}$(2nn)	-0.013	-	0.047^w, $(0.047, 0.086)^R$
E_b^{FourCr}(2nn)	0.097	-0.97	0.54^w, $(0.031, 0.197)^R$
Interstitial			
$E_f^{<110>Fe-Fe}$	3.90	3.41	3.66^w,4.15^R,Exp.^{z}:4.7-5
$E_f^{<110>Fe-Cr}$	4.55	3.06	3.31^w,$(4.16, 3.98)^R$

References: f [181], x [149], w [195], y [131], z [232], R [228]$_{FM10,PM10}$

In Table (4.5) the binding energy of divacancy E_b^{V-V} in pure Fe shows the second nearest neighbour (2nn) configuration is most stable as predicted by others. The tendency of Cr to segregate can be assessed by calculating the binding energy of the solute atoms with vacancies E_b^{V-Cr} and with themselves. From Table (4.5), the vacancy Cr interaction is repulsive at second nearest neighour in agreement with ab initio while in disagreement with others. The binding energy of Cr solute to a dimer E_b^{Cr-Cr} or high order cluster $E_b^{Cr-Cr-Cr}$

can be attractive or repulsive dependently of the separation distance. However, the second nearest distance displays attraction in all Cr aggregate similarly with ab initio. The formation energy of self interstitial $E_f^{<110>Fe-Fe}$ Fe is within the experimental range and it is slightly lower for a mixed interstitial $E_f^{<110>Fe-Cr}$ with a solute Cr.

4.4.2 Monitoring Equilibrium and Damping

Each atom in the generated crystallite can have a relative velocity because of the temperature, whereas the velocity of the centre of mass is not affected. Then, the distribution of the velocities have to obey the Maxwell-Boltzman distribution (Eq. 4.36) at a given temperature T, where m is the mass of the atom, k_B Boltzmann's constant.

$$f(v) = \sqrt{\frac{m}{2\pi k_B T}} exp(-\frac{mv^2}{2k_B T}) \qquad (4.36)$$

Each atom is assigned a velocity drawn randomly from velocity Gaussian distribution (Eq.4.36) corresponding to the temperature T. After initialisation, all velocities are translated so that the total linear momentum of the system is zero. This prevents the system from drifting in space. Then, the simulation is run to equilibrate the system at a given temperature in presence of Berendsen heat bath. We have monitored equilibrium for the whole set of systems size and temperature (see Table 4.3) but we limited our discussion to the largest system.

Velocity Distribution and H-function

As shown in Figure 4.12, it takes a few iterations to drive the temperature towards the desired value, and then the system appears to be in equilibrium. The velocity distribution $f(v)$ given by Eq.(4.37), measures the fraction of N
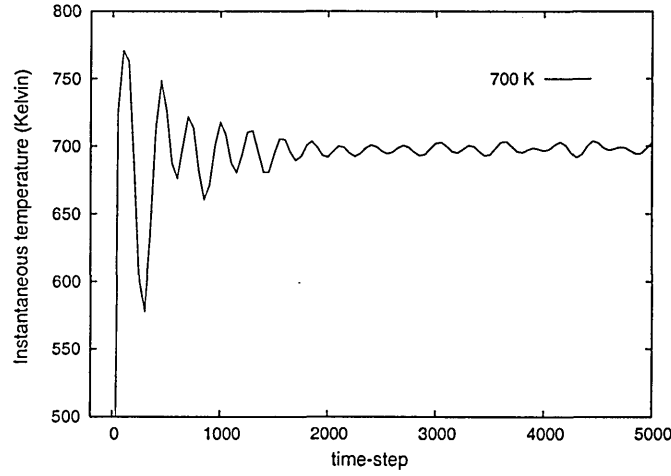
Figure 4.12: Time evolution of the instantaneous temperature for a system size of 51056 Fe atoms
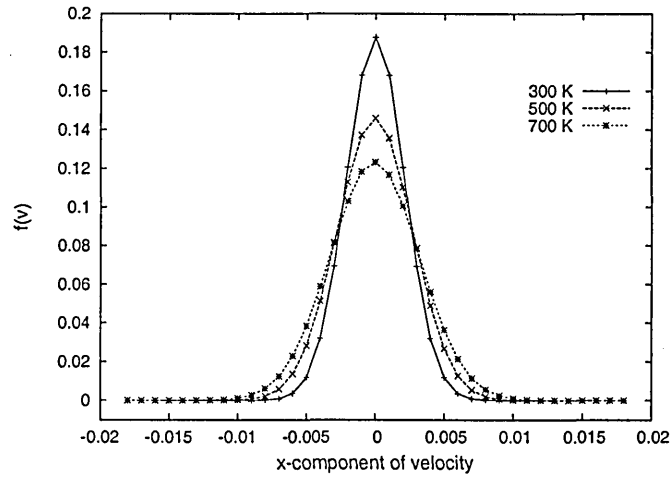
Figure 4.13: Effect of the temperature on the distribution of one component of the velocity for a system of 51056 atoms at 300 K, 500 K and 700 K

atoms having velocity within an interval dv of a particular value v,

$$f(v)dv = \frac{1}{N}N(v)dv \qquad (4.37)$$

Figure 4.13 confirms, as expected, that each velocity component is Gaussian distributed with mean zero. The form of the Gaussian tends to broaden as the temperature of the system is increased since the width is proportional to $\sqrt{T}$. In addition to checking the velocity distribution, Haile suggests another method to detect the presence of metastabilities in momentum space
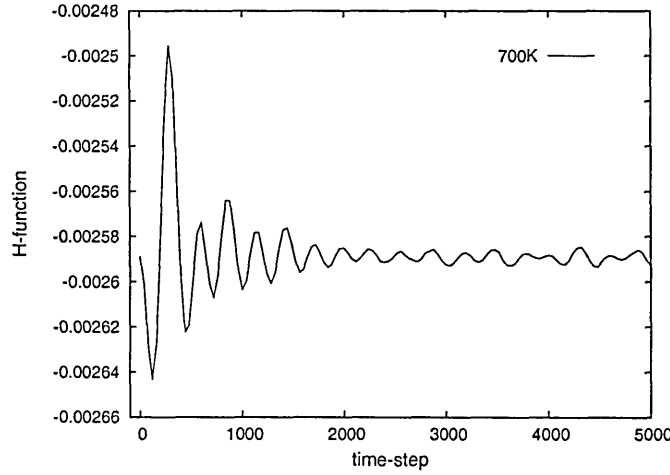
Figure 4.14: Instantaneous H-function for the run of Fig(4.12)

as well as to identify the approach to equilibrium [22]. This method consists of monitoring the time evolution of the Boltzman H-function, which is given by:

$$H = \frac{1}{3}(H_x + H_y + H_z) \qquad (4.38)$$

where H_x, H_y, and H_z have the following form

$$H_x(t) = \int_{-\infty}^{+\infty} f(v_x) \ln f(v_x) dv_x \qquad (4.39)$$

and $f(v_x)$ is given by Eq.(4.37). In Figure 4.14 a typical example from our results which shows the instantaneous H-function versus time-step. Clearly, after a short equilibration period, the H-function fluctuates in a very narrow range, suggesting that a stable thermal equilibrium has emerged.

Radial Distribution Function

One of the important quantities for monitoring the solidity of a system is the Radial distribution function (also known as a structure factor), $G(r) = 4\pi\rho(r)$, where $\rho(r)$ is the density of atoms at a distance, r, away from a given atom. Figure 4.15 shows such a function obtained from MD after the equilibration of a bcc Fe crystallite at different temperatures. The distribution of nearest

83
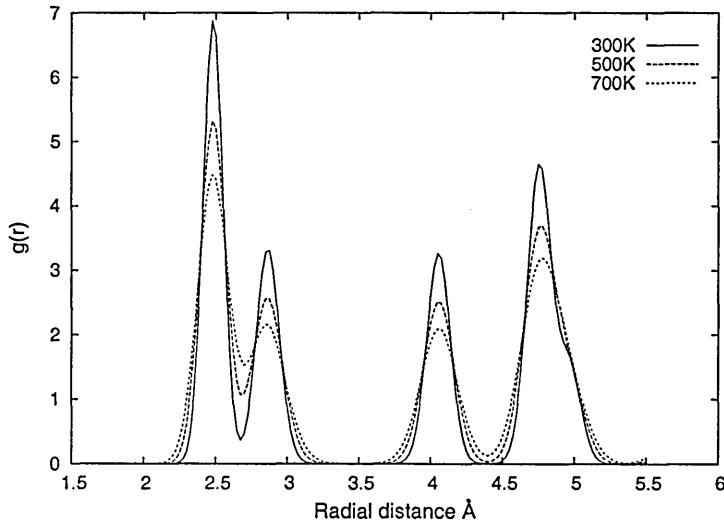
Figure 4.15: The radial distribution function of a bcc Fe crystal at different temperatures

neighbours distances is considerably broadened for high temperature compared to that at room temperature suggesting that our simulated solid, is responding realistically to changes in temperature. The first and second peak in Fig. 4.15 tend to overlap with the temperature. They correspond to the first and second neighbours which are located at 2.45 Å and 2.866 Å in a static bcc Fe. The symmetry of the crystal is blurred by thermal displacements of the atoms from their lattice sites. From these results, we conclude that the atoms in our simulation do reach a realistic thermal equilibrium, which again gives us confidence in the validity of our potential model and the overall functionality of the code.

Monitoring Damping

For the integrated solution of the Langevin dynamics to be stable, the time step, δt, should be small compared to the damping time γ^{-1}, $\gamma \delta t < 1$, otherwise the quality of the damping resembles the effects of a quench [177, 180]. A damping of value $\gamma = 0.01$ was used. To monitor how this choice of γ can gently damp out the heat at the boundaries during an impact simulation, we set up a prototype model. We started by equilibrating a bcc Fe crys-
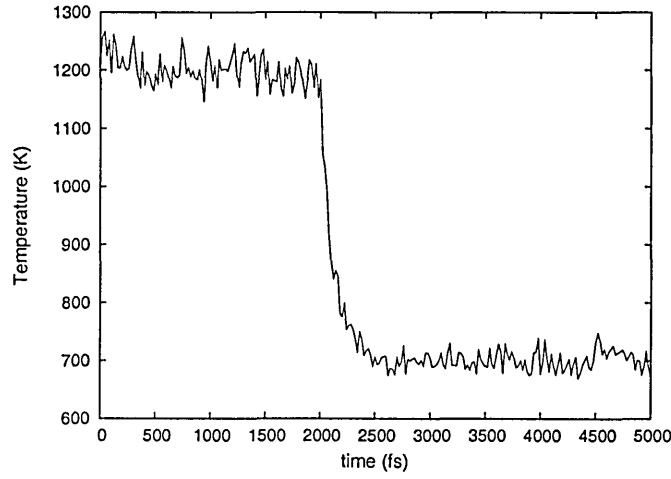
Figure 4.16: Temperature profile versus time of the prototypical annealing scheme, starting from an equilibrated bcc Fe at temperature 1200 K to 700 K.
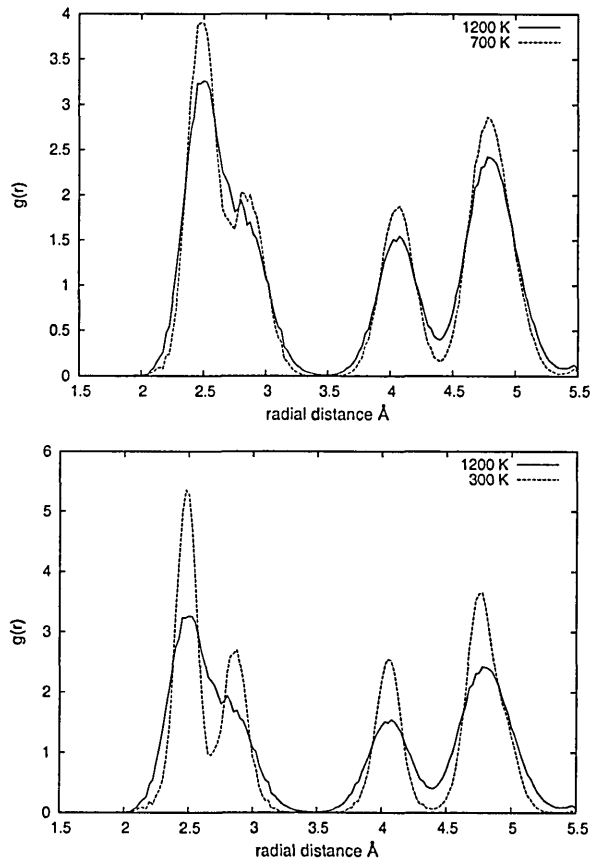
Figure 4.17: Radial distribution function of bcc Fe at 1200 K annealed to 700 K (upper figure), and at 1200 K annealed to 300 K (lower figure)

85

tallite at higher temperature about 1200 K, then we annealed the crystallite by applying the friction and the stochastic forces. The temperature profil in Fig.4.16 shows the instantanous temperature decreasing to the annealing temperature of 700 K. Additionally, Figure 4.17 demonstrates that the radial distributions after the annealing are well reproduced.

Conclusion

This chapter has introduced the different ideas that constitute the MD method employed to obtain the results of this thesis. The description of the interactomic potential given in part in the previous chapter, is built up here in a manner to model the interaction range appropriate to simulate energetic bombardment. The implemented potential shows a good agreement with reported equilibrium properties calculation. The validated potential and the functionality of the MD code dictate the launch of dynamical calculation.

Chapter 5

Impact of Cr on Pure α-Fe

Introduction

We examine by molecular dynamics simulation the impact of a single Cr ion at normal incidence on a pure α-Fe crystal. The energy of the Cr ion lies in the range 200 eV to 5 keV and the Fe crystal is assumed to be at temperature zero, 300 K and 700 K. Detailed results will be presented for bombardment energy 1.2, 2.4 and 5 keV. These are the regimes of experimental interest where the ion energy $E = QU_b$ is proportional to the mean ion charge state and the bias voltage applied to steels substrate during a typical etching process operating at temperature 700 K in the cathodic arc plasma [19]. However, 5 keV regime is at the limit of what might be expected experimentally, although it may be possible for a highly ionized Cr. The ion charge state distribution of a vacuum arc plasma from a Cr cathode amounts to 9.6% Cr^{+1}, 71.8% Cr^{+2}, 18.6% Cr^{+4} and 0.056% Cr^{+4}, with the mean charge state of about 2.09 [233].

We begin by describing the time evolution of the cascade generated by the impact as a function of energy and crystal temperature. Besides sputtering from the surface and defect production, the temperature in the core of the cascade and the penetration depth are analysed. Distribution profiles of defects under different bombardment conditions are also examined.

5.1   Simulation Model

At normal incidence a Cr ion at energies between 200 eV and 5 keV, impacts onto the surface (100) of the crystalline iron at temperatures 0 K, 300 K and 700 K. The stochastic nature of the ion impact on a solid surface has been taken into account by simulating over 150 impacts selected randomly over an area of the surface, which is representative of the crystal as whole (using an irreducible symmetry zone). The reported results are obtained by taking averages over these 150 impacts

5.2   Cascade Development

A cascade develops when an energetic particle hits a solid surface and prompts a collisional or ballistic phase, involving an avalanche of displaced or moving target atoms. A region of disorder is then created and a cooling phase becomes established, during which a hot zone is formed and begins to anneal.

Typically, cascades have dimensions of nanometres and lifetimes of picoseconds. Their detailed investigation by experiment is impossible and atomic scale computer simulation by molecular dynamics (MD) provides a unique insight into these processes.

5.2.1   Description of a Cascade

The state of the cascade as a function of time is illustrated by the computer generated defect plots in the Figures (5.1) to (5.5) for crystal temperature 0 K and in the Figures (5.6) to (5.9) for crystal temperature 700 K.

Four stages of the temporal evolution of the cascade have been chosen on the ground that they contain the significant features observed in the entire evolution of each cascade initiated in the centre of the crystal.
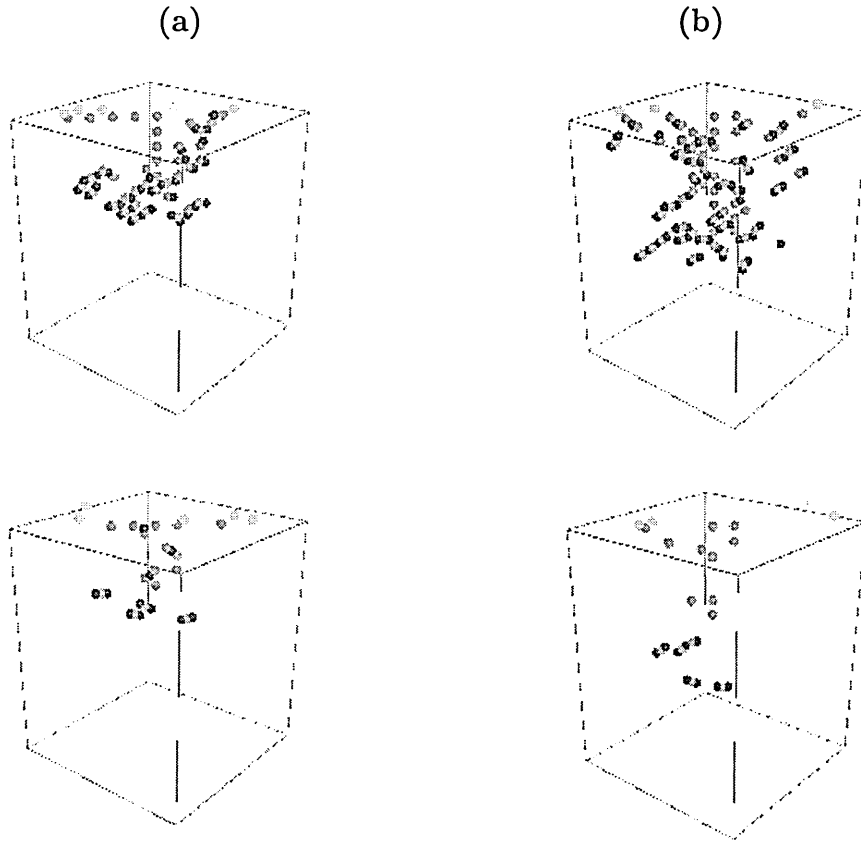
Figure 5.1: The damage induced by (a) : 200 eV and (b): 400 eV Cr ion in the Fe crystal at 0 K. Snapshots are at times 0.25 ps (upper fig.) and 0.75 ps (lower fig.)

As shown in Fig.5.1, the cascade of 200 eV and 400 eV at 0.25 ps is made up of separated chains of displaced atom to interstitial like site with vacancy left behind. These low energy cascades anneal very rapidly at 0.75 ps. Few defects are left such as single vacancies and dumbbells interstitials.

Two mechanisms have been proposed for the separation of vacancies and interstitials within a cascade, Replacement Collision Sequence (RCS) and momentum transfer following defect clustering [234].

In Fig.5.2 for the cascade of 1.2 keV, more radial chains of displaced atoms occur at 0.25 ps due to channelling. By 1.5 ps these chains vanish leaving

89
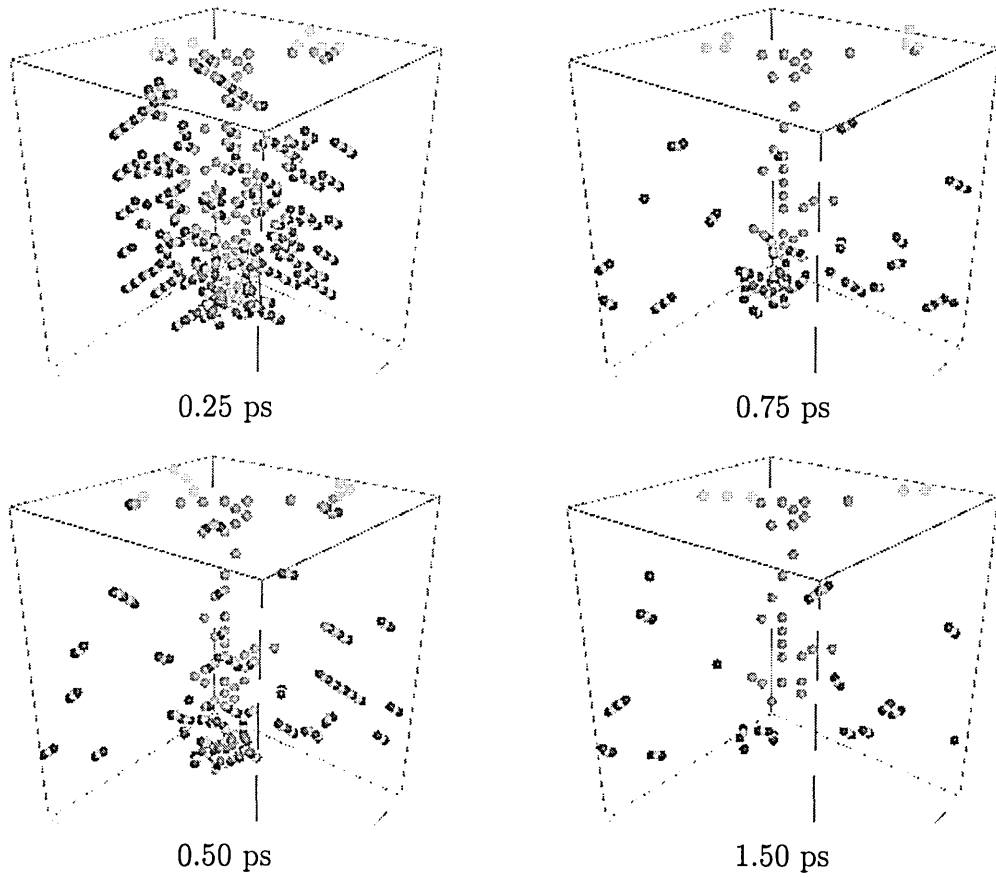
Figure 5.2: The damage induced by 1.2 keV Cr ion in Fe crystal at 0 K

farther radial defects with single vacancies retracing the channel along the crystal depth. At the same energy but different trajectory, Fig.5.3 shows a core like of displaced atoms with emission of two long chains which quickly annealed out by 0.75 ps and by 1.50 ps a shallow damage is left.

At 2.4 keV (Fig.5.4) a core has formed from the closely coupled displacement chains and with very few single chains at the periphery of the cascade. This coupling is much more important at 5 keV (Fig.5.5), where high density core has formed. The bombardment of a static crystal (0 K), favorizes the formation and propagation of long RCS chains.

We explore next the cascades generated at temperature 700 K and at keV bombardment of experimental interest to surface treatment.

0.25 ps   0.75 ps

0.50 ps   1.50 ps
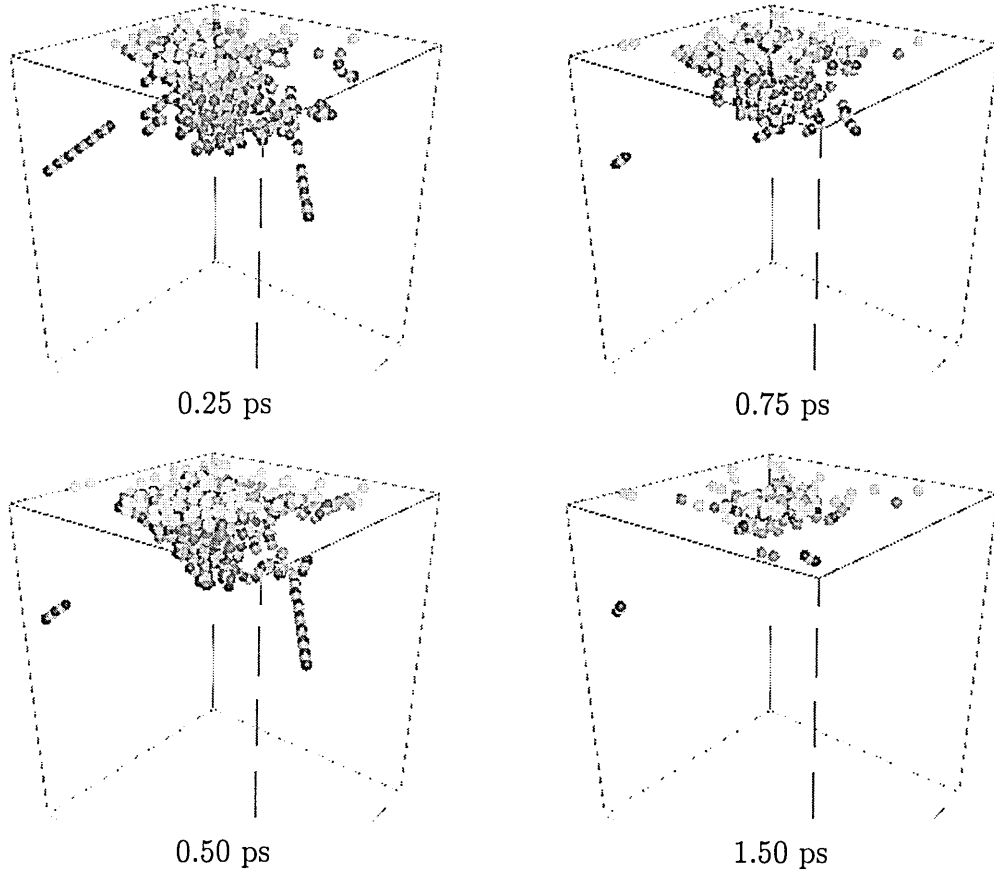
Figure 5.3: Same bombardment conditions as Fig.5.2 but at a different impact on Fe crystal at 0 K

Fig.5.6 shows the first 1.5 ps of 1.2 keV event. After 0.25 ps the displaced atoms move to interstitial positions with the subsequent vacant sites and form a sort of cone. The separate RCS on the left is of 8-replacement sequence which is the maximum length observed in this cascade. By 0.5 ps just after the peak disorder (see section 5.2.3) there are more adatoms and some deep damage detached to the right of the cascade. At 0.75 ps, most of defects have already started to anneal and this trend continues throughout the cascade.

By contrast to Fig.5.6, Fig.5.7 shows the extreme changes in 1.2 keV cascade shape when some partial channelling occurs which is typical of choice of the trajectory. In this case, the cascade becomes elongated in the direction of
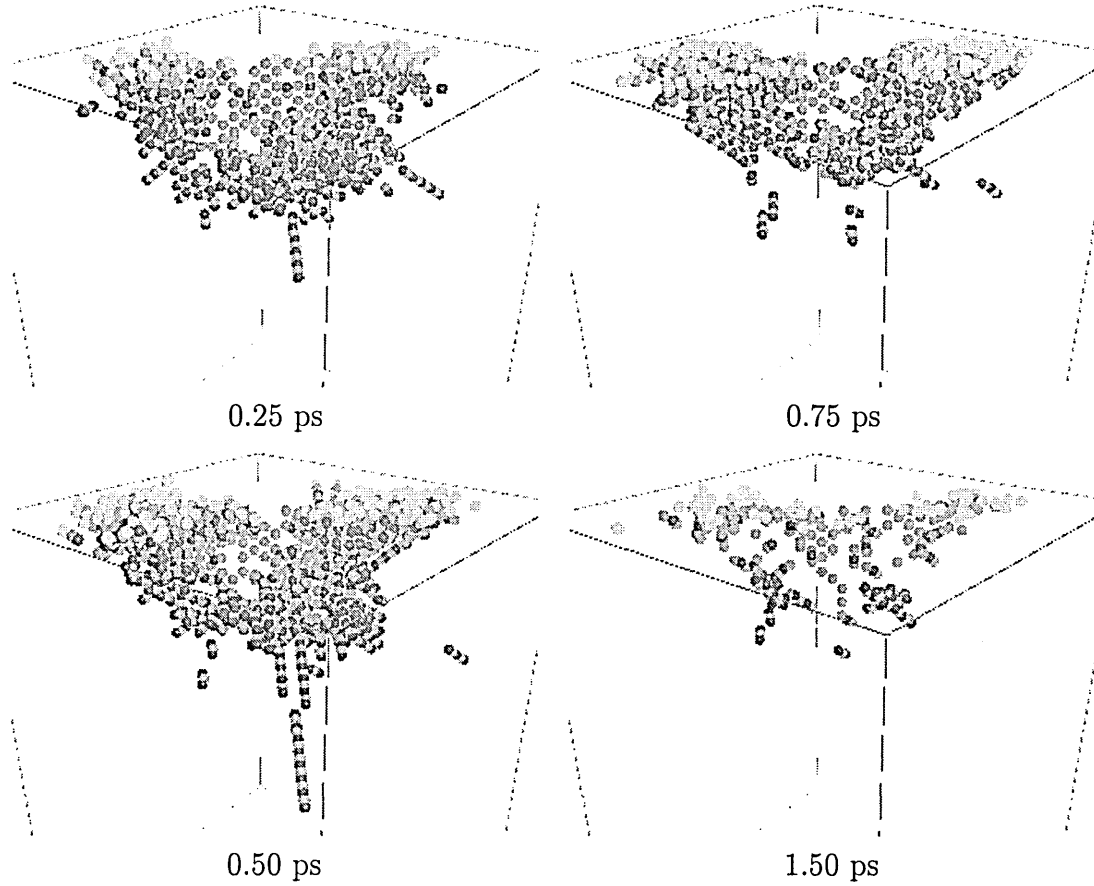
Figure 5.4: The damage induced by 2.4 keV Cr ion in Fe crystal at 0 K

the ion path where a string of vacancies is produced. Interstitials are ejected radially from the path via RCS. Only 3 adatoms form and 4 vacancies cluster near the impact point. The deepest defect is located at 60.9 Å.

The cascade at 2.4 keV (Fig. 5.8), has a more compact appearance than the one at 1.2 keV (Fig. 5.6). Few separate replacement chains are emitted from the core of this cascade by 0.25 ps. First layer adatoms forms after 0.5 ps, a few fs before the peak damage , and the volume occupied by the disordered zone increases. Thereafter, recombination of interstitials and vacancies starts extensively from the bulk where less energetic displacement fail to produce a permanent defect.

0.25 ps   0.75 ps

0.50 ps   1.50 ps
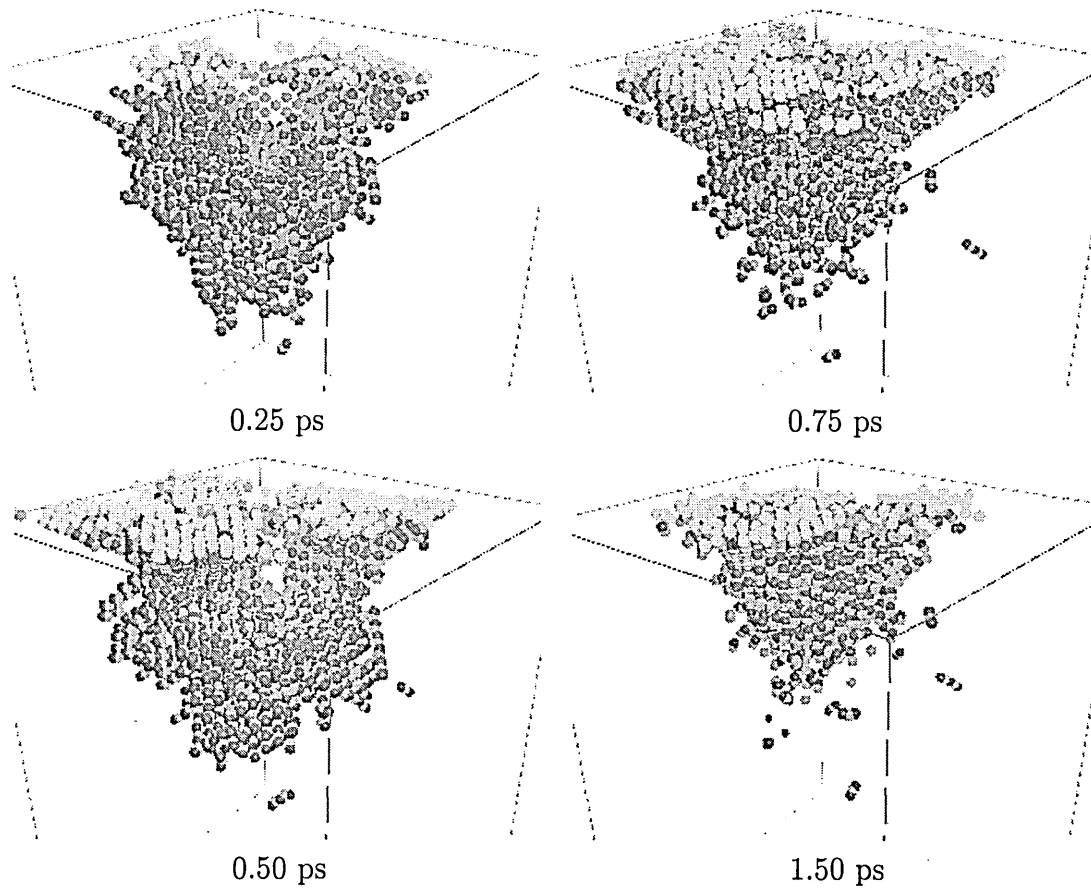
Figure 5.5: The damage induced by 5 keV Cr ion in Fe crystal at 0 K

The same general observations apply to the spectacular 5 keV cascade in Fig. 5.9. A concentrated coverage of adatoms occurs for this energy. This can be attributed to a disrupted surface atoms in the early stages of the cascade. Some delayed RCSs emerge by 0.75 ps and the depth range of the damage exceeds the one at 2.4 keV.

RCSs have been observed in all the cascade. However, it becomes difficult to discern RCS as the energy increases and collective replacement chains predominate over single ones. The morphology of the cascade does change substantially with the impact energy and the trajectory. From visual inspection of keV cascades at 0 K and 700 K, we can see that the density of the cascade and the formation of over layer adatoms are important in a hot crystal.

93

0.25 ps   0.75 ps

0.50 ps   1.50 ps
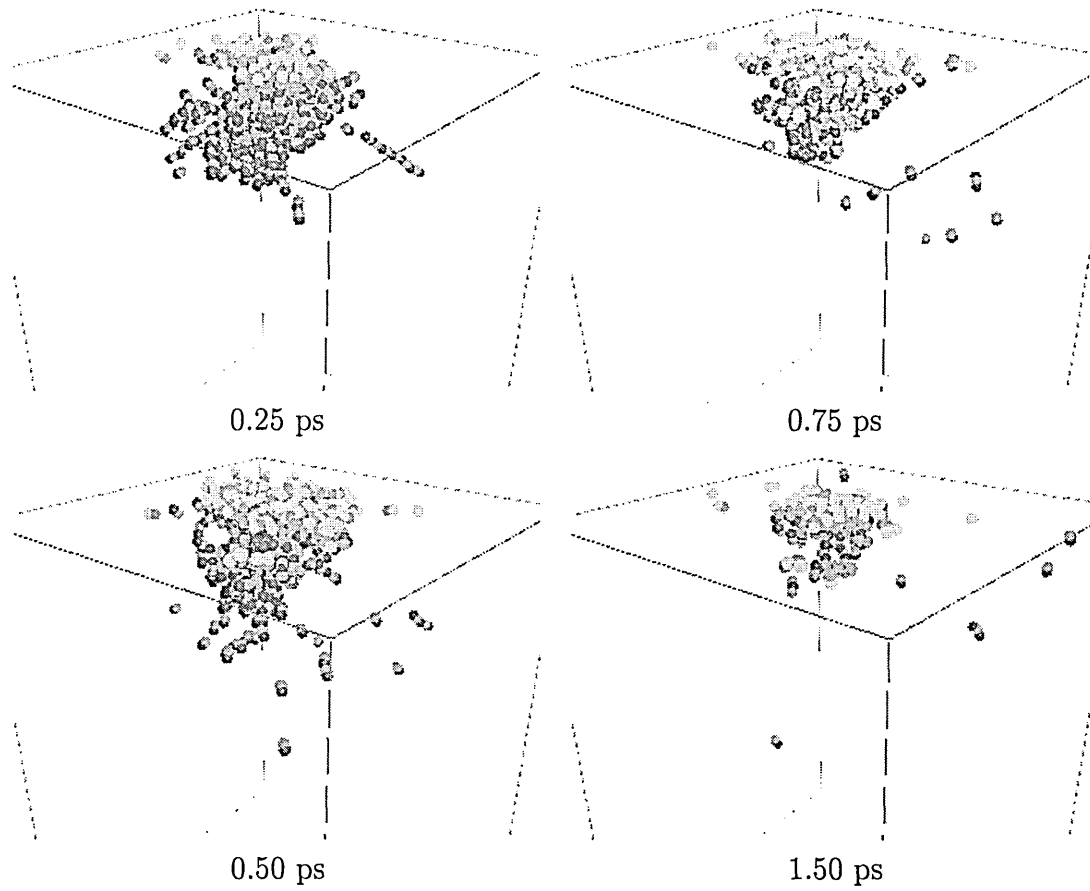
Figure 5.6: The damage induced by a 1.2 keV Cr ion in Fe crystal at 700 K

After 10 ps, the final state of defects that have survived recombination is displayed in Fig. 5.10 and Fig. 5.11.

At 1.2 keV (Fig. 5.10(a)), the well separated vacancy-interstitial pair along <111> direction, emanates from the longest RCS shown earlier in Fig. 5.6 at 0.25 ps. Only one deeper interstitial is left at 23.34 Å, and 18 adatoms are closely dispersed around the impact region. Vacancies are located between the first and sixth layers (-1.1-6.7 Å). Note that 5 ps is sufficient at this energy to attain the above defect state.

Considerable damage remains at 2.4 and 5 keV compared to 1.2 keV. For 2.4 keV (Fig. 5.10(b)) more defects survive in the proximity of the surface than in the bulk and about 54 adatoms agglomerate around a vacancy rich surface region. Particularly in this region vacancies are arranged in rows while
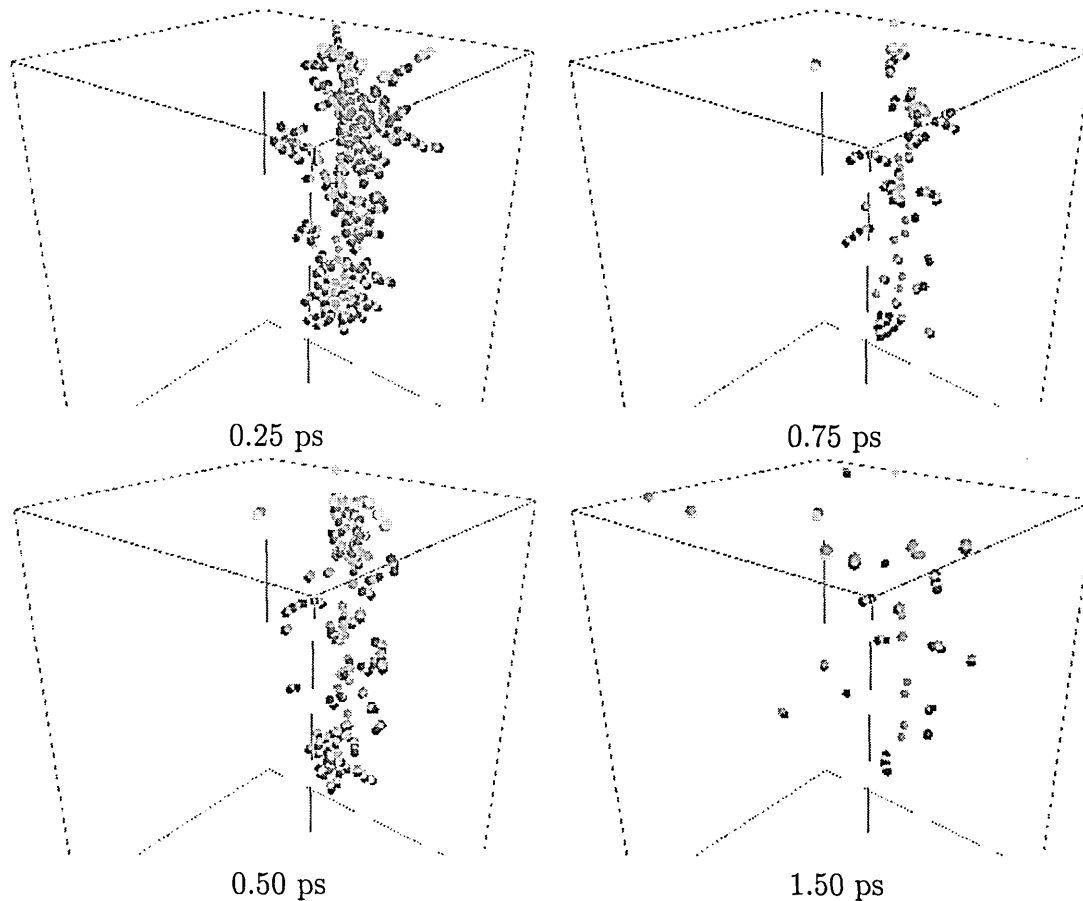
Figure 5.7: Same bombardment conditions as Fig.5.6 but a different impact point on the crystal

the rest of them are distributed rather widely through and down to 15 Å below the subsurface. The deepest defect is located at about 30 Å. About 14 of the interstitials (65 in total)are in form of dumbells.

The visual inspection of 5 keV in Fig. 5.11(C) shows a high number of adatoms (117 in total), slightly more than double the value at 2.4 keV, with a large surface vacancy crater. A visible cluster of 6 vacancies formed in the centre, with one single and one dumbell interstitial merging to the right side of this cluster. No tendency of clustering appears for interstitials.

In the same figure, the 5 keV defect state at 0 K (Fig. 5.11(a)) and 300 K (Fig. 5.11(b)) are also shown. The significant feature here is more damage has

0.25 ps   0.75 ps

0.50 ps   1.50 ps
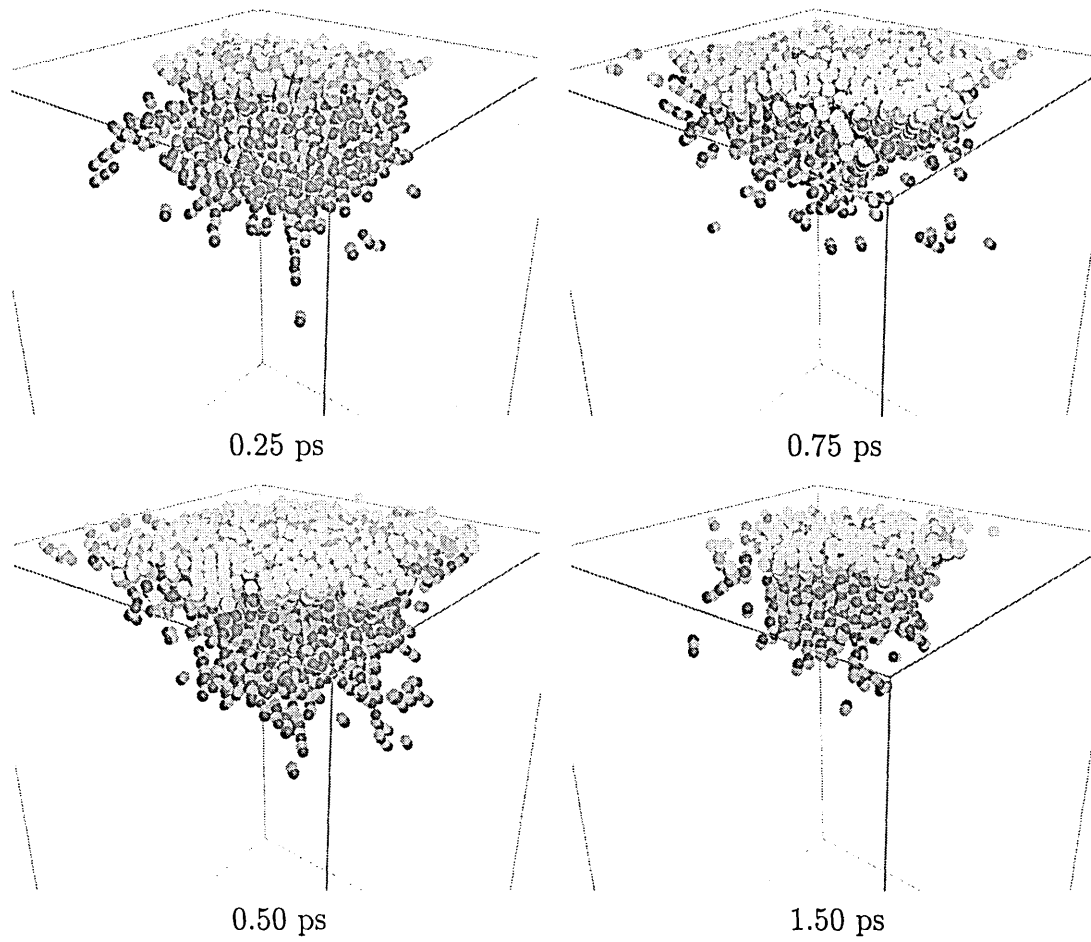
Figure 5.8: The damage induced by a 2.4 keV Cr ion in Fe crystal at 700 K

formed towards the surface as the crystal temperature increases and at the same bombardment energy.

Worth noting that the damage state remains stable after simulation time greater than 10 ps.

For all cascades, apart from those interstitials which are absorbed by the surface as adatoms, the rest tend to lie to one side of the vacancies. This clearly tracks a forward momentum developed in the early stage of the collisional phase.

0.25 ps	0.75 ps
0.50 ps	1.50 ps
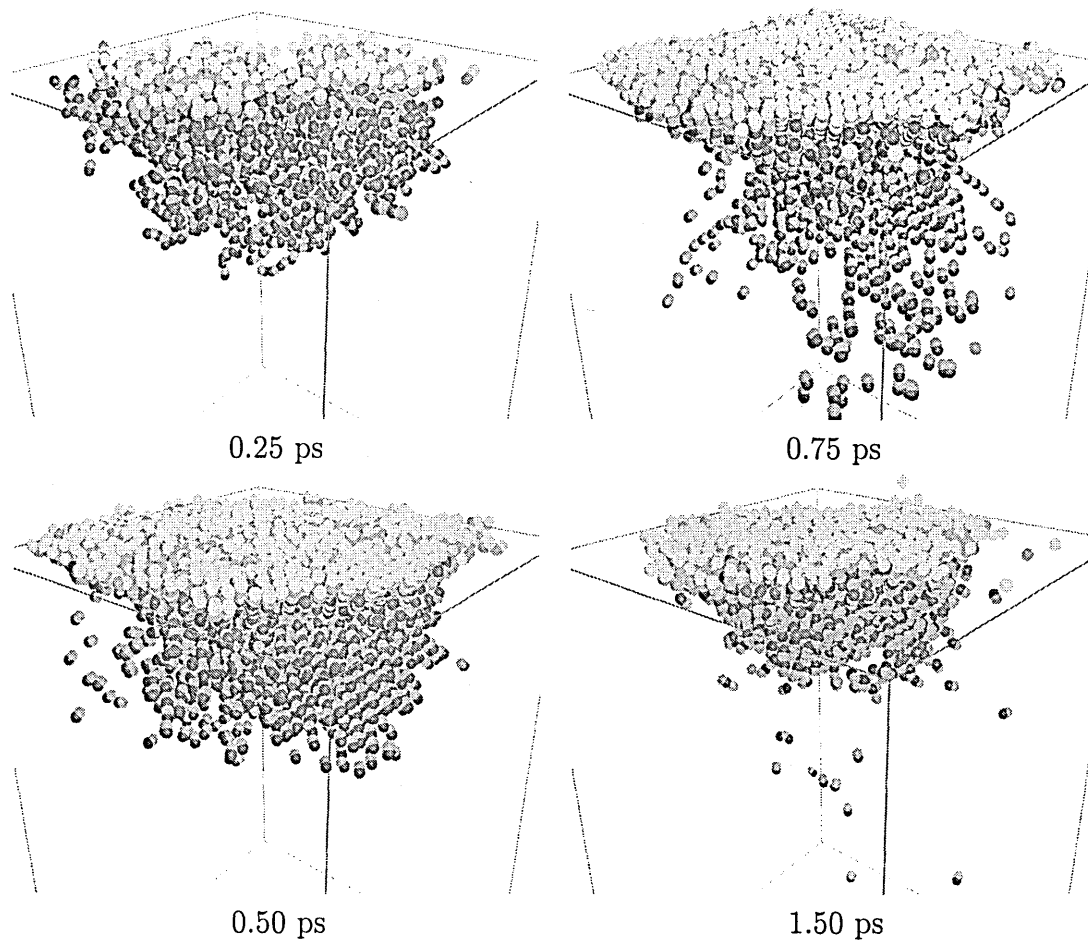
Figure 5.9: The damage induced by a 5 keV Cr ion in Fe crystal at 700 K

These results for temporal evolution of cascades triggered by Cr impacts are in good qualitative agreement with the trends drawn by previous work [197, 221, 234] in a bulk model of α Fe which has no free surfaces. However, the presence of a surface does induce a different morphology of damage which is more accentuated in the near surface region. A correlation between surface vacancies and both adatoms and sputtering can be advanced, since these two quantities are mainly originated from the first and sometimes second atomic layers, this will be discussed later in section 5.4.
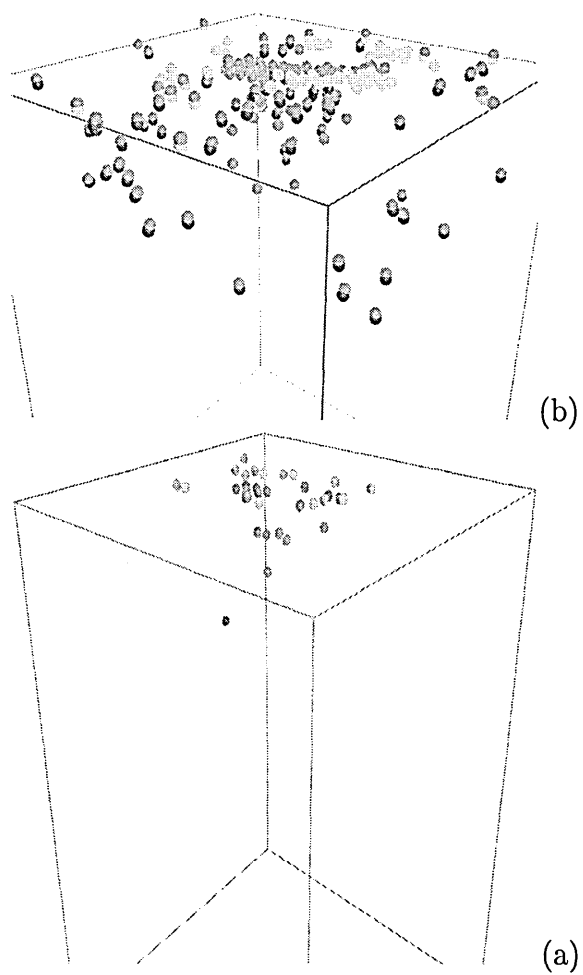
Figure 5.10: The final defect state for (a) 1.2 keV and (b) 2.4 keV Cr bombardment of Fe at temperature 700 K
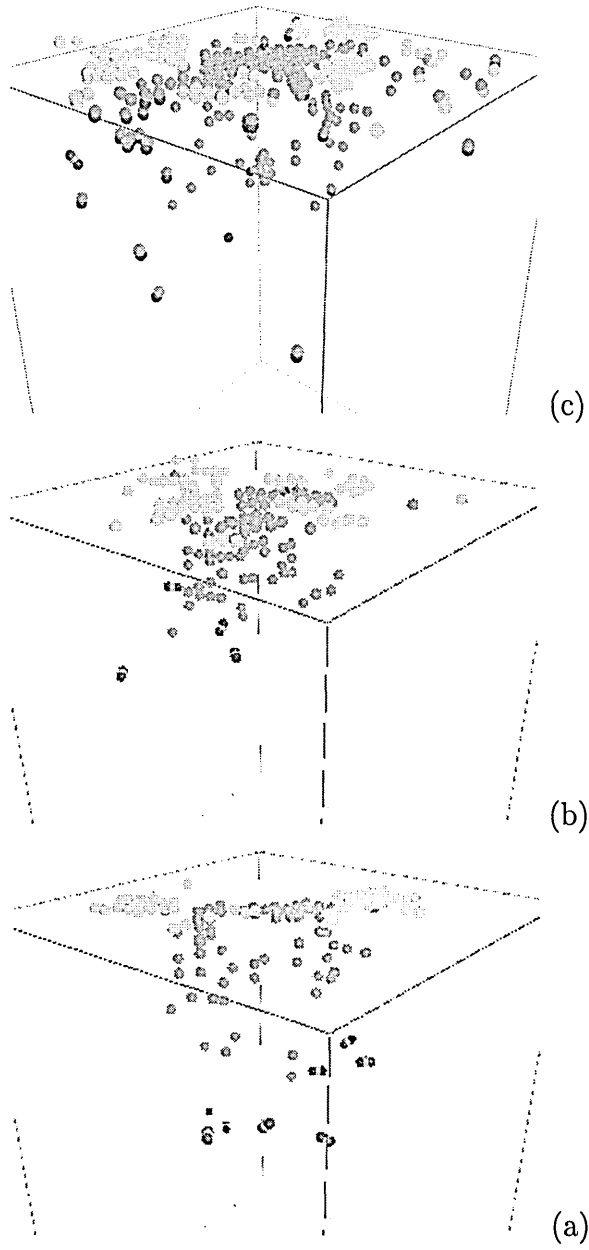
Figure 5.11: The final defect state for 5 keV Cr bombardment of Fe at crystal temperature: a)0 K, b)300 K and c) 700 K
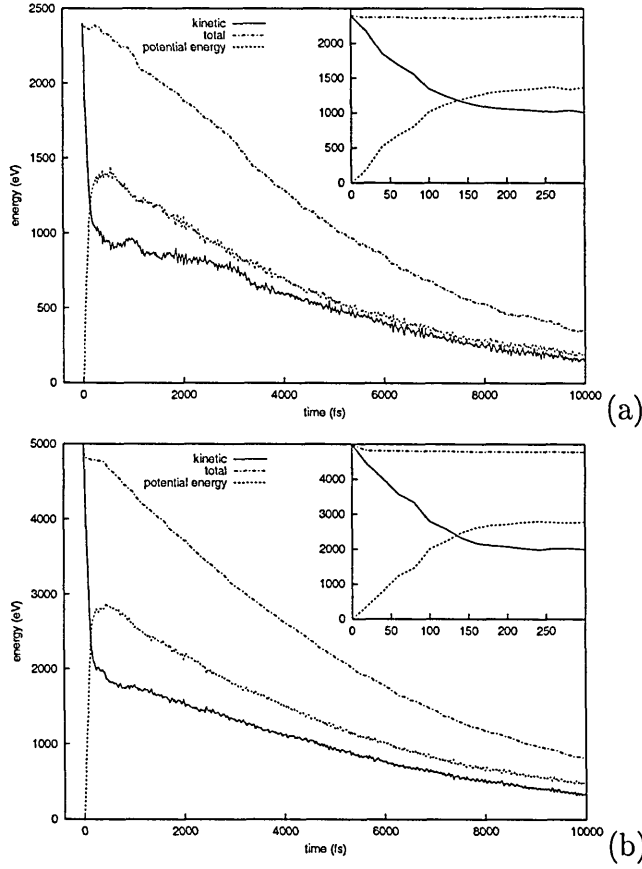
Figure 5.12: Time evolution of the total, kinetic and potential energy for 2.4 keV (a) and 5.0 keV (b) Cr impacting Fe crystal at temperature 700 K

5.2.2 Time Evolution of Energy

To investigate the energy transfer between the impinging Cr ions and the Fe crystal, we measure the kinetic, potential and total energies of all atoms in the simulation, with respect to the equilibrium crystal configuration so that at the time $t = 0$ the kinetic energy of the system is given by the incident ion while the potential energy is nul. Figures 5.12(a) and 5.12(b) represent the results for two impact runs at 2.4 and 5 keV. A similar trend of the temporal evolution of energy was observed for all runs, as reported in Ref. [80,223]. The total energy E_{tot} shows a monotonic decrease for times larger than 0.4 ps. This occurs when the energy reaches the dissipative boundaries of the crystallite. The time dependence of the kinetic energy and the potential energy is particularly interesting. At the time $t = 0$ when the Cr ion has just entered the (cutoff)

100
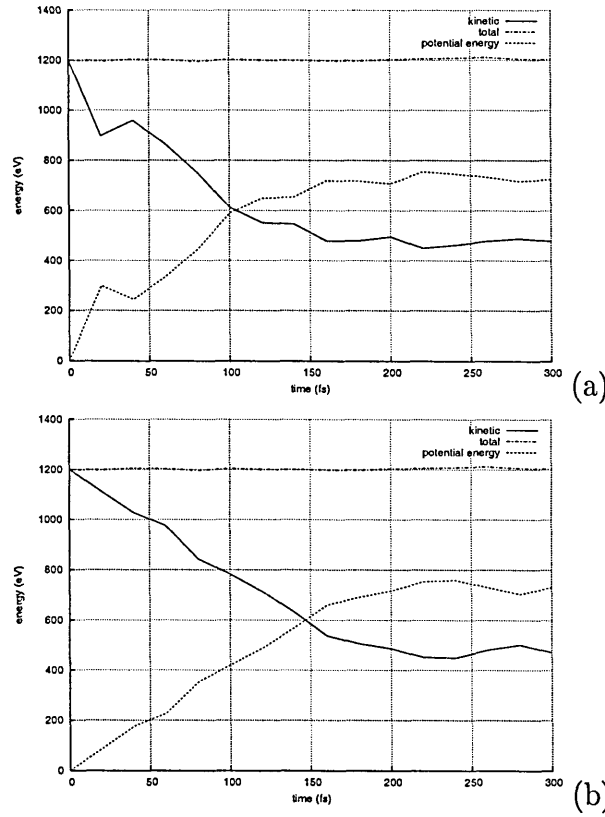
Figure 5.13: Time evolution of the total, kinetic and potential energy for 1.2 keV (a) no-channelling, (b) channelling

potential of the crystalite, and during the first few femtoseconds the Cr travels toward the surface and then by violent collision, kinetic energy is exchanged to repulsive potential energy and a concentrated thermal phase establishes which is evidenced next from the temperature profile. The injected kinetic energy is absorbed into the lattice by about 0.14 ps for each of 2.4 and 5 keV and by 0.1 ps for 1.2 keV. This time is delayed if the ion experiences channeling as shown in Fig. 5.13(a) and Fig. 5.13(b). The thermal or cooling phase lasts longer for 5 keV impact while it is present until 5 ps for 2.4 keV but to a lesser degree, as depicted from the gap between tails of kinetic and potential energy. The long life time of the cooling phase is an important feature of high energy cascade .

5.2.3 Time Evolution of damage

The time evolution of the number of displacements together with the number of defects at each energy event 1.2, 2.4 and 5 keV, are assembled in Figures 5.14 and 5.15. Fig. 5.14 reconfirms what was previously visualised (section 5.2.1), that most of displacements are short lived and the time, t_{peak}, taken to achieve peak disorder, is featured by the maximum number, Nd_{peak}, of displacements. The value of Nd_{peak} increases almost linearly with energy, and t_{peak} increases from about 0.4 ps at 1.2 keV to about 0.6 ps at 5 keV. The form of N_d as it increases and then declines with time shows a pronounced tail at $E > 1.2$ keV. Notice at about 2 ps a bump indicating a weak shock wave reflection from the periodic boundaries. The percentage of permanently displaced atoms with respect to the peak damage increases with energy from 5 to 14 %.

The number of adatoms in Fig.5.14 peaks at a time greater than at which sputtered particles are emitted for each of the three events but adatoms take a longer time to equilibrate at higher energy because they may originate from ejected atoms which had the y component of the velocity directed towards the surface. The number of vacancies balances the number of interstitials, adatoms and sputtered target atoms so the mass conservation is fulfilled.

In Fig. 5.15, the number of vacancies decreases as a consequence the number of replacements increases reaching a stable value of 200 at 1.2 keV (Fig. 5.15.a), 650 at 2.4 keV (Fig. 5.15.b) and 1500 at 5 keV (Fig. 5.15.c). Such saturation occurs more rapidly at 1.2 keV than at 2.4 and 5 keV, an evidence of the long time for disorder to anneal out at high energy events. Also, the high number of replacements in a hot crystal and high energy reflects the importance of atomic mixing. Note that the extended tail of vacancies at crystal temperature 700 K surpasses those at 0 and 300 K for the same impact energy.

The maximum number of displacements, Nd_{peak} and the corresponding time t_{peak} are shown in Fig. 5.16 as a function of the impact energy and target temperature, where the values and bars represent respectively averages and standard deviations. Both parameters t_{peak}, Nd_{peak} increase with energy.
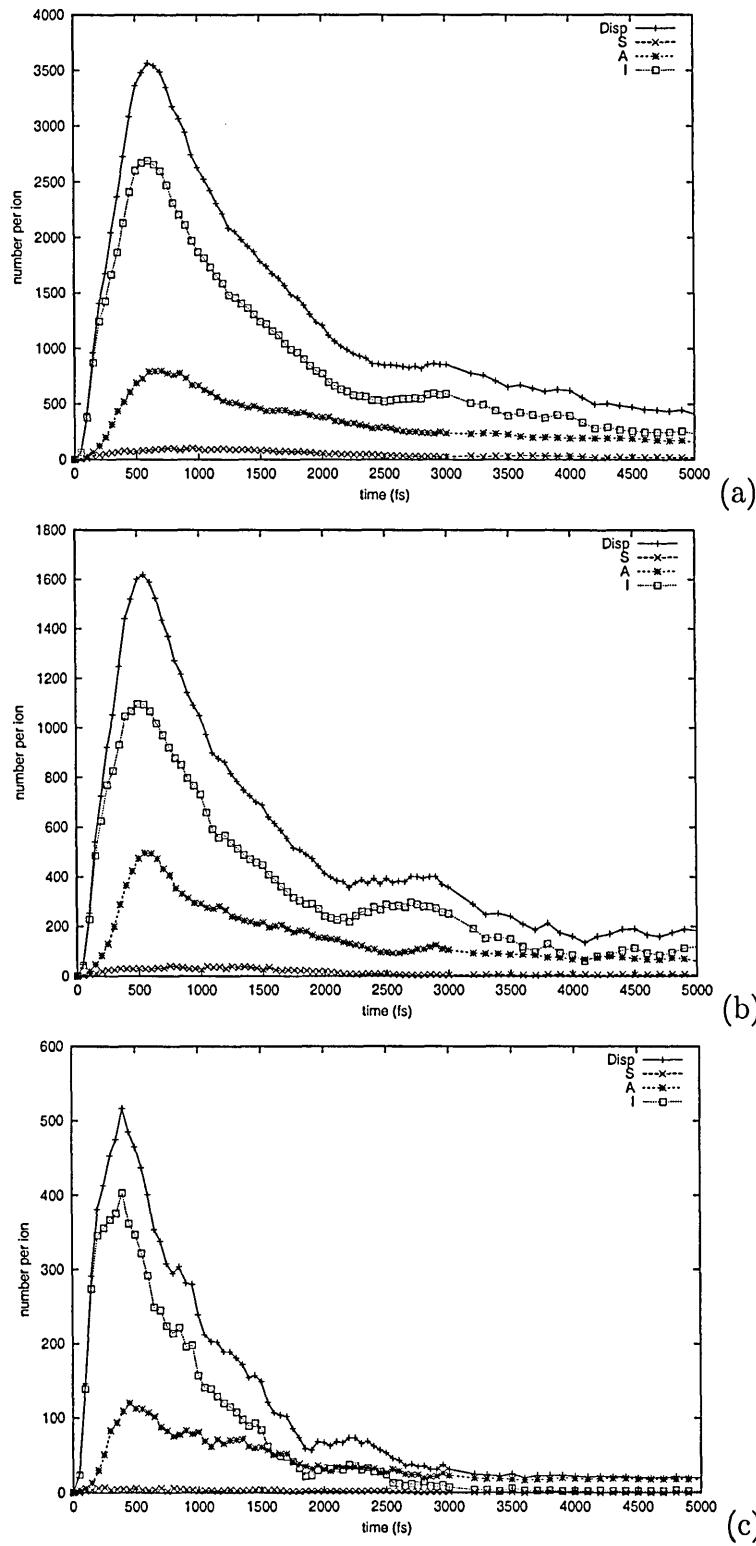
Figure 5.14: Time evolution of the number of interstitials (I),adatoms (A), displaced (N_d) and sputtered atoms (S) in a 5.0 keV (a) and 2.4 keV (b) 1.2 keV (c) Cr bombardment at substrate temperature 700K
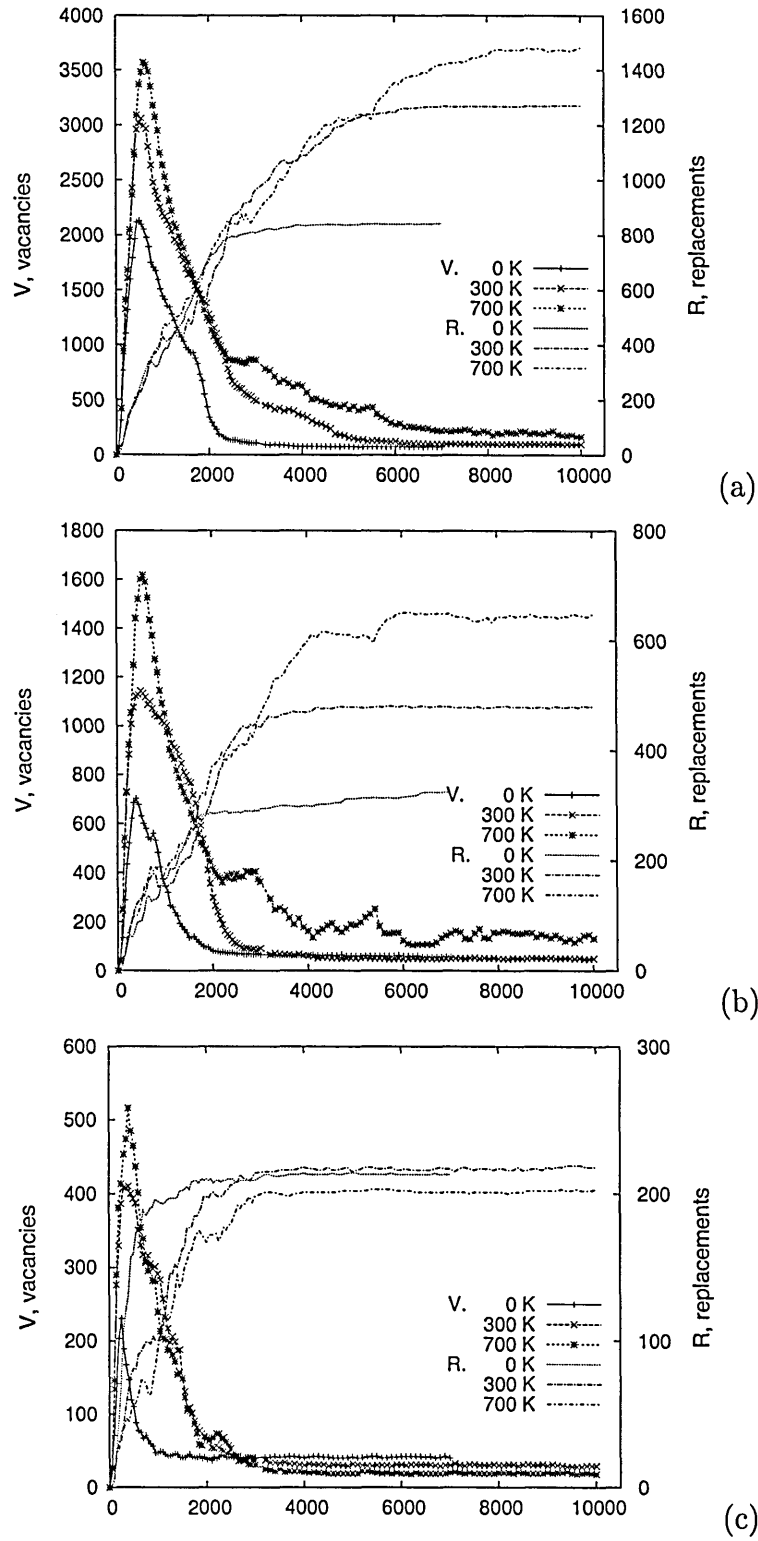
103

Figure 5.15: Time evolution of vacancies (V) and replacement atoms in a 5.0 keV (a), 2.4 keV (b) and 1.2 keV (c) Cr bombardment at substrate temperature 0 K, 300 K anf 700 K
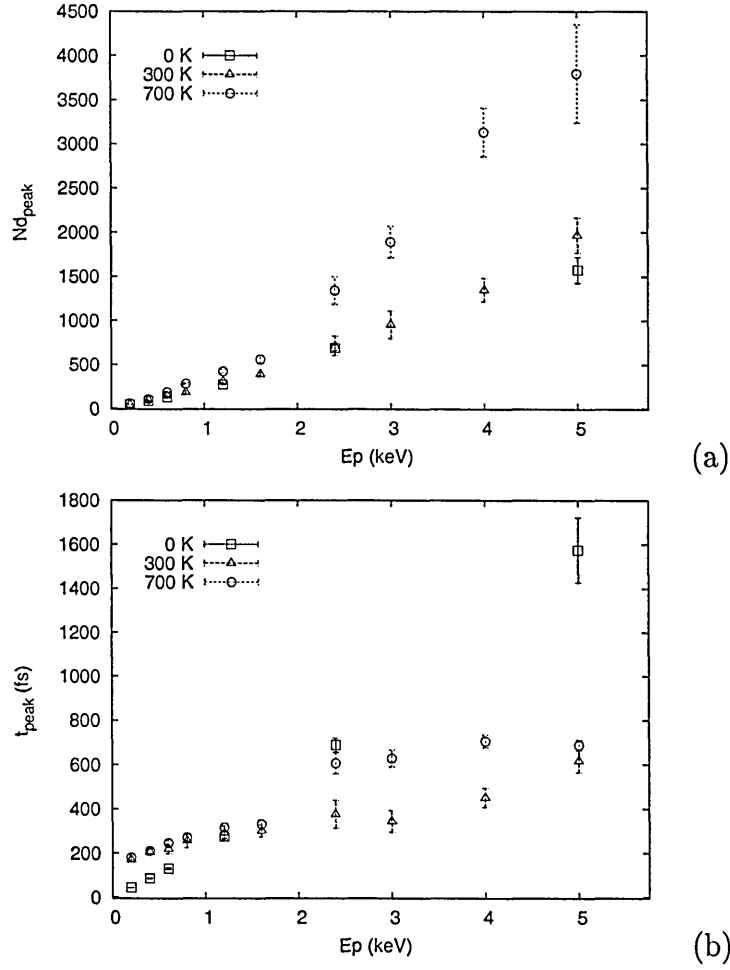
Figure 5.16: Variation of (a) t_{peak} and (b) Nd_{peak} with Cr projectile energy E_p for the two crystal temperatures considered

The effect of crystal temperature on t_{peak}, Nd_{peak} arises in the keV region where damage is important. A similar trend was reported for bulk cascade in Fe [197, 221]. Note at temperature 0 K and energy 5 keV , t_{peak} is higher due to delay by quasi-channelling effect. The behaviour of the damage with energy and temperature is consistent with earlier observation of cascade morphology (section 5.2.1) where the distinction between lower and higher energy cascade can be made.
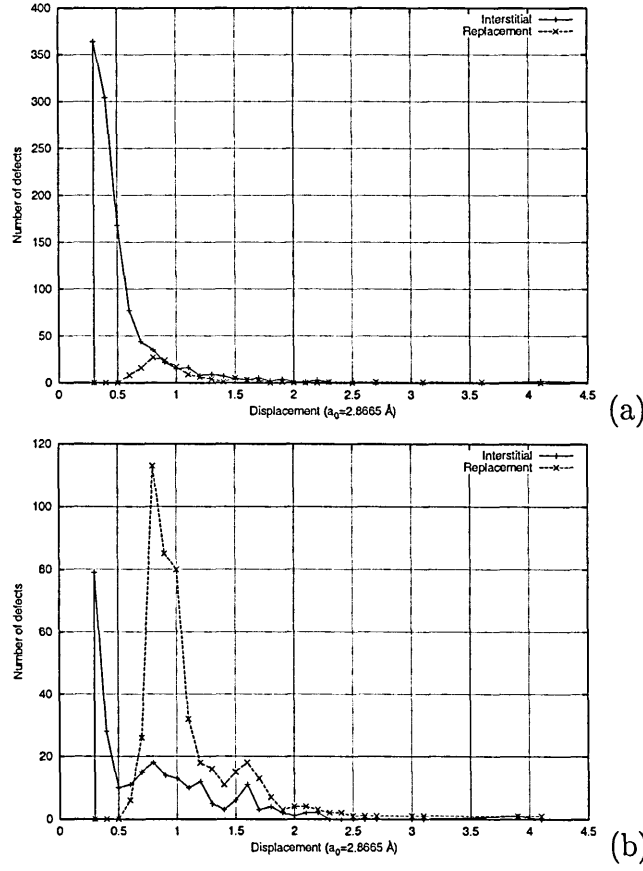
Figure 5.17: Atomic displacement distance in Fe at 2.4 keV cascade at: 0.5 ps (a) and 3.0 ps (b)

5.2.4 Displacement Distance

Monitoring the displacement distance is useful in order to gain an insight into how far all displaced atoms have moved from their initial lattice site during the course of the surface impact generated cascade. Such a distance is implied in Fig. 5.17 for displacement events to interstitial like sites and to foreign lattice sites at 2.4 keV cascade. Just before the peak t_{peak} at time 0.5 ps (Fig. 5.17a), the majority of atoms are displaced next to their initial site. However, in the cooling phase at time 3.0 ps (Fig. 5.17b), the majority of displacements are first-neighbor replacements $(0.866a_0)$. This is the evidence of replacement collision sequences in the <111> directions in Fe bcc lattice. Cascades at 1.2 and 5 keV exhibit the same spatial behaviour in agreement with higher energy 10 keV bulk cascades simulations in Fe reported by Vascon and Doan [79].

106

However, quasi-channelling happens to displace some atoms far from their original site.

5.2.5 Temperature Profile

A set of cylindrical shells of radius r concentric to the impact zone, are used as a volume to calculate the temperature profile at various instants of time during the impact simulation. The temperature $T(r)$ is defined from the average kinetic energy as $E_k = 3k_BT(r)$ (k_B is Boltzman's constant), after subtracting the average velocity in each shell from the velocity of atoms in that shell.

In Fig. 5.18 the temperature profiles for 1.2, 2.4 and 5 keV cascades are shown. After few hundred femtoseconds (200 fs), the temperature is well above the melting point at 5 and 2.4 keV (T_m= 2200 K for the present model [197], experimental value for iron is 1809 K) while it is only about 1600 K at 1.2 keV. The high transient in temperature is characteristic of the thermal phase as demonstrated for all cascade simulation to date [221, 235–238].

The radius of the melted region is larger by a factor of about 2 in size and 4 in volume for 5 keV (10 a_0) than for 2.4 keV (5 a_0), (a_0 is the lattice parameter of Fe), local melting thus occurred. Over a few picoseconds the temperature decreases rapidly and gradually to its ambient value of 700 K.

In addition, radial $T_r(r)$ and axial $T_y(r)$ temperatures were also calculated and $T_r(r)$ is much larger than $T_y(r)$. This suggests that the motion was not truly random but radial motion prevails (system not in equilibrium).

To investigate the state of the material at the temperatures shown in Fig. 5.18, a common approach is to plot the positions of atoms within a cross-sectional slab of thickness (0.5 a_0) below the surface. This is produced in Fig. 5.19 at four simulation times. On the whole, the disordered region first grows in size attaining a maximum at 0.2 ps up to 2 ps for 5 keV cascade, and then shrinks subsequently. In the 5 keV cascade the local density is greatly reduced, with

107
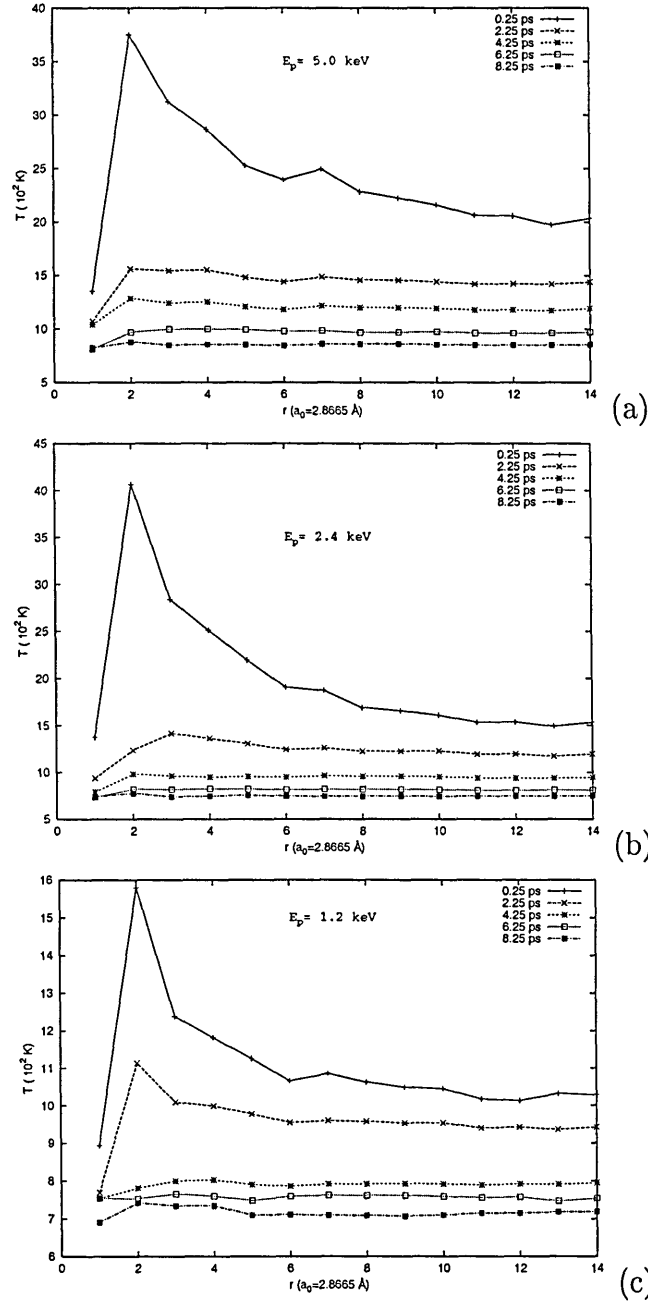
Figure 5.18: Temperature profile from the impact centre for 5.0 keV (a), 2.4 keV (b), 1.2 keV (c) trajectory at different times.
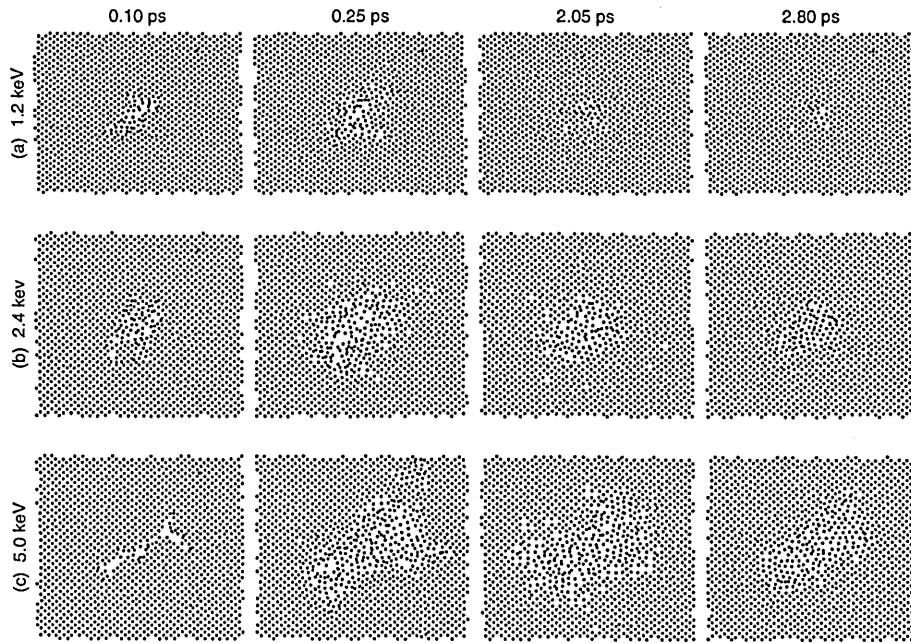
Figure 5.19: Planar-sectional views of a 1.2 keV (a), 2.4 keV (b), 5 keV (c) trajectory four different times and at one atomic layer depth below the surface.

more voids compared to 2.4 and 1.2 keV. A liquid like drop in the centre has developed at 2.4 and 5 keV confirming again the local melting, whilst a few hot-spots can be attributed to 1.2 keV.

The reported values of $T(r)$ for 1-5 keV bulk cascades temperature in iron [197] are rather less compared to bombardment generated cascades. On the other hand Ghaly and Averback [239,240] showed that the temperature exceeds 6000 K for times up to 3 ps, from MD simulation of 10 keV Au impacting on Au target, and they related this to surface mecanisms namely relief of pressure and viscous flow through the surface [241]. Local melting has a far more profound effect on displacement cascade processes near surfaces than in the crystal interior.

5.3 Fate of the Projectile

When an ion impacts a surface, it may either reflect, adsorb above the surface, substitute a target atom, or become an interstitial or part of a defect complex.
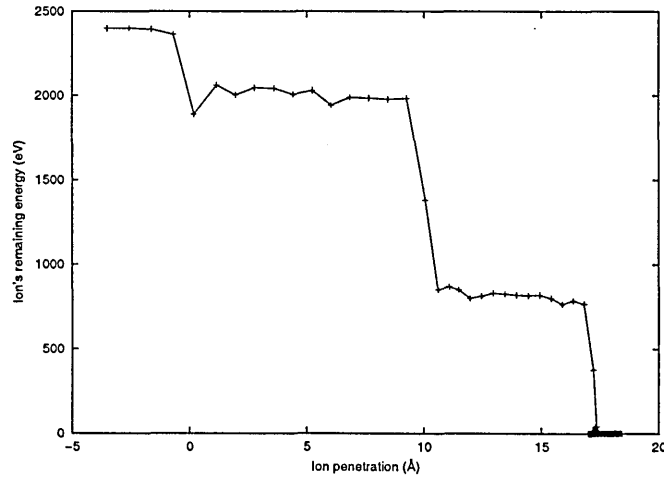
Figure 5.20: Plot of ion remaining energy vs. depth for one Cr at 2.4 keV impacting Fe crystal at 700 K during 2.0 ps

In all simulations no ion was backscattered, 99.99% of the ions are implanted on substitutional sites and very few end as an adatom. The fate of an ion is dependent on where the strongest collisions occur. In Fig 5.20, 70 % of the energy is deposited at a depth of 10 Å and the remaining at a depth of 17 Åwhere the ion comes to rest. Therefore, more simulations was carried out to deduce the mean penetration depth, which has shown to increase with projectile or ion energy as follows: 1.08 Å at 100 eV, 2.65 Å at 200 eV, 23.9 Å at 1.2 keV and 47.7 Å at 2.4 keV, similar trend to Cu self bombardment simulations [223]. It is worth noting that no channeling was observed at energy less than 1.2 keV, while at greater energy total channelling occured and the Cr ion is transmitted causing little or no disturbance to the lattice. This is enhanced by the open structure of bcc Fe crystal. Channelling events were more accentuated at zero and room temperature than at temperature 700 K. Thus, raising the crystal temperature to 700 K blurred the symmetry of the lattice via the thermal agitations.

110

	0 K		300 K		700 K	
	y_S	y_{Vs}	y_S	y_{Vs}	y_S	y_{Vs}
200 eV	0.02	2.74	0.05	2.15	0.20	2.70
400 eV	0.16	4.50	0.30	3.25	0.50	3.50
600 eV	0.57	7.81	0.70	8.05	0.90	11.20
1.2 keV	0.67	9.06	0.81	8.44	1.08	14.25
2.4 keV	1.96	16.15	1.12	10.33	2.43	26.96
5.0 keV	1.85	13.64	2.60	16.20	3.86	28.71

Table 5.1: The sputtering (y_S) and surface vacancy (y_{Vs}) yields function of the bombardment energy. The results are shown for three crystal temperatures 0, 300 and 700 K

5.4 Energy and Temperature Effects

5.4.1 Sputtering and Defect Yields

The results of sputtering, adatoms and interstitials yields for all energies (up to 5 keV) at 0 K, 300 K, 700 K are presented in Table 5.1 and 5.2. The sputtering yield increases with energy. Despite the lack of experimental data relevent to metallic ion bombardement of single crystal Fe, there is a reasonable agreement with experimental sputter yields measured for polycrystalline Fe under noble gas ion bombardment, for example Ar the yields are 0.5 at 200 eV, 1 at 400 eV, 1.3 at 600 eV, 1.4 at 1 keV, 2 at 2 keV and 2.5 at 5 keV [242,243]. Enhancement of sputtering with temperature is relatively modest but not negligible. This dependency enters through the surface binding enery U_b (usually taken equal to the heat of sublimation), as predicted from the analytical theory of sputtering [244,245], the yield is inversely proportional to U_b and for most materials U_b is lowered at high temperature (30 % of the melting point). Also reported elsewhere [246] that the effect of temperature on the sputtering is more accentuated at low energy (near the threshold region at which Y_S is null). This could explain the factor of four enhancement of the sputtering yield at 200 eV, from temperature 0 K to 700 K. Note that no clusters are formed for energy less than keV. Sputtered clusters detected at keV energy are in majority dimers.

	0 K		300 K		700 K	
	y_A	y_I	y_A	y_I	y_A	y_I
200 eV	3.44	1.42	3.30	1.65	3.50	0.50
400 eV	5.20	2.96	4.85	3.20	3.50	2.40
600 eV	8.51	5.40	9.25	3.75	13.10	2.20
1.2 keV	9.93	10.30	11.38	8.31	17.90	5.30
2.4 keV	18.70	17.28	15.88	19.00	33.04	57.26
5.0 keV	18.81	31.96	25.20	27.10	41.48	59.95

Table 5.2: The adatom (y_A) and interstitial (y_I) yields function of the bombardment energy. The results are shown for three crystal temperatures 0, 300 and 700 K

The yield of surface vacancies is greater than the sputtering yield. This suggests that more adatoms are formed as shown from adatom yield in Table 5.2.

The yield of all vacancies (surface+bulk) is represented in Fig 5.21. The bulk vacancy production by surface bombardment is in agreement with the one by bulk bombardment predicted by NRT and power law dependence, but only for temperatures less than 700 K. At high temperature the presence of a surface alters the density of the bulk vacancies. In Table 5.1, two features can be extracted for bulk vacancy and interstitial production. The same tendency of defect reduction with temperature for bulk damage [79, 238, 247] occurs here for energies over 1.2 keV. Then, a two order of magnitude increase is observed beyond this energy range. These effects can be explained by the importance of mobility of point defects with temperature and the role played by the surface at high temperature as a buffer competing recombinations and yielding more residual defects.
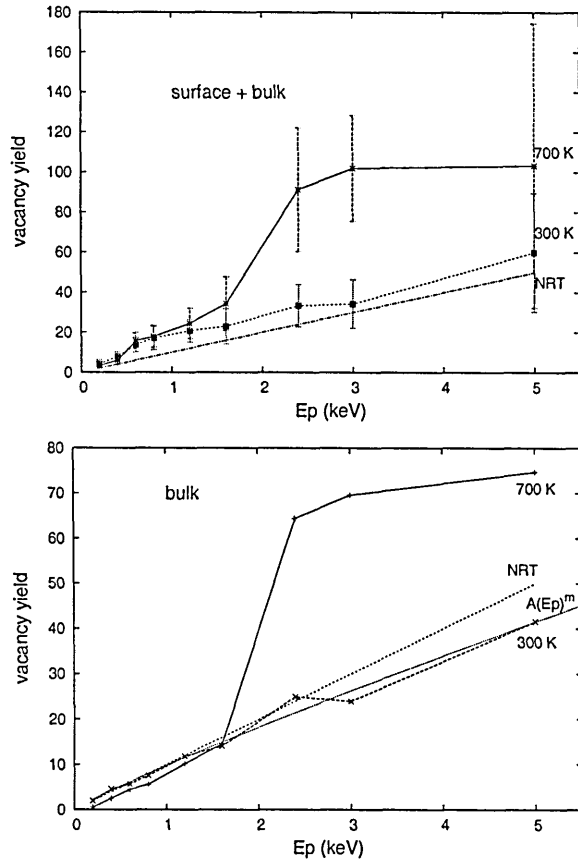
Figure 5.21: The number of surviving vacancies as a function of energy at temperature 300 and 700 K, with the value predicted by the NRT model in addition to the power law fit, involving all vacancies and also only bulk vacancies
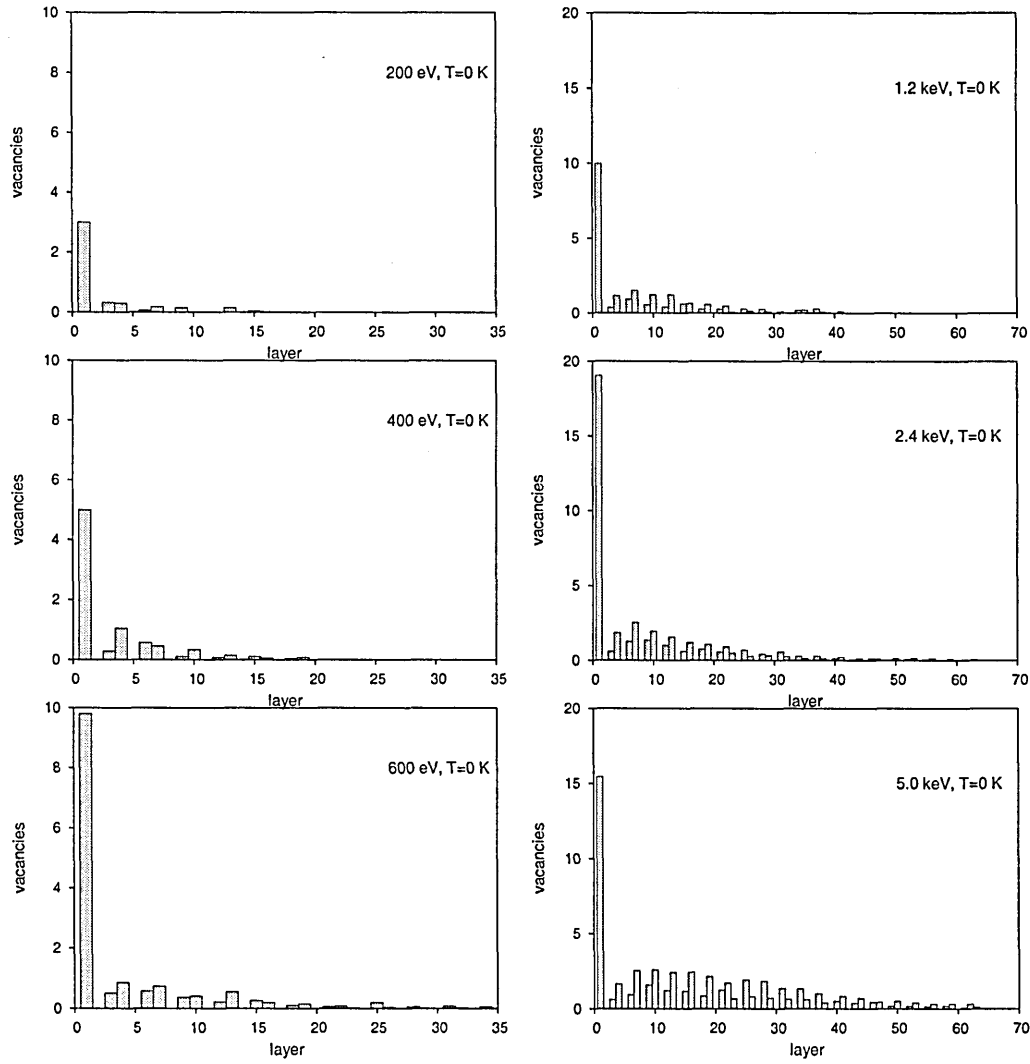
Figure 5.22: The depth distribution of vacancies at different Cr energy at temperature 0 K

5.4.2 Defect Distribution

The depth distribution of vacancies and interstitials is presented in Fig. 5.22 to Fig. 5.26 for different energy and crystal temperature. In Fig. 5.22 and Fig. 5.23 the vacancies assemble close to the target surface whilst an extended tail of the distribution arises as the energy increases. Note that the only difference on the vacancy profile as a function of the crystal temperature is the subsurface layer which appears to be depleted of defects at 0 K. In Fig. 5.24, a Gaussian like distribution of interstitials is observed with the peak distribution shifting farther along the depth as the energy increases. A similar

114
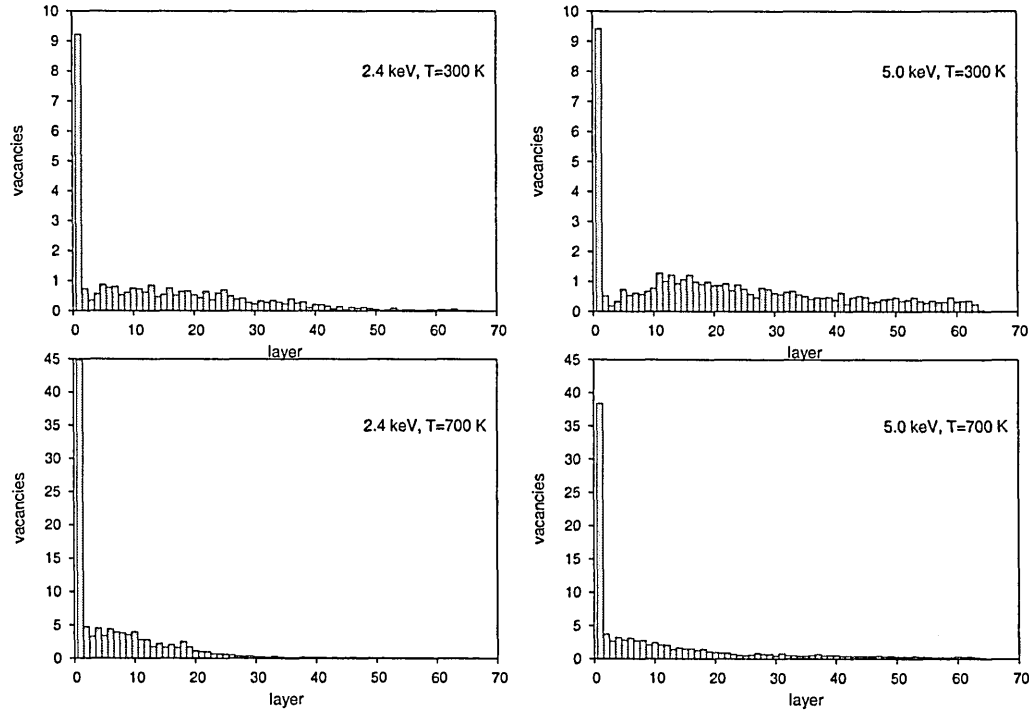
Figure 5.23: The depth distribution of vacancies at 2.4 and 5 keV impacts at temperature 300 and 700 K

profile is found in Fig. 5.25(b), Fig. 5.26(a) and Fig. 5.26(b) for the case of crystal temperature of 300 K, with a slightly broaden distribution at high energy. In contrast, the smooth decay with depth of interstitials in Fig. 5.25(c), Fig. 5.26(c) and Fig. 5.26(d) at crystal temperature 700 K is clearly a sign of temperature effect on recombination mechanism.

The difficulty in observing the separation between vacancies and interstitials from their depth distributions arises from the non-spherical shapes of the cascades near to a free surface and does not indicate inadequate annealing.

For sputtered particles and adatoms it is appropriate to analyse the depth origin since this is clearly an important quantity in surface science, where accurate composition depth profiles are required. Our MD simulations show that mostly the top surface atoms were sputtered. This is in agreement with experiments [248] of sputtering being mainly the result of collisions near the surface. Adatoms are originated from the three first atomic layers for all the cascades as in Ni bombardment [78].
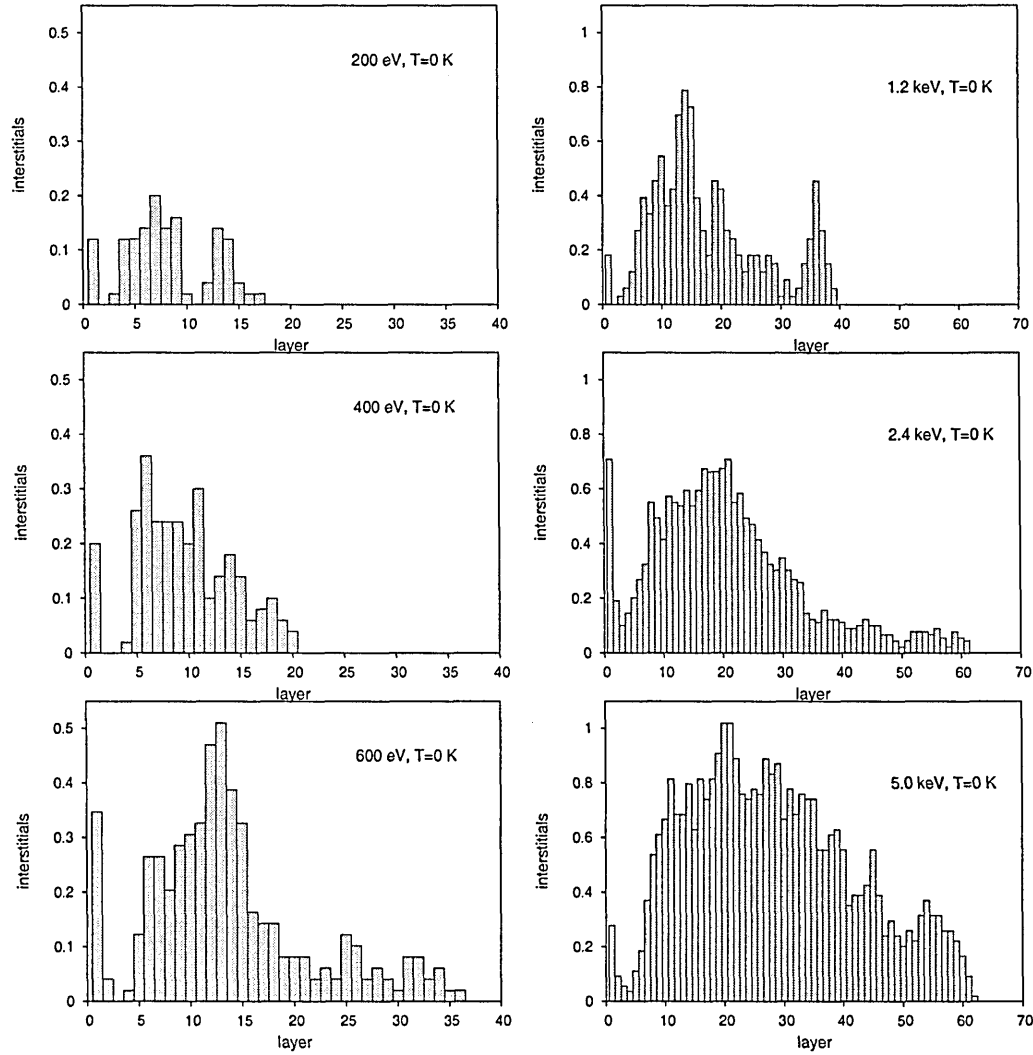
Figure 5.24: The depth distribution of interstitials at different Cr energy at temperature 0 K
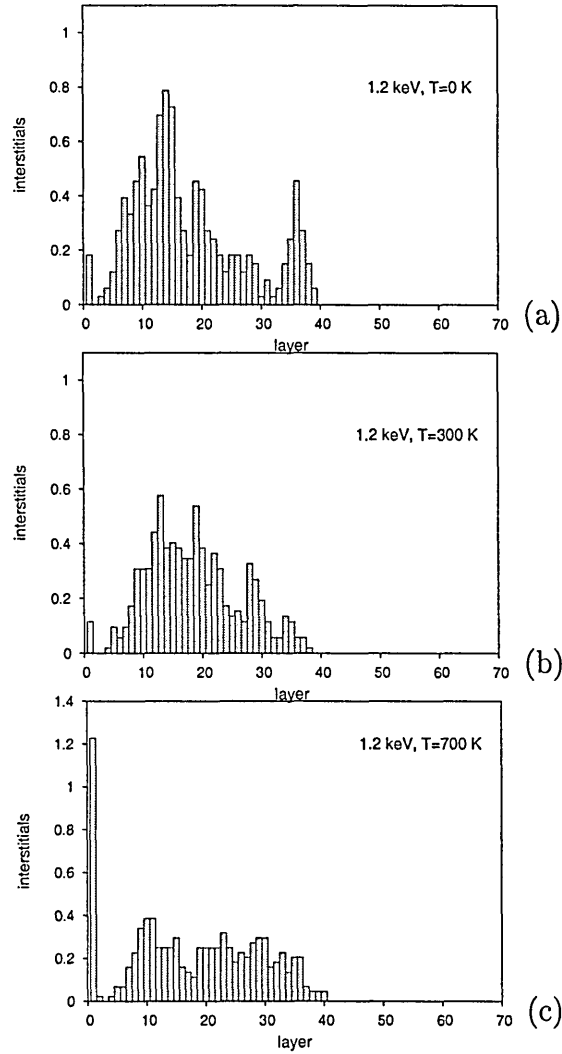
Figure 5.25: The depth distribution of interstitials at different temperatures for 1.2 keV

117
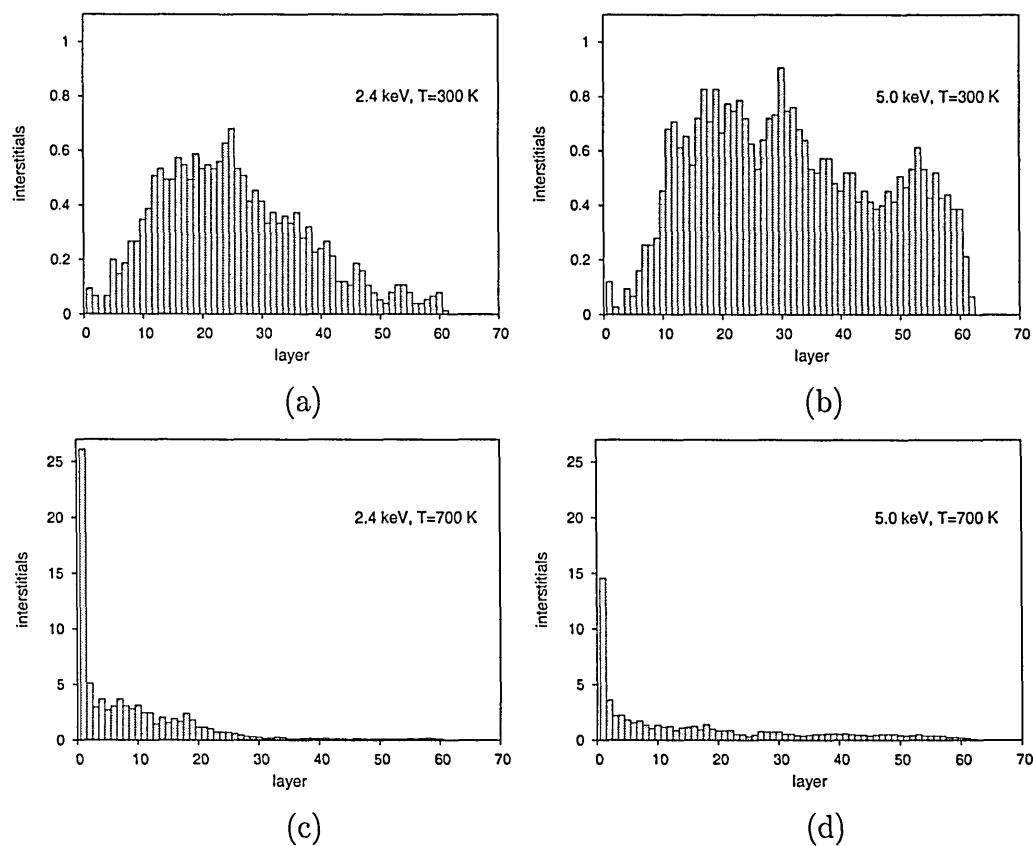
Figure 5.26: The depth distribution of interstitials at 2.4 and 5 keV impacts at temperature 300 and 700 K

Conclusion

Molecular dynamics simulations were carried out to investigate the phenomena occurring under bombardment of Cr ions on α-Fe crystalline target as a function of the impact energy and crystal temperature. The main conclusions to be drawn from the present study are relevant to the initial stages of damage formation in the bombardment of a perfect surface.

- sputtering yield increases with the energy of bombardment and the crytal temperature.

- the production efficiency for vacancies and adatoms is enhanced at crystal temperature of 700 K with a tendency in vacancy clustering.

- channelling increases with increasing energy above 1 keV and lowering temperature.

- vacancy production is higher than NRT efficiency, there is a large increase in the rate at which defects are generated near the surface compared to the bulk. Also, for energy below 1 keV the number of interstitials and bulk vacancies decreases with temperature as in a bulk damage

- the defects distribution shows a diffusive and smooth form at crystal temperature of 700 K with a short range compared to crystal temperatues 0 K and 300 K.

These conclusions reinforce the experimental choice of bias voltage and target temperature for achieving high etching rate. Even though high temperature is routinely preferred to stabilise the discharge system.

We believe that the temperature dependence on surface dynamic conditions via sputtering and defect is not negligible. Although, it has been considered not to affect the sputtering yield in polycrystalline target but in crystalline target the temperature effect is not negligible. Besides, the reported effect of temperature in single crystal on the enlargment of the spot related to the angular emission of sputtered species [249].

Chapter 6

The Directional Effects Of Bombardment

Introduction

Directional effects of bombardment arise either from variation of the projectile angle of incidence in situations where transport in an inert gas atmosphere causes scattering of metallic particles, or from rough surfaces where a local distribution of incident angles occurs. From measurements of surface topography, Kustner et al [250] found that at a nominal incidence angle 0°, the angular distribution broaden with its centre shifted to higher angle 38° while at incidence angle 80° the centre shifted to smaller angle 44°. The use of ion bombardment at different incidence angles with the aid of computer simulation has also allowed in addition to surface compositional information, structure to be obtained as metal overlayer systems [222, 251]. Directional effects are encountered in sputtering processes and it is of technological interest to know how sputtering and surface damage can be affected. This chapter examines the directional effects of Cr ion bombardment on crystalline iron at the energy and temperature of interest 2.4 keV and 700 K, respectively, and in the oblique and near grazing incidence. The results are tailored to make comparison with the case of normal incidence presented in the previous chapter.
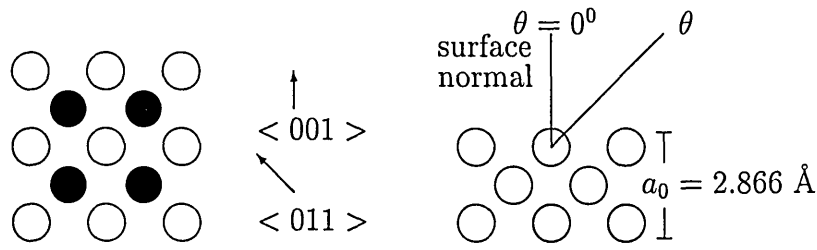
Figure 6.1: Incidence geometry for Cr on bcc Fe (100) surface: on the left hand side is the azimuthal direction (top layer atoms (open circle), second layer atoms (solid circle)), on the right hand side is the polar direction

6.1 Simulation Model

A single crystal of Fe(100) equilibrated at temperature 700 K was bombarded with Cr ion at 2.4 keV at an incidence angle θ ranging from 5 to 75 degree with respect to the surface normal. Two azimuthal ϕ directions $\langle 001 \rangle$,$\langle 011 \rangle$ were considered as shown in Fig. 6.1. Over 150 impacts were simulated for each incidence geometry and the results of sputtering and defects were analysed following the same criteria as in chapter 4. Clusters were identified in the flux of sputtered atoms at the equilibrium inter atomic distance 2.09 Å, which is the equilibrium bond length for Fe_2 dimer [252].

6.2 Bombardment characteristics

The maximum number of recoils or displacements N_d, occurring at a given time t_{peak} is shown in Fig. 6.2(a) as a function of the incidence angles θ and ϕ. The average number N_d increases then decreases with θ independently of the azimuth direction ϕ. Within the θ range 5°-30° the damage is slightly greater than the one at normal incidence, but then it starts to drop off at $\theta > 60°$. Note that the slope is steeper in the azimuthal direction $\langle 011 \rangle$ than in $\langle 001 \rangle$. The peak damage time in Fig. 6.2(b) is slightly longer for the damage to develop in oblique incidence compared to normal incidence at angle $\theta < 50°$. As θ increases the time shortens which correlates with the less damage induced. N_d and t_{peak} display similar trends towards the directional incidence geometry.
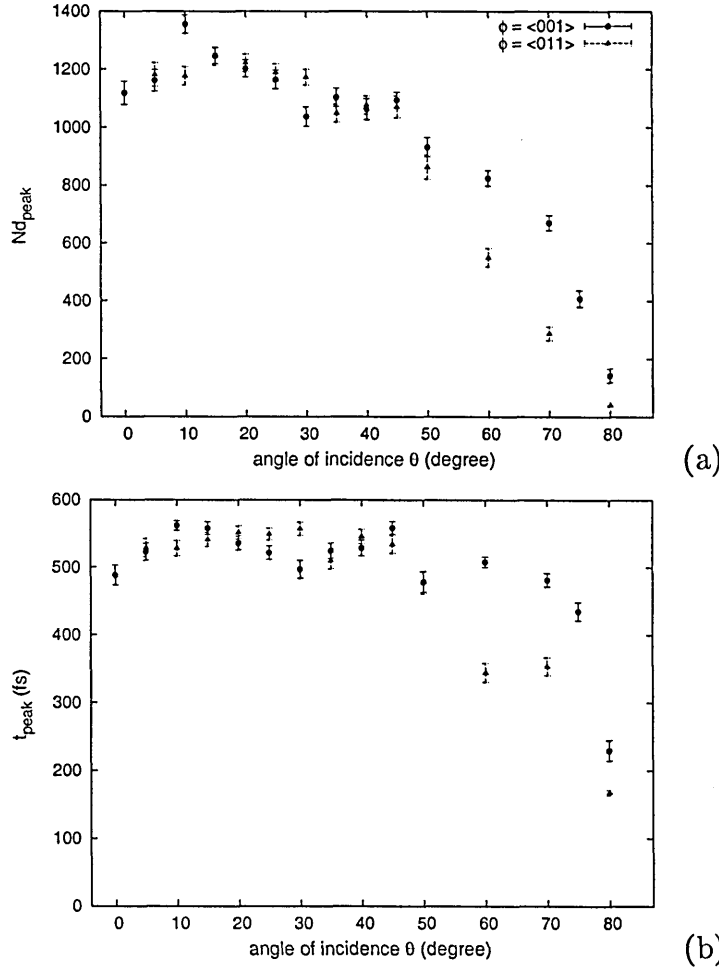
Figure 6.2: Peak damage (a) Nd_{peak} and (b) t_{peak} time versus the angle of incidence θ in the two azimuthal directions

6.3 Reflection and implantation

The fraction of Cr particles backscattered from the surface or implanted in the bulk is shown in Fig.(6.3). The reflection coefficient Rn (number of reflected projectiles/total number of projectiles) is less than 1 % in the θ region 5° to 50°, so it is a rare event and can therefore usually be neglected in front of the high sticking probability. The reflection of chromium steeply increases for θ above 50° at $\phi\langle 001\rangle$ and above 60° at $\phi\langle 011\rangle$. Thus, at some critical angle, ion implantation does not take place and the value of this angle depends on the azimuthal direction which defines the surface semichannel width [253]. In agreement with other work [23, 253, 254], the backscattering

122
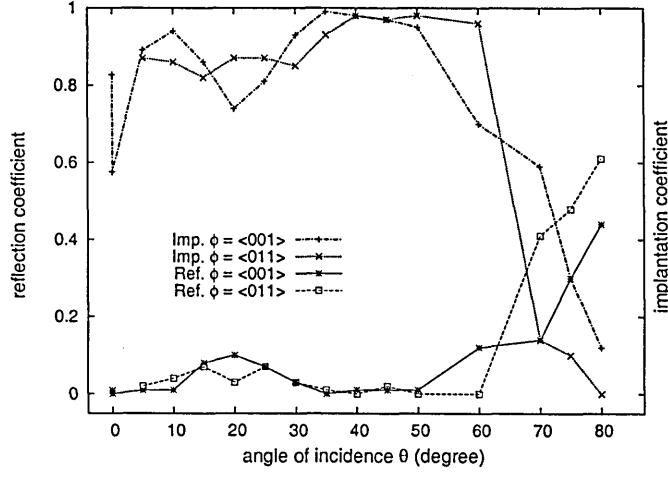
Figure 6.3: The particle reflection (Ref.) and implantation (Imp.)coefficient versus the angle of incidence θ and ϕ
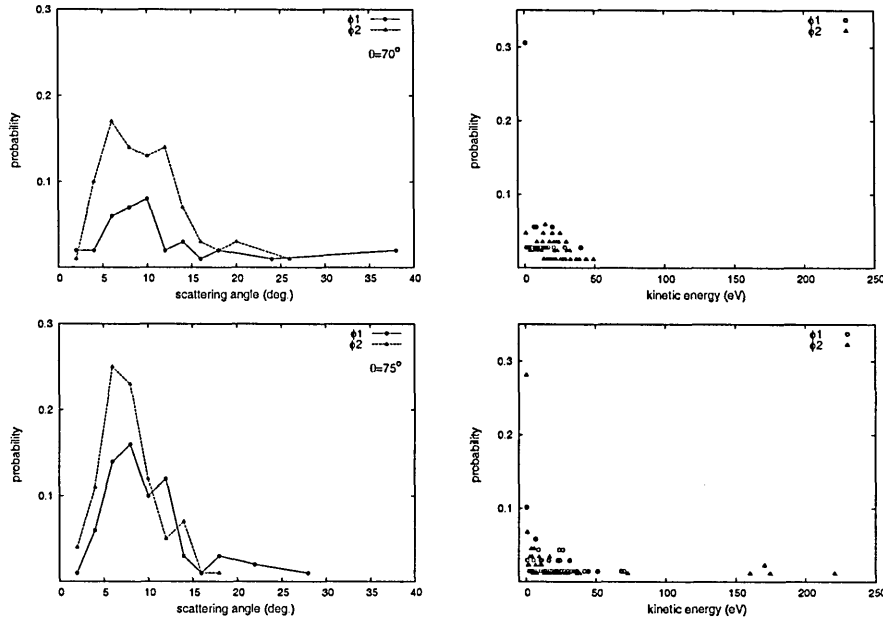
Figure 6.4: Angular and kinetic energy distributions of reflected Cr from Fe(100) surface at incidence angles θ : $70°, 75°$ and at $\phi_1\langle 001\rangle$ $\phi_2\langle 011\rangle$, respectively

coefficient is shown to be a universal function of the angle of incidence. The scattering angle (defined with respect to the surface) and kinetic energy distributions of reflected Cr are given in Fig. 6.4 for the two incidence angles $\theta = 70^0$ and 75^0. The backward scattering at $\theta = 70°$, occurs up to $38°$ and $26°$ for ϕ
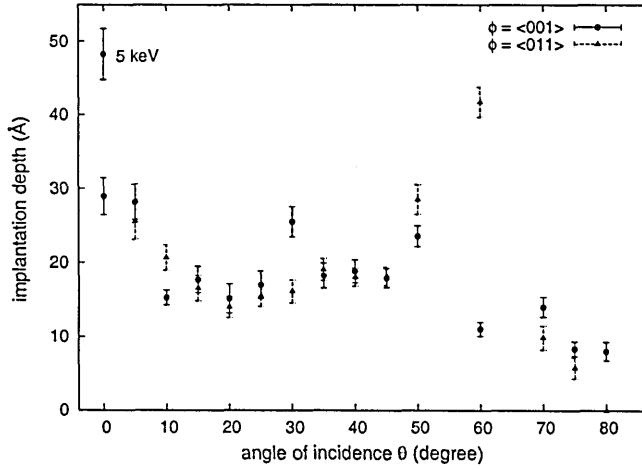
Figure 6.5: The particle implantation depth at energy of 2.4 keV versus the angle of incidence θ in the two azimuthal directions. The implantation depth at 5 keV is included

$\langle 001 \rangle$ and $\langle 011 \rangle$, respectively, while it is only up to 28° and 18° at $\theta = 75°$. The maximum probabilities are located at small angles (approximately 5-8°) and increases in the azimuthal direction $\langle 011 \rangle$ as well as θ increases. The highest energies of backscattered Cr is about 240 eV, only 10 % of its initial energy 2.4 keV. This is due to backscattering from subsurface atom and not directly from surface atom for which high reflected energy and forward direction of the backscattering are expected [23]. The average depth of implanted Cr varies with the incidence angle in Fig.(6.5). At incidence angles 10°, 30°, 50° and 60°, the effect of the azimuthal direction is discernable, substantially, at 60° and $\phi \langle 011 \rangle$, where Cr can be implanted far more deeply than at θ 0°. These cases can be interpreted by the opening of semi and true channels where the projectile encounter few collisions and so can penetrate more deeply before coming to rest. With the exception of these directions, the depth decreases with the incidence angle θ independently of the azimuthal direction ϕ and remains in general lower compared to the perpendicular incidence. So shallow implantation at high angles of incidence occured as a result of the projectile travelling a long distance above the surface with its momentum vector being prone to deflection into surface channels.
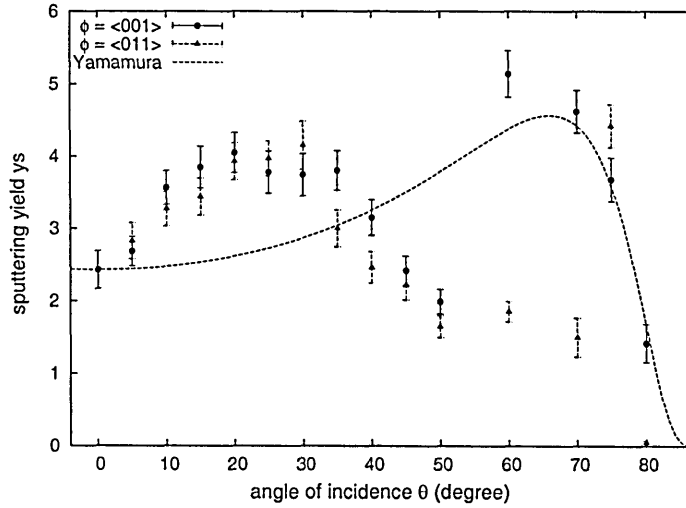
124

Figure 6.6: Sputtering yield versus the angle of incidence θ in the two azimuthal directions $\langle 001 \rangle$ and $\langle 011 \rangle$

6.4 Sputtering parameters

6.4.1 Sputtering yield

Fig.(6.6) shows the variation of the sputtering yield Y for Fe, as the projectile polar angle θ of incidence spans the normal to near grazing directions. The $Y - \theta$ curve has a numbers of peaks and troughs which are a common feature of crystalline targets [251, 255]. Peaks are located at θ angles θ 15° and 60° for the $\langle 001 \rangle$ azimuthal incidence, while at angles 30^0 and 75^0 for the $\langle 011 \rangle$ azimuthal incidence. The maxima could be associated to either the shadow cone yield enhancement model [255, 256] or on the basis of the relative number of ion interactions with atoms in the surface layers. Sputter yield minima or troughs are located at normal incidence and near 50° and near 70° for $\langle 011 \rangle$ azimuthal incidence. The minima arise because of projectile channelling effects. A similar number of maxima and minima was observed for other metallic surfaces [251] but it has been recognised that an increase in bombardment energy gives an increase in this number [255]. An important feature in the the $Y - \theta$ curve is attenuation of the sputtering yield at near grazing angle $\theta > 60°$ which can be explained by two mechanisms. First, at grazing incidence colli-

125

sion cascades are located so closely to the surface that backscattering prevents the cascade from developing fully resulting in a drastic reduction of low energy recoils atoms and thus a relative decrease in sputtering yield. The second mechanism is that the ion may be deflected from the surface by a mechanism similar to planar channelling (target surfaces that are sufficiently flat for the planar channelling mechanism to work).

We attempt to fit $Y - \theta$ for $\phi\langle 100 \rangle$ azimuthal incidence to the semi-empirical formula of Yamamura (Eq. (2.50) in chapter 2) for the angular dependence of the sputter yield. The fitted value of θ_{opt} is very close to the one calculated here. This formula may still agree at near glancing incidence for crystalline target although it was validated for polycrystalline and amorphous targets [250, 257]. In a polycrystalline material, the effects of the close-packed directions of each individual crystal are superimposed, the reason for the monotonic increase of the sputtering yield with the angle of incidence. The maximum sputtering yield of steels under oblique bombardment of Xe at 15 keV is measured at the incidence angle $\theta = 60^0$ [258]. The same high yield angle was observed at 2.5 keV Kr bombardment and self sputtering of nickel metal [259]. At very high Xe energy of about 100 keV the maximum of the sputtering yield is shifted to $\theta = 81^0$ [260].

The probability of sputtering simultaneously a certain number of atoms by a single impact is shown in Figure 6.7 for different bombardment geometries. This probability is also known as the emission statistics of Atoms per Single Impact (ASI). No huge event was detected and the largest emission is about 20 atoms corresponding to the high yield incidence angle. The ASI distribution contracts for low yield angle or the minima. So, enhancement of the sputtering yield at oblique incidence arises from collision events in which many atoms are ejected [261]. The ASI with zero yield, is no longer an important factor in oblique incidence as it is at normal incidence.

126

Figure 6.7:

The atoms-per-single-ion (ASI) distribution of sputtering for different bombardment geometry θ and $\phi_{1,2} :< 001 >, < 011 >$
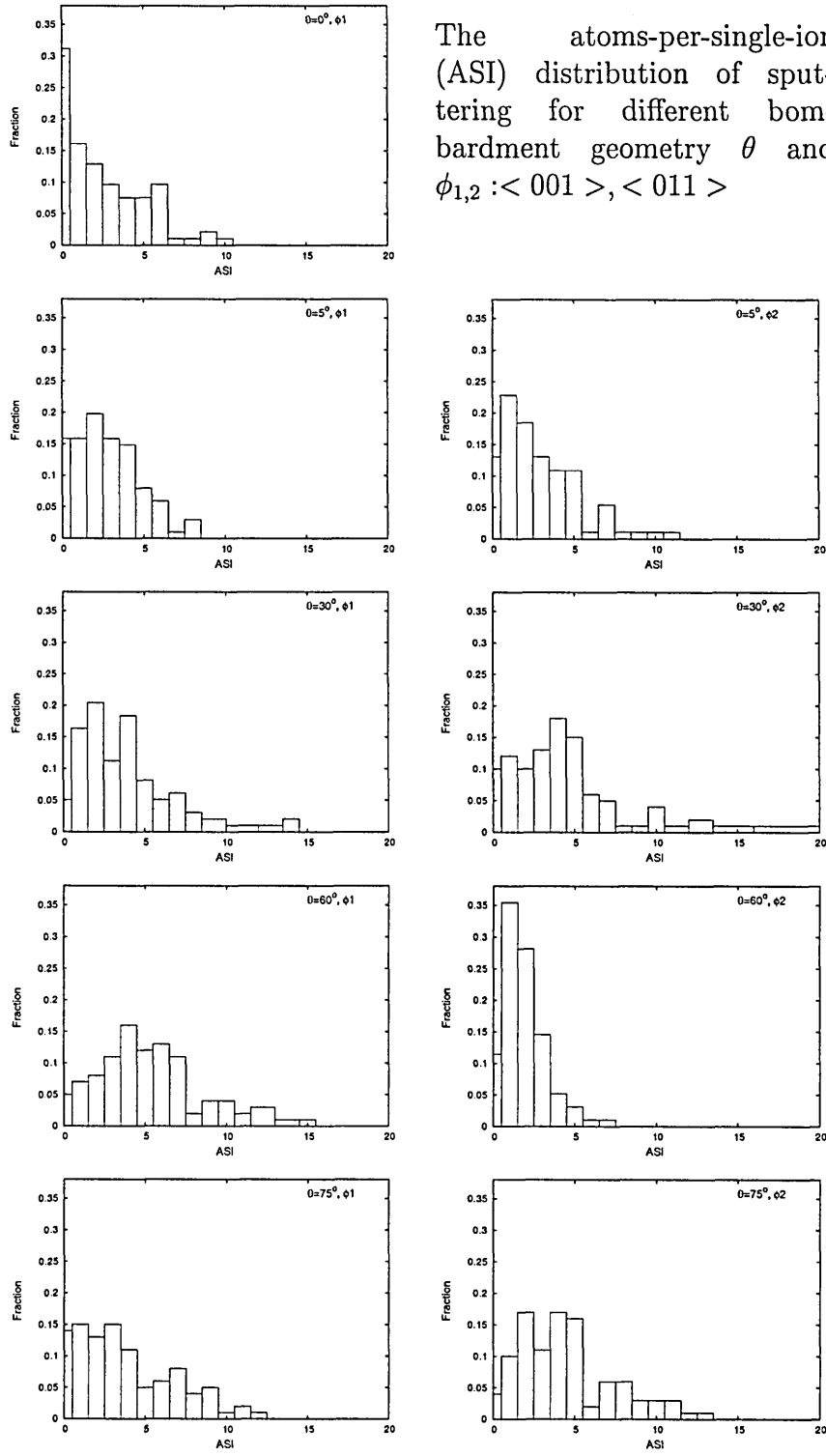
6.4.2 Cluster emission

The number of atoms sputtered ys_2 in a dimer bond state, per impact versus the incidence angle is shown in Fig. 6.8. The dimer yield ys_2 variations broadly track those of the total sputtering yield. Since more dimers are formed at high yield angles, this indicates that the probability of clustering grows with the number of sputtered atoms. The trimer yield varies between zero where no trimers are formed to 0.12. Trimers are more probable to form at high yield angles, however, no trimers are found at high yield angle $\theta = 75^0, \phi\langle 011\rangle$ this can be due to the surface origin of trimer constituants which constraints the trimer geometry formation. The sputtered dimer polpulation is abundant compared to the trimer population which is in agreement with experiment and other simulation for keV bombardment of metal surface [262–264]. Although, we looked for higher clusters which may have formed in the sputter process most well fragment at times larger than those considered here. Note that the largest cluster detected in all our simulation is Fe_6. The mean separation distance of origin of the constituant atoms of dimers is the first and second neighbour distances and there is no systematic effect arising from the variation of projectile incident angle.
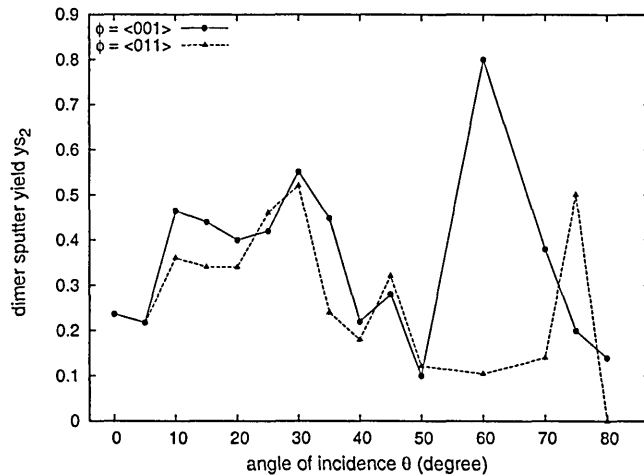
Figure 6.8: Sputtering yield of Fe dimers versus the angle of incidence θ in the two azimuthal directions

(a)

(b)
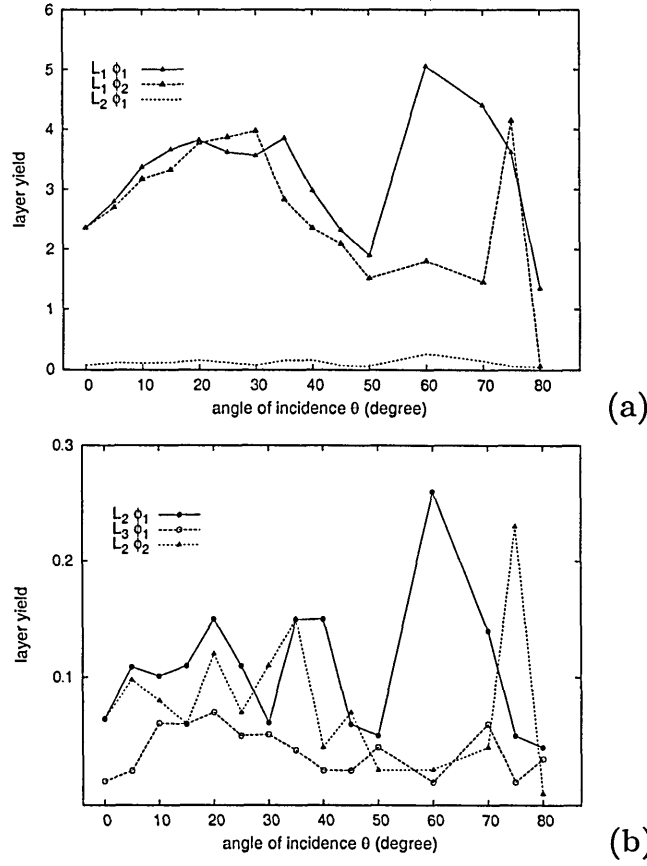
Figure 6.9: Dependence of the layer yield L_n on incidence angle θ in the azimuthal directions $\phi_1\langle 001\rangle, \phi_2\langle 011\rangle$

6.4.3 Escape depth

A useful measure of the depth of the crystal layer from which the sputtered atom originated is the layer yield L_n. The first, second and third layer yield are examined since fourth layer and beyond are usually zero. Fig.6.9 shows L_1, L_2 and L_3 for the azimuthal directions $\phi\langle 001\rangle$ and $\langle 011\rangle$ as a function of the polar incidence angle θ. In Fig.6.9(a) L_1 displays angular variations which match broadly the total sputtering yield shown in Fig.6.6, whereas L_2 is several order of magnitude smaller than L_1 (this result also applies for L_3 which is not shown). When presented separatly in Fig. 6.9(b), the evolution of L_2 resembles that of L_1 but L_3 is almost constant. Under all bombardment geometries, most of the sputtered atoms come from the surface layer of the target, and essentially all of the remainder come from the second layer. L_2 never exceeds L_1 and 50%

129

change in L_2 values is only a 5% change in L_1. It was predicted that the more opaque bcc (111) targets exibit significantly smaller mean depths of origin than the corresponding bcc (100) but yet the majority of sputtered atoms come from the first atomic layer [265]. Surface layer makes significant contribution to the total sputtering yield and this contribution varies systematically with projectile incident angle.

6.4.4   Emission angle

The polar angle distribution integrated over azimuthal direction of sputtered atoms is shown in Fig 6.10. In all incidence geometries the angular distribution is a cosine distribution as reported in the keV region [266] Note that at incidence angle $\theta = 60$ and $\phi < 001 >$, the distribution tends to be less anisotropic compared to the rest. Spots occur around the $< 111 >$ ejection direction which happen to be the directions of closest packing in a body-centered cubic structure or also know as the easy exit. The average energy of sputtered atoms at various projectile incident angles is shown in Fig. 6.11. The significant decrease at angles near grazing is due to the increase of the reflection which led to the decrease of the energy deposited into the surface. Note that the energy carried by sputtering at 5 keV is of the same order to that at 2.4keV at near grazing angle. Note that, no systematic change of the energy distribution of sputtered atoms for oblique incidence was observed. This is more visible for sub keV region [267, 268] or from oblique cluster bombardment [266].
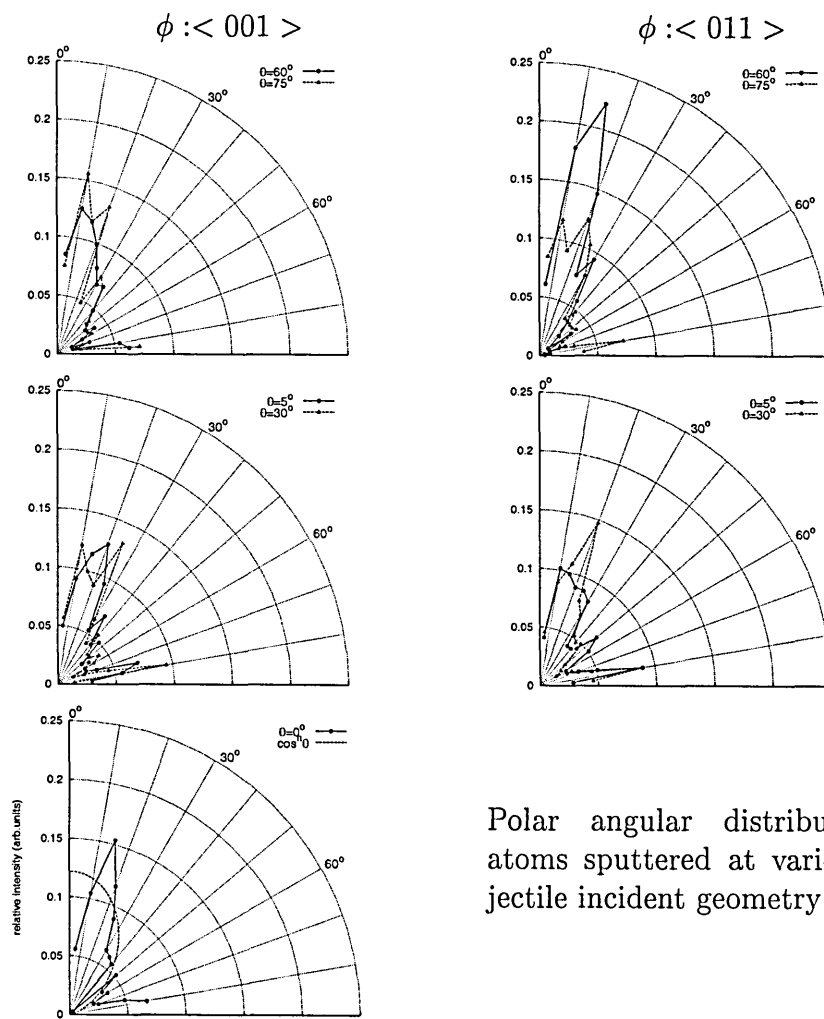
Figure 6.10:

Polar angular distribution of atoms sputtered at various projectile incident geometry
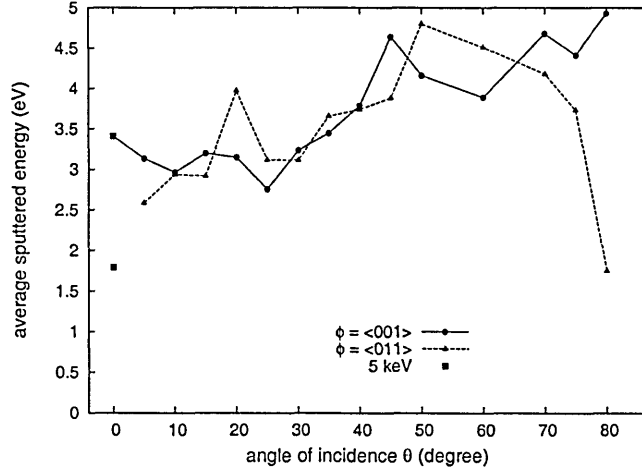
Figure 6.11: Average emission energy versus the angle of incidence θ in the two azimuthal directions

6.5   Defect yields

The average yields of stable defects are displayed in Figures 6.12 and 6.13 as a function of the projectile incidence angle θ for each of the azimuthal directions ϕ $\langle 001 \rangle$ and $\langle 011 \rangle$. In Fig. 6.12(a) the maxima in the surface vacancies and adatoms both arise at $\theta = 20^0, 60^0$ for azimuthal $\langle 011 \rangle$ and at $\theta = 30^\circ, 75^\circ$ for $\langle 001 \rangle$. The maxima location correlate well with the sputter yield maxima. Variation of surface vacancies substantially affects adatoms. The same trend is observed in Fig. 6.12(b) for the total number of vacancies but is less accentuated because large bulk vacancies mask surface vacancies variation. For interstitials the yield consists of a background which slightly increases at $\theta > 70^\circ$.

Atom relocation from their lattice sites to other lattice sites shown in Fig. 6.13 is more effective in the region $\theta < 30^0$. A considerable decrease of relocation towards more oblique incidence occurs at rapid rate in the azimuth direction ϕ $\langle 011 \rangle$. There is an obvious resemblance between displacement in Fig. 6.2 and relocation in Fig. 6.13 since this derived from those permanent displacements to lattice sites.

Fig. 6.14 displays the depth dependence of replacement for oblique and perpen-
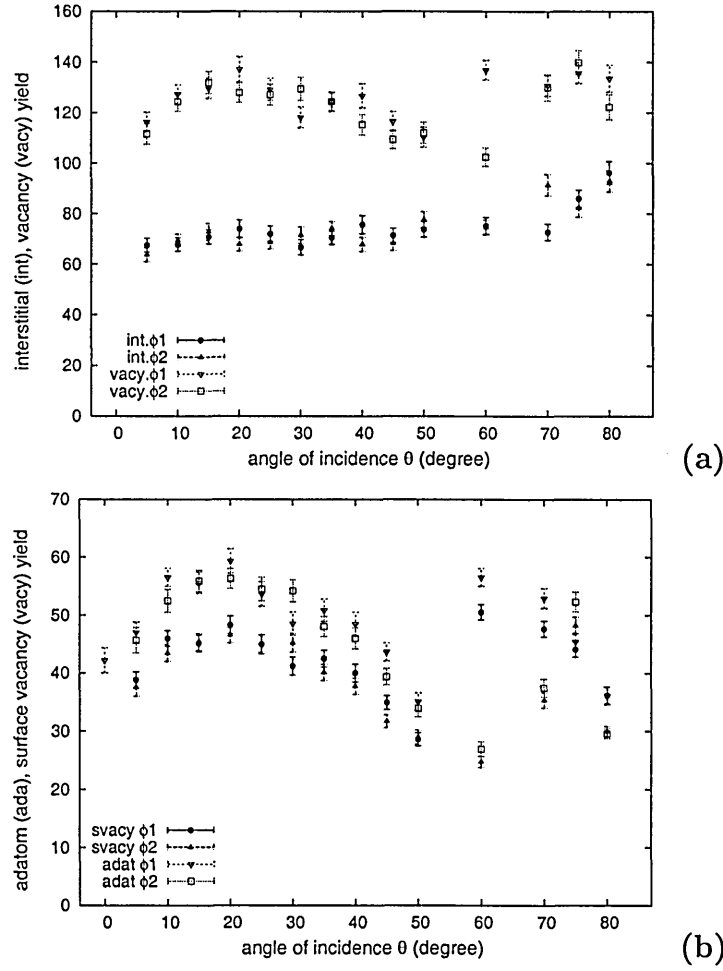
Figure 6.12: Defect yield versus projectile angle of incidence θ in azimuthal directions $\langle 001 \rangle, \langle 011 \rangle$: (a)interstitial and vacancy, (b) adatom and surface-vacancy

dicular incidence at $\phi \langle 001 \rangle$ and $\langle 011 \rangle$. The normalised distributions narrow when θ increases irrespective of the azimuthal direction so damage quickly come close to the surface [269]. However, in Fig. 6.14(b) the distribution at incidence angle $\theta = 60°$ exhibits a Gaussian like form and surpasses the distribution at perpendicular incidence. This buried relocation is simply a consequence of projectile channelling. Note that for all incidence geometries relocation remains strong at the surface.
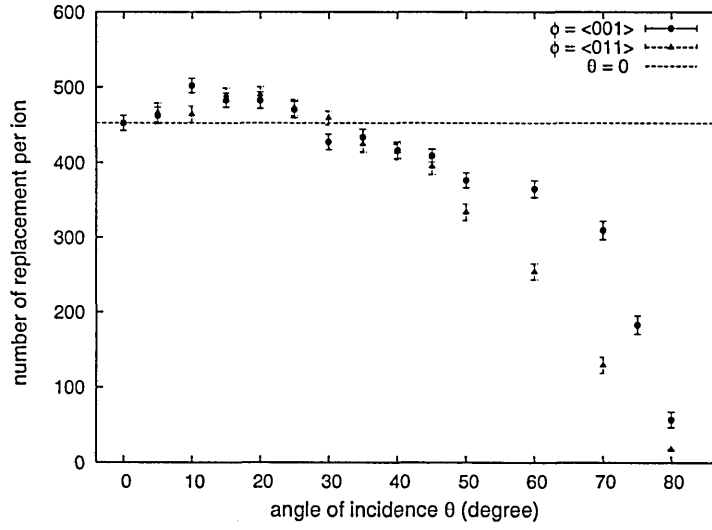
Figure 6.13: number of replacement (relocated atoms) versus the angle of incidence θ in the two azimuthal directions $\langle 001 \rangle, \langle 011 \rangle$

(a)

(b)
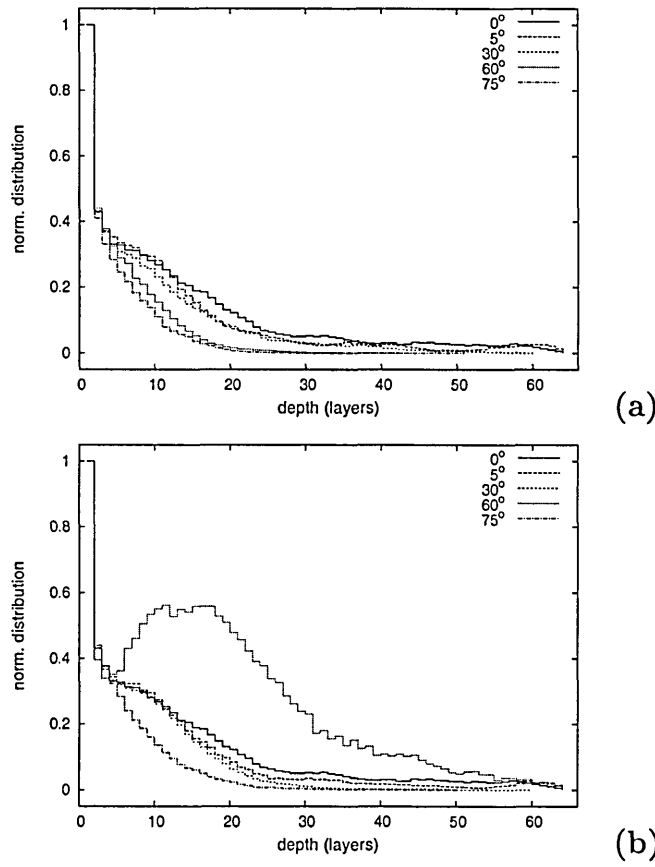
Figure 6.14: depth profile of replacements sites for different angle of incidence θ in the two azimuthal directions: a)$\phi\langle 001 \rangle$,b) $\phi\langle 011 \rangle$

134

$\theta = 5^0 \; \phi < 001 >$

$\theta = 20^0 \; \phi < 001 >$

$\theta = 60^0 \; \phi < 001 >$

$\theta = 60^0 \; \phi < 011 >$

0.25ps   0.50ps   1.00ps
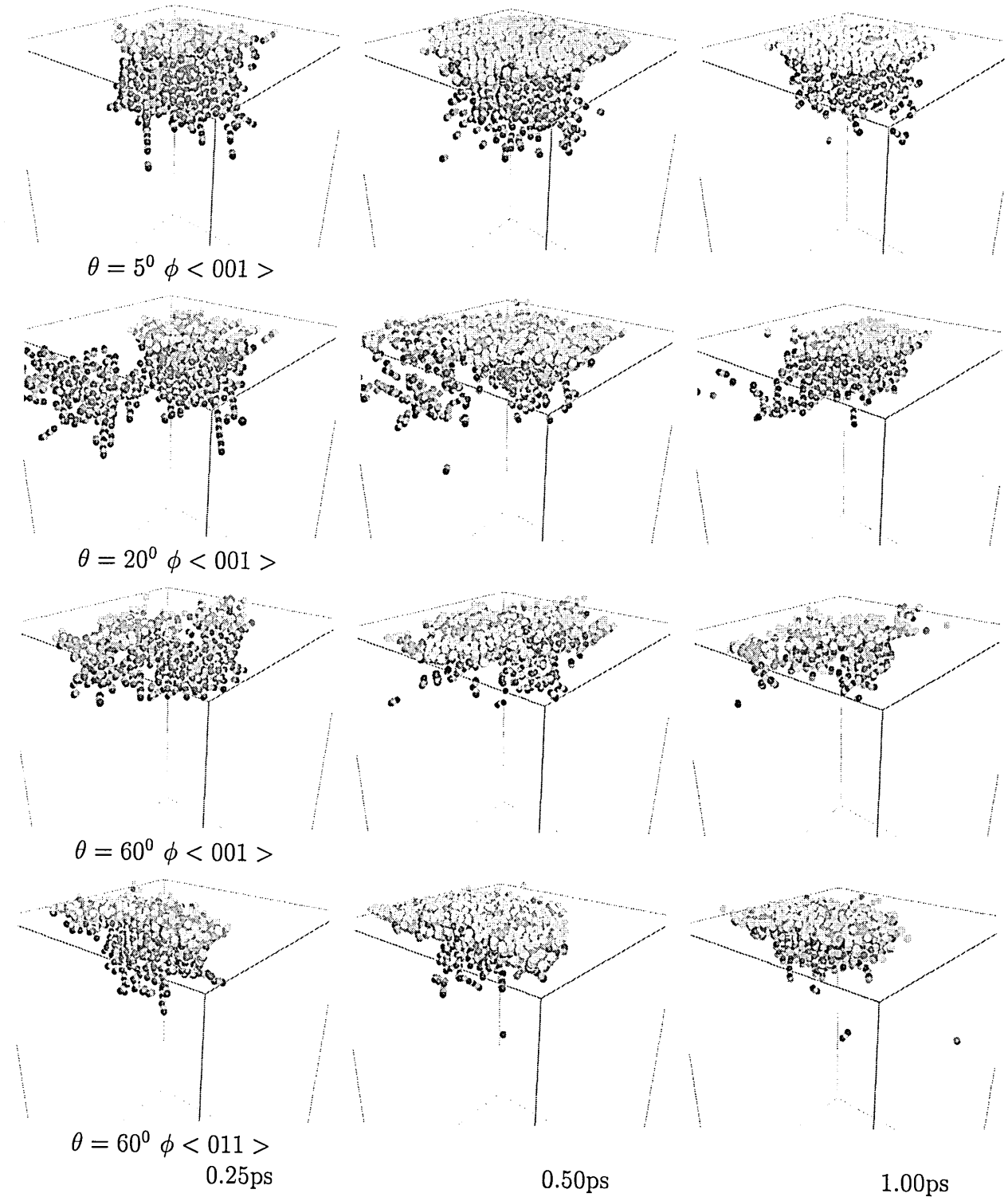
Figure 6.15: Sequence of snapshot at 0.25 ps, 0.50 ps and 1 ps for cascade generated by Cr 2.4 keV at different incidence geometry

135

6.6   Cascade evolution case study

To gain an insight into how the ion in an oblique incidence trigger a cascade of recoils or atoms being displaced from their original lattice, we examined here by visualisation of the cascade evolution for two cases of low ($\theta = 5°, 20°$) and high ($\theta = 60°$) oblique incidence (Fig. 6.15). In the first case, at small oblique incidence angle, the cascade structure preserves the conical shape as in normal incidence independently of the azimuthal direction. In the second case, at large oblique from the surface normal, the cascade is shallow with no particular shape. However, the change in the azimuthal direction has allowed the cascade to propagate deeper in the crystal as shown at the final stage where defects survived up to few layers deep. The damage induced at oblique bombardment tends to be close to the surface.

Conclusion

We have examined the directional effect in the bombardment of Fe(100) surface at temperature 700 K, with 2.4 keV Cr projectiles. The sputtering yield of Fe is predicted to display a strong dependance on the projectile polar angle of incidence θ as well as the dimer yield. A factor of two enhancement in the yield is observed at low oblique angles θ : 20° and 30° and at near grazing angles θ : 60° and 75° where the maximum is attained. The empirical angular sputtering formula can be used to predict sputtering for single crystal at near grazing incidence since crystalline details are less exposed to the projectile The implantation and reflection of Cr atoms varies in reverse with projectile incident angle and the critical angle for total reflection varies with the azimuthal incidence. No specular or superspecular reflection occurs. The susceptibility of crystalline target to channelling is dependent on the projectile direction.

Chapter 7

Ion Species Effects on Bombardment of Fe

Introduction

In the present chapter, we investigate the effect of different ion species of varying mass, on the sputtering and damage production in a single crystal Fe. We consider the case of inert gas ion and metallic ion bombardment at an impact energy of 2.4 keV and target temperature of 700 K . The motivating factor for carrying out these simulations is to understand the experimentally observed behaviour following surface etching process of steels with different transition metals Nb, V and Ti in addition to inert Ar gas [19]. It was shown at the nanometre scale by AFM [1] imaging and at the micron scale by optical micrographs that the development of structures within the individual single crystalline grains is typical of surface erosion in a polycrystalline target. Although such features are not found for Nb and Ti ion bombardment of steel surfaces, this has been attributed to less material removal.

The second focus of this chapter is the size of the projectile, ultimately related to the projectile nuclearity where several atoms are used as projectile species. In a series of experiments with polyatomic bombardment, a great increase of

---

[1] Atomic force microscopy

137

the total sputtering yield with respect to monoatomic projectile was observed [270,271]. In some cases the nonlinear enhancement of the sputtering yield was large whereas in other cases, it was only slight or non-existent when switching for instance from monoatomic to diatomic projectiles. Furthermore, the non-linear effect has a complex behaviour in its dependence on the incident energy and incident particle type. In this respect, we investigate the possibility of a diatomic Cr_2 projectile at energy 1.2 keV and 2.4 keV per atom, to create favorable conditions for non-linear enhancement of both the total and cluster yield for Fe substrate.

7.1   Gas and Metal Bombardment

7.1.1   Simulation Model

The simulation model considered here is the same as in previous chapters. The bombardment is at normal incidence using different ion species from metals to inert gases. For metallic ions we have substituted the Cr mass by relatively light and heavy metals like Ti, Fe, Cu and Nb. The interaction of these ions with Fe target is taken to be the same as the Cr interaction in order to separate artificially the mass effect with the change in the atomic number from the potential function. For inert gases of varying mass, we have considered the following noble gases Ar, Kr, Xe for which a purely repulsive interaction potential is subscribed. The Fe crystallite equilibrated at 700 K was exposed via the irreducible zone impact to over 150 projectiles from each ion species and for a simulation time of 10 picoseconds per projectile.

7.1.2   Sputtering yield

The average total sputtering yield Y_s of Fe obtained in our simulations by noble gas and metal ions bombardment is depicted in Fig. 7.1. The sputtering yield increases with the ion mass for noble gas showing a reasonable agreement with
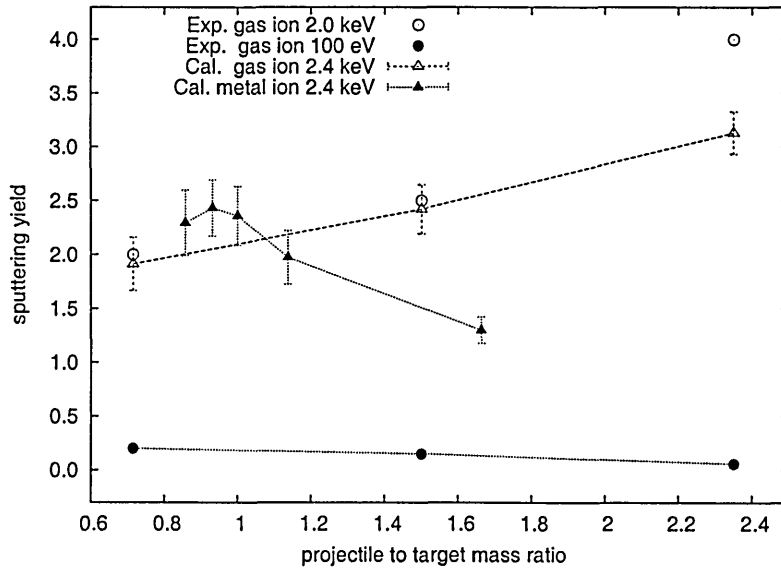
Figure 7.1: Fe sputtering yield versus projectile to target mass ratio. Experimental yield by noble gas bombardment at eV and keV energy (Ar and Kr at 2 keV while by Xe at 3 keV keV)is included. The dashed line and dotted line are guide to the eye.

experiment. In contrast, it decreases for metal projectiles from a maximum value at mass ratio near one, no experimental data were available for this case. Worth noting in Fig. 7.1 that the ion mass effect is reversed for noble gas at low energy i.e. 100 eV. Thus noble gas mass effect on sputtering can be positive, negative or even neutral depending on energy. In ref [272], it was shown from experiment that the gas sputtering efficiency for light ions is low compared to more massive inert ions. Also the sputtering efficiency variations with the discharge gas as Xe < Kr < Ar in the low energy regime, shows that the mass effect is negative [273]. Various etching chracteristics are found to depend evidently on the mass of the gases [274]. The experimentally measured sputtering yield of Fe cathode by neon plasma is four times higher than that by nitrogen plasma despite the similarity of the energy flux characteristic of both plasmas [275]. This lowering of the sputtering for nitrogen was related to mass as well as to the reactive nature of the gas responsible on backdeposition of sputtered material on the cathode [275].

139
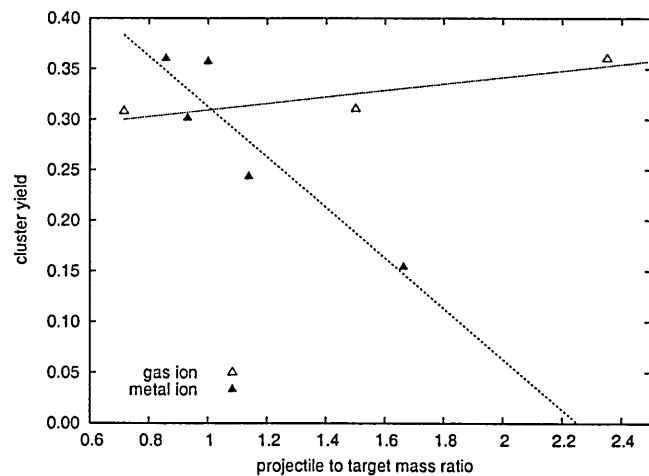
Figure 7.2: Fe cluster sputtering yield versus projectile to target mass ratio. Lines are to guide the eye.
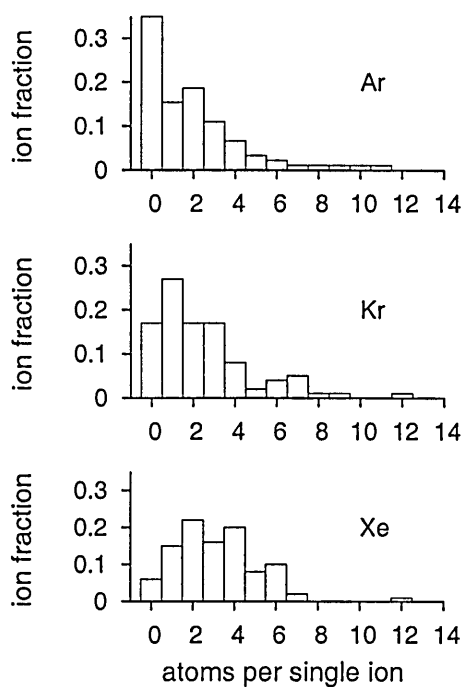
Figure 7.3: ASI distribution for gas bombardment

The yield of sputtered clusters in Fig. 7.2 follows the same trend as the total sputtering yield, so the probability of clustering increases with the sputtering yield. Moreover, the number of atoms sputtered per ion (ASI) that cannot be measured experimetally is shown in Figures 7.3 and 7.4 for gas and metal ion.

140

The ASI distribution can extend to around five or four times the average yield. There are also trajectories along which an ion channels and deposits its energy deep within the crystal ejecting no particle (ASI = O). Chanelling decreases remarkably for heavy noble gas ion while it remains important for metal ions. Also the peak of the distribution shifts to higher ASI for increasing gas mass while the tail contracts to lower ASI for increasing metal mass.

In Fig. 7.5, the ratio of the sum of adatoms and sputtered yield to the yield of surface vacancy is greater than unity, evidence of subsurface layers contribution. However, 95 to 98 % of sputtered atoms originate from the surface layer, thus the sublayer contribution is due mainly for adatom yield which show a significant increase with gas ion mass. In an elemental target the mass effect on sputtering is significant and it can be more important in compoud targets causing preferential sputtering of the light component, as reported for nitride sputtering with component mass difference, especially at low energy [276]. Experiment and simulation of rare gas bombardment of Pt(111) [262, 277] have shown similar trends of the dependance of sputtering yield on ion mass, as calculated here for Fe metal.
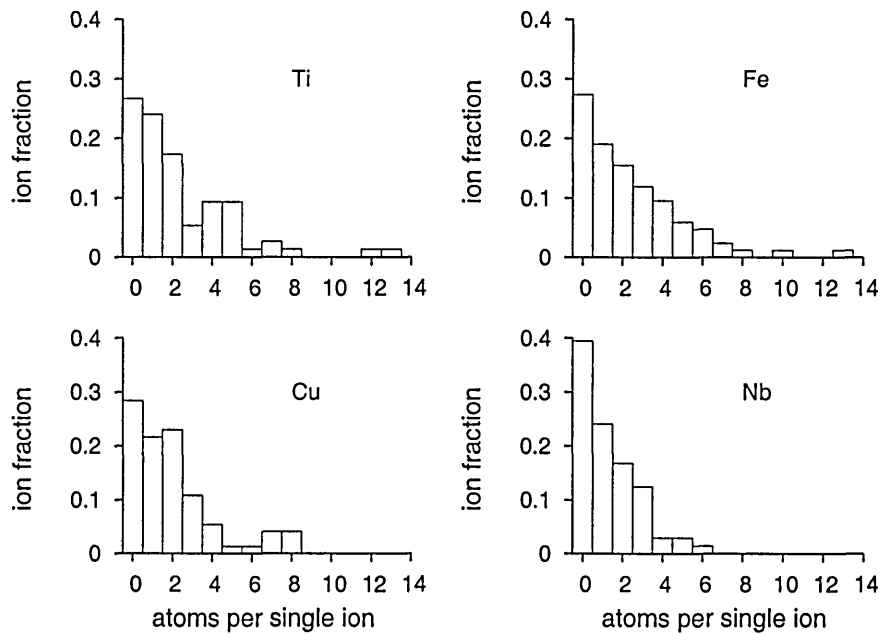
Figure 7.4: ASI distribution for metal bombardment
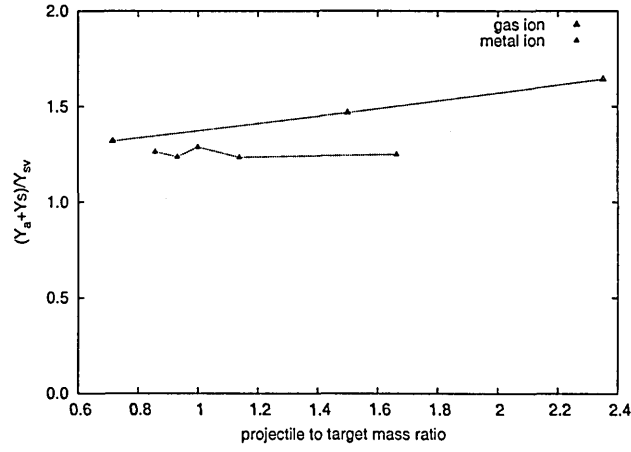
Figure 7.5: Ratio of the sum of adatoms and sputtered yields to the yield of surface vacancies for rare gas and metal ion bombardment

7.1.3 Defects distribution

We plot in Figures 7.6 and 7.7 the depth distribution of the defects formed by metal and noble gas bombardment, averaged over all trajectories.
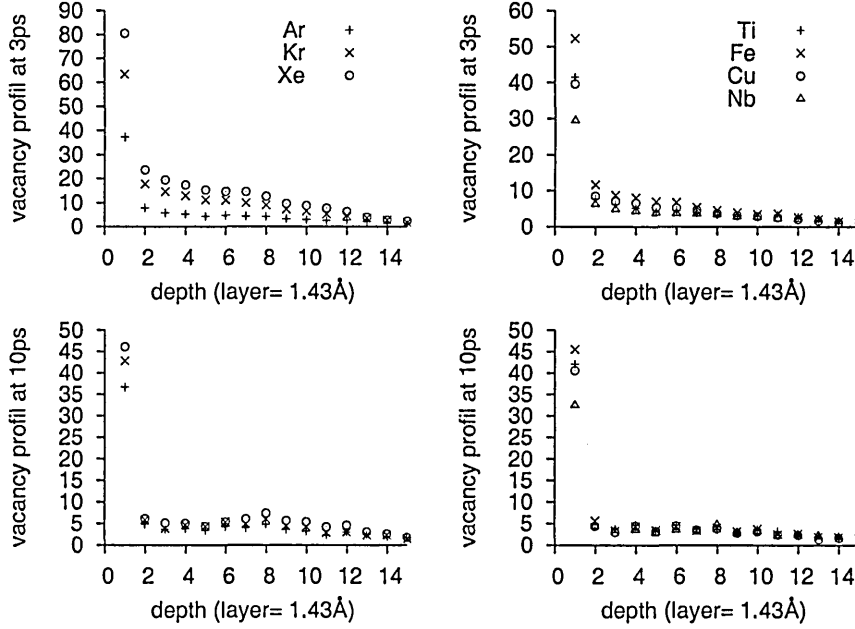

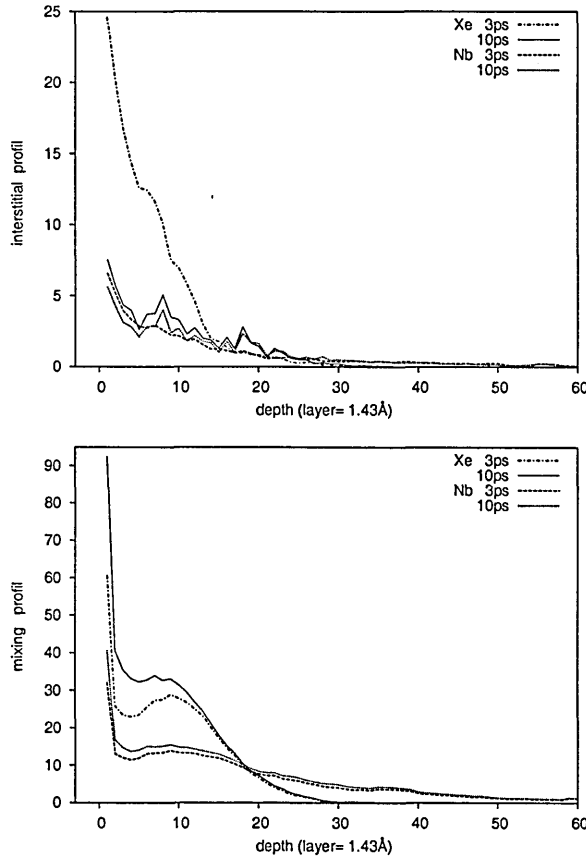Figure 7.6: Depth profile of vacancies in Fe by metal and noble gas bombardment

Figure 7.7: Depth profile of interstitials (a) and mixed Fe atoms (b) produced by metal and noble gas bombardment

Most of the defects are found in the first layer or surface layer rather than in the bulk. This layer is adjacent to the zeroth layer where adatoms sit.

In Fig. 7.6 (upper panel) the heavy gas ion Xe produced the highest number of surface vacancies while the heavy metal ion Nb produced the lowest value. Such a number of vacancies decreases with time in Fig. 7.6 (lower panel) where it has fallen by approximately the same amount for both ion species. For Xe the mass effect is sensed at the early stage of the collision within the time scale of sputtering event. By considering the two heavy species Xe and Nb, the interstitials shown in Fig.7.7.a exibit the following behaviour: they are five to three times higher for Xe impact than for Nb impact over the first ten layers of the Fe crystal at time 3 ps and then the two distributions converge by 10 ps. Their range is approximately three times the range of the vacancies.

In Fig. 7.7.b the profile of replacement is shallower for gas impact while it can extend furthermore for metal impact. This results in a strong mixing in the first layer for gas impact in addition to a local maximum at about the tenth atomic layer with increasing value with respect to the gas mass. Such a feature is not apparent for the metal impacts. Experimental ion beam mixing at metal-oxide interface induced by noble gas Xe is higher compared to Ar, Kr for the case of silicon [278]. Note that interstitials at the surface and subsurface layer equilibrated to a lower value while local mixing increases this can be understood by vacancy-interstitials recombination rather then interstitial migration to adatom layer.

At a fixed kinetic energy, the depth distribution of defects appears to be dependent on the species of the ion initiating the damage event rather than on the ion mass.

7.1.4   Ion range and profile

Figure 7.8 illustrates the projected and lateral range (known also as depth and spread, respectively) of implanted ion as function of projectile to target mass ratio. In Fig. 7.8.a the lateral spread decreases with increasing ion mass for both metal and inert gas ions. This is in agreement with the intuitive picture that heavy ions will undergo small deviations. The magnitude of the deviations is higher for metal ion than inert gas ion.

The average depth of penetration is sensitive to ion species as demonstrated in Fig.7.8.b. It increases for metallic ion while it decreases for noble gas ion. This decrease is shown by the implantation depth profile of gas ion in Fig.7.9, where the profile becomes more shallower with a pronounced gaussian like form for heavy gas ion. It was shown by bombardment of several ion species He, Ne, Ar, Kr and Xe at low energy that the sticking coefficient at low energy is mass dependent [279]
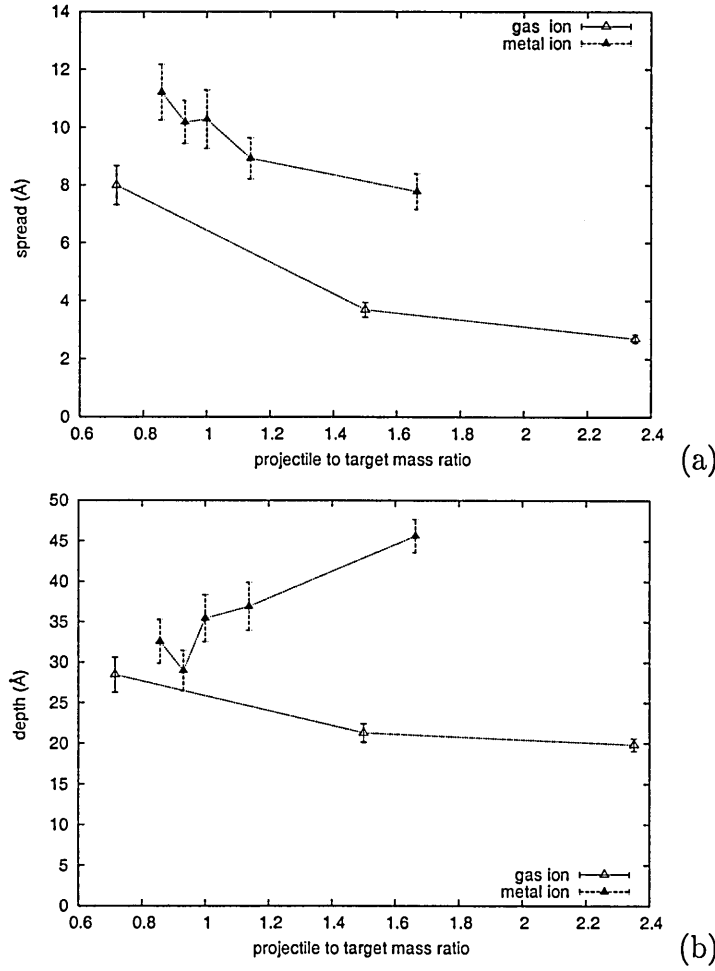
Figure 7.8: Average spread (a) and depth (b) of implanted metal and noble gas ions in Fe

7.1.5 Cascade evolution

An important property of a cascade is its density which is described by the maximum number of displaced atoms. The effect of projectile mass on the cascade is elucidated in fig. 7.10 where the average number of displaced atoms at the peak damage time (about 0.5ps) is greater for gas impact compared to metal impact and the trend of the curve demonstrates a positive mass effect for gas bombardment in contrast to metal bombardment.

Figures 7.11 and 7.12 show the temporal evolution of the cascade of displaced atoms induced by different ions species at the same impact zone on Fe crystal at temperature 700 K. In the early stages of the cascade, the volume of the
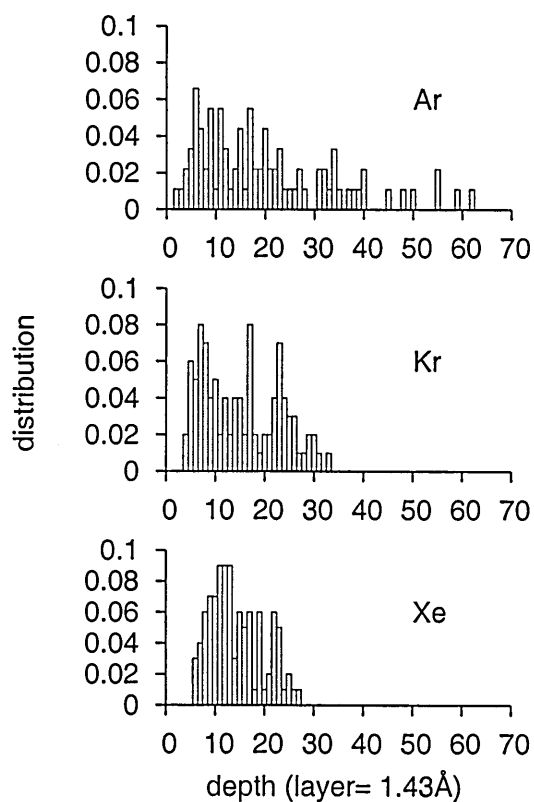
Figure 7.9: Depth profile of implanted noble gas ions in Fe
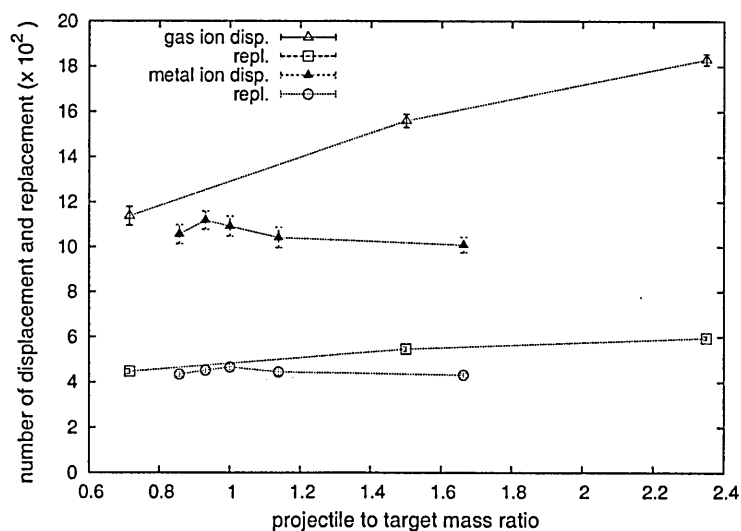
Figure 7.10: Mean displaced atoms at peak damage (filled) and mean replacement (non-filled) at equilibrium as a function of target to projectile mass ratio

146

cascade shows a slight increase for both heaviest gas and metal ions. However, the shape of the cascade is independent of the ion mass in contrast to its strong energy dependence (see chapter 5) since here the energy is constant.

Back again to Fig. 7.10, the damage after it has annealed leads to the final number of replaced sites which tends to converge as the ion mass becomes lighter. The effect of the heavy gas Xe remains dominant.

7.1.6 Discussion

The mass ratio sensitivity with fixed potential functions for each of the following species inert gas and metal, was explored by varying the ion mass. No ion mass effect was observed on the number and distribution range of survived defects. The mass effect appears to be significant only in the early collisional stage of the bombardment in particular for inert gas. This translates into an increase of the sputtering yield due to its timescale occurrence and with the most likely difference is the strength of repulsive potential for noble gas and metal ions. It was found by MD calculation that the total sputtering yield is sensitive to the strength of the ion-atom potential at separation radius of approximately 0.7Å [280], besides the potential effect for Ar bombardment of Ni (surface) [281]. It was reported also, that the repulsive part of the potential has a strong influence on the cascade morphology [282].

Shulga studied the density and binding effects in sputtering by ions of widely varying masses and he came to the conclusion that the different scattering behaviour of light and heavy ions allow for the effect of focused collision sequences [66]. In alloy sputtering, the mass effect lie in the preferential sputtering which can have an important effect on surface composition change (depletion and enrichment) [283]. It was revealed by simulation that direct ejection by ions contributes significantly to the total sputtering of the fcc W(100)

Figure 7.11: Computer-generated defect plots of the damage induced by metal and noble gas bombardment at 0.25 ps (left column), and 0.5ps (right column)
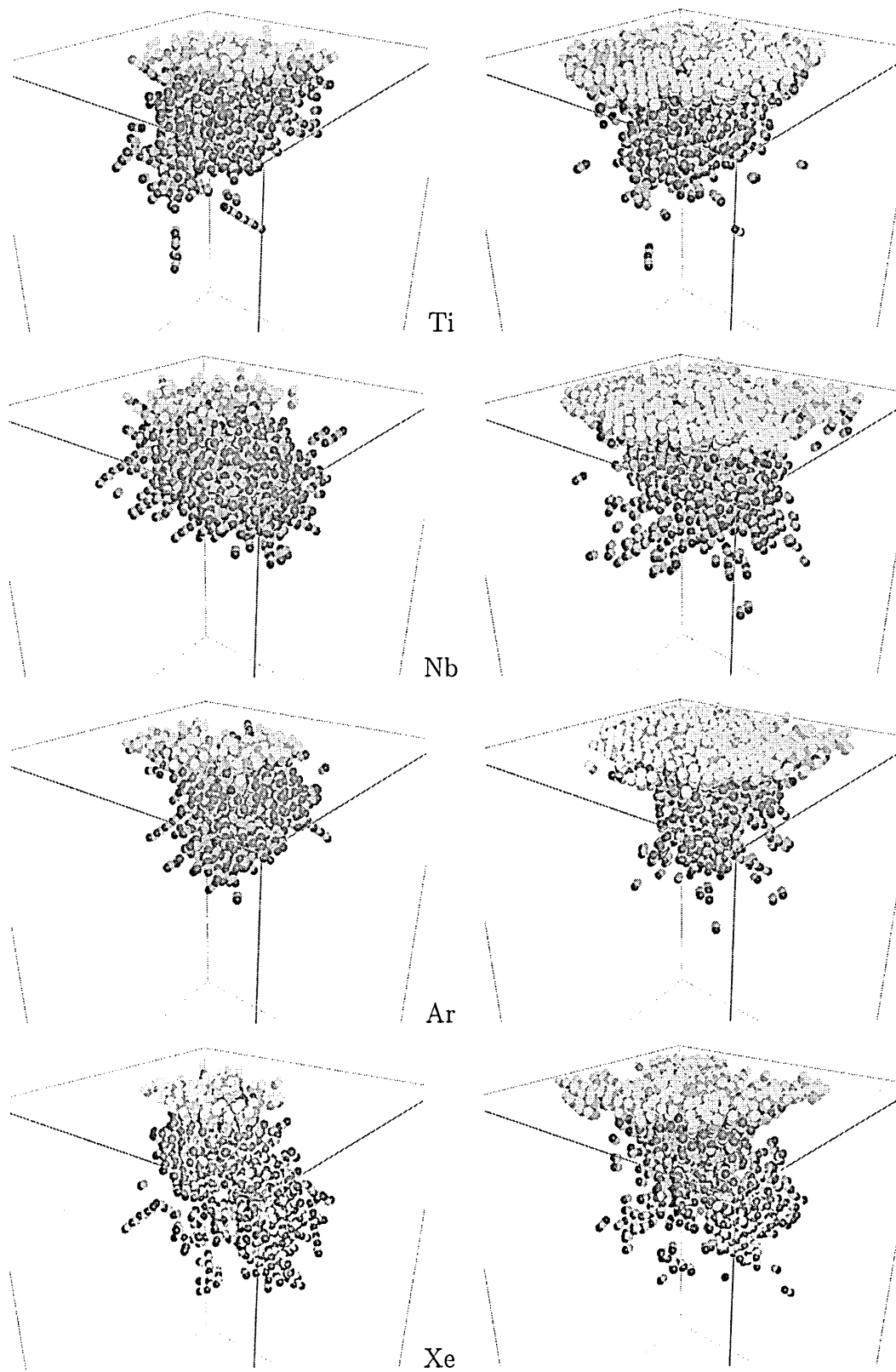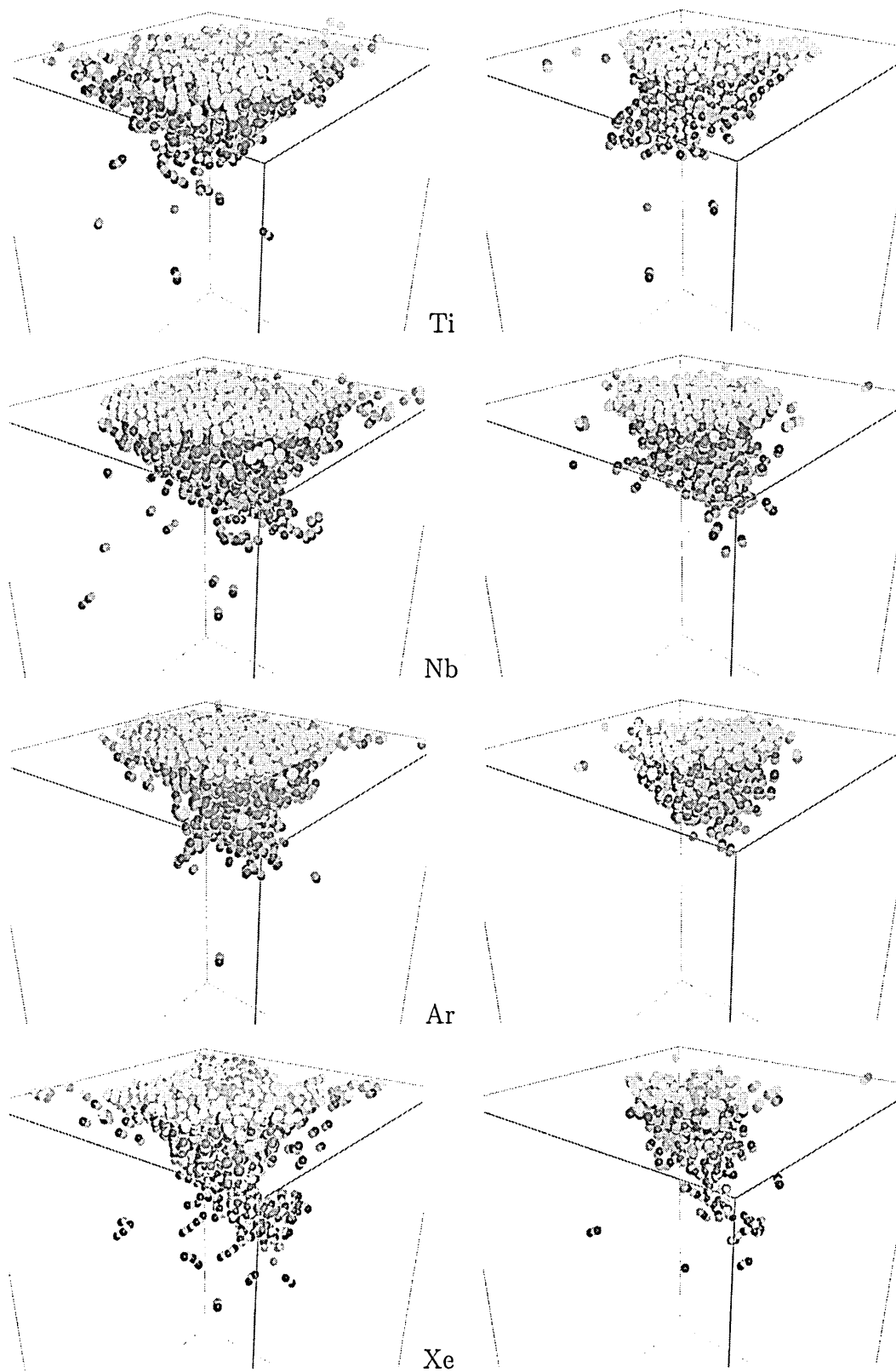

Ti

Nb

Ar

Xe

Figure 7.12: Computer-generated defect plots of the damage induced by metal
and noble gas bombardment at 0.75 ps (left column), and 1ps (right column)

Ti

Nb

Ar

Xe

for all ions i.e. He, Ar, Kr (400 eV), this is explained by the large mass difference between the incident ion and the target in addition to the similar angular distribution [284]. In Ref. [285] an increase in atomic mass of the gas manifests into a more disparate behaviour of the studied superlattice structure. No studies was know to us on mass effect of metal ion bombardment.

7.2 Dimer Bombardment

7.2.1 Simulation Model

To investigate the effect of projectile size on bombardment, the number of projectile constituents was increased by switching from monoatomic to polyatomic. The simplest conceivable polyatomic projectile is a dimer in which two atoms are clustered at a given internuclear distance r_0. That is the bond length of the gas phase Cr_2 dimer which is one of the most extreme cases of multiple metal-metal bonding [286,287]. It was evaluated to 1.68 Å from the vibrational energy measurement, and 3.25 Å from ab initio calculation [288]. The internuclear distance r_0 of a dimer has shown no influence on bombardment [270], and the vibrational energy is always negligible compared to the kinetic energy introduced by the projectile dimer, we therefore choose $r_0 = 2.02$ Å , which falls within the above experimental and theoretical values. An additional parameter for the structure of the dimer is the orientation parameter which is characterised by the polar angle θ and azimuth ϕ. For the specific case of perpendicular incidence $\theta = 0^o$, the azimuth is meaningless. Thus, each atom of the dimer or diatomic projectile and its centre of mass impact at the same surface point. The simulations were performed for Cr_2 projectile dimers normally incident onto the Fe crystallite equilibrated at temperature of 700 K. A set of 150 dimers were calculated at two impact energy 1.2 keV and 2.4 keV per atom dimer and with impact points being distributed over the irreducible surface cell. Diatomic and dimer are interchangeably used in this section same is for monoatomic and monomer.

Figure 7.13: The damage induced by Cr_2 bombardment at 2.4 keV (1.2 keV per atom) during 1 ps


0.25ps

0.75ps

0.50ps

1.00ps
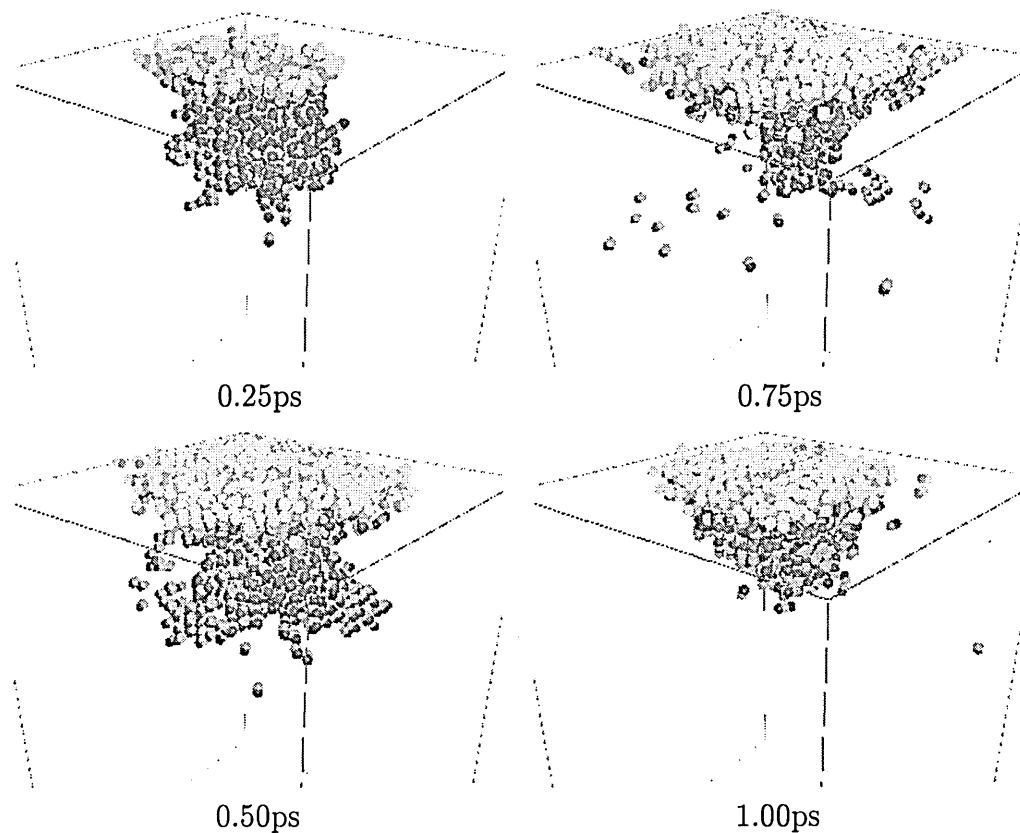
7.2.2 Damage by Dimer

The damage induced in a crystalline iron by diatomic projectiles at bombardment energy 1.2 and 2.4 keV per atom, is shown in Fig. 7.13 and Fig. 7.14. The cascade of displaced atoms are more dense than those generated by monoatomic projectile at the same atom velocity (see Fig. 5.6, 5.8) [1]. This can be understood by the double amount of energy input. The volume of the cascade is not double the one produced by a monoatomic impact and the abscence of subcascades are clear indications of cascade overlap where collisions between

[1]Chapter 5 page 94, 96

Figure 7.14: Damage induced by Cr_2 bombardment at 4.8 keV (2.4 keV per atom)

0.25ps

1.25ps

0.50ps

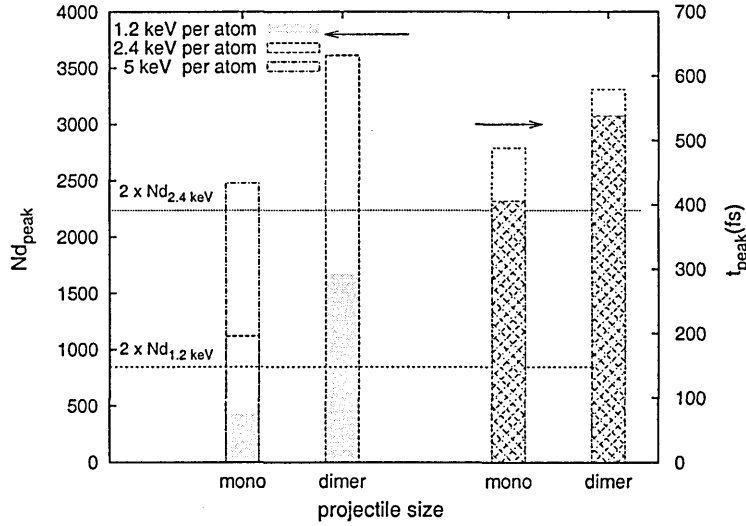1.50ps

0.75ps

1.75ps

1.00ps

10ps
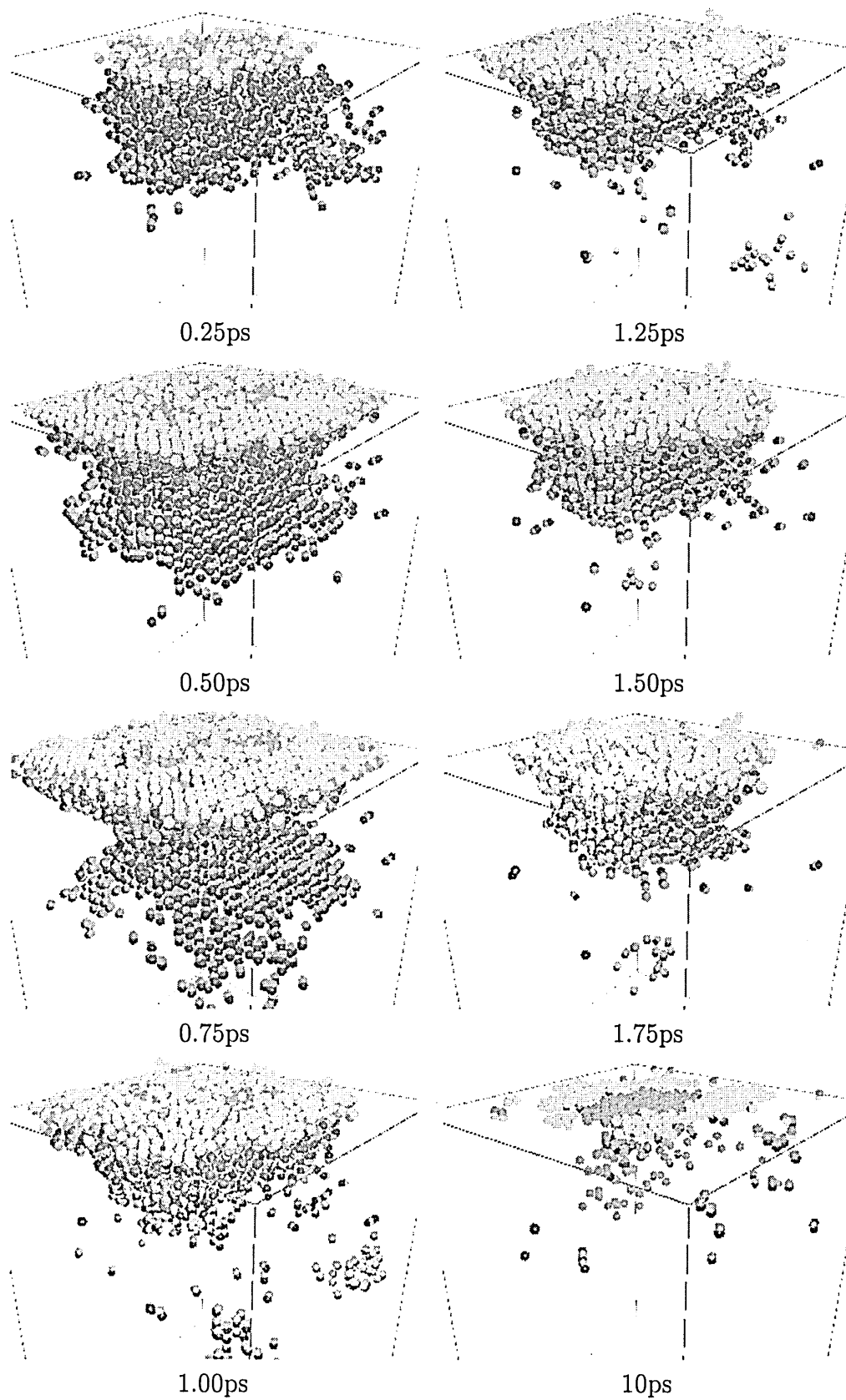
Figure 7.15: The average peak damage Nd_{peak}, t_{peak} induced by diatomic projectile compared to monoatomic projectile Cr at 1.2 keV (shaded box) and 2.4 keV (empty box)per atom. Dashed line: doubled average damage Nd_{peak} of monoatomic projectile

moving atoms occur. This is called a collisional spike which differs from linear collision cascade where collision occurs between moving atom and an atom at rest and it is of low density.

The average peak damage due to a diatomic projectile is shown in Figure 7.15. By comparison to monoatomic projectile, the peak damage time increases slightly while the peak damage displacement has enhanced significantly. Such enhancement is non linear since it is greater than the linear sum of the damage generated by each atom at the same atom velocity. We have examined the case of constant total bombardment energy when monoatomic and diatomic projectiles are considered with different atoms velocity. The peak damage N_d increased for the diatomic projectile (Fig. 7.15) demonstrating the effect of the projectile size. Also worth noting is the large vacancy crater surrounded by a ring of adatoms which is more evident for a diatomic projectile at 4.8 keV (Fig.7.14, at 10 ps) compared to a monoatomic projectile at 5 keV (see Fig. 5.9.c)[2]. Thus, the energy dissipation mechanism is different when the
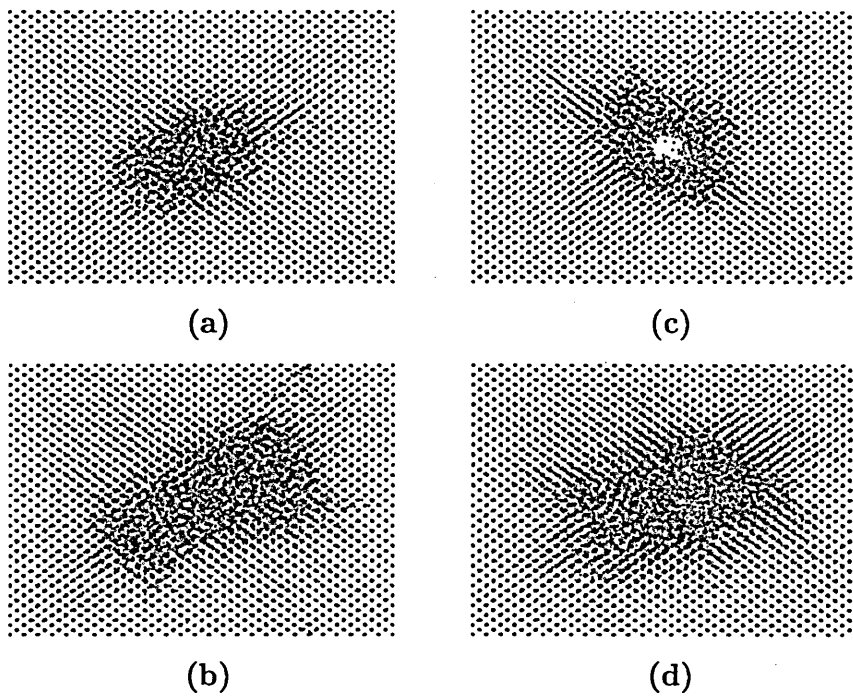
---

[2]Chapter 5 page 97

Figure 7.16: Plan-view of subsurface layer upon bombardment by a monoatomic a):2.4 keV, b):5 keV and a diatomic c):2.4 keV, d):4.8 keV Cr projectile

same energy is shared by discrete entities. Furthermore, the positions of atoms within a plan-sectional slab of thickness ($0.5\ a_0$) below the surface (Fig.7.16) and a longitudinal section slab in the central impact point on the crystal (Fig. 7.17) were monitored and accumulated for the first pico second of the diatomic impact and presented together with those for monoatomic impact. The lateral extent of damage did not change from monoatomic (Fig.7.16.a,b) to diatomic impact (Fig.7.16.c,d) at the same impact energy while it did at the same atom velocity as seen from Fig.7.16.a and 7.16.d . In Fig.7.17.c and 7.17.d a void like zone is observed which might be due to the clearing away effect of perpendicular dimer projectile. This is in line with the depleted or void like zones observed by TEM in the near surface region due to dimer irradiation of tungsten [289]
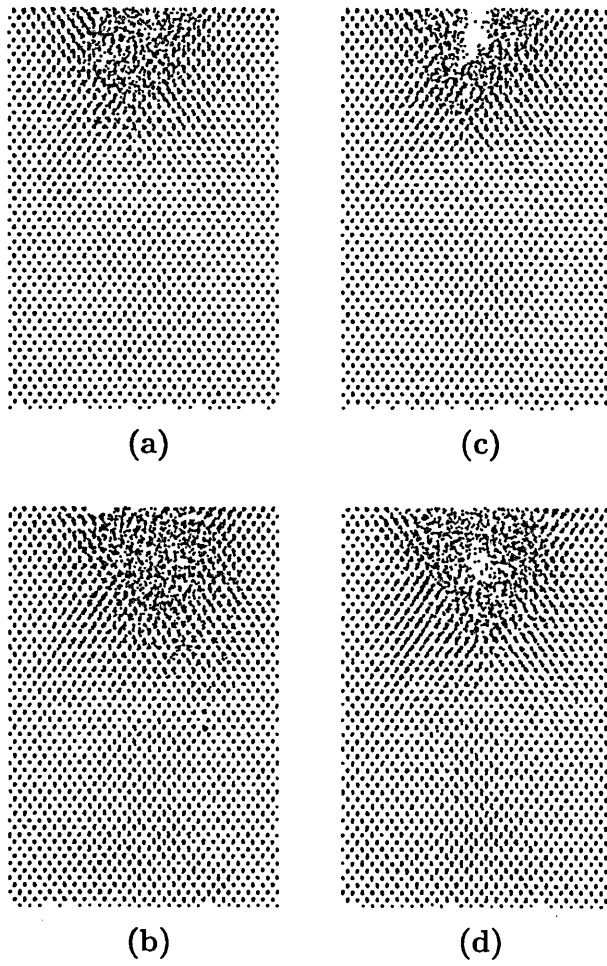
Figure 7.17: Longitudinal-section through the crystal at the impact of Cr a):2.4 keV, b):5 keV and Cr_2 c):2.4 keV, d):4.8 keV Cr projectile

7.2.3 Enhancement of the sputtering yield

The average total and cluster sputtering yields are given in Table 7.1 for Cr_2 bombardment at energy 1.2 and 2.4 keV per atom together with those for Cr calculated previously. The yields are significantly enhanced upon moving from mono- to diatomic projectile. This effect is quantified by an enhancement factor defined in general by [270, 271, 290]

$$k_{n,m} = \frac{mY_n}{nY_m} \qquad (7.1)$$

Table 7.1: The average sputtering yields and enhancement factors for Cr and Cr_2 bombardment at energy 1.2 keV and 2.4 keV per atom

Energy	Projectile	Total yield	$k_{2,1}$	Cluster yield	$k_{2,1}$	Cluster fraction
1.2	Cr	1.07		0.21		0.19
	Cr_2	3.82	1.79	0.80	1.9	0.21
2.4	Cr	2.43		0.30		0.12
	Cr_2	7.77	1.60	2.2	3.7	0.24
5.0	Cr	3.86		0.39		0.10

where Y_n and Y_m are the emission yields induced at identical atom velocity by polyatomic projectile containing respectively n and m atoms. If $k_{n,m} > 1$ for $n > m$, then the ratio in Eq. 7.1 reflects the amount of non-linear enhancement of the emission yield. In Table 7.1, $k_{2,1} > 1$ for all cases when going from atomic to dimer bombardment. Typical values slightly larger than 1 for the enhancement factor have been reported for dimer bombardment [271, 290]. The enhancement factor for the cluster yield increases with increasing energy while for the total yield slightly decreases. This indicates a complex behaviour of the sputtering yield with the incident energy for dimer bombardment.

In Fig. 7.18 we have plotted the probability distributions of trajectories leading to the simultaneous emission of a given number of particles. High yield events where more than 40 atoms are ejected, occur for dimer projectile at 2.4 keV per atom. This explains the important enhacement factor for cluster yield (Table 7.1).

Emission sites

For a diatomic projectile at 1.2 keV per atom, more than 94% of the sputtered atoms stem from the uppermost atomic layer of the solid. This value is reduced to 87% at 2.4 keV, owing to the contribution of second and third subsurface layer but still the large majority of sputtered atoms originates from the surface. We therefore looked at the original separation distance of sputtered dimers since they are abundant. In Fig. 7.19, almost 60 % of

Figure 7.18:

ASI for a monoatomic (left column) and diatomic Cr projectile (right column) at the same atomic energy
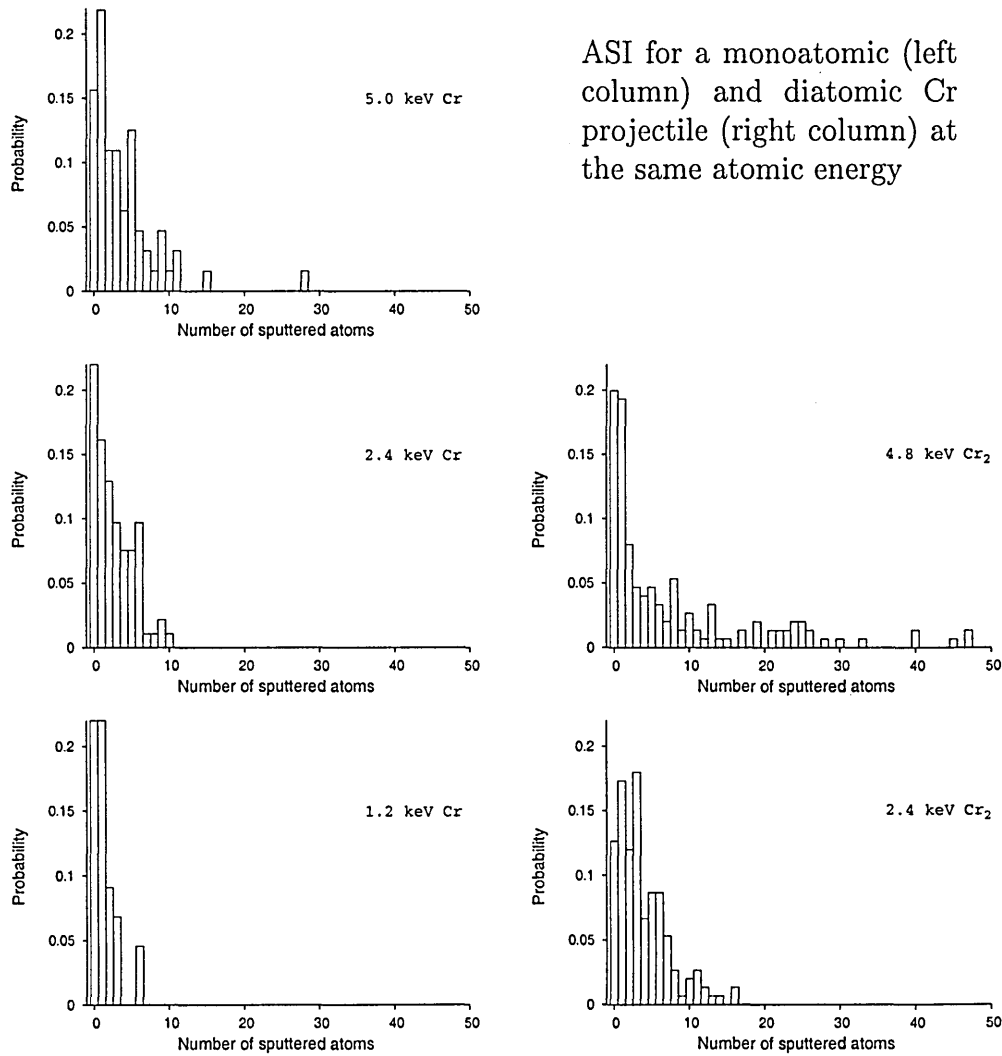
the sputtered dimers have been nearest neighbours. The percentage decreases monotonically with increasing initial separation. This result suggests that the overwhelmimg majority of dimers have already been bound in the solid as investigated elsewhere [264, 269].

Cluster size distribution

The non linear enhancement of the cluster yield translates to the emission of trimers and higher clusters. This occurs in high yield events as exemplified in Fig. 7.20 for two Cr_2 trajectories where respectively 48 and 47 atoms
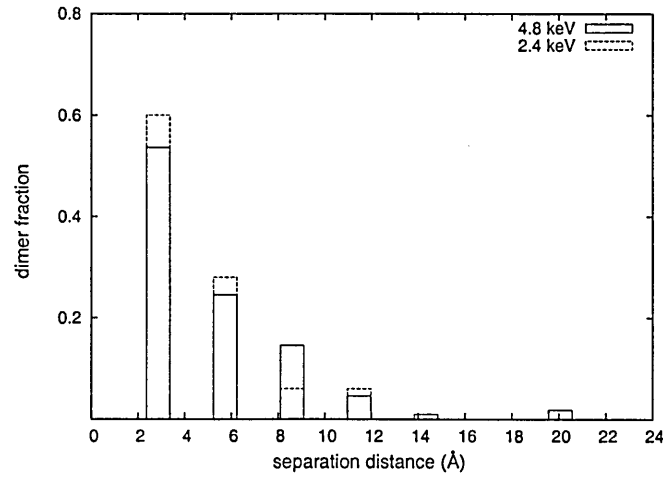
Figure 7.19: Probability that two atoms constituent of a sputtered dimer were at a given distance in the solid before emission

(a)   (b)
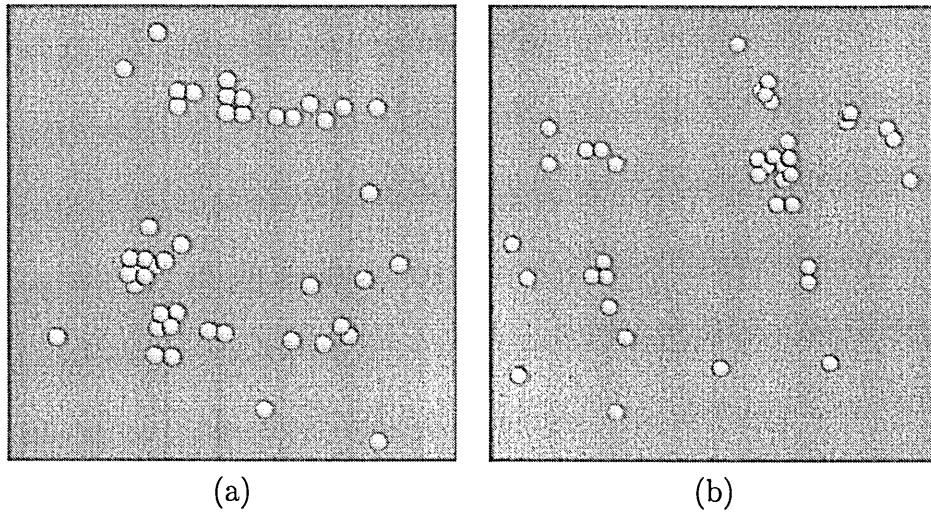
Figure 7.20: Top view of sputtered atoms at two high sputtering yield of (a)48 and (47) upon an impact of dimer Cr_2 at 2.4 keV per atom

were emitted. Since the mass distribution of sputtered particles is exclusively composed of Fe atoms and Fe_n clusters, the relative yields, i.e., the partial yield Y_n normalised to that of sputtered monomers Y_1, of Fe_n clusters produced under bombardment with diatomic projectile of 2.4 keV and 4.8 keV. The relative yield is represented in Fig.7.21 as a function of cluster size. It appears that the distribution of clusters in all cases can be approximated by a power law size dependence given by Eq.7.2 and in good accordance with
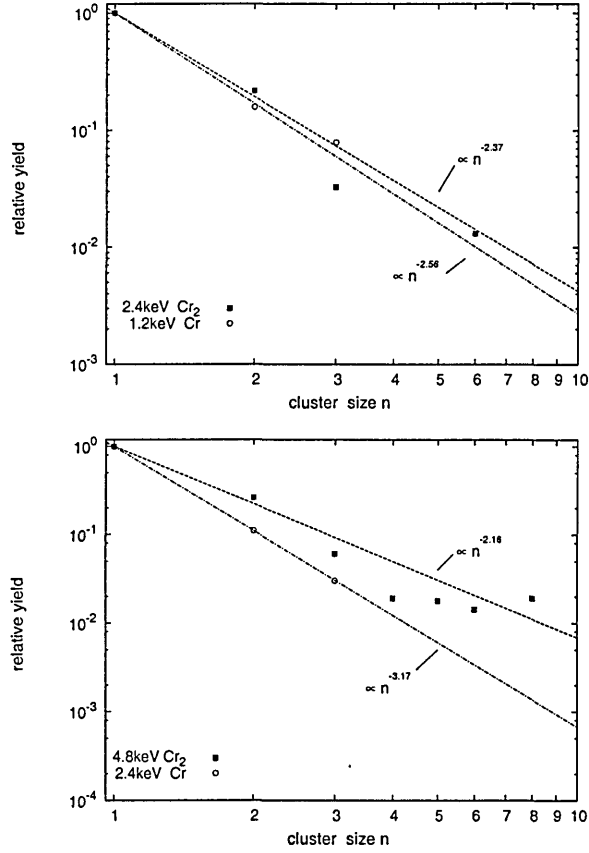
158

Figure 7.21: relative yield of Fe_n clusters sputtered from a crystalline iron surface under bombardment with monoatomic and diatomic projectiles at (a) 1.2 and (b) 2.4 keV per atom

previous simulations of gold and silver sputtering with mono and polyatomic projectiles [263, 270, 291].

$$Y(n) = Y_n/Y_1 \propto n^{-\alpha} \tag{7.2}$$

From a least square fit to the data presented in Fig.7.21, one finds decay exponents α of 2.56 and 2.37 at 1.2 keV per atom, and 3.17 and 2.16 at 2.4 keV per atom, for mono- and diatomic Cr projectiles, respectively. The decrease of the values between mono- and diatomic projectiles is in principle expected since the sputtering yield increases upon switching from Cr to Cr_2 projectile. Probably the most important observation in Fig.7.21 is that the relative abundance of clusters among the flux of sputtered particles increases upon

159

switching from mono- to diatomic projectile. A similar trend was reported for Ag_n clusters between mono- and diatomic Ag projectiles but between di- and triatomic projectiles the yield decreased [291].

Internal Energy Distribution

Due to the collisional nature of clusters' formation, the so called nascent clusters can contain a relatively high amount of internal energy and are mostly unstable with respect to dissociation. Investigation of their internal energy is unaccessible by experiment, since they reside at a distance of nanometres above the surface and can undergo fragmentation before detection, so simulation is an asset. At this point, the total internal energy of the cluster is determined from the positions and velocities of the constituant atoms as follows [270]:

$$E_{int} = E_{tot} + E_a(n) \tag{7.3}$$

where E_{tot} is the total energy of the cluster which is negative and is given by

$$E_{tot} = \sum_{i=1}^{n} E_i^{rel} + V_i \tag{7.4}$$

E^{rel} is the kinetic energy of the cluster relative to its centre of mass (CM) velocity. $E_a(n)$ is the atomization or binding energy of the cluster, *i.e. the energy of the ground state of the cluster.* $E_a(n)$ for iron clusters with 2-20 atoms were calculated in Ref. [292], and V_i is the potential energy.

Since, dimer bombardment triggers high yield events and subsequently clusters, the internal energy is investigated here as function of clusters size and bombardment conditions, as shown in Fig.7.22. It is interesting to note that in all cases internal energy exhibits a linear dependence on the cluster size, a behaviour which has been observed elsewhere [291]. The slope , however changes upon transition from monoatomic to diatomic projectile indicating that nascent clusters produced by diatomic projectile are "hotter" than those produced by monoatomic. This is in contrast to the trend observed for Ag_n
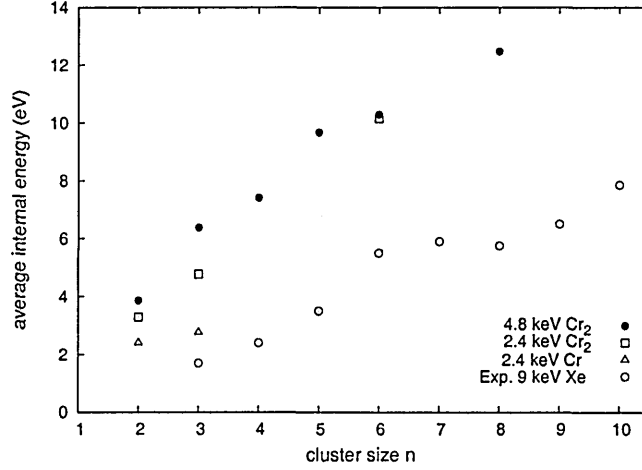
Figure 7.22: Average internal energy of Fe_n cluster sputtered from Fe surface by mono and diatomic Cr projectile. Experimental values are also presented for Fe_n cluster sputtered from a pollycrystalline Fe surface by 9 keV Xe

clusters [270]. The internal energy of Fe_n clusters sputtered from a polycrystalline Fe surface under 9 keV Xe [293] is within the same order of the calculated one but of lower value. Since in experiment clusters have undergone fragmentation before detection.

7.2.4 Microscopic view of the dimer interaction with Fe surface

The non linear enhancement of the sputtering yield with the production of high yield events are unambiguously connected with the amount of energy deposited in the substrate and the degree of the energy localisation with respect to the depth and bulk. In this respect, we have monitored the distribution of the average energy deposited by one incoming atom over the crystal depth after the impact of a diatomic and monoatomic projectiles. The Fe crystal is divided into slabs of 1 Å depth and the kinetic energies of Fe atoms in a given slab at a specific time are summed over all trajectories and are then divided by the number of all incoming atoms. The results are presented in Fig. 7.23, and reveal that an incoming Cr atom which is part of a dimer deposits more
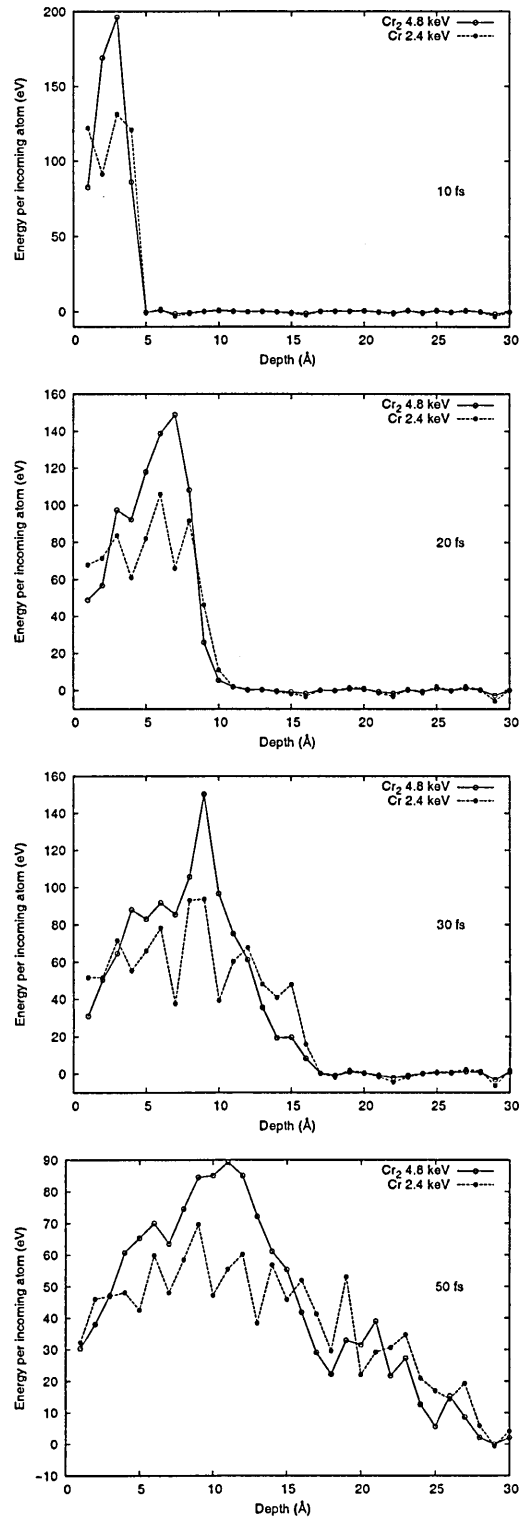
161

Figure 7.23: Distribution of the average energy deposited by one incoming atom over the crystal depth and over all trajectories for Cr 2.4 keV and Cr_2 4.8 keV.
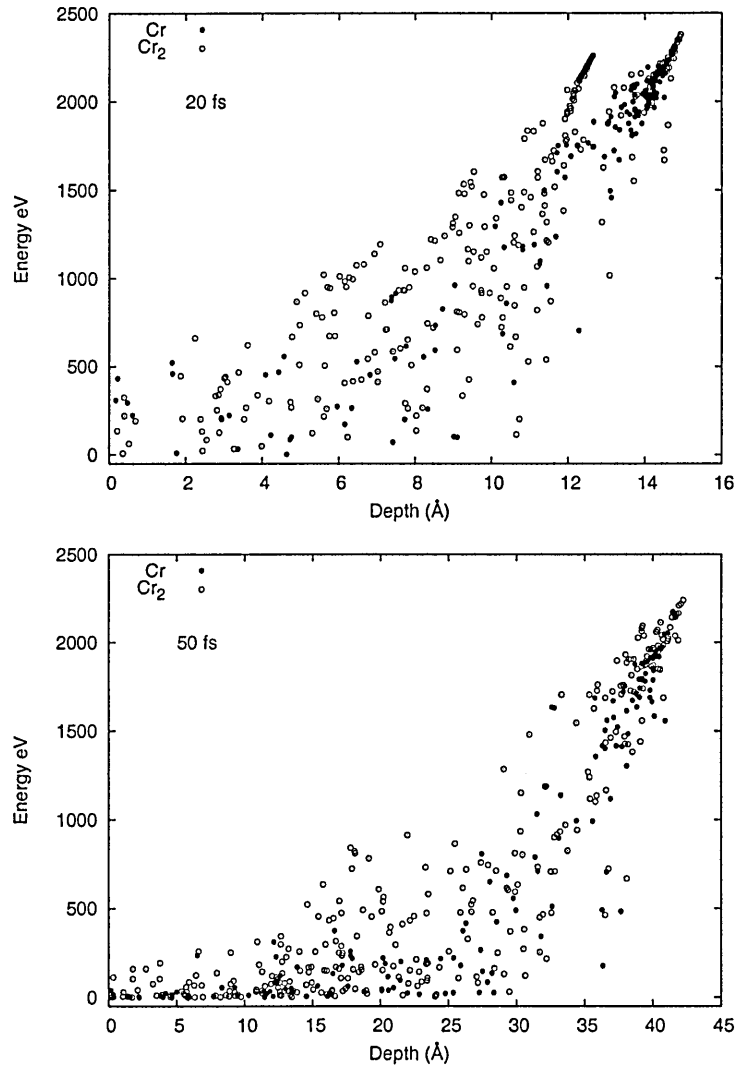
162

Figure 7.24: Scatter plot distribution of the Cr atom energy over the crystal depth at 20 and 50 fs for 150 trajectories at the same atom velocity for Cr 2.4 keV and Cr_2 4.8 keV projectiles

energy than an individual atom at the same velocity. Thus, the process of sharing and depositing energy is slow allowing an adequate depth for effective sputtering. Complemented by analysis of the remaining energy of Cr atoms at 20 and 50 fs in Fig.7.24 for monoatomic and diatomic Cr projectile at constant atom velocity. It is seen that the Cr atoms that are part of a dimer penetrate less deeply in the bulk than the atomic projectile. Dimer bombardment atoms keep more of their initial energy after 50 fs compared to monoatomic bombardment. The concept that the Cr atoms maintain their identity as a dimer
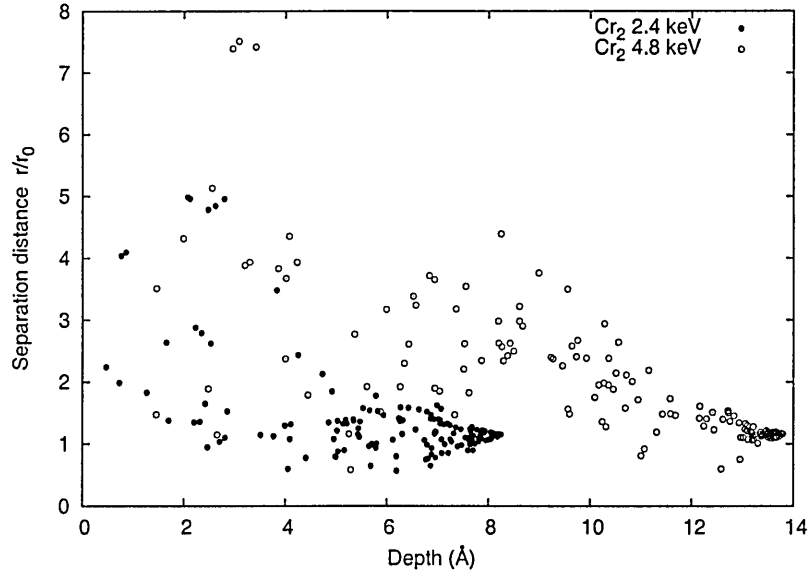
Figure 7.25: Separation distance between dimer constituents vs. the depth of the dimer centre of mass penetration at 20 fs and at energy 2.4 and 4.8 keV

is shown clearly in Fig. 7.25. The separation distances expressed in units of the equilibrium internuclear distance, r_0, between constituents for each dimer versus the depth of dimer center mass penetration at 20 fs are plotted for the 150 trajectories of Cr_2 at 1.2 and 2.4 keV per atom. It is seen that upon penetrating into the substrate, the Cr_2 constituents at energy 2.4 keV quickly disintegrate on the initial part of the trajectory acting independently thereafter. In contrast, Cr_2 constituents at 1.2 keV stay together. This localized the deposited energy within a relatively small narrow region and can explain the value of enhancement coefficient given in Table 7.1.

Experiment of Au_n bombardment of silicon (Si) and aluminium (Al) substrates shows that yield enhancement of adsorbate is larger on Si than on Al [294]. This is argued to be due to the substrate structure rather than the composition since Si and Al have similar atomic weights but different structures, and Al is a face centered cubic metal whereas Si has a more open diamond structure. For Au_n the projectile will undergo a large number of collisions on the Al in the near surface region than in Si and the constituent atoms will move apart faster than in Si dependent on substrate composition and structure [294].

164

The average depth of implanted Cr in Fe crystal amounts to 19 and 34 $\mathring{A}$ for diatomic projectile at energy of respectively 1.2 and 2.4 keV per atom. For a monoatomic projectile at these energies, the Cr depth is 37 % less and 20 % greater compared to dimer projectile. Such an increase can be related to the clearing the way effect which can be important at high energy for perpendicular dimer.

To sum up, when the consituent atoms likely remain close together, a substrate atom can be struck simultaneously by a number of them. Thus more energy is deposited into individual substrate atoms at the surface of the substrate than deeper in the material.

Conclusion

We have examined the effects of ion mass on the sputtering and damage range for crystalline Fe under bombardment with inert gas and metal ions at 2.4 keV. Our results show that except for total sputtering yield, dimer yield and atom per single ion (ASI) distributions, most sputtering parameters (angular and energy spectra of sputtered atoms) are independent of the ion mass and ion species. The ion mass effect is positive for inert gas ions, i.e. the sputtering yield increases with ion mass. The effect, however is negative for heavy metal ion. The damage range is independent of ion mass but the range of implanted ion is sensitive to the ion mass. The projectile size enhances non-linearly the sputtering yield when switching from monoatomic projectiles to diatomic projectiles. The size effect prevails on the mass effect. However, the combination of the two has been reported from experiment and simulation, to give a strong non-linear enhancement of the sputtering yield.

Chapter 8

Conclusions and Future Prospect

8.1   Conclusions

In this thesis, we have presented a survey of modelling and simulations for the exploration of bombardment of metallic surface of Fe. We have emphasised the molecular dynamics technique for the atomic level simulation of damage generation and sputtering. The main conclusions to be drawn are relevant to a single Cr impacting a perfect α Fe crystalline surface.

The results of MD impact simulations have shown that bombarding at high energy and at elevated temperature enhances the sputtering and alter the near surface region. Hence, more residual defects are yielded with more surface vacancies acting as anchoring sites for the subsequent coating, in addition to the shallow implantation of Cr. The effect of temperature on defect production at increased impact energy is proposed to be the result of crystal distortion via channelling and blocking interactions or in other words energy transfer efficiency and defect mobility enhancement through long lifetime of the cooling phase.

We have examined the directional effect in the bombardment of Fe(100) surface at temperature 700 K, with 2.4 keV Cr projectiles. The sputtering yield of Fe is predicted to display a strong dependence on the projectile polar angle of incidence θ. A factor of two enhancement in the yield is observed at low oblique angles θ : 20° and 30° and at near glancing angles θ : 60° and 75° where the maximum is attained. The attenuation of the sputtering yield at near grazing incidence happens to be a strong function of the incidence angle since crystalline details are less exposed to the projectile in the same way as a polycrystalline surface. The implantation and reflection of Cr atoms varies in reverse with projectile incident angle and the critical angle for total reflection varies with the azimuthal incidence. No specular or superspecular reflection occurs. The susceptibility of crystalline target to channelling is dependent on the projectile direction.

We have examined the effects of ion mass on the sputtering and damage range for crystalline Fe under bombardment with inert gas and metal ions at 2.4 keV. Our results show that except for total sputtering yield and atom per single ion (ASI) distributions, most sputtering parameters are independent of the ion mass and ion species. The sputtering is efficient under noble gas bombardment. The projectile size enhances non-linearly the sputtering yield when switching from monoatomic projectiles to diatomic projectiles. The size effect prevails on the mass effect. However, the combination of the two has been shown by experiment and simulation to give a strong non-linear enhancement of the sputtering yield.

To sum up, the increase of the total and cluster sputtering yield for different conditions of bombardment is related to the occurrence of high yield event. The generated damage is ultimately related to the energy of bombardment but at a constant energy other bombardment parameters can contribute to alter the defect production and defect depth profile as well as the implantation profile.

8.2 Future Work

Subsequent ion impacts into the damaged crystal or surface roughness state are the next topic of interest to be investigated. Since from initial results (see appendix A) the clustering tendency of defects and their distribution over depth have shown to depend on the dose of bombardment.

Even though the study of sputtering from a single crystal is not useful for practical applications, simulation studies of single crystal sputtering serve as a basis for theoretical understanding of sputtering. It is of great interest to consider further parameters such as surface orientation in order to average for polycrystalline measured values.

Another important issue is that bombardment of smooth and clean surfaces is far from being realistic since surface roughness can greatly affect the sputtering efficiency. In addition to the presence of metal oxide on surface which is undesirable for the subsequent coating interface. This opens a need to investigate over-layer metal oxide, its type and coverage structure upon bombardment.

Another component is Carbon which can be allocated in an interstitial site in bcc Fe, it is important to consider an appropriate potential integration to covalent metal-Carbon bonding.

The most attractive work is the growth of coating on a sputtered Fe surface under different bombardement condition and investigating the structure of the interface upon considering the diffusion of the implanted etching species. Also, Nitriding of the implanted Chromium

For that, an accurate description of bcc metal Fe necessitates the introduction of angular terms in the interaction potential which can make a major contribution to the structural energy of defect at the interface.

Appendix A

# Fluence dependance bombardment of Fe-initial results

A.1 Introduction

This thesis was focused on the bombardment at zero fluence where each ion impacts on a perfect crystalline iron. At non zero fluence, the history of each impact is accounted. That is an ion sees the damage produced by its antecedent. This demands large scale computation and statistics since the crystal size has to allocate the energy input accumulated. Thus, MD simulations in this case are scarce [295, 296] although they are appropriate to study defect accumulation. A preliminary investigation of the fluence dependance at normal incidence is given here for two species Ar and Cr at energy of 2.4 keV. In addition to non-monoenergetic bombardment for Cr. In this case energy are drawn randomly from a square distribution with probability weigh corresponding to the Cr ion charge state distribution.

A.2 Simulation model

A single crystal Fe equilibrated at temperature 700 K is used. The total number of projectiles considered are 10. The first projectile hits a perfect target at random into an irreducible zone in the centre while the consecutive ones impact quasi-randomly into a square area region. This region is centered on the region used at zero fluence and has an area comparable to the damage cross section associated with a single projectile impact that is about about 10Å.

A.3 Case study

The damage accumulated upon multi impact Ar is represented through sequences of snapshots in Fig. A.1, Fig. A.2 and Fig. A.3. In which defects start to cluster after the fifth impact. The surface damage depicted has not changed significantly after the eighth impact. In Fig.A.4, the size of the relocated region expands after the sixth impact and remains the same there after. For Cr accumulation at non-monoenegetics impact in Fig. A.5, Fig. A.6 and Fig. A.7, the defect are less distributed along the crystal depth and defect clusters are very few compared to the monoenergetic impact. More simulation runs are needed to investigate the sputtering yield fluence dependance.
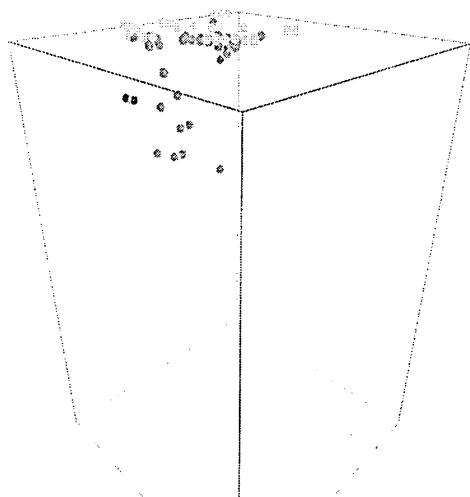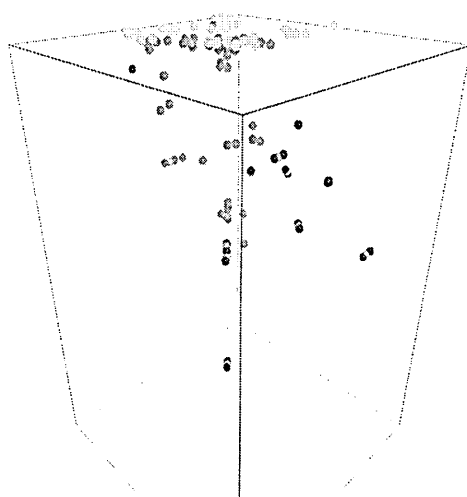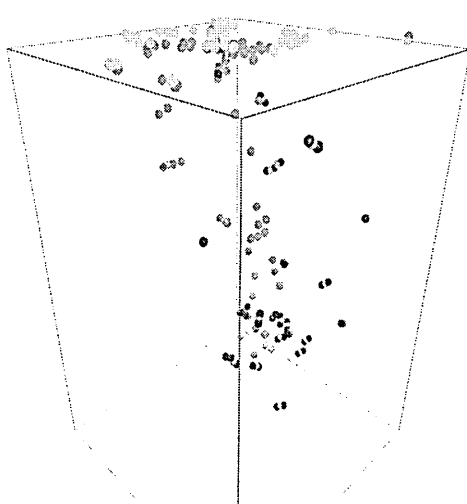
1th impact   2nd impact
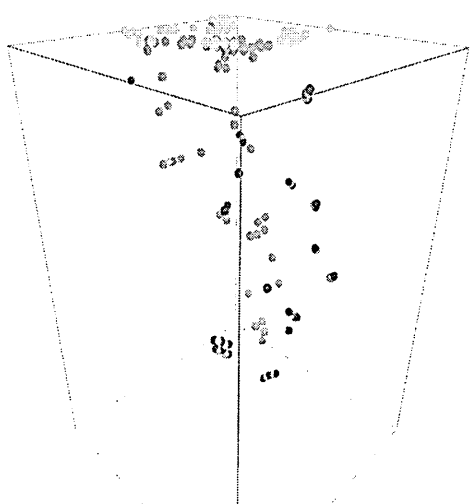
3th impact   4nd impact

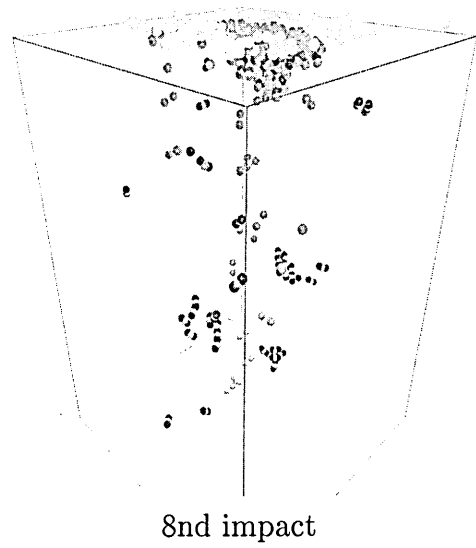Figure A.1: Snapshot of defect survived after 4th impact of Ar at 2.4 keV
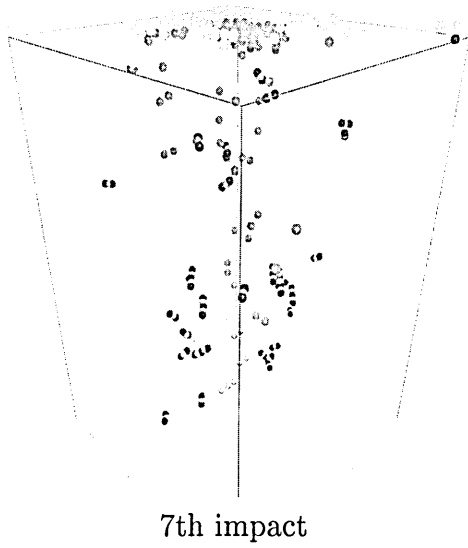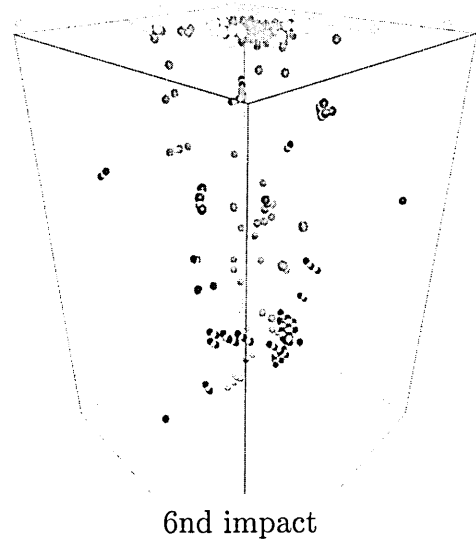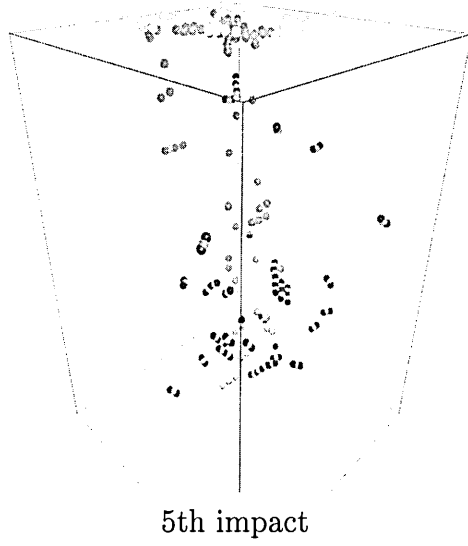
5th impact

6nd impact

7th impact

8nd impact

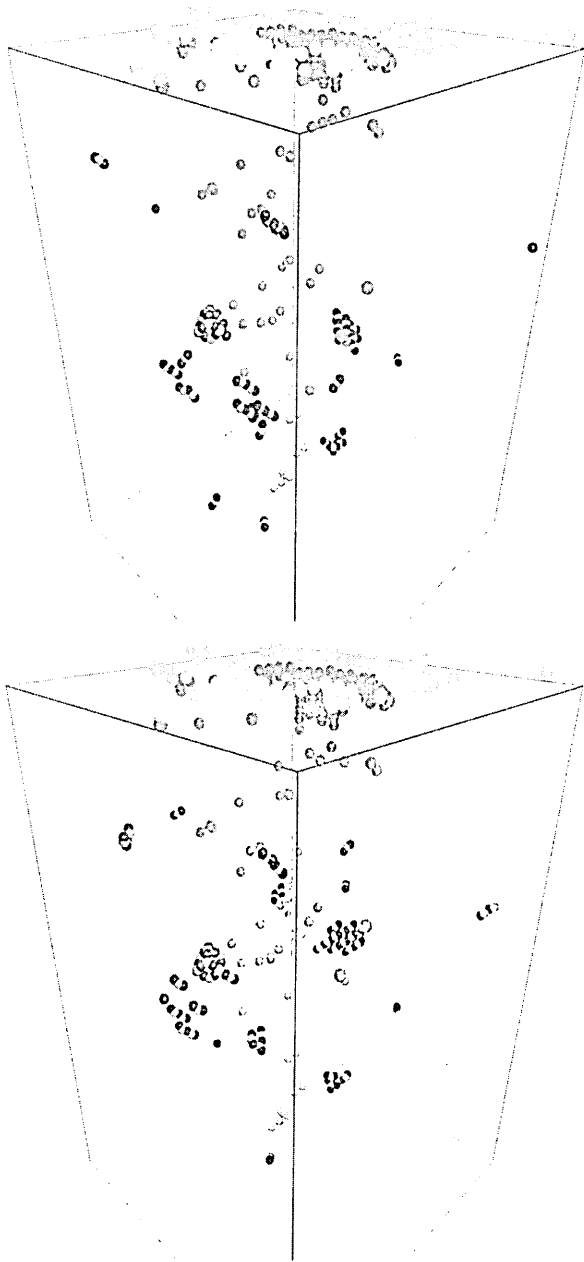Figure A.2: Snapshot of defect survived after 8th impact of Ar at 2.4 keV

Figure A.3: Snapshot of defect survived after 9th (upper),10th (lower) impact of Ar at 2.4 keV
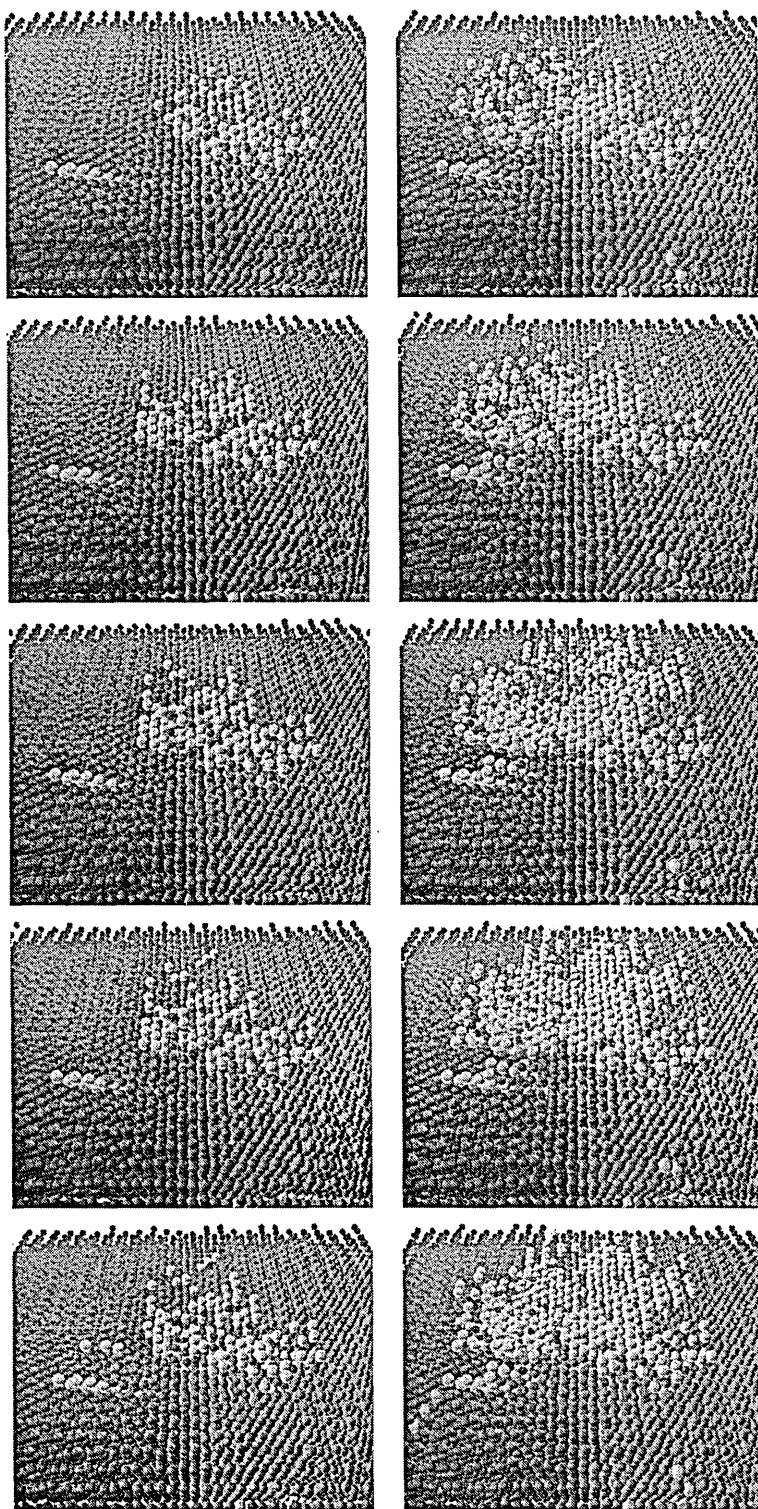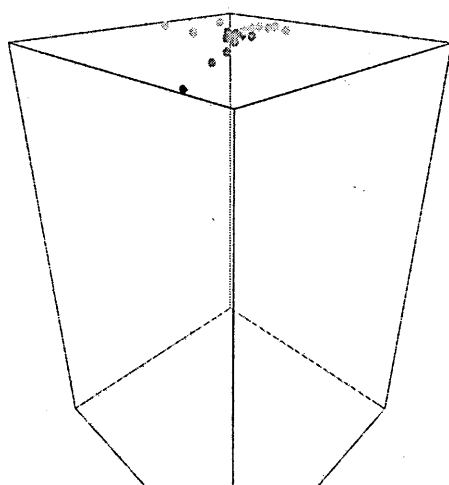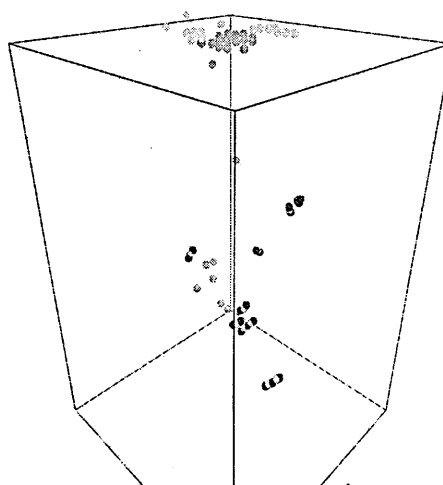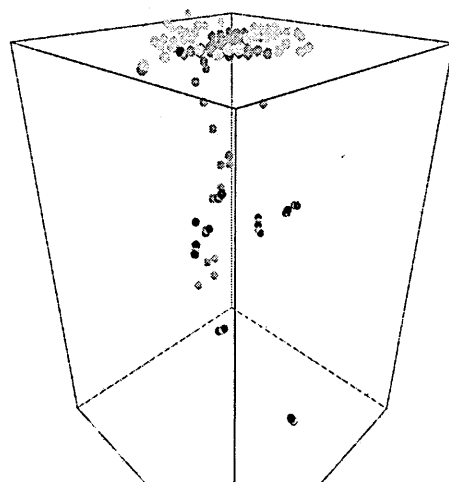
Figure A.4: Snapshot of surface replacement after 10 impacts of Ar at 2.4 keV (snapshot for the first impact is at the upper left and for the 10 is at the lower right corner)

174

1th impact 0.38 keV

2nd impact 1.56 keV

3th impact 2.25 keV
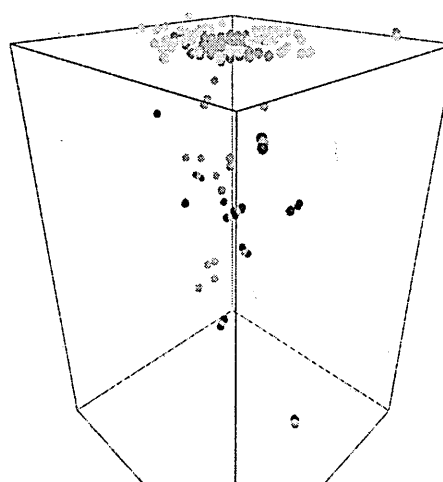
4nd impact 0.89 keV

Figure A.5: Snapshot of defect survived after 4th impact of Cr non-monoenergetic

5th impact 0.72 keV
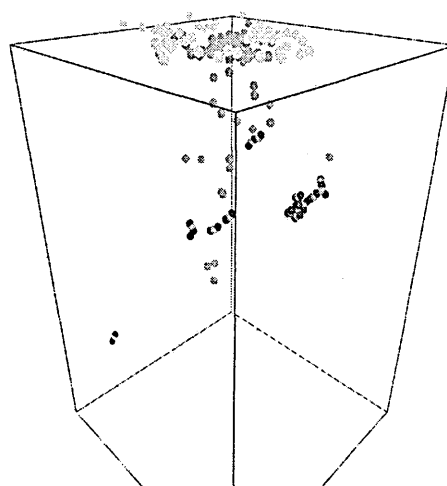
6th impact 1.27 keV
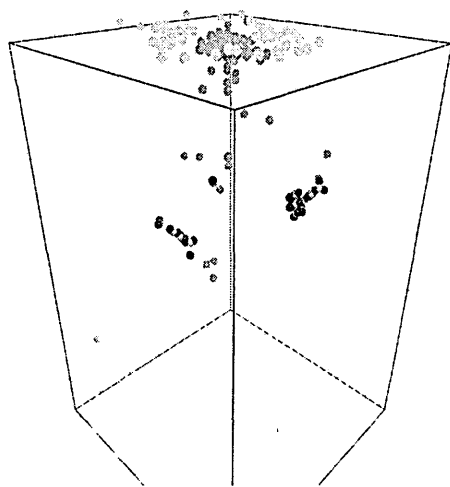
7th impact 1.17 keV
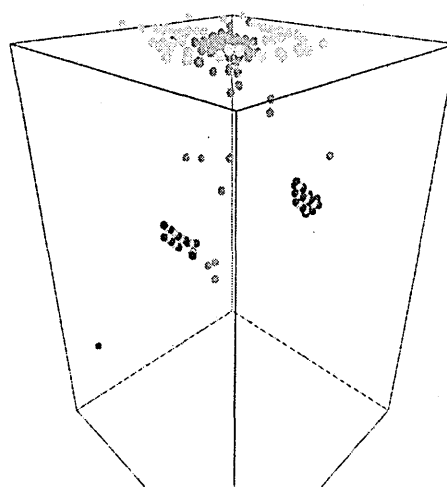
8th impact 0.54 keV

Figure A.6: Snapshot of defect survived after 8th impact of Cr non-monoenergetic bombardment
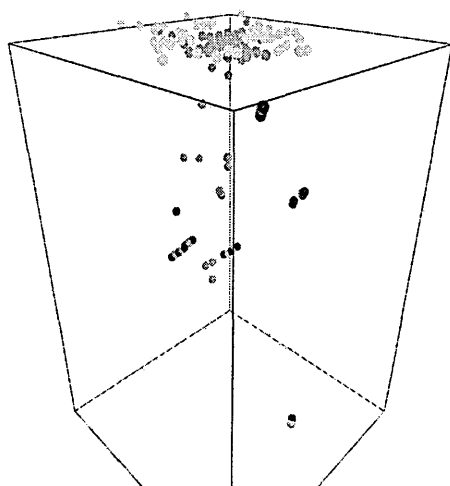
. 8th impact 2.29 keV

9th impact 2.25keV

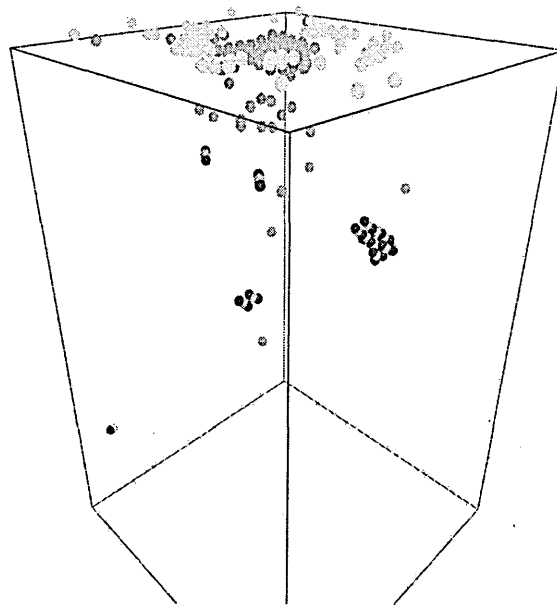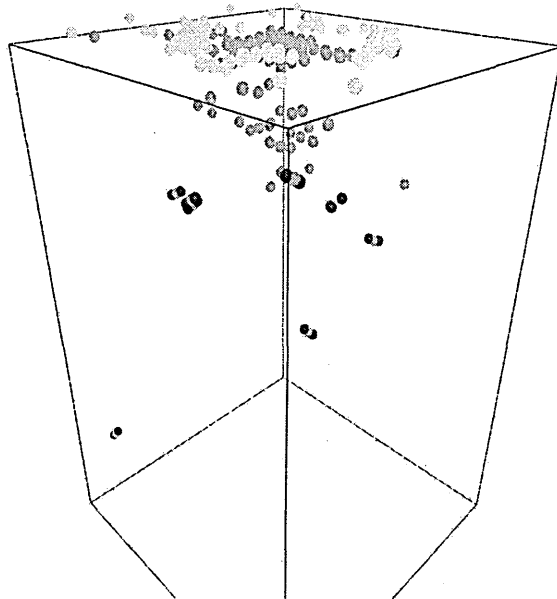Figure A.7: Snapshot of defect survived after 9,10 impacts of Cr non-monoenergetic bombardment

Appendix B

ABS coating
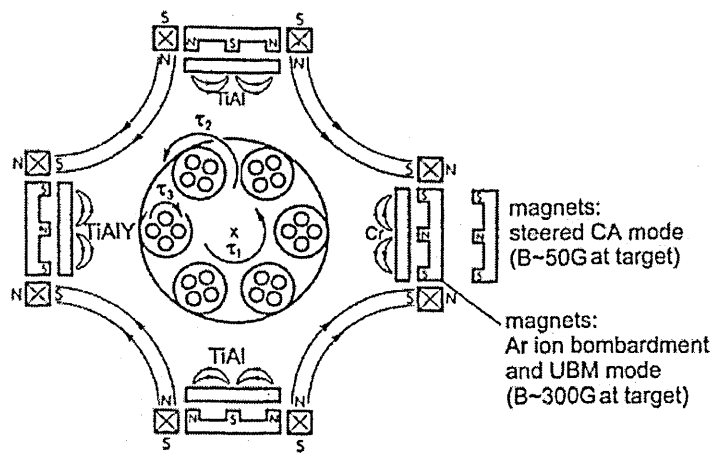
Figure B.1: Schematic cross section of ABS system where up to four cathode materials can be used in two different PVD modes .(after Ref. [19])

Bibliography

[1] Yue Kuo. *Vacuum*, 74:473, 2004.

[2] S.D.Park. *Surface and Coating Technology*, 171:285, 2003.

[3] Christophe Cardinaud. *Applied Surface Science*, 164:72, 2000.

[4] M.Nordin, M.Lanson, S.Hogmark. *Surf. Coat. Technol.*, 106:234, 1998.

[5] Chun-Che and al. *Corrosion Science*, 46:427, 2004.

[6] E.Bemporad,C.Pecchio, S. De Rossi,F.Carrassiti. *Surface and Coating Technology*, 146:363, 2001.

[7] J.P.Riviere. *Surface and Coating Technology*, 108:276, 1998.

[8] M.M.Morshed et al. *Surface and Coating Technology*, 174-175:579, 2003.

[9] H.Schulz. Proc. 1st french-german conf. on high speed machining, metz. page 1, June 1997.

[10] T.Cselle. Proc. 1st french-german conf. on high speed machining, metz. page 307, June 1997.

[11] Lembke et al. *Surface Engineering*, 17(1):153, 2001.

[12] W.D.Munz,D.B.Lewis et al. *Surface Engineering*, 17(1):15, 2001.

[13] M.M.Morshed. *Surface and Coating Technology*, 174:579, 2003.

[14] C.Schonjahn, D.B.Lewis, W.-D Munz, I.Petrov. *Surface Engineering*, 16 No. 2:176, 2000.

[15] C.Schonjahn, A.P.Ehiasarian, D.B.Lewis, R.New, W.-D Munz. *J. Vac. Sci. Technol.*, A 19(4):1415, 2001.

[16] D.Q.Pengetal. *Applied Surface Science*, 230:73, 2004.

[17] IvesCawleyBrooks. *Surface and Coating Technology*, 61:127, 1993.

[18] C.Leyens et al. *Surface and Coating Technology*, 155:103, 2002.

[19] Cornelia Schonjahn. *Surface treatment in a cathodic arc plasma*. PhD thesis, Sheffield Hallam University, February 2001.

[20] J.Faber,G.Hotzsch,Chr.Metzner. *Vacuum*, 64:55, 2002.

[21] G.Hakansson, J-E.Sundgren et al. *Thin Solid Films*, 153:55, 1987.

[22] J.M.Haile. *Molecular Dynamics Simulation*. A Wiley-Interscience Publication, 1992.

[23] W.Eckstein. *Computer Simulation of Ion-Solid Interactions*. Springer-Verlag, 1991.

[24] Mark T.Robinson, Ian M.Torrens. *Phys. Rev. B*, 9-12:5008, 1974.

[25] Mark T. Robinson. *Phys.Rev.B*, 40(16):10717, 1989.

[26] R.E.Stoller and A.F.Calder. *J.Nucl.Mater.*, 283-287:747, 2000.

[27] F.Javier Perez-Perez, Roger Smith. *Nucl. Instr. and Meth. B.*, 164-165:487, 2000.

[28] M.J.Caturla et al. *J.Nucl.Mater.*, 276:13, 2000.

[29] GaoBaconFlewittLewis. *Nucl. Instr. and Meth. B.*, 180:187, 2000.

[30] Yu.N.Osetsky, D.J.Bacon. *Nucl. Instr. and Meth. B*, 202:31, 2003.

[31] Roger E.Stoller. *J.Nucl.Mater.*, 307-311:935, 2002.

[32] R.Smith. *Atomic and Ion Collision in Solids and at Surfaces*. Cambridge University Press, 1997.

[33] K.M.Case and P.F.Zweifel. *Linear Transport Theory*, volume Addison-Wesley, Reading, Massachussets. 1967.

[34] M.M.R.Williams. *Mathematical Methods in Particle Transport Theory*. Butterworth and Co., London, 1971.

[35] L.H.Thomas. *Cambridge Philos.Soc.*, 23:542, 1927.

[36] E.Fermi. *Z.Phys.*, 48:73, 1928.

[37] J. Lindhard, V. Nielsen, M. Schar. *Det Kgl. Danske Videnskabernes Selskab-Mat. Fys. Meddr.*, 36:10, 1968.

[38] R. Behrisch. *Sputtering by Particle Bombardment I:Physical Sputtering of Single-Element Solids*. Springer-Verlag, New York, 1981.

[39] N.Matsunami, Y.Yamamura, Y.Itakawa, N.Itoh,Y.Kazumata, S.Miyagawa, K.Morita, R.Shimizu. *Radia.Eff.Lett.*, 57:15, 1980.

[40] J.Lindhard, M.Scharff, H.E.Schiott. *Mat.Fys.Medd.Dan.Vid.Selsk*, 33(14):1, 1963.

[41] W.D.Wilson,L.G.Haggmark,J.P.Biersack. *Phys.Rev.B*, 15:2458, 1977.

[42] J.F. Ziegler, J.P. Biersack, U. Littmark. *The Stopping and Range of Ions in Solids*. Pergamon Press, New York, 1985.

[43] O.B.Firsov. *Sov.Phys.:J.Exp.Theor.Phys.*, 36:1076, 1959.

[44] O.Oen, M.T. Robinson. *Nucl. Instr. and Meth. B*, 19/20:101, 1976.

[45] J.Lindhard, M.Scharff. *Phys.Rev.*, 124:128, 1961.

[46] M. Kitagawa and Y. H. Ohtsuki. *Phys.Rev. B*, 9:4719, 1974.

[47] L.E.Porter. *Phys.Rev.A*, 50:2397, 1994.

[48] J.Ziegler, J.P.Biersack . *Nucl.Inst.and Meth.*, 194:pp 93, 1982.

[49] Werner Brandt and M.Kitagawa. *Phys.Rev.B*, 25(2):5631, 1982.

[50] H.Y.Chan, K.Nordlund, H-J.L.Gossman et al. *Thin Solid Films*, 504:121, 2006.

[51] M.J.Puska, R.M.Nieminen. *Phys.Rev.B*, 27:6121, 1983.

[52] D.J.Land, J.G.Brennan. *At.Dat.Nucl.Dat.Table*, 22:236, 1978.

[53] V.Kuzmin. *Nucl. Instr. and Meth. B*, 249:13, 2006.

[54] R.L.Klueh, K.Ehrlich, F.Abe. *J.Nucl.Mater*, 191-194:126, 1992.

[55] A.F.Tavassoli. *J.Nucl.Mater*, 302:73, 2002.

[56] K.L.Merkle, W.Jager. *Phil.Mag.A*, 44:741, 1980.

[57] S.E.Donnelly, R.C.Birtcher. *Phys.Rev.B*, 56:13599, 1997.

[58] P.Sigmund. *Phys.Rev.B*, 184:383, 1969.

[59] J.Bohdansky. *Nucl. Instr. and Meth. B*, 2:587, 1984.

[60] C.Garcia-Rosales, W.Eckstein, J.Roth. *J.Nucl.Mater.*, 218:8, 1994.

[61] W.Eckstein, R.Preuss. *J.Nucl.Mater.*, 320:209, 2003.

[62] N.Matsunami,Y.Yamamura, Y.Itakawa, N.Itoh,Y.Kazumata, S.Miyagawa, K.Morita, R.Shimizuet, H.Tawara. *Atom. Data Nucl. Tables*, 31:1, 1984.

[63] Y.Yamamura, H.Tawara. *Atom. Data Nucl. Tables*, 62:149, 1996.

[64] M.P.Seah. *Nucl. Instr. and Meth. B*, 229:348, 2005.

[65] R.K.Janev, Yu.V.Ralchenko, T.Kenmotsu, K.Hosaka. *J.Nucl.Mater.*, 290-293:104, 2001.

[66] V.I.Shulga. *Nucl. Instr. and Meth. B.*, 195:291, 2002.

[67] Y.Yamamura, Y.Itakawa, N.Itoh. *IPPJ-AM-26*. Nagoya, 1983.

[68] M..W. Thompson. *Defects and radiation damage in metals* . Cambridge U.P., 1969.

[69] H.E.Wilhem. *Australian Journal of Physics*, 38(2):125, 1985.

[70] Y.Kitazoe,N.Hiraoka and Yamamura. *Surface Science*, 111(3):381, 1981.

[71] M.M.Jakas. *Rad.Eff.and Defects in Solids*, 152(2):157, 2000.

[72] J.Bohandsky, J.Roth and H.Bay,. *J.Appl.Phys.*, 51:2861, 1980.

[73] G.H. Kinchin, R.S. Pease. *Reports on Progress in Physics*, 18:1, 1955.

[74] M.J. Norgett, M.T. Robinson, I.M. Torrens. *Nucl.Eng.Des.*, 33:50, 1975.

[75] A.Messiah. *Quantum Mechanics*. John Wiley, New York, 1976.

[76] J.P.Perdew and A.Zunger. *Phys.Rev.B*, 23:5048, 1981.

[77] P.Hohenberg and W.Kohn. *Phys.Rev.*, 136:864, 1964.

[78] R.Smith, B.King, K.Beardmore. *Rad.Eff.and Defects in Solids*, 141:425, 1997.

[79] R.Vascon, N.V.Doan. *Rad.Eff.and Defects in Solids*, 141:375, 1997.

[80] S.Pronneck, A.Caro, M.Victoria, T.Diaz de la Rubia, M.W.Guinan. *J.Mater.Res.*, 6 No. 3:483, 1991.

[81] L. Malerba, D. Terentyev, P. Olsson, R. Chakarova, J.Wallenius. *J. Nucl. Mater.*, 329-333:1156., 2004.

[82] P.M.Morse. *Phy.Rev.*, 34:57, 1929.

[83] J.N. Murrell, R.E.Mottram. *Mol.Phys.*, 69(3):571, 1990.

[84] Murray S.Daw, M.I.Baskes. *Phys.Rev.B*, 29(12):6443, 1984.

[85] M.W.Finnis, J.E.Sinclair,. *Philos. Mag. A*, 50:45; erratum: Philos. Mag. A 53(1986)161, 1984.

[86] M.I.Baskes. *Phys.Rev.B*, 46(5):2727, 1992.

[87] J.E.Lennard-Jones. *Proc.Roy.Soc.A*, 106:441, 1924.

[88] R.Ryberg. *Z.Physik*, 73:376, 1931.

[89] F.H.Stillinger and T.A.Weber. *Phys.Rev.B*, 31(8):5262, 1985.

[90] J.Tersoff. *Phys.Rev.Lett.*, 56:632, 1986.

[91] J.Tersoff. *Phys.Rev. B*, 37(12):6991, 1988.

[92] P.N. Keating. *Phy.Rev.*, 145:637, 1966.

[93] M.P. Allen, D.J. Tildesley. *Computer Simulation in Chemical Physics.* Kluwer Academic Publishers, 1992.

[94] Ian M.Torrens. *Interatomic Potentials.* Academic Press, 1972.

[95] R.A.Johnson. *Phys.Rev.*, 134(5A):A1329, 1964.

[96] R.A.Johnson. *Phys.Rev.*, 145(2):423, 1966.

[97] R.A.Johnson. *Acta Metallurgica*, 13:1259, 1965.

[98] R.A.Johnson. *Acta Metallurgica*, 12:443, 1964.

[99] R.A.Johnson. *Phys.Rev.*, 27(4):2014, 1983.

[100] M.Dijkstra, R.van Roij, R.Evans. *Phys. Rev. Lett.*, 81(11):2268, 1998.

[101] L. Woodcock. *Faraday Discuss.*, 106:325, 1997.

[102] D. J. Malcolme-Lawes. *J. Chem. Soc., Faraday Trans. 2*, 68:1613, 1972.

[103] T.Mohri, T.Horiuchi, H.Uawa, M.Igarashi, F.Abe. *J.Alloys and Compounds*, 317-318:13, 2001.

[104] T.Horiuchi, M.Igarashi, F.Abe, T.Mohri.

[105] F.F.Abraham, C.R.Brundle. *J.Vac.Sci.Technol.*, 18:506, 1981.

[106] L.A.Girifalco AND V.G.Weizer. *Phys. Rev.*, 114 (3):687, 1959.

[107] R.C.Lincoln, K.M.Koliwad, P.B.Ghate. *Phys. Rev.*, 157(3):463, 1967.

[108] P.Shah, P.Chakrabarti, C.Chakravarty. *Molecular Physics*, 99 (7):573, 2001.

[109] Kevin Cahill and V.Adrian Parsegian. *Journal of Chemical Physics*, 121 (22), 2004.

[110] A.J.C. Ladd, L.V. Woodcock. *Molec. Phys.*, 36:611, 1978.

[111] F.Ercolessi, M.Parrinello, E.Tosatti. *Philo.Mag.A*, 58:213, 1988.

[112] M.Born. *Cambridge Phil. Soc.*, 36:160, 1940.

[113] C.C.Matthai, P.J.Grout, N.H.March. *J.Phys.Chem.Solids*, 42:317, 1981.

[114] A.Lindgren, L.Wallden, J.Rundgren, P.Westrin. *Phys.Rev.B*, 29:576, 1984.

[115] Y.Kuk, L.C.Feldman. *Phys.Rev.B*, 30:5811, 1984.

[116] S.E.Imamova, P.A.Atanasov, N.N.Nedialkov,F.Dausinger, P.Berger. *Nucl. Instr. and Meth. B*, 227:490, 2005.

[117] C.C.Matthai,D.J.Bacon. *J.Nucl.Mater.*, 114:22, 1983.

[118] H. Cox, R.L. Johnston, J.N. Murrell. *J. Sol. State. Chem.*, 145:517, 1999.

[119] J.E.Hearn, R.L.Johnston,S.Leoni,J.N.Murrell. *J.Chem.Soc. Faraday Trans.*, 92:425, 1996.

[120] Fei Gao, Eric J. Bylaska,William J. Weber, L.Rene Corrales. *Nucl. Instr. and Meth. B*, 180:286, 2001.

[121] Fei Gao, William J. Weber. *Nucl. Instr. and Meth. B*, 191:504, 2002.

[122] Fei Long. *Computer Simulation Technique of Pseudoptential- Theory and Molecular Dynamics*. PhD thesis, University of Hull, 2000.

[123] D.E.Ashenford, Fei Long, W.E.Hagston, B.Lunn, A.Mathews. *Surface Coating Technology*, 116-119:699, 1999.

[124] M.M.Ali. *Pramana-Journal of Physics*, 53:775, 1999.

[125] K.W.Jacobsen, J.K.Norskov, M.J.Puska. *Phys.Rev.B*, 35(14):7423, 1987.

[126] Murray S. Daw. *Phys.Rev.B*, 39(11):7441, 1989.

[127] Murray S. Daw, M.I.Baskes. *Phys.Rev.Letters*, 50(17):1285, 1983.

[128] S.M.Foiles. *Phys.Rev.B*, 32(12):7685, 1985.

[129] Shao Ping Chen, A.F.Voter, D.J.Srolovitz. *Mat.Res.Soc.Symp.Proc.*, 82:515, 1987.

[130] C.L.Liu,J.M.Cohen, J.B.Adams, A.F.Voter. *Surface Science*, 253:334, 1991.

[131] R.A. Johnson, D.J. Oh. *J. Mater. Res.*, 4 (5):1195., 1989.

[132] R.Pasianot, D.Farkas, E.J.Savino. *Phys. Rev. B*, 43(9):6952, 1991.

[133] A.M. Guellil, J.B. Adams. *J. Mater. Res.*, 7 (3):639., 1992.

[134] Wangyu Hu,Xiaolin Shu, Bangwei Zhang. *Computational Materials Science*, 23:175, 2002.

[135] A.Voter. *Materials Research Society Bulletin*, 21 (2):17, 1996.

[136] A.F.Voter,Shao Ping Chen. *Mat.Res.Soc.Symp.Proc.*, 82:175, 1987.

[137] R.A.Johnson. *Phys. Rev. B*, 39:17, 1988.

[138] M.Ruda, D.Farkas, J.Abriata. *Scripta Materialia*, 46:349, 2002.

[139] Mario Del Popolo, Ezequiel Leiva. *J.Electroanal.Chem.*, 440:271, 1997.

[140] R.C.Pasianot, A.M.Monti. *J.Nucl.Mater.*, 264:198, 1999.

[141] D.Farkas,M.J.Mehl,D.A.Papaconstantopoulos.
Mat.Res.Soc.Symp.Proc., 653:Z6.4.1, 2001.

[142] James H. Rose,,John R. Smith, Francisco Guinea, John Ferrante,.
Phys.Rev.B, 29(6):2963, 1984.

[143] G.J.Ackland, M.W.Finnis, V.Vitek. *J.Phys.F:Met.Phys.*, 18:L153, 1988.

[144] M.W.Finnis, A.T.Paxton,D.G.Pettifor. *Philos. Mag. A*, 58(1):143, 1988.

[145] C.Kittel. *Introduction to Solid State Physics.* 6th Ed, John Wiley, 1987.

[146] C.C.Matthai, D.J.Bacon. *Philos. Mag. A*, 52(1):1, 1985.

[147] G.J.Ackland, M.W.Finnis. *Philos. Mag. A*, 54(2):301, 1986.

[148] J.M.Harder, D.J.Bacon. *Philos. Mag. A*, 54(5):651, 1986.

[149] G.J. Ackland, R. Thetford. *Philos. Mag. A*, 56(1):15, 1987.

[150] J.M.Harder, D.J.Bacon. *Philos. Mag. A*, 58(1):165, 1988.

[151] G.J.Ackland, G.Tichy, V.Vitek, M.W.Finnis. *Philos. Mag. A*, 56(6):735, 1987.

[152] F.Gao, D.J.Bacon, G.J.Ackland. *Philos. Mag. A*, 67(2):275, 1993.

[153] G.J.Ackland, V.Vitek. *Phys.Rev.B*, 41(15):10324, 1990.

[154] F.Gao, D.J.Bacon. *Philos. Mag. A*, 67(2):289, 1993.

[155] Graeme J.Ackland. *Philos. Mag. A*, 66(6):917, 1992.

[156] A.P.Sutton,J.Chen. *Philos. Mag. A*, 61(3):139, 1990.

[157] H.Rafii Tabar, A.P.Sutton. *Philos. Mag. A*, 63(4):217, 1991.

[158] Fabrizio Cleri, Vittorio Rosato. *Phys. Rev. B*, 48(1):22, 1993.

[159] John A. Moriarty. *Phys.Rev.B*, 38:3199, 1988.

[160] M.I.Baskes. *Mater.Chem.Phys.*, 50:152, 1997.

[161] Byeng-Joo Lee, M.I. Baskes. *Phys.Rev.B*, 62(13):8564, 2000.

[162] Byeng-Joo Lee, M.I. Baskes, Hanchul Kim, Yang Koo Cho. *Phys.Rev.B*, 64:184102, 2001.

[163] Kan Hachiya, Yasuhiko Ito. *J. Alloys.Comp.*, 337:53, 2002.

[164] Ronald E. Cohen. *Phys.Rev.B*, 50(19):14694, 1994.

[165] A.E.Carlsson. *Phys.Rev.B*, 44(13):6590, 1991.

[166] M.Born, J.E.Mayer. *Z.Phys.*, 75:1, 1932.

[167] F.Maury, M.Biget, P.Vajda,A.Lucasson, P.Lucasson. *Phy.Rev.B*, 14:5303, 1976.

[168] D.C.Rapaport. *The Art of Molecular Dynamics Simulation*. Cambridge University Press, 1995.

[169] Daan Frenkel, Berend Smit . *Understanding Molecular Simulation*. Academic press, 1996.

[170] L.Verlet. *Phys.Rev.*, 159:98, 1967.

[171] D.Beeman. *J.Comput.Phys.*, 20:130, 1976.

[172] R.Smith, D.E.Harrison. *Computers in Physics*, 68:7, 1989.

[173] William Mattson, Betsy M. Rice. *Computer Physics communications.*, 119:135, 1999.

[174] H.J.C.Berendsen et al. *J.Chem.Phys.*, 81:3684, 1984.

[175] S.Nose. *Prog.Theor.Phys.Suppl.*, 103:1, 1991.

[176] W.G.Hoover. *Phys.Rev.A*, 31:1695, 1985.

[177] Guihua.Zhang, Tamar Schlick. *Molecular Physics.*, 84:1077, 1995.

[178] K.Cho,J.D.Joannopoulos, Leonard Kleinman. *Phys.Rev.E*, 47:3145, 1993.

[179] P.Olsson, R.Chakarova, J.Wallenius, V.Pontikis. *Chemical Physics*, 236:243, 1998.

[180] R.Biswas, D.R.Hamann. *Phys.Rev.B*, 34, 1983.

[181] M.I. Haftel, T.D. Andreadis, J.V. Lill. *Phys. Rev. B*, 42:11540, 1990.

[182] R.J. Harrison, A.F. Voter, S.P.Chen. *Atomistic Simulation of Materials-Beyond Pair Potentials,*. Plenum, New York, 1989.

[183] G.J.Ackland, D.J.Bacon, A.F.Calder, T.Harry. *Phil.Mag.A*, 75:713, 1997.

[184] G.J.Ackland, M.I.Mendelev, D.J.Srolovitz, S.Han, A.V. Barashev. *J. Phys.: Condens. Matter*, 16:S2629, 2004.

[185] G.Simonelli, R.Pasionat, E.J.Savino. *Mat.Res.Soc.Symp.Proc*, 291:567, 1993.

[186] Yoshiharu Shimomura, Kenjiro Sugio, Yoshiaki Kogure, Masao Doyama. *Computional Materials Science*, 14:36, 1999.

[187] Zhang Bangwei, Ouyang Yifang, Liao Shuzhi, Jin Zhanpeng. *Physica B*, 262:218, 1999.

[188] H.Chamati, N.I.Papanicolaou, Y.Mishin, D.A.Papaconstantopoulos. *Surface Science*, 600:1793, 2006.

[189] T.Konishi, K.Ohsawa, H.Abe, E.Kuramoto. *Comp.Mat.Science*, 14:108, 1999.

[190] J.Wallenius et al. *J. Nucl. Mater.*, 329-333:1175, 2004.

[191] P.Olsson,R.Chakarova,J.Wallenius, V.Pontikis. *Phys.Rev*, 25:527, 2002.

[192] B.J.Lee et al. *Calphad*, 25(4):527, 2002.

[193] Tatsuya Ohira, Yikihiko Inoue. *Mat.Res.Soc.Symp.Proc.*, 492:401, 1998.

[194] Tatsuya Ohira, Yikihiko Inoue,Kazutoyo Murata,Jiro Murayama. *Applied Surface Science*, 171:175, 2001.

[195] D.Farkas,C.G.Schon,M.S.F De Lima,H.Goldenstein . *Acta Mater.*, 44:409, 1996.

[196] J.H.Shim, H.J.Lee, B.D.Wirth. *Fusion Materials: Semiannual Progress Report*, 37:120, 2004.

[197] A.F.Calder, D.J.Bacon. *J.Nucl.Mater.*, 207:25, 1993.

[198] N. Soneda, T. Diaz de la Rubia. *Philos. Mag. A*, 78:995, 1998.

[199] C.S. Becquart, C. Domain, A. Legris, J.-C. Van Duysen. *Mater. Res. Soc. Symp. Proc.*, 650:R3.24.1., 2001.

[200] G.A.KimmelCooper, B.H.Cooper. *Phys. Rev. B*, 48:12164, 1993.

[201] Philip.B. Allen. *Phys.Rev.B*, 36(5):2920, 1987.

[202] J.Kroger. *Rep.Prog.Phys*, 69:899, 2006.

[203] Philip.B. Allen. *Phys.Rev.Lett.*, 59(13):1460, 1987.

[204] R.Bauer,A.Schmid,P.Pavone,D.Strauch. *Phys.Rev.B*, 57(18):11276, 1998.

[205] C.P.Flynn, R.S.Averback. *Phys. Rev. B*, 38:7118, 1988.

[206] I.Kopopen. *J.Appl.Phys.*, 72:1194, 1992.

[207] K.Nordlund, J.Tarus, J.Keinonen, M.Ghaly, R.S.Averback. *Nucl. Instr. and Meth. B.*, 164-165:441, 2000.

[208] A.Caro and M.Victoria. *Phys.Rev. A*, 40(5):2287, 1989.

[209] M.W.Finnis, A.Agnew, A.J.E.Foreman. *Phys. Rev. B*, 44:567, 1990.

[210] F.Gao, D.J.Bacon, P.E.J.Flewitt, T.A.Lewis. *Modelling Simul.Mater.Sci.*, 6:543, 1998.

[211] M.L.Jenkins, C.A.English, B.L.Eyre. *Philos.Mag.*, 38:97, 1978.

[212] Kirk MA, Robertson IM, Vetrano JS, Jenkins ML, Funk LL. *Proc. 13th Int. Symp. on Effects of Irradiation on Materials. Rad. Eff.*, page 12, 1987.

[213] V.G.Kapinos, D.J.Bacon. *Phys.Rev.B*, 53(13):8287, 1996.

[214] J.G.Fujimoto,J.M.Liu,E.P.Ippen, N.Bloembergen . *Phys.Rev.Lett.*, 5:1837, 1984.

[215] A.E.Stuchbery, E.Bezakova. *Phys. Rev. Lett.*, 82:3637, 1999.

[216] K.Nordlund,L.Wei,Y.Zhong, R.S.Averback. *Phys.Rev.B*, 57(22):R13965, 1998.

[217] Eugeni E.Zhurkin, Anton S.Kolesnikov. *Nucl. Instr. and Meth. B*, 202:269, 2003.

[218] R.E.Stoller, G.R.Odette, B.D.Wirth. *J.Nucl.Mater.*, 251:49, 1997.

[219] R.E.Stoller. *Nucl.Eng.Des*, 195:129, 2000.

[220] W.H.Hoover,B.P.Flannery, S.A.Teukolsky, W.T.Vetterling,. *Numerical Recipes*. Cambridge University Press, 1986.

[221] D.J.Bacon, T.Diaz de la Rubia. *J.Nucl.Mater.*, 216:275, 1994.

[222] Andrea Friedrich, Herbert M. Urbassek. *Surface Science*, 547:3:315, 2003.

[223] Frank Karetta, Herbert M. Urbassek. *J.Appl.Phys.*, 71 No. 11:5410, 1992.

[224] C.Domain, C.S.Becquart. *Phys.Rev.B*, 65:24103, 2002.

[225] B.Mayer,H.Anton,E.Bott et al. . *Intermetallics*, 11:23, 2003.

[226] G.Simmons, H. Wang. *Single Crystal Elastic Conctants and Calculated Aggregate Properties: A Handbook.* MIT, Cambridge, 1971.

[227] L.D. Schepper, D. Segers, L. Dorikens-Vapaert, M. Dorikens, G.Knuyt, L. Stals, P. Moser. *Phys. Rev. B*, 27:5257, 1983.

[228] R. Chakarova, V. Pontikis, J. Wallenius. Development of fe(bcc)-cr many body potential and cohesion model. *WP6 Delivery Report Nr. 6, SPIRE project, EC contract no. FIKW-CT-2000-00058*, June 2002. Available from: www.neutron.kth.se/publications/library/DR-6.pdf.

[229] K. Maier, H. Metz, D. Herlach, H.-E. Schaefer. *J. Nucl. Mater.*, 69(70):589, 1978.

[230] A. Seeger. *Phys. Stat. Sol. (a)*, 167, 1998.

[231] C.S.Becquart, C.Domain. *Nucl.Inst.and Meth. B*, 202:44, 2003.

[232] H. Wollenberger. *Physical Metallurgy,*, volume vol. 2. R. Cahn, P. Haasen (Eds.) North-Holland, 1996.

[233] Andre Anders . *Phys.Rev.E*, 55 No. 1:969, 1997.

[234] A.J.E.Foreman, W.J.Phythian, C.A.English. *Phil.Mag.A*, 66 No.5:671, 1992.

[235] T.Diaz de la Rubia, A.Caro, M.Spaczer. *Phys.Rev.B*, 47 No.17:11483, 1993.

[236] Huilong Zhu, Nghi Q. Lam. *Nucl. Instr. and Meth. B*, 95:25, 1995.

[237] Antonio Miotello, Roger Kelly . *Nucl. Instr. and Meth. B*, 122:458, 1997.

[238] F.Gao, D.J.Bacon, L.M.Howe, C.B.So . *J.Nucl.Mater.*, 294:288, 2001.

[239] Mai Ghaly, R.S.Averback. *Phys.Rev.Lett*, 72 No.3:364, 1994.

[240] M.Ghaly , R.S.Averback, T.Diaz de la Rubia. *Nucl. Instr. and Meth. B*, 102:51, 1995.

[241] K.Nordlund, J.Keinonen,M.Ghaly, R.S.Averback. *Nucl. Instr. and Meth. B*, 148:74, 1999.

[242] J.L.Vossen. *J. Vac.Sci.Technol.*, 8:S12, 1971.

[243] D.Rosenberg, G.K.Wehner. *J.Appl.Phys.*, 33:1842, 1962.

[244] P.Sigmud. *Phys.Rev.*, 184:383, 1969.

[245] C.Lehman, P.Sigmud. *Phys. Status Solidi*, 16:507, 1966.

[246] R.Behrish, W.Eckstein. *Nucl. Instr. and Meth. B*, 82:255, 1993.

[247] N.V.Doan, R.Vascon. *Nucl. Instr. and Meth. B*, 135:207, 1998.

[248] J.M.Walls, R.Smith. *Surface Science Techniques*. British Library Cataloguing, 1994.

[249] S.W.Rosencrance, N.Winograd, B.J.Garrison. *Phys.Rev.B*, 53(5):2378, 1996.

[250] M.Kustner,W.Eckstein,E.Hechtl,J.Roth. *J.Nucl.Mater.*, 265:22, 1999.

[251] M.A.Karolewski. *Nucl. Instr. and Meth. B.*, 194:26, 2002.

[252] X.G. Gong, Q.Q.Zheng. *J.Phys:Condens.Matter*, 7:2421, 1995.

[253] A.A.Dzhurakhalov, I.I.Khafizov. *Nucl. Instr. and Meth. B.*, 153:326, 1999.

[254] I.S.Tilinin, G.Betz. *Nucl. Instr. and Meth. B.*, 115:565, 1996.

[255] Roger Smith, Don E. Harrison, Barbara J. Garrison. *Nucl. Instr. and Meth. B.*, 46:1, 1990.

[256] Che-Chen Chang and Nicholas Winograd . *Phys.Rev.B*, 39:6:3467, 1989.

[257] Shuzo Ueda, Toshira Ohsaka, Satoru Kuwajima. *J.Nucl.Mater.*, 283-287:1100, 2000.

[258] Jae S.Lee,Jae H.Lee. *Surface and Coatings Technology*, 196:358, 2005.

[259] E. Hechtl, W. Eckstein and J. Roth. *J.Nucl.Mater.*, 90:505, 1994.

[260] P.Wetz, W.Kruger, A.Scharmann, K.H.Schartner. *Radiation Measurements*, 27:569, 1997.

[261] M.A.Karolewski. *Nucl. Instr. and Meth. B.*, 211:190, 2003.

[262] Heinrich Gades, Herbert M. Urbassek. *Phys. Rev. B*, 50:11167, 1994.

[263] A.Wucher, B.J.Garrison. *J.Chem.Phys.*, 105(14):5999, 1996.

[264] Nicholas Winograd, Don E. Harrison and Barbara Garrison. *Surface science*, 78:467, 1978.

[265] M.H.Shapiro, E.Trovato, T.A.Tombrello. *Nucl. Instr. and Meth. B.*, 180:58, 2001.